Flexible Superconducting Microwave Interconnects and Connectors

by

Simin Zou

A dissertation submitted to the Graduate Faculty of
Auburn University
in partial fulfillment of the
requirements for the Degree of
Doctor of Philosophy

Auburn, Alabama
May 07, 2018

Keywords: Superconductor, resonators, interconnects, microwave connectors, polyimide, niobium

Approved by

Michael C. Hamilton, Chair, Associate Professor of Electrical and Computer Engineering
Lloyd S. Riggs, Professor of Electrical and Computer Engineering
Mark L. Adams, Assistant Professor of Electrical and Computer Engineering
Minseo Park, Professor of Physics
Ryan Comes, Assistant Professor of Physics

Abstract

One of the major limitations to constructing densely-integrated cryogenic electronic systems is the electrical interconnect technology. Superconducting cables with multiple signals, high signal density, low loss, low thermal leakage and small cross-sections are desirable. The superconducting characteristics of thin-film niobium (Nb) make it a viable material for realizing low-temperature (4 K or below) superconducting cables, such as high density DC cables and RF cables including microstrip and stripline. Thin-film flexible superconducting ribbon cables incorporating polymer dielectrics are particularly useful for making multiple interconnections between different substrates and/or different temperature zones.

Half-wavelength, capacitively coupled superconducting microstrip transmission line resonators and stripline transmission line resonators were used to study the RF/microwave properties (such as loss tangent) of various flexible substrates and compare the performance of transmission lines with similar structure. These high quality factor resonators were used to characterize substrate' dielectric loss and superconductor loss at multiple frequencies from 10 MHz to 21 GHz and temperatures from $\sim$ 1.2 K to 4.2 K. As a transition structure, embedded microstrip transmission line resonators were used to investigate impact of encapsulation layer thickness, and related fabrication processes, on resonator performance, which is related to materials properties (i.e. superconductor loss and dielectric loss).

Nb-based superconducting thin-film microstrip transmission lines and microwave connectors were also designed, fabricated and characterized. To investigate the feasibility of a superconducting microwave connector, Ti/Cu/Au DC cables and RF cables were used and tested at different temperatures (room temperature, 77 K and 4.2 K) with this type of connector. Fabrication procedures, assembly and characterization results are demonstrated. The microwave performance of Nb microstrip exhibited significantly low transmission loss

of less than 0.85 dB/m up to 14 GHz at 4.2 K. Microwave connectors were used to connect microstrip cables end-to-end. The connectors were designed to be easily aligned for narrow trace widths and use pressure to make electrical connection, providing sufficiently low resistance of ∼15 mΩ and excellent microwave performance. A distributed element model was used to model the microstrip-to-microstrip interconnection of a reconnected structure. The proposed microwave connection methods exhibited a return loss better than 15 dB and an insertion loss less than 0.12 dB up to 14 GHz. Moreover, the microwave connector showed both encouraging thermal and re-assembly reliability and performance.

To aid in the design of the superconducting flexible cables using Nb, it is important to evaluate not only the electrical performance, but also mechanical reliability performance, since these cables should be robust when flexed. In this study, fatigue and bending tests on Nb-only and Ti/Nb/Cu multilayer signal lines on flexible Kapton substrates were performed. Critical current (I_c) of these wires during fatigue and bending testing were measured. From the fatigue test, I_c decreased with increasing number of bending-flattening cycles. I_c degradation of Nb-only cables occurred at a lower number of cycles than the Ti/Nb/Cu cables. After 250 fatigue cycles, Ti/Nb/Cu wires with the thickest Ti adhesion layer and Cu capping layer exhibited the lowest I_c degradation of $\sim$ 1.2 % and 0 % in tensile and compressive cases, respectively. The I_c degradation values for the Nb-only cables were $\sim$ 32.8 % and $\sim$ 27.2 % for tensile and compression, respectively. From bending tests, where the sample was held in an intentionally curved configuration during testing, I_c degradation of the Nb-only cables was more severe than that of the Ti/Nb/Cu cables during tensile bending. When the cables were subjected to compressive bending tests, the I_c of Ti/Nb/Cu cables was minimally affected, even for the smallest bending radius tested (5 mm), while the I_c of the Nb-only cables exhibited a degradation of $\sim$ 27.9 %. These results demonstrate that Ti adhesion layer and Cu capping layer provide reliability enhancement for superconducting Nb flex cables fabricated on Kapton. Superconducting properties (T_c and I_c) and mechanical reliability performance (fatigue behavior) for embedded and non-embedded Nb DC cables on PI-2611 polyimide

were investigated. A slightly lower T_c value of $\sim$ 8.2 K was found for Nb embedded cables compared to non-embedded Nb DC testing lines with a T_c of $\sim$8.8 K, which was explained as due to subsequent fabrication steps causing a degradation of the superconducting properties of Nb. I_c of embedded DC cables was comparable with that for non-embedded ones, with values of $\sim$ 0.2 A at 4.2 K. We found that the use of a properly-cured PI-2611 encapsulation layer can effectively enhance the mechanical reliability performance (i.e. bending fatigue behavior) of Nb superconducting cables. Embedded Nb DC cables showed degradation of I_c less than 5 %, while that of non-embedded DC cables was more than 26.5 % after 500 fatigue cycles.

This projects and work presented in this dissertation not only provide design guidance for constructing ultralow-loss flexible thin-film superconducting interconnects and connectors, but also discuss methods to build interconnects with enhanced mechanical reliability. The results presented here are critical for future high performance interconnects that are expected to find great use in cryogenic electronics systems, including systems for superconducting quantum computing and related technologies.

Acknowledgments

First and foremost, I would like to express my great gratitude and thanks to my academic advisor Dr. Michael C. Hamilton for providing significant guidance, assistance, and financial support throughout my PhD study and research at Auburn University. Dr. Lloyd Riggs, Dr. Mark Adams and Dr. Minseo Park are also thanked for their review and commentary, as is Dr. Ryan Comes for serving as the University Reader for this work. Their comments and advice are very valuable and helpful.

Special thanks go to Dr. David B. Tuckerman and Microsoft Research for financial support and technical guidance in this work.

The author would also like to thank Dr. Charles Ellis, John Sellers, William Baugh, John Tennant, Tamara Isaacs-smith, and my lab-mates and friends Vaibhav Gupta, Bhargav Yelamanchili, Yang Cao, Zhangming Zhou, Shiqiang Wang, Ran Cheng, Pingye Xu, Jinzi Cui, Fang Yu, Uday Sravan Goteti for their cooperative support and encouragement through my PhD study. Most of these colleagues are also co-authors on the papers that make-up this dissertation and I sincerely recognize their contribution to those paper and this dissertation.

A personal note of appreciation goes to my parents Xiaohui Zou and Yao Ma and my husband Dr. Di Zhang for their support, care and love throughout the author's academic endeavors.

Table of Contents

List of Figures

List of Tables

List of Abbreviations

$\Delta(T)$	Energy gap at a specific temperature in Kelvin
ϵ_r	Relative permittivity (Dielectric constant)
λ	Wavelength
λ_L	London penetration depth
ξ	Coherence length
AC	Alternating current
BCS	Bardeen Cooper Schrieffer
DC	Direct current
EMI	electromagnetic interference
FFC	flexible flat cables
FPC	flexible printed circuit
I_c	Critical current
k_B	Boltzmann constant
L_K	Kinetic inductance
LHe	Liquid helium
LN_2	Liquid nitrogen
MgB_2	Magnesium diboride

PCB printed circuit board

PR Photoresist

PT Pulse Tube Cryostat

Q Quality factor

$Q_{coupling}$ Quality factor related to coupling loss

Q_c Quality factor related to conductor loss

Q_d Quality factor related to dielectric loss

Q_l Loaded quality factor

Q_r Quality factor related to radiation loss

Q_u Unloaded quality factor

RF Radio frequency

RRR Residual-resistance ratio

RT Room temperature

SOLR Short Open Load Reciprocal Thru

STL Stripline

T_c Critical transition temperature

UBM Under bump metallurgy

YBCO Yttrium barium copper oxide, $YB_2Cu_3O_{7-\delta}$

YSZ Yttria-stabilized zirconia

ZIF zero-insertion-force

Chapter 1

Introduction

1.1 Background and Motivation

In the past decades, interest in quantum computation and quantum computing hardware has increased significantly because of the following critical insights. One insight is that quantum algorithms are expected to outperform important and corresponding algorithms performed on a classical digital computer. However, preventing quantum decoherence completely is impossible, which will cause problems in quantum machine implementation [1-2]. This is important to note that, to prevent fast decoherence, some quantum systems (e.g. superconducting qubits) must be cooled to mK temperatures. The other important insight is that, with the discovery of quantum error-correction [3-5], the operation of a quantum computer can be realized experimentally even with noise and decoherence. A practical quantum computer [6-10] may require millions of physical qubits, along with corresponding infrastructure and interconnects, in order to overcome high physical error rate. However, limited attention has been given to the problem of how to transmit and receive a great number of RF/microwave/high speed signals, to and from these qubits, to operate quantum computers, especially when the signal needs to communicate between different temperature stages in cryogenic systems (e.g., a dilution refrigerator). The work presented in this dissertation is intended to address the challenge of cryogenic interconnection and microwave connectors.

Currently, semi-rigid coaxial cables were widely used in cryogenic and dilution refrigerator systems. However, a dilution refrigerator only has limited physical volume and cooling capacity. Moreover, considering the physical size, thermal leakage and cost issue, it becomes impractical to use these cables in the long run. The solution we presented in this work is to develop thin-film, flexible superconducting transmission lines with controlled-impedance,

small cross section, wide bandwidths (DC to >14 GHz), low insertion loss and low thermal leakage. Considering the low surface impedance of superconducting conductors and using thin-film dielectric substrate, small dimension of the cable can be achieved. Also, by using low loss dielectric material and superconducting metal, we are able to decrease the microwave loss of the cables. Additionally, ultra-low thermal conductance of the thin-film superconducting cables can address the thermal leakage issue, which is a significant problem with coaxial cables made using normal conductors. An Optimized material stack-up needs to be considered in regards to mechanical reliability aspects, because the cables are very likely to be subjected to large deformation in the real working environment (e.g., bend during cable handling and assembly). Finally, microwave connectors that are compatible with thin-film transmission lines are needed. Assembly convenience, loss, weight and reliability of microwave connectors also need to be considered.

In this work, in order to select a low loss dielectric to build desired cables, half-wavelength, capacitively coupled superconducting microstrip resonators were used to characterize high frequency properties (e.g., loss tangent) of spin-on, flexible dielectric materials (e.g., polyimide PI-2611) at cryogenic temperatures. These resonators were designed to have 50 Ω characteristic impedance of the microstrip to represent similar-fabricated transmission lines and to provide a sensitive measure of the overall microstrip loss as a function of frequency and temperature. Stripline resonators fabricated on HD-4110 substrate are also discussed in this work. Design, fabrication, assembly method, simulation and measurement results of microwave connectors designed to be interface with thin-film superconducting Nb-based microstrip transmission lines were demonstrated and are described in this dissertation. Corresponding DC testing cables were used to test current carrying capacity (e.g., critical current, I_c) at different temperatures. DC testing cables with different material stack-ups were fabricated and tested. Mechanical tests (e.g., fatigue test and bending test) to study the critical current as a function of fatigue cycles and bending radius, were also performed and

provide insight into the mechanical reliability of the present generation of superconducting flex cables.

The work presented in this dissertation provide guidance for the design and fabrication of thin-film superconducting flexible cables with enhanced mechanical reliability and new microwave connectors that are compatible with the thin-film cables.

1.2 Dissertation Outline

In this dissertation, I discuss microwave flexible superconducting interconnects and connector technology. Design, fabrication process and measurement results for various superconducting resonators, superconducting flexible cables and microwave connectors are presented. Also this dissertation specifically evaluates the mechanical performance of superconducting cables with different material stack-ups. The purpose of this dissertation is not only to show current results of this work but also offer useful information for future generations of superconducting cables fabricated using thin film processes in embedded or multilayer configurations. Furthermore, I also describe superconducting microwave connectors for cable-to-cable connections within the cryogenic systems. This dissertation is organized as follows:

- In Chapter 2, I discuss superconducting microwave resonators. I present the purpose of using Nb microstrip transmission line resonators in this work, which is to characterize microwave properties of dielectric material and provide a sensitive measure of properties that impact performance of transmission lines. Experimental techniques, including resonator design, layout, simulation, fabrication procedures, sample assembly processes and experimental setup are reported. I also present measurement and characterization results of Nb microstrip resonators fabricated on different thin-film polyimides HD-4110 and PI-2611. RF performance of non-embedded resonators and embedded resonators were also evaluated and are described. Temperature dependence and encapsulation layer impact on BCS loss and dielectric loss of resonators has also been demonstrated.

I also discuss the design, fabrication processes and characterization results of stripline transmission line resonators on HD-4110 polyimide.

- In Chapter 3, I present RF/microwave cable design, fabrication processes and characterization results of cryogenic RF/microwave cables. I tested microstrip transmission lines with different length up to 20 cm and successfully implemented distributed element models using Keysight ADS, which matched the RF/microwave performance of the superconducting microstrip flex cables at 4.2 K.

- In Chapter 4, I present our solution for cryogenic microwave connection of fabricated thin-film transmission lines. Connector design/layout, fabrication processes and assembly procedures are discussed. I performed DC, time-domain reflectometry (TDR) and S-parameter measurements on intact microstrip and reconnected microstrip and compared the performance. I extracted the intrinsic loss of the new microwave connectors, using reconnected microstrip with different numbers of reconnections. I implemented a distributed element model for the reconnection region. I also evaluated connector thermal reliability and re-assembly reliability performance.

- In Chapter 5, I describe enhance fabrication procedures for superconducting DC cables fabricated on free-standing Kapton substrates and thin-film polyimide substrates specifically with a goal of enhancing reliability. T_c and I_c measurement set-ups and experimental results are presented. I also report T_c and I_c of superconducting DC cables with different thickness of normal metal (Ti, Cu and Al) interfacial layers and different thickness of polyimide encapsulation layer. By performing mechanical tests (e.g., fatigue tests and bending tests), I evaluated the mechanical reliability of these cables. I report that there is I_c degradation in pure Nb cable after mechanical testing and the I_c degradation becomes more serious as the number of fatigue cycles increases and as the bending radius decreases. Surface morphology of cables with I_c degradation are presented in this chapter and provided evidence that cracks on the surface

due to mechanical test lead to I_c degradation. Solutions of improving cable material stack-up (e.g., using normal metal interfacial layer or polyimide encapsulation layer) are illustrated to address the problem.

- In Chapter 6, I summarize the main results of this dissertation.
- In Chapter 7, I discuss the related future research.

Bibliography

[1] A. Ekert and R. Jozsa, "Quantum computation and Shor's factoring algorithm," *Reviews of Modern Physics*, vol. 68, no. 3, p. 733, 1996.

[2] L. K. Grover, "Quantum mechanics helps in searching for a needle in a haystack," *Physical Review Letters*, vol. 79, no. 2, p. 325, 1997.

[3] A. M. Steane, "Error correcting codes in quantum theory," *Physical Review Letters*, vol. 77, no. 5, p. 793, 1996.

[4] S. Lloyd, "A potentially realizable quantum computer," *Science*, vol. 261, no. 5128, pp. 15691571, 1993.

[5] D. A Lidar and T. A Brun, "Quantum error correction," *Cambridge University Press*, 2013.

[6] D. Castelvecchi, "IBM's quantum cloud computer goes commercial," *Nature News*, vol. 543, no. 7644, p. 159, 2017

[7] S. Debnath, N. M. Linke, C. Figgatt, K. A. Landsman, K. Wright and C. Monroe, "Demonstration of a small programmable quantum computer with atomic qubits," *Nature*, vol. 536, no. 7614, p. 63, 2016.

[8] D. Wecker, M. B. Hastings, N. Wiebe, B. K. Clark, C. Nayak, and M. Troyer, "Solving strongly correlated electron models on a quantum computer," *Physical Review A*, vol. 92, no. 6, p. 062318, 2015.

[9] M. Reiher, N. Wiebe, K. M. Svore, D. Wecker and M. Troyer, "Elucidating reaction mechanisms on quantum computers," *Proceedings of the National Academy of Sciences*, p. 201619125, 2017.

[10] L Gomes, "Quantum computing: Both here and not here," *IEEE Spectrum*, vol. 55, no. 4, pp. 42-47, 2018.

Chapter 2

Basics of Superconductivity

Chapter 3

Flexible Superconducting Microwave Resonators

Superconducting microwave resonators are simple but versatile devices. Interest in these devices has increased rapidly over recent decades. Superconducting resonators are targeted for various applications including quantum circuits [1-4], cryogenic detector arrays [5-10] and so on. In this chapter, I discuss another important application of superconducting resonators: material microwave characterization [11-14]. For example, in [15], $YB_2Cu_3O_{7-\delta}$ (YBCO) superconducting microstrip transmission line resonators were used to characterize loss tangent values of thin film ferroelectric materials. In [14], YBCO microstrip ring resonators were used to extract effective dielectric constant of $LaAlO_3$ and London penetration depth (λ) of YBCO. Here, I mainly describe using superconducting microstrip transmission line resonators and stripline transmission line resonators to characterize the loss tangent of dielectric materials because my purpose is to better understand the loss properties for materials used to build superconducting flexible cables. Moreover, by measuring the quality factor of resonators with different material stack-ups, I am able to deduce the microwave performance of transmission lines with the same material stack-up, since transmission line resonators provide a sensitive measure of transmission line characteristics.

3.1 Resonator Theory

3.1.1 Parallel Resonant Circuit Concepts

Near a resonant frequency, a microwave resonator can be modeled by either a series or a parallel RLC lumped-element equivalent circuit. In this study, in order to characterize RF/microwave properties of dielectric material, I used a microstrip circuit consisting of an open-circuited length of transmission line. When the length of the transmission line is one

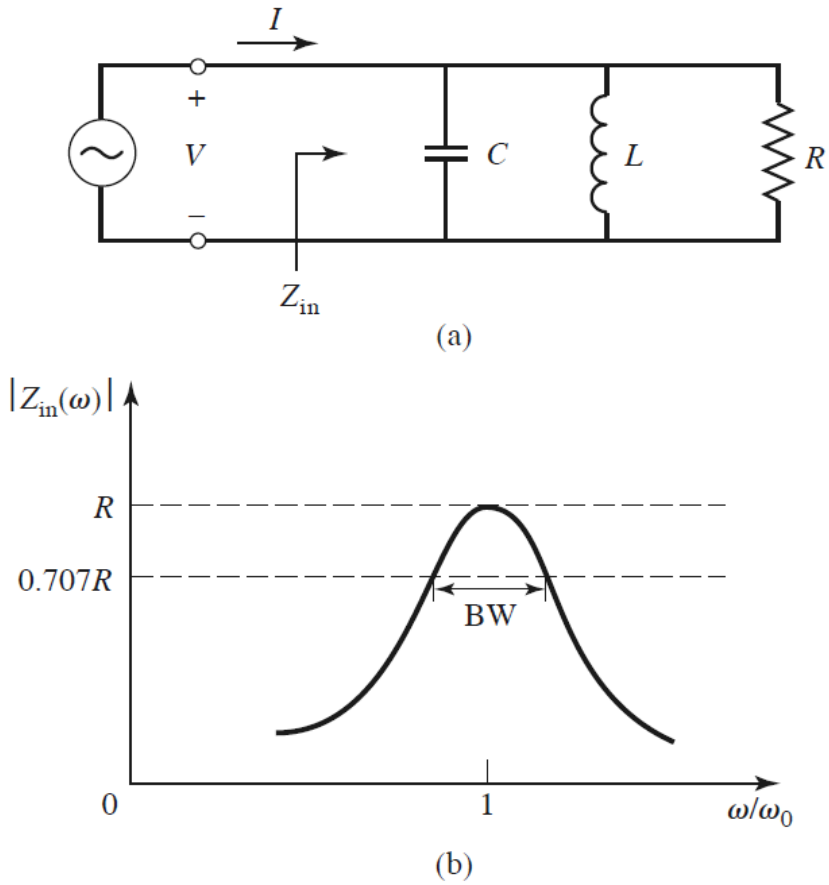

Figure 3.1: (a) A parallel RLC circuit and (b) magnitude of input impedance vs. frequency. Adapted from [16].

or multiple half wavelength ($\lambda/2$), the resonator behaves as a parallel resonant circuit. Next, parallel resonant circuits are discussed.

Figure 3.1(a) shows a typical parallel RLC resonant circuit. The equation for input impedance is:

$$Z_{in} = (\frac{1}{R} + \frac{1}{j\omega L} + j\omega C)^{-1} \tag{3.1}$$

A representative plot of the frequency dependent input impedance is shown in Figure 3.1(b). It can be observed that when frequency is equal to resonant frequency, ω_0, magnitude of input impedance of parallel resonant circuit reaches its maximum value.

The power transmitted to the resonator is give by:

$$P_{in} = \frac{1}{2} \mid V \mid^2 (\frac{1}{R} + \frac{1}{j\omega L} + j\omega C) \tag{3.2}$$

The power dissipated by the resistor is give by:

$$P_{loss} = \frac{1}{2} \frac{\mid V \mid^2}{R} \tag{3.3}$$

and average power stored in the capacitor and inductor are give by:

$$W_e = \frac{1}{4} \mid V \mid^2 C \tag{3.4}$$

and

$$W_m = \frac{1}{4} \mid I_L \mid^2 L = \frac{1}{4} \mid V \mid^2 \frac{1}{\omega^2 L}, \tag{3.5}$$

respectively, where I_L is the current through the inductor [16].

Resonance occurs when W_e=W_m, from Equation 3.4 and Equation 3.5, therefore, the first resonant frequency can be calculated as follows:

$$w_0 = \frac{1}{\sqrt{LC}} \tag{3.6}$$

For a half wavelength resonator, the resonance curves are usually expressed in two different ways. Either amplitude or phase of a signal at various frequency can be measured. Figure 3.2 shows that a $\lambda/2$ resonator generates a sharp peak in the amplitude and a steep slope in the phase of the transmission when $\omega = \omega_0$.

A gap coupled microstrip resonator is a type of resonator used heavily in this research. Consider a $\lambda/2$ open-circuit microstrip resonator coupled to a microstrip feedline, as shown in Figure 3.3. The gap between resonator and feedline can be modeled as a series capacitor and the geometry of the coupling gap determines the level of coupling between the microstrip resonator and the feedline. The equivalent circuit of a gap coupled microstrip resonator is presented in Figure 3.4.

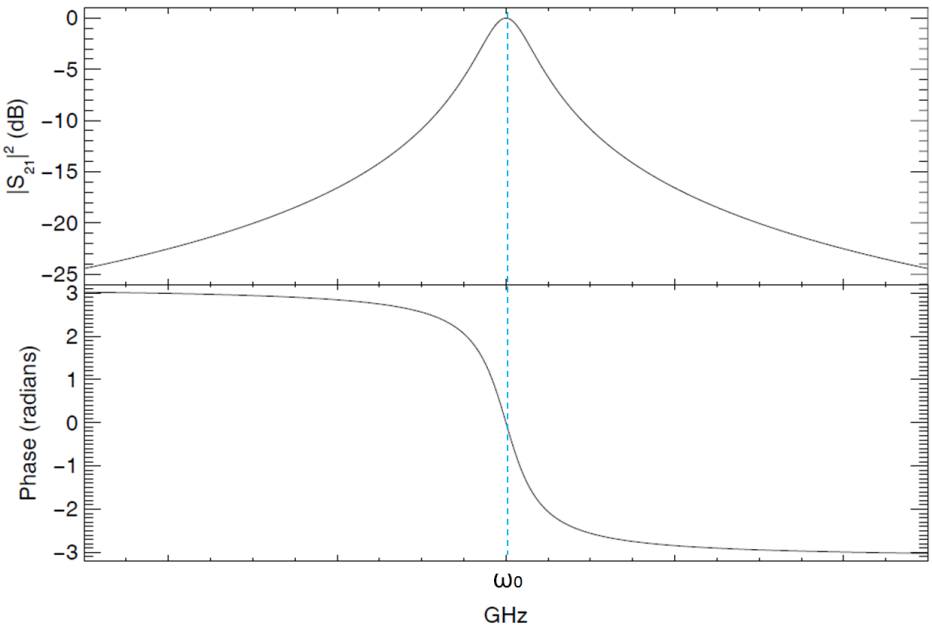

Figure 3.2: The amplitude and phase of a microwave signal transmitted though a $\lambda/2$ resonator near its resonant frequency.

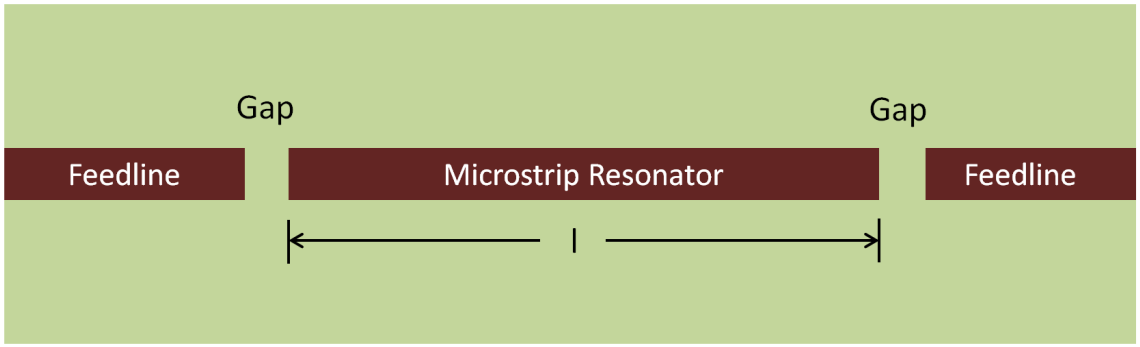

Figure 3.3: A top-view schematic diagram of the open-circuited microstrip resonator coupled to microstrip feedline. Feedline and resonator sections are connectors, surrounding area (including gap) are dielectric/substrate.

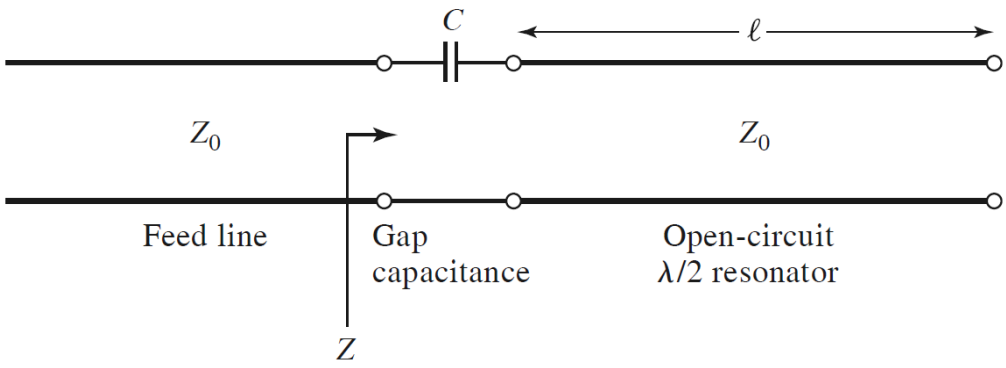

Figure 3.4: Equivalent circuit model of one end of a gap coupled microstrip resonator with length of $\lambda/2$. Adapted from [16].

3.1.2 Quality Factor of Resonators

An electrical resonator is a system characterized by a resonant frequency ω_0. ω_0 gives a rate of periodic exchange of magnetic and electrical energy in the system. Quality factor (Q) is a very important parameter of a resonator. Its definition is given by [17]:

$$Q = 2\pi \times \frac{energy \quad stored}{energy \quad dissipated \quad per \quad cycle}, \tag{3.7}$$

Thus Q is a sensitive measure of circuit system's loss and a high Q implies low loss. Resonator losses are associated with conductor loss, dielectric loss, coupling loss and radiation loss. An external connecting network introduces additional losses to the resonator circuit and each of these losses will reduce the Q. The Q of the resonator itself, disregarding the external loss, is called unloaded Q (Q_u) and is expressed by:

$$\frac{1}{Q_u} = \frac{1}{Q_c} + \frac{1}{Q_d} + \frac{1}{Q_r} \tag{3.8}$$

where

$$Q_c = \frac{2\pi(f_0)U}{W_c} = \frac{\pi}{\alpha_c \lambda_g} \tag{3.9}$$

$$Q_d = \frac{1}{tan\delta}(1 + \frac{1-q}{q\epsilon_r}) \tag{3.10}$$

$$Q_r = \frac{2\pi(f_0)U}{W_r} \tag{3.11}$$

where Q_c, Q_d, Q_r are quality factor related to conductor loss, dielectric loss and radiation loss. f_0, U, $\epsilon_r, W_c, W_r, \alpha_c$,tan δ and q are center frequency, stored energy, relative dielectric constant, average power loss in the conductors, average power loss due to radiation, conductor, attenuation constant, dielectric loss tangent and dielectric filling factor, respectively. Equation (3.9)-(3.11) are given in [18].

In practice, a resonator must be coupled to external circuitry to allow measurement. Coupling to external circuitry introduces additional losses to the system, resulting in a reduced Q for the system. This Q is called the external Q (Q_e). This external loss will also have some effects of lowering the overall Q, which is known as loaded Q (Q_l). Q_l can be expressed as:

$$\frac{1}{Q_l} = \frac{1}{Q_u} + \frac{1}{Q_e}. \tag{3.12}$$

Q_e can be calculated or evaluated for a given coupling structure. Q_l is often difficult to calculate precisely but it can be measured directly using either S_{21} or S_{11}. Note that S_{21} is the forward voltage gain and S_{11} is the input port voltage reflection coefficient and Equation 3.13:

$$Q_l = \frac{f_0}{BW_{-3dB}} \tag{3.13}$$

gives another definition of Q_l, where f_0 is the center frequency of the resonant response and BW_{-3dB} is the 3 dB bandwidth, which is the width between the upper frequency and lower

frequency at which the response of the circuit is 3 dB down from the its response at f_0. Figure 3.5 shows a typical S_{21} vs. frequency plot of a resonator close to its resonance frequency.

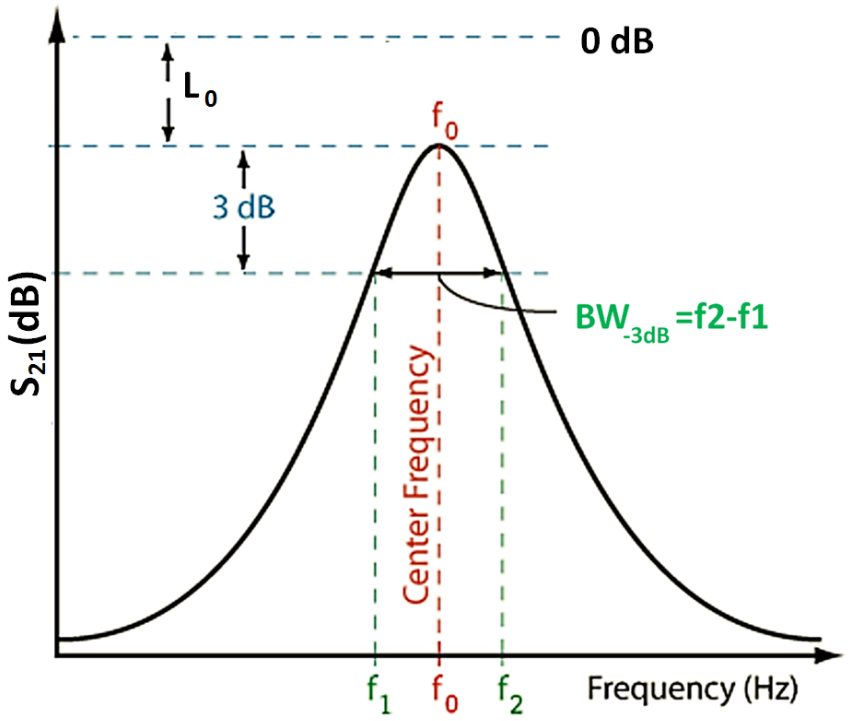

Figure 3.5: Typical transmission spectrum of S_{21} of a resonator close to its resonance frequency in decibel (dB).

For known $|S_{21}|$ versus frequency data, Q_l can also be extracted by performing a fit to a Lorentzian line shape [19]. The resonant frequency (f_0), bandwidth (Δf_{Lorent}), constant background (M_1), slope on the background (M_2), skew (M_3) and maximum magnitude $|S_{max}|$ are the fitting parameters for the Lorentzian, given by:

$$| S_{21}(f) | = M_1 + M_2 f + \frac{| S_{max} | + M_3 f}{\sqrt{1 + 4(\frac{f - f_0}{\Delta f_{Lorent}})^2}} \tag{3.14}$$

A least squares fit is iterated until the change in "chi squared" is less than $1/10^3$. Q_l can be calculated using f_0 and Δf_{Lorent} from the fit parameters, as Equation 3.15:

$$Q_l = \frac{f_0}{\Delta f_{Lorent}} \tag{3.15}$$

3.1.3 Determination of Dielectric Loss Tangent

The requirement of coupling level between a resonator and external circuit depends on the applications. A resonator used for a tuned amplifier or oscillator usually needs to be tightly coupled in order to achieve better power transfer. However, in order to characterize a low loss tangent value of a dielectric material, high Q and high sensitivity are needed. Therefore, the resonators used in this work are "under-coupled" to the feed lines, or in other words, loosely coupled. The "loose" here does not mean a too large couple gap, because that will cause huge signal attenuation, resulting in a resonance peak much lower than the noise level during the resonator measurement. The goal is to have a resonator with sufficiently low coupling that causes the resultant Q to be independent of the coupling level, but high enough to result in sufficient signal transmission. In addition, the length of coupling region effects on the coupling strength. Also, considering fabrication tolerances, both parameters are optimized to achieve a practical weakly-coupled microstrip resonator. Note that parallel or shunt resonators can be used in this research, but they were not used and are not discussed here.

In dielectric microwave properties measurements, frequency response of the two-port resonator is measured using a network analyzer, such as an Anilent N5227A PNA. The method used to determine dielectric loss tangent ($\tan\delta$) value in this work uses a superconducting microstrip transmission line resonator or a superconducting stripline transmission line resonator. In order to characterize $\tan\delta$, Q_u needs to be determined first. Based on Equation 3.12, Equation 3.16 is derived as:

$$\frac{1}{Q_u} = \frac{1}{Q_l} - \frac{1}{Q_e} \tag{3.16}$$

For the transmission line resonators used in this work, resonator external loss is dominated by coupling loss, the Q associated with coupling loss is called $Q_{coupling}$. Then Equation 3.16 becomes Equation 3.17:

$$\frac{1}{Q_u} = \frac{1}{Q_l} - \frac{1}{Q_{\text{coupling}}}. \tag{3.17}$$

Interestingly, for a superconducting resonator, especially when the temperature is much lower than the superconductor's critical transition temperature, the conductor loss is negligible. Also, based on the structure of our transmission line resonator, radiation loss is ignorable compared to the dielectric loss. Thus, $1/Q_c$ and $1/Q_r$ terms can be ignored and the resonator loss is assumed to be dominated by dielectric loss, as shown in Equation 3.18:

$$\frac{1}{Q_d} = \frac{1}{Q_l} - \frac{1}{Q_{\text{coupling}}}. \tag{3.18}$$

According to Equation 3.10, $\tan\delta$ of a microstrip transmission line resonator can be calculated using Equation 3.19:

$$tan\delta = (\frac{1}{Q_d})(1 + \frac{1-q}{q\epsilon_r}) \tag{3.19}$$

Since q, ϵ_r, Q_l and Q_{coupling} are known in this case, extraction of $\tan\delta$ is completed. While for a stripline transmission line resonator, q=1. Thus, the $\tan\delta$ for stripline is simplified to Equation 3.20:

$$tan\delta = \frac{1}{Q_d} \tag{3.20}$$

3.2 Flexible, Superconducting Microstrip Transmission Line Resonators

3.2.1 Resonator Design and Layout

Half-wavelength, capacitively coupled microstrip transmission line resonators were designed and Keysight Advanced Design System (ADS) was used to simulate the designed structures and generate the microstrip transmission line resonator layouts. An ADS circuit simulation schematic for a non-embedded microstrip transmission line resonator is shown in

Figure 3.6. The layout of non-embedded and embedded versions of resonators was identical and a top view of the critical pieces of the design are shown in Figure 3.7(a). A 3-D perspective image of an embedded resonator is shown in Figure 3.7(b). All dimensions for the two types of resonators are the same except the embedded resonator had an encapsulation layer of polyimide. Key dimensions of the resonator designs are listed in Table 3.1. The resonator length was chosen to yield a fundamental resonant frequency, f_0, of 2 GHz, which provides sufficient harmonic resonances up to 20 GHz. The width of the signal line was designed to provide a characteristic impedance of 50 Ω, in order to be representative of corresponding 50 Ω transmission lines. Metallization of microstrip transmission line resonator was ∼ 250 nm-thick Nb and resonator substrate was polyimide with a thickness of ∼20 µm. Note that both PI-2611 [21] and HD-4110 [22] polyimide from HD MicroSystems were used in this work. Both polyimide materials are widely used in electronics packaging applications. HD-4110 is photodefineable, which can be directly patterned through photolithography techniques, while PI-2611 has a matched thermal expansion with silicon but is not photodefinable. Dielectric constant ϵ_r of PI-2611 and HD-4110 are quite similar, which is ∼3.2 based on [23] over a frequency range from 1 GHz to 20 GHz.

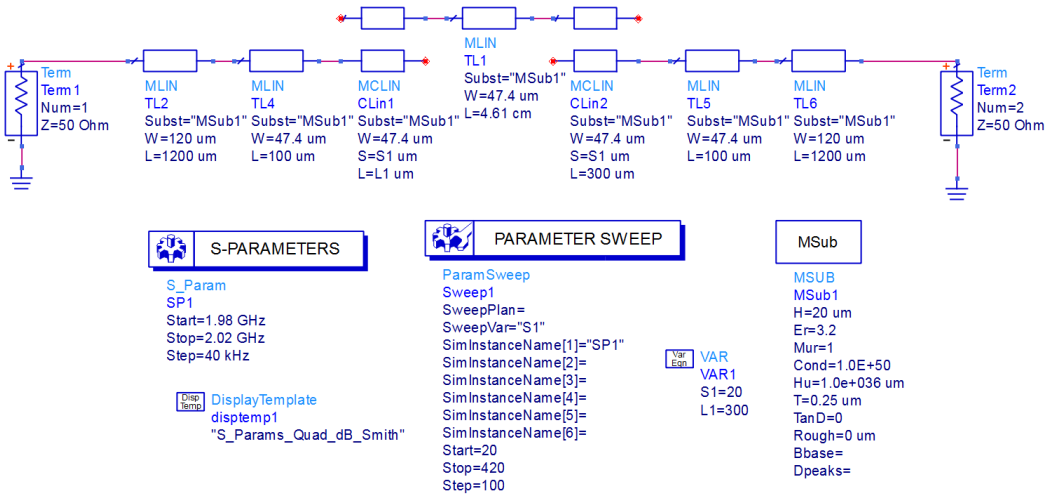

Figure 3.6: ADS circuit simulation schematic model of microstrip transmission line resonator on thin-film polyimide.

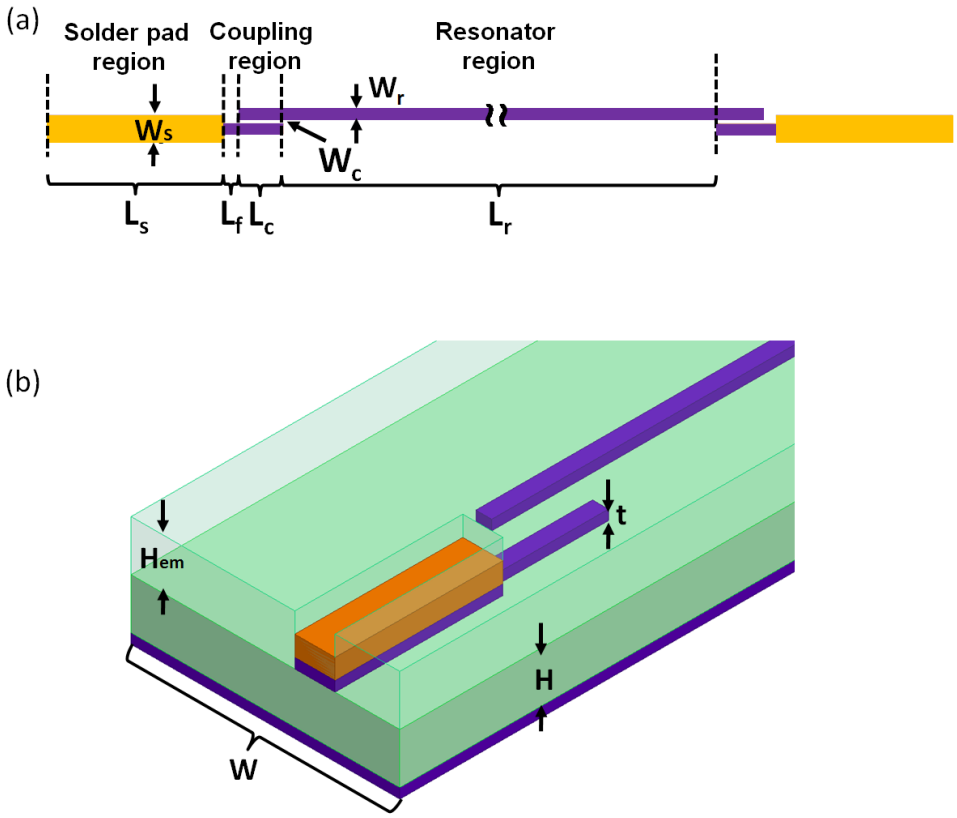

Figure 3.7: (a) Top view of half-wavelength, capacitively-coupled microstrip transmission line resonators on thin-film HD-4110. (b) 3-D view of one end of an embedded resonator.

Symbol	Value	Description
W	6 mm	Width of dielectric
H	20 µm	Height of dielectric
t	0.25 µm	Thickness of Nb layer
H_{em}	0, 4, 8, 20 µm	Thickness of encapsulation layer
W_s	120 µm	Width of solder pad
L_s	1200 µm	Length of solder pad
L_f	100 µm	Length of feed line
L_c	300 µm	Length of coupling gap
W_c	20 µm	Width of coupling gap
W_r	47.4 µm	Width of resonator
L_r	46.1 mm	Length of resonator

Table 3.1: Key dimensions of the resonator designs.

3.2.2 Fabrication and Sample Assembly Process

An outline of sample fabrication is presented here and the reader is referred to Appendix A for further details.

In this work, microstrip resonators have been fabricated on different thin-film polyimide materials, PI-2611 or HD-4110, based on different fabrication process needs. Figure 3.8 schematically illustrates the fabrication procedures for superconducting Nb microstrip transmission line resonators fabricated using HD-4110 polyimide, including non-embedded (Figure 3.8(1)-(8a)) and embedded (Figure 3.8(1)-(10b)) configurations. Starting with two oxidized Si handle wafers, 25-nm thick Cr and 200-nm thick Al were deposited on these wafers as a sacrificial release layer [24]. Polyimide HD-4110 was spun onto both wafers to achieve a ∼20 µm-thick film, followed by curing at 375°C in a N_2 environment. Resonator

signal lines of ∼250 nm-thick Nb connected to Ti(50 nm)/Cu(500 nm)/Au(10 nm) under-bump metal (UBM) pad stacks were formed using conventional photolithography and film lift-off techniques. The Nb film was RF sputter deposited with a power of ∼8 W/cm^2 and Ar pressure of 4 mTorr. The UBM pads were deposited by electron-beam thermal evaporation after a two minute in-situ ion beam milling surface clean. For the embedded microstrip transmission line resonators, small Kapton tape "dots" were then used to cover the UBM pad area to be used for electrical connection. This was followed by spin-on deposition of a top HD-4110 encapsulation layer. The embedding layer was cured at lower temperature (225°C) to protect the superconductivity of the embedded Nb, and was ∼20 µm thick post-cure. Subsequently, both non-embedded and embedded samples were protected with a layer of photoresist during a film release process (soaking in a sodium chloride solution with 0.5 V applied to the Cr/Al release layer). After releasing and stripping of the photoresist, the samples were then inverted and mounted onto Si handle wafers, followed by a ground plane deposition of ∼250 nm-thick Nb.

Note that, for the resonators fabricated on PI-2611 polyimide, the fabrication procedure is almost identical as for HD-4110 resonators. More fabrication details can be found in fabrication travelers provided in Appendix A.

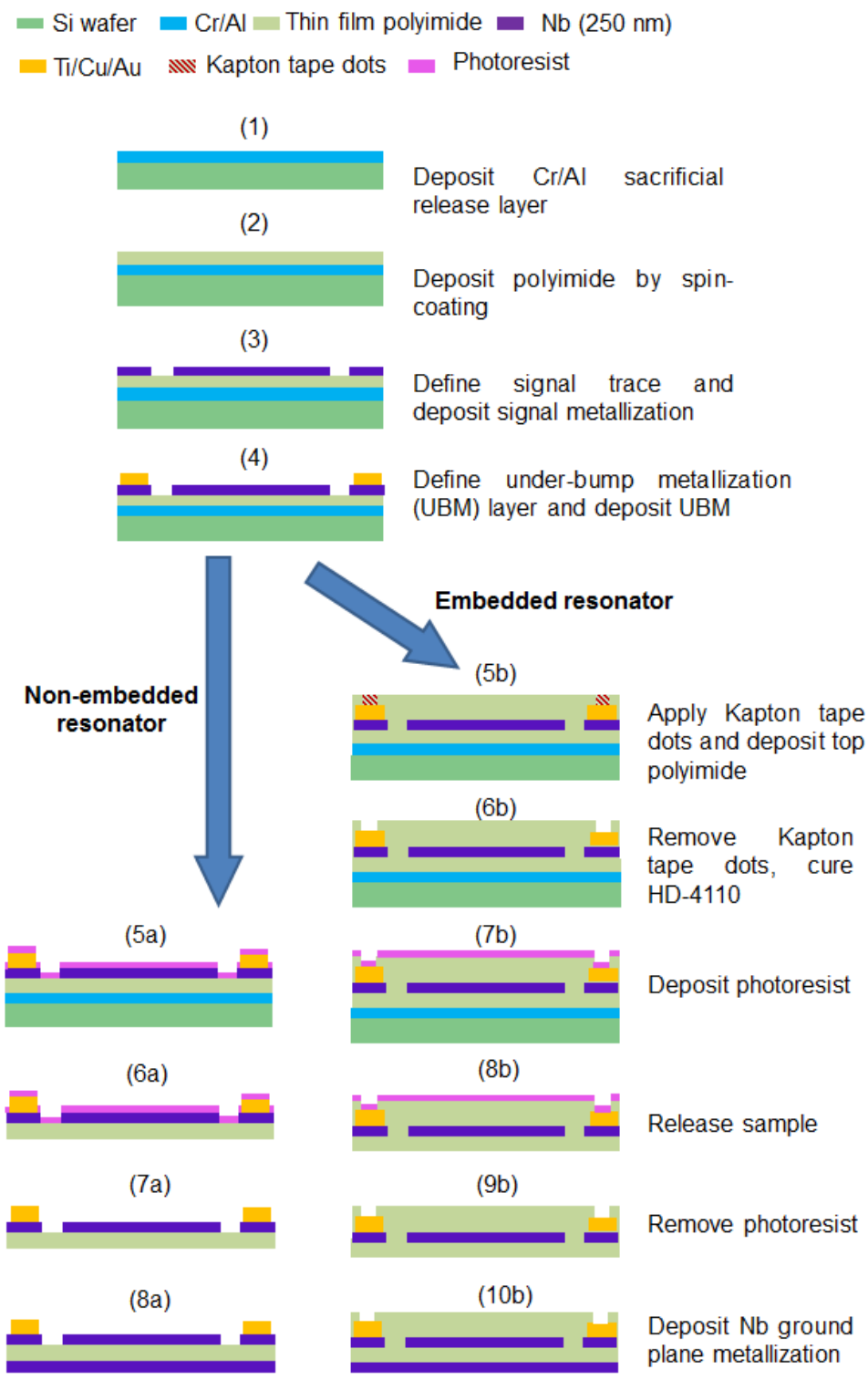

Figure 3.8: Schematic of fabrication procedures and flow for non-embedded and embedded Nb microstrip transmission line resonators fabricated on HD-4110 polyimide.

Figure 3.9(a) shows four fabricated embedded Nb resonators, prior to dicing and assembly. In order to assemble the resonator for testing, edge launch SMA connectors from Southwest Microwave, Inc. were used to facilitate microwave connections to the flex cable. High purity In solder was used to provide reliable connections in a cryogenic temperature environment. A close up view, showing details of the connection area, is shown in Figure 3.9(b). The sample and the connectors were mounted on support boards made of scrap PCB material, as shown in Figure 3.9(c), to help prevent the resonators from being damaged or stretched, after assembly and during measurement.

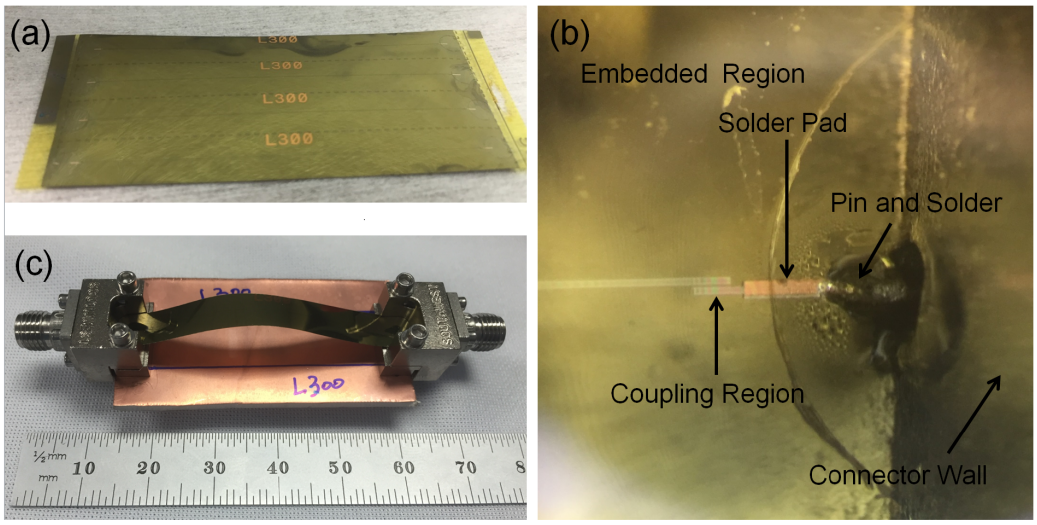

Figure 3.9: (a) Embedded Nb resonators before dicing and assembly. (b) Detailed image of pin and solder area, the opening defined by the Kapton dots can be seen as the arcing line in the image. (c) Assembled embedded sample with edge launch SMA connectors mounted onto a support board.

3.2.3 Microwave Measurement Experimental Setup

Figure 3.10 shows the measurement setup for Nb superconducting transmission line resonators. A Keysight N5227A performance network analyzer (PNA) was used to measure the scattering parameters. Measurements were carried out in a pulse-tube based cryostat (PT) with cryogenic stainless steel RF coaxial cables. The PT with stainless steel cryo-cables

stabilizes at ~ 3 K and can cool down further to ~ 1 K by vacuum pumping down the sample space, which has been back-filled with He gas that condenses to the He liquid. Temperature sensor was located at the sample holder near the top of the sample. More details of the PT rod can be seen in Figure 3.11.

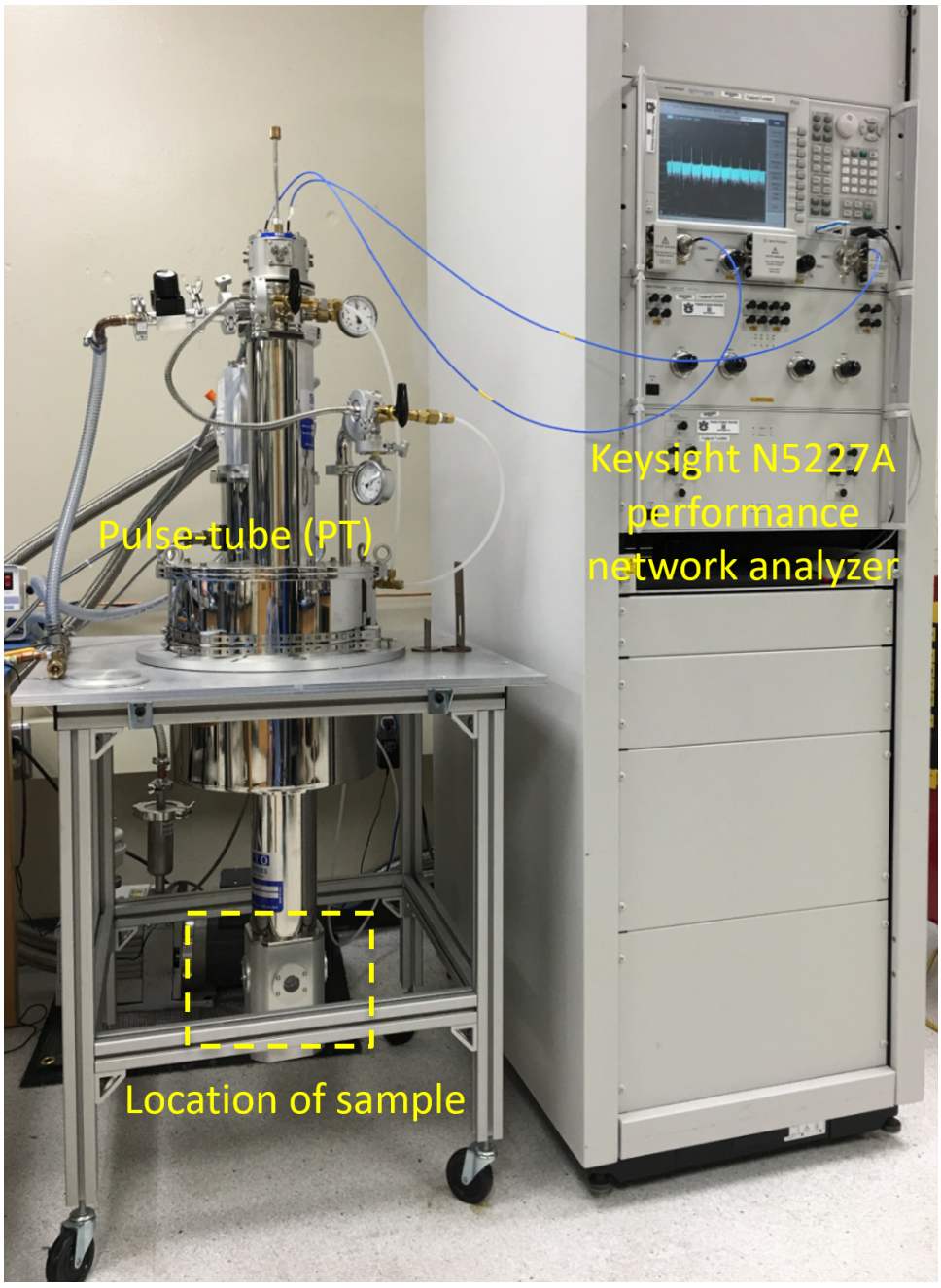

Figure 3.10: Network analyzer setup for high frequency device measurement in pulse-tube cryostat system.

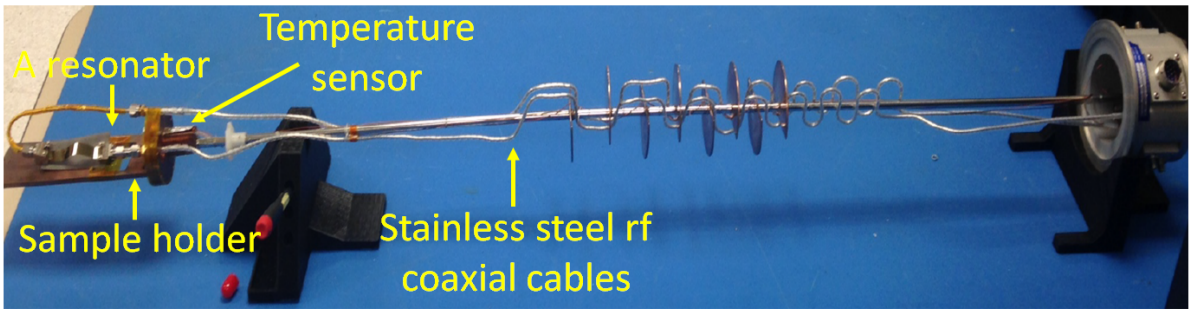

Figure 3.11: Details of the PT rod with sample mounted.

3.2.4 Results and Discussion

3.2.4.1 Microstrip Resonators Fabricated on HD-4110 Polyimide

Polyimide HD-4110 [22] as a photosensitive polyimide has been widely used for electronic packaging [25-26] and flexible electronics [27-28] applications due to its excellent mechanical properties. It is also as a low out-gassing, low conductivity dielectric material. The microwave properties (i.e. dielectric loss tangent) of HD-4110 at cryogenic temperatures have not been previously reported before. Furthermore, the influence of HD-4110 as an encapsulation layer over a superconductor in RF/microwave applications have yet to be studied.

In this section, details of microwave characterization of non-embedded and embedded Nb superconducting microstrip transmission line resonators were presented. 20 µm-thick HD-4110 film as the thickest suggested single layer cured film, was used as the substrate for both type of Nb resonators and the encapsulation layer for embedded resonators. Loaded quality factor (Q_l) of resonators have been measured in a frequency range of 1 - 21 GHz and in a temperature range of 1.2 - 4.2 K.

In order to precisely model and perform predictions for flexible superconducting transmission lines, the information of dielectric loss tangent ($\tan\delta$) of polyimide material is needed. By measuring the Q_l of structurally comparable resonators, combined dielectric loss and superconductor loss can be obtained [29]. A wide range frequency (1 GHz $\sim$ 21 GHz) view of S_{21} measured at 1.2 K for a non-embedded Nb microstrip transmission line resonator on

HD-4110 is shown in Figure 3.12. It can be found that the fundamental lowest frequency resonance exhibits higher Q-factor than other harmonics. In order to precisely determine Q_l information, a sufficient number of data points was taken for each resonance peak. Figure 3.13 shows the measured fundamental resonance of a non-embedded Nb microstrip transmission line resonator at 1.2 K and Lorentz fit of this resonance. In this figure, one can find a center frequency (f_0) of 2.0531 GHz and 3 dB bandwidth of 99.9248 kHz, which yields a Q_l of 20547 at 1.2 K and at an incident power of -30 dBm. Q_l value of non-embedded Nb resonator have been computed for each resonance at different temperatures, which is shown in Figure 3.14. Note that in order to alleviate the measurement error and system temperature drift effect, measured Q_l is the average value of 10 individual measurement results from 3 resonators with a 3σ error bar. It can be observed that at a fixed temperature, as the frequency increases, the Q_l is lower. In addition, at a fixed frequency, resonators yield higher Q_l at a lower temperature, which is in agreement with reduced conductor-associated loss for superconductors as temperature is further reduced below the T_c of the superconductor.

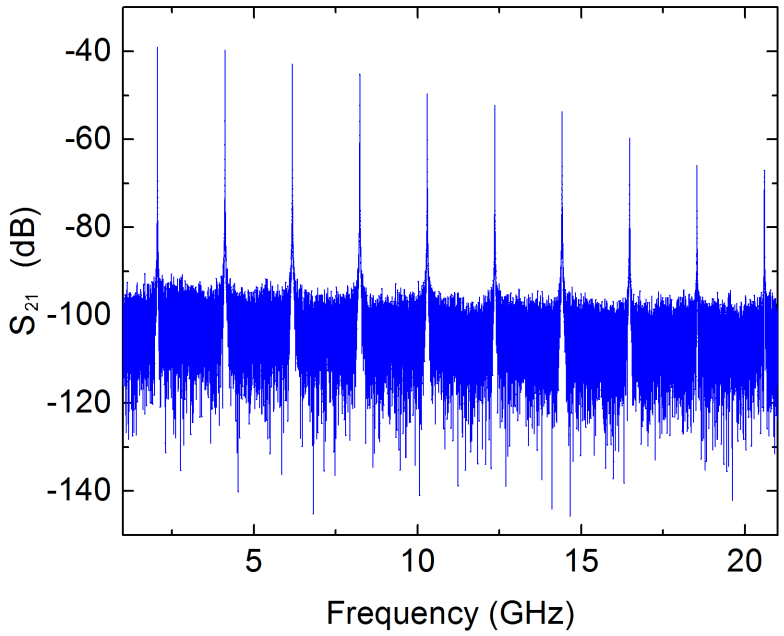

Figure 3.12: S_{21} measurement results of a non-embedded Nb/HD-4110 flexible microstrip resonator measured at 1.2 K. Broadband view of S_{21} response versus frequency from 1^{st} to 10^{th} mode.

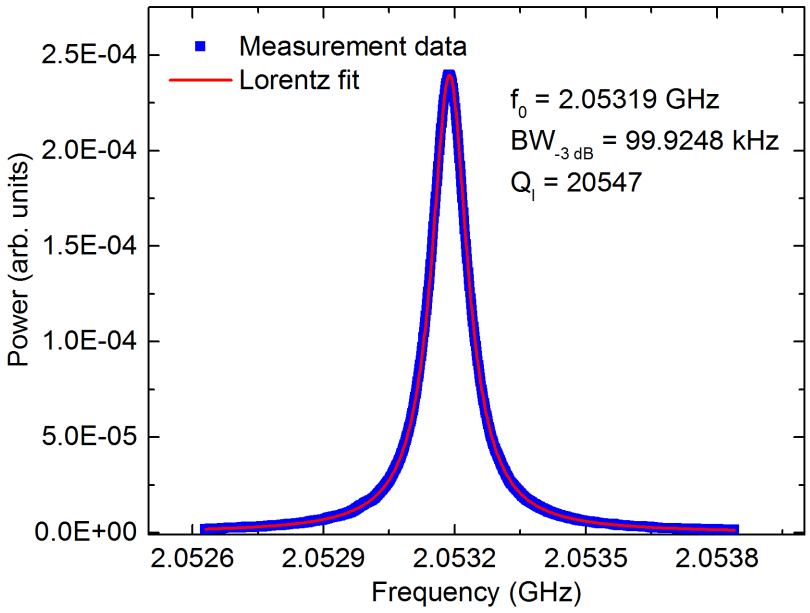

Figure 3.13: Fundamental resonance (1^{st} mode) measurement result and corresponding Lorentz fit. The best-fit center frequency, 3 dB bandwidth and loaded Q information are provided.

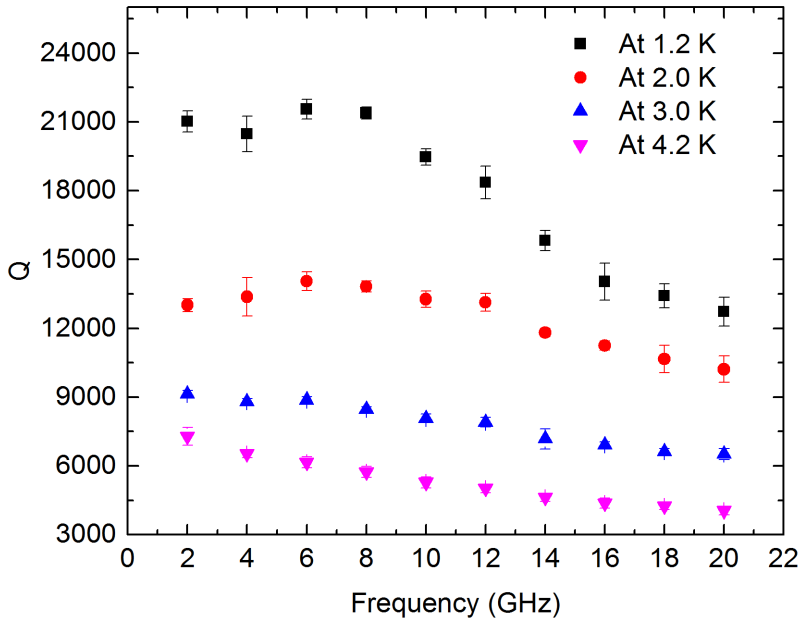

Figure 3.14: Q_l for multiple harmonics of non-embedded Nb/HD-4110 resonators at different temperatures.

The following analysis is based on superconducting transmission line resonator theory along with an assumption that the dielectric loss tangent is relatively constant over the measured range of frequencies. From this, it can be found that the slopes and zero-frequency intercepts of the 1/Q plots correspond to the superconductor quasiparticle loss (i.e., from BCS theory) and dielectric loss, respectively. Details in support of these statements can be found in [16, 23]. Slopes and the zero-frequency intercepts are observed to decrease as the temperature decreases from 4.2 K to 2.0 K. Fitting lines of the 1.2 K and 2.0 K data are nearly parallel with the simulation data ($\tan\delta = 0$). This indicates that Nb quasiparticle loss is negligible at these temperatures and the loss in the resonator is dominated by dielectric loss (HD-4110 in this case). Low quasiparticle loss is also in agreement with high intrinsic Q_0 reported in [30]. The unloaded quality factor (Q_0) of the resonators includes the impact of conductor, dielectric and radiation loss can be described by [18]:

$$\frac{1}{Q_0} = \frac{1}{Q_\mathrm{c}} + \frac{1}{Q_\mathrm{d}} + \frac{1}{Q_\mathrm{r}} \tag{3.21}$$

where Q_c, Q_d and Q_r are Q associated with conductor loss, dielectric loss and radiation loss, respectively. Q_0 also can be expressed as Equation 3.22 [16]:

$$\frac{1}{Q_0} = \frac{1}{Q_\mathrm{l}} - \frac{1}{Q_\mathrm{e}} \tag{3.22}$$

where Q_e is external Q, which is often dominated by coupling Q ($Q_{coupling}$). With this substitution, Equation 3.21 becomes:

$$\frac{1}{Q_\mathrm{l}} = \frac{1}{Q_\mathrm{c}} + \frac{1}{Q_\mathrm{d}} + \frac{1}{Q_\mathrm{r}} + \frac{1}{Q_\mathrm{coupling}} \tag{3.23}$$

Radiation loss was determined to be negligible for these resonators, owing to their very small cross sections. Conductor loss is also negligible below ~2.0 K, which is well below the critical transition temperature. Therefore, Q_0 is dominated by Q_d, which can be found from the measured Q_l and simulated $Q_{coupling}$. From Q_d, the dielectric loss tangent ($\tan\delta$) can be extracted using Equation 3.19 [18].

An ϵ_r value of 3.2 was found using an iterative process to match ADS simulation results to measurement results for similarly-constructed Cu resonators. More details can be found in [31]. The filling factor q of these non-embedded and embedded microstrip transmission lines are 0.703 and 0.828, respectively, using Equation 3.24.

$$q = \frac{\epsilon_{eff} - 1}{\epsilon_r - 1} \tag{3.24}$$

where ϵ_{eff} and ϵ_r are effective dielectric constant and relative dielectric constant, respectively.

Detailed $Q_{coupling}$, Q_l and $\tan\delta$ values at 1.2 K and 2.0 K and at each resonant frequency are listed in the second and the third columns in Table 3.2. Note that, since other parasitic losses not related to the dielectric cannot be completely ruled out, the actual loss tangent

could be less than the extracted values. These results provide important information for cryogenic high frequency structure simulation and design with HD-4110. Furthermore, they indicate that HD-4110 is a promising dielectric material for flexible cryogenic electronics, packaging and interconnect structures.

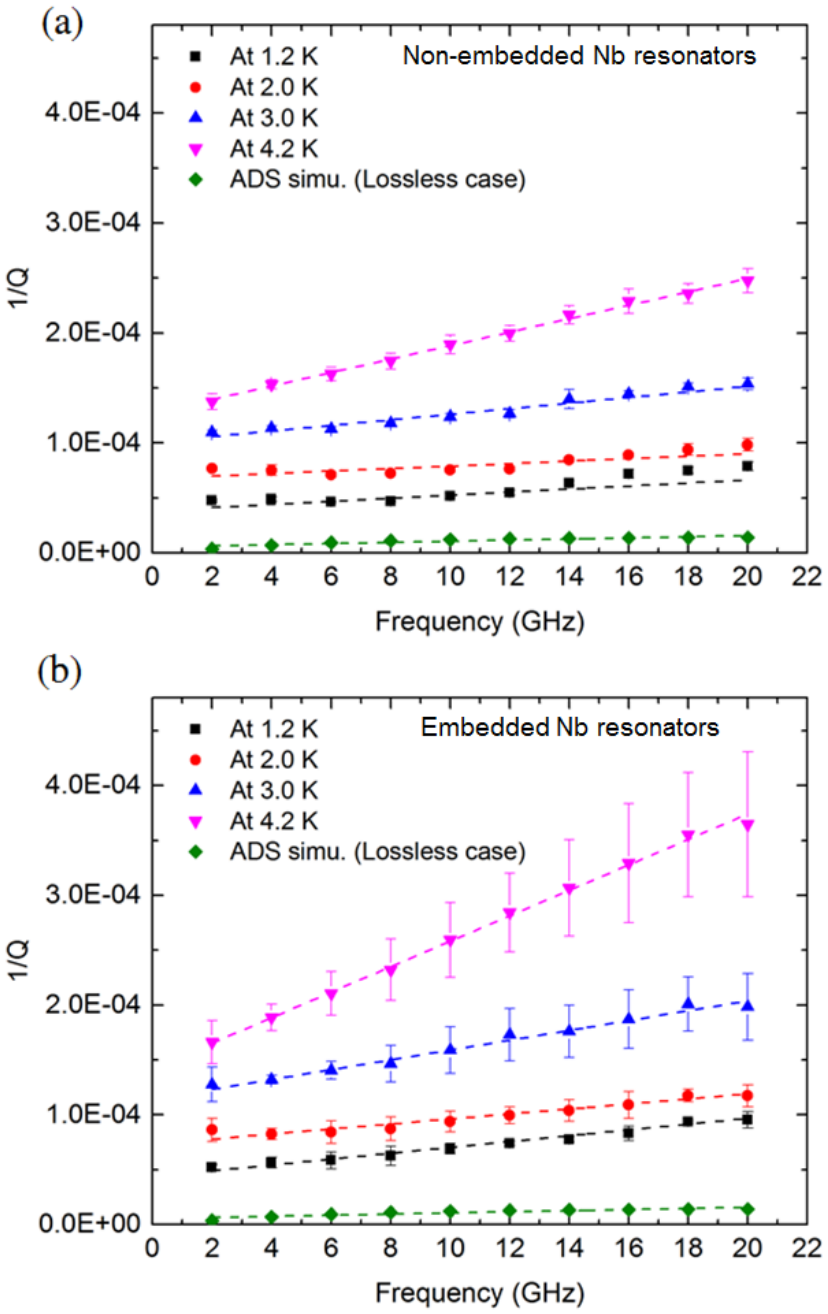

Figure 3.15: $1/Q_l$ for multiple resonant frequencies of (a) non-embedded and (b) embedded Nb resonators at different temperatures, along with corresponding ADS simulation results with no conductor or dielectric loss. Note the increase of slopes and variance in the embedded resonators, at higher temperatures, which indicates higher quasiparticle losses in the Nb.

$Q_{coupling}$	Non-embedded resonator		
	$\sim f_0$ (GHz)	Q_l ($\tan\delta$) @ 1.2 K	Q_l ($\tan\delta$) @ 2.0 K
267 846	2.0	21 040 (4.97E-05)	13 010 (8.29E-05)
143 400	4.0	20 427 (4.76E-05)	13 372 (7.69E-05)
105 959	6.0	21 575 (4.19E-05)	14 052 (7.00E-05)
89 884	8.0	21 351 (4.05E-05)	13 821 (6.94E-05)
81 977	10.0	19 436 (4.45E-05)	13 265 (7.17E-05)
77 781	12.0	18 271 (4.75E-05)	13 136 (7.17E-05)
75 337	14.0	15 759 (5.69E-05)	11 810 (8.10E-05)
73 659	16.0	13 908 (6.61E-05)	11 239 (8.55E-05)
72 186	18.0	13 339 (6.93E-05)	10 663 (9.06E-05)
70 578	20.0	12 668 (7.34E-05)	10 208 (9.50E-05)

Table 3.2: Simulated $Q_{coupling}$, measured Q_l and extracted upper bound on $\tan\delta$ at resonant frequencies at 1.2 and 2.0 K for non-embedded Nb transmission line resonators.

In order to evaluate the performance of embedded resonators and to determine the influence of the lower-temperature cured encapsulation layer and additional fabrication processing, three embedded Nb resonators were measured at the same temperatures and in the same frequency range, as shown in Figure 3.15(b). compared to non-embedded resonators, a larger variance can be seen in this plot, which is likely due to the additional embedding fabrication process. An increase in slope of the $1/Q_l$ versus frequency lines is also evident, especially at higher temperatures. Through analysis of the results shown in Figure 3.15, slope and intercept values of both types of Nb resonators were obtained (Figure 3.16). As temperature increases from 1.2 K to 4.2 K, for each material stack-up, loss due to the HD-4110 dielectric increases gradually, as is evident from the increased intercept values. Growth of conductor (quasiparticle) loss starts from 2.0 K for these resonators, as is evident from

the increased slopes. Furthermore, at each temperature, with the use of a 225°C cured encapsulation layer, the combined dielectric loss increases slightly. It is possible that solvent and moisture may still exist in lower temperature cured HD-4110, which may be the source of the additional dielectric loss and increased variation for the embedded samples. Also, it can be seen that the quasiparticle loss increases for the embedded structures, and this may be due to the availability of degrading substances (i.e. acids and/or H_2O) in the embedding layer during the curing process that could lead to the degradation of the superconducting properties of the Nb, even with a lower temperature curing process. Measured Q_l and computed $\tan\delta$ of embedded resonators corrected with $Q_{coupling}$ and filling factor q at 1.2 K and 2.0 K are shown in Table 3.3. Even with the slight degradation due to the low-temperature cure of HD-4110 on top of Nb, the performance of embedded transmission lines fabricated with this process would be quite suitable for propagating microwave signals in cryogenic and superconducting electronics systems over meter-scale distances [32].

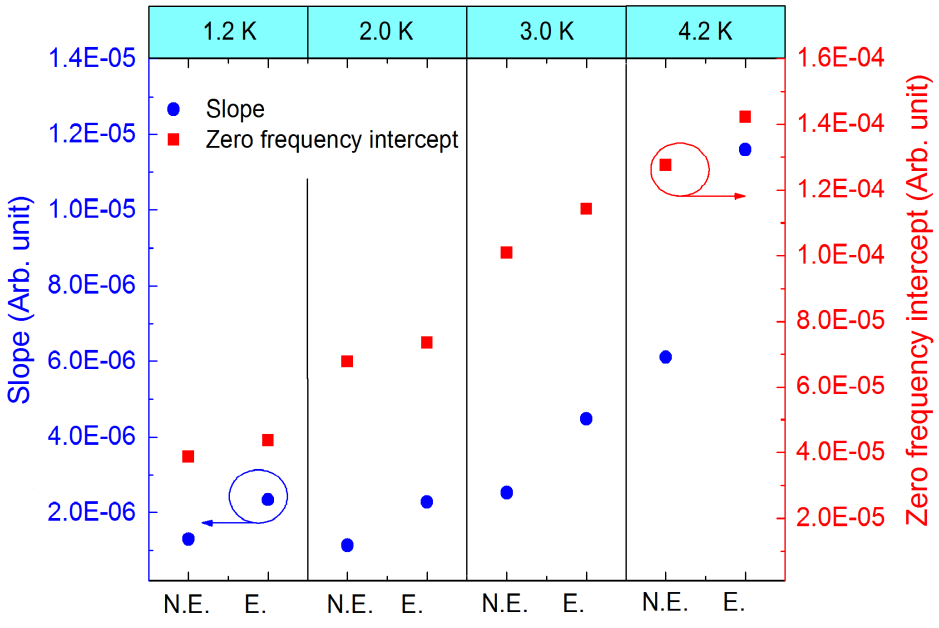

Figure 3.16: Comparison of slope and zero-frequency intercept values of linear fitting lines of $1/Q_l$ vs. frequency plot of non-embedded and embedded Nb resonators at different temperatures "N.E." is for non-embedded and "E." is for embedded.

$Q_{coupling}$	Embedded resonator		
	$\sim f_0$ (GHz)	Q_l ($\tan\delta$) @ 1.2 K	Q_l ($\tan\delta$) @ 2.0 K
266 676	1.9	19 209 (5.15E-05)	11 588 (8.79E-05)
142 144	3.8	17 723 (5.27E-05)	12 133 (8.03E-05)
103 834	5.7	17 066 (5.22E-05)	11 855 (7.98E-05)
88 993	7.6	15 974 (5.47E-05)	11 454 (8.11E-05)
80 783	9.5	14 507 (6.05E-05)	10 646 (8.70E-05)
76 734	11.4	13 522 (6.52E-05)	10 056 (9.22E-05)
74 876	13.3	12 883 (6.84E-05)	9 626 (9.65E-05)
73 113	15.2	12 021 (7.43E-05)	9 180 (1.02E-04)
71 383	17.1	10 697 (8.48E-05)	8 510 (1.10E-04)
69 378	19.0	10 497 (8.63E-05)	8 521 (1.10E-04)

Table 3.3: Simulated $Q_{coupling}$, measured Q_l and extracted upper bound on $\tan\delta$ at resonant frequencies at 1.2 K and 2.0 K for embedded Nb transmission line resonators.

3.2.4.2 Microstrip Resonators Fabricated on PI-2611 Polyimide

To investigate the impact of encapsulation layer on RF performance for microstrip resonators, PI-2611 polyimide was used as the embedding (or encapsulant) layer because its low viscosity allows for a relatively thin layer. Microstrip transmission line resonators with different thickness of encapsulation layers (e.g., 0, 4 and 8 µm) were constructed.

Figure 3.17 shows measured frequency-normalized fundamental resonance responses and corresponding Lorentz fits of Nb/PI (0 µm), Nb/PI (4 µm) and Nb/PI (8 µm) resonators at 1.2 K. Looking at measurement results, encapsulation layer thicknesses of 0, 4 and 8 µm provide corresponding fundamental resonance frequencies of 1.9987 GHz, 1.9255 GHz and 1.9057 GHz at 1.2 K. I note that the Nb/PI (0 µm) resonator exhibits a Q_l greater than 16300 at 1.2 K and the Nb/PI (4 µm) and Nb/PI (8 µm) resonators exhibit Q_l values of

14481 and 13995, respectively. For each measurement, the microwave signal power level was adjusted for each resonance to provide the highest Q_l value.

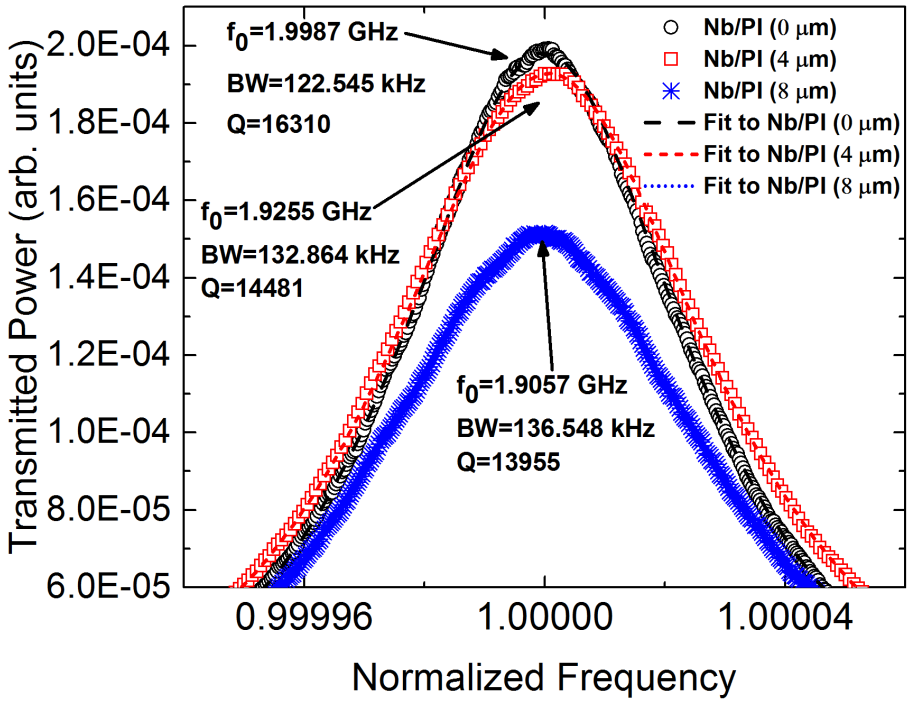

Figure 3.17: Measured frequency-normalized fundamental resonance of various resonators at 1.2 K and corresponding Lorentz fits. Center frequency, 3 dB bandwidth and loaded Q-factor are provided for each resonator.

A plot of $1/Q_l$ versus frequency for the various Nb/PI resonators at different temperatures is shown in Figure 3.18. In order to alleviate the measurement error and system temperature drift effects, the presented values are for an average of 10 individual measurement results along with a 3σ error bar. It can be seen that for each type of resonator and at each measurement temperature, $1/Q_l$ versus resonant frequency plot yields a straight line, as shown by the dashed lines in the figure. Based on superconducting transmission line resonator theory, for each of the linear fitting lines, the slopes and y-intercepts are related to the superconductor loss and dielectric loss, respectively. Corresponding slope and y-intercept information is shown in Figure 3.19. It can be observed that, with increase in temperature,

for each material stack-up, loss due to superconductor quasi-particles (i.e., from BCS theory) and loss due to the PI-2611 dielectric both increase, as evident from the increased slopes and intercepts. Furthermore, at each temperature, with increase of the thickness of the encapsulation layer, the dielectric loss increases slightly, as expected. The noted exception is for the Nb/PI (8 µm) resonator at 1.2 K, which exhibits slightly lower dielectric loss than the Nb/PI (4 µm) resonator. This could be due to the combination of very low dielectric loss for PI-2611 at 1.2 K and the measurement tolerance related to small sample temperature drifts. At each temperature, a proportional relationship is observed between BCS-related conductor loss and embedding layer thickness, and this may be due to higher availability of degrading substances (for example acids and/or H_2O) in the thicker embedding layer that arise during the curing of the embedding layer and can lead to degradation of the superconducting properties of the Nb [33].

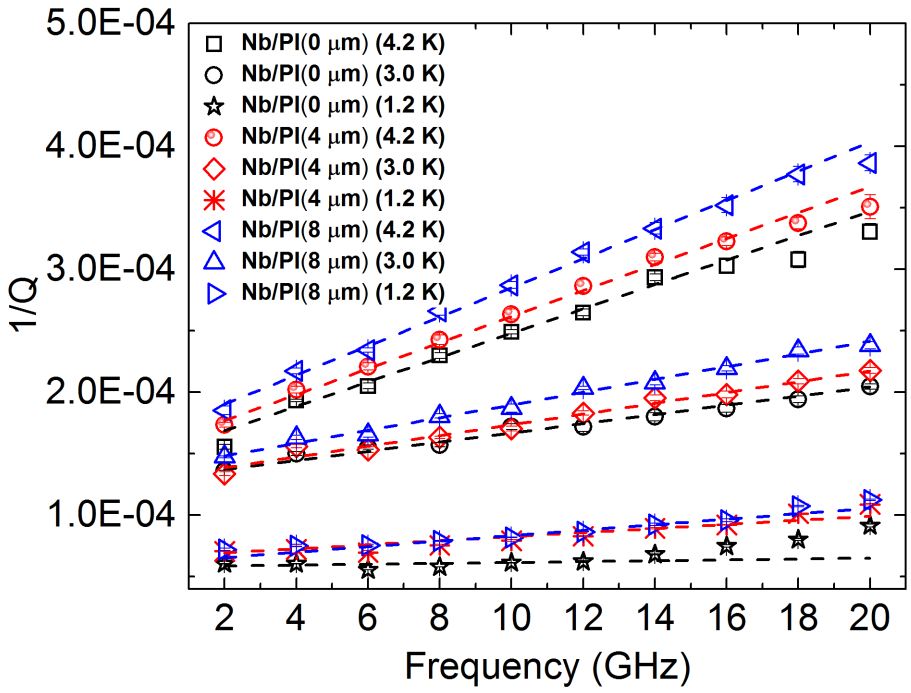

Figure 3.18: $1/Q_l$ for multiple resonant frequencies of resonators at different temperatures. Corresponding linear fits are shown as dashed lines.

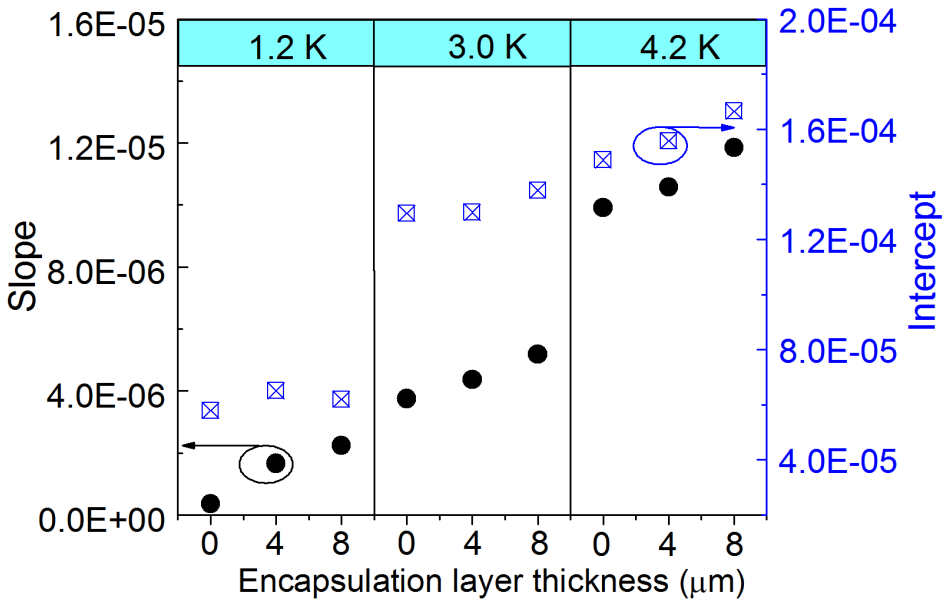

Figure 3.19: Slope and y-intercept information of linear fitting lines of $1/Q_l$ vs. frequency plot of various resonators at different temperatures.

3.3 Stripline Transmission Line Resonators

A stripline structure consists of an inner conductor completely surrounded by dielectric material which is itself surrounded by a ground plane. To avoid unwanted propagation modes in stripline, the two ground planes must be connected, often by means of vias. Compared to microstrip, the stripline format affords more isolation between adjacent circuit traces, allowing more densely integrated circuits for the same amount of crosstalk. Also, stripline circuits are well suited for constructing multilayer circuits, with good isolation between layers [16].

The major challenge to making stripline was the degradation in the superconducting properties (i.e., reduced T_c and I_c) of the Nb films caused by subsequent high temperature curing of polyimide. After exploring material stack-up selection and fabrication process improvement, functional stripline and stripline transmission line resonators were successfully

fabricated. In this section, the stripline resonator design, fabrication processes and characterization results are discussed. RF performance of stripline resonators with embedded microstrip resonators with and without Cu vias are also compared.

3.3.1 Resonator Design and Layout

The mask design for stripline resonators on HD-4110 polyimide is shown in Figure 3.20. This design includes transmission lines (embedded microstrip and stripline test structures), stripline resonators and via chain test structures.

The transmission lines were used in a separate work to measure the T_c, I_c and the RF properties of different structures. Also, for microstrip transmission lines, to achieve better impedance matching, anti-pad size was varied in the design to cancel the reflections from impedance-mismatched solder pad structures. For stripline transmission lines, traces with different pitch and pinning vias were designed to study cross talk and isolation performance. But the measurement results of stripline transmission lines will not be discussed in this dissertation and it will be the subject of future work. The stripline resonators had a line length of ∼13.2 cm, which yields a fundamental resonant frequency of ∼0.632 GHz. Solder pads at each end of the structure, connecting with the feedline, were 1200 µm long by 120 µm wide. There were pinning vias with a diameter of 20 µm along the traces. The spacing between trace and vias is 200 µm. The ADS layout of a stripline resonator is shown in Figure 3.21.

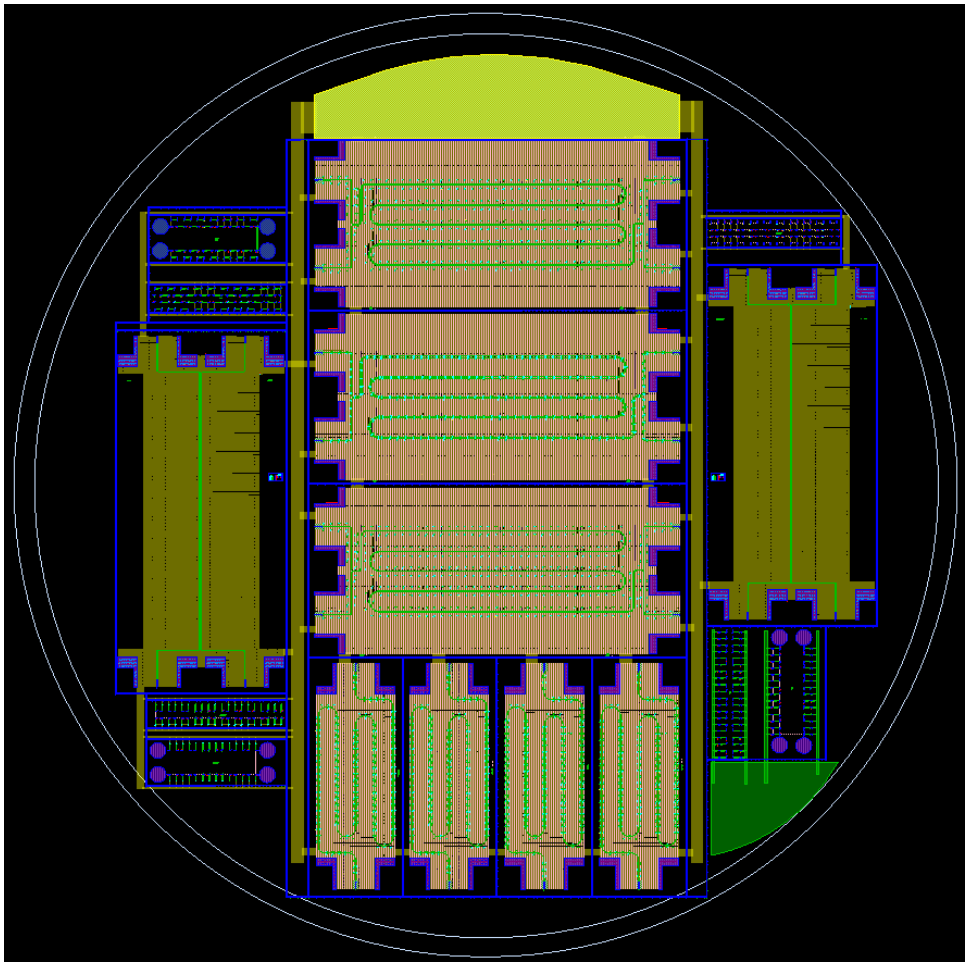

Figure 3.20: ADS layout of 3 stripline transmission lines, 4 stripline resonators, 2 microstrip transmission lines and via chain test structures.

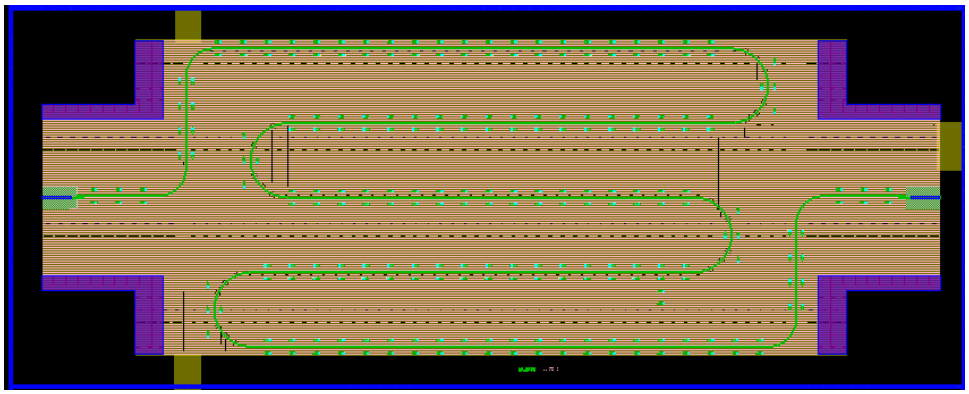

Figure 3.21: A close-up view of a stripline resonator.

3.3.2 Sample Fabrication

Test structures were fabricated using similar thin-film fabrication processes, as discussed in Section 3.2.2. Here, I outline the long steps and details of the fabrication processes can be found in Appendix A.

The resonator fabrication process began with deposition of a Cr/Al sacrificial release layer with thicknesses of 25 nm and 200 nm, respectively, on a 150 mm diameter Si wafer. HD-4100 polyimide was spin-coated and cured at 375°C to achieve a ∼10 µm film. Al (20 nm)/Nb (250 nm)/Al (20 nm) bottom ground plane of the resonator was then patterned and deposited on the cured HD-4100. A seedlayer of Ti (50 nm)/Cu (200 nm) was then deposited on the ground plane by electron-beam thermal evaporation with a deposition rate of 2 Å/s. Wafers were then coated with HD-4110 polyimide with via hole patterned. After the polyimide was developed in the PA-401D solution, samples were rinsed in PA-400R solution. Next, wafers were cured at 225°C to yield a ∼20 µm bottom dielectric. To electroplate the Cu vias, the samples were soaked into 1% HCl solution for ∼35 s to remove the oxide layer on the seedlayer. Then Cu was electroplated to fill the polyimide via hole. After Cu plating, Al (20 nm)/Nb (250 nm)/Al (20 nm) signal traces were patterned and deposited on the cured HD-4110 polyimide. After this step, wafers were divided into two groups. One group was fabricated to be embedded microstrip transmission line resonators and the other group was fabricated to be stripline transmission line resonators. RF/microwave performance of these different types of resonators was studied. Figure 3.22(1) to (10) illustrates the above fabrication procedure.

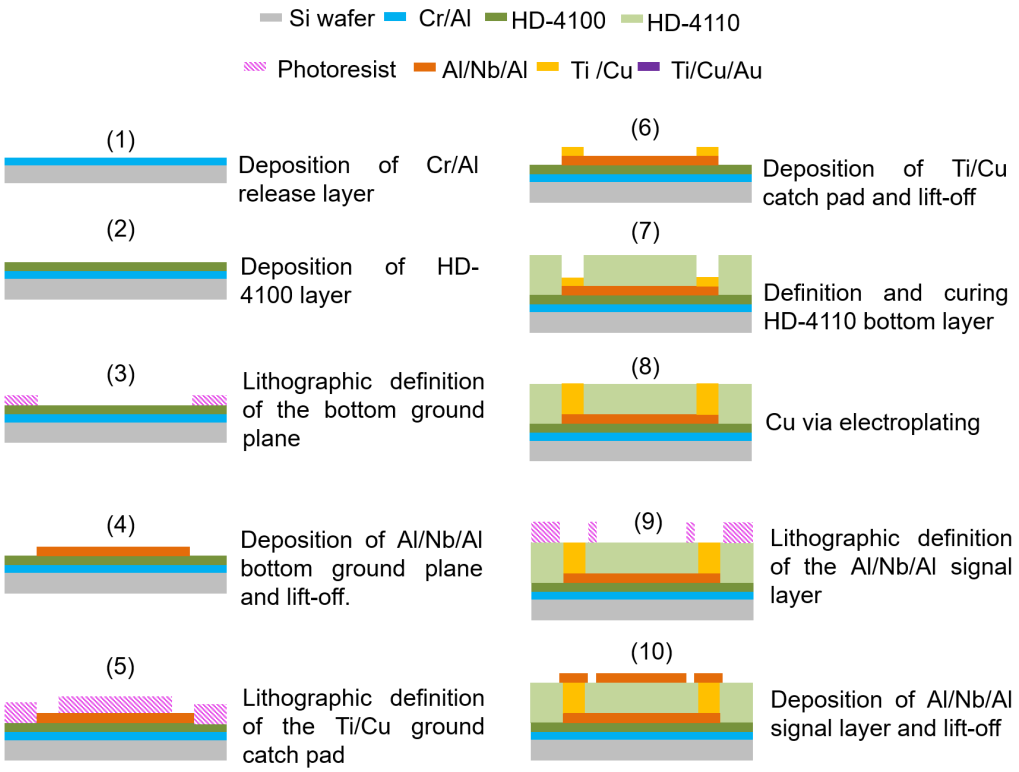

Figure 3.22: Stripline resonators and embedded microstrip resonators fabrication process flow (step 1 to step 10).

For stripline resonators, a Ti (50 nm)/Cu (200 nm) seedlayer was pattered and deposited on signal layer, followed by lift-off process. Next, another 20 µm HD-4110 polyimide layer was patterned, developed and cured at 225°C to form a ∼20 µm film. Cu was then electroplated to fill the second layer via holes in the polyimide. Top ground plane was then patterned. Wafers were loaded into the metal deposition chamber and deposited with Al/Nb/Al metallization with the same parameters as the bottom ground plane. These fabrication procedures was illustrated in Figure 3.23(11a) to (16a).

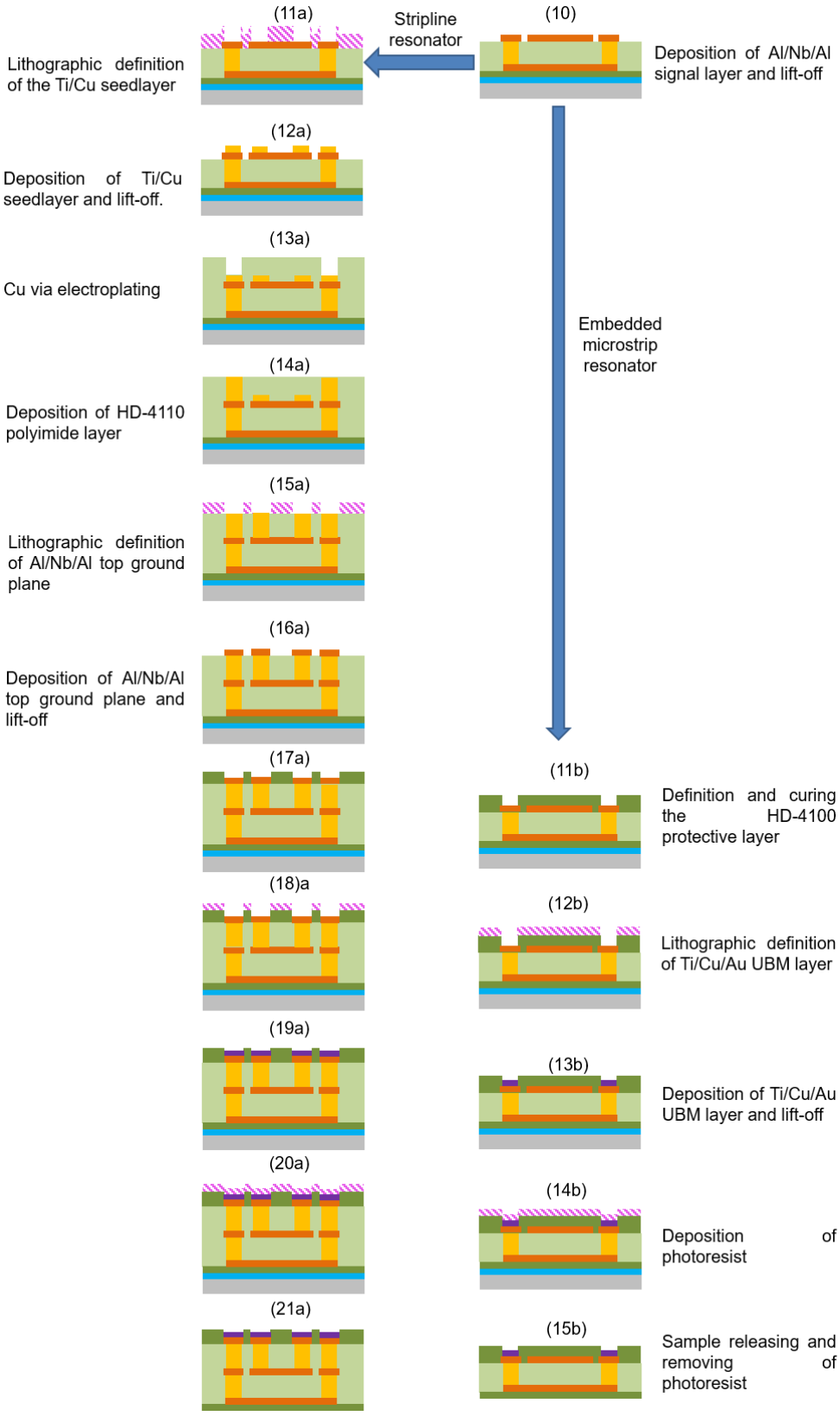

Figure 3.23: Stripline resonators (step 11a to step 21a) and embedded microstrip resonators (step 11b to step 15b) fabrication process flow continued.

Figure 3.23(17a) to (21a) and (11b) to (15b) show the rest of the fabrication procedures for stripline resonators and embedded microstrip resonators, respectively. A HD-4100 polyimide protective layer was spin-coated, patterned and cured at 225°C to achieve a ∼4 µm film as a top protective layer. Finally, a Ti (100 nm)/Cu (500 nm)/Au (10 nm) UBM layer was patterned and deposited on top of the ground plane, followed by a standard lift-off process. To release the sample, a similar anodic dissolution process was performed. After releasing from the Si supporting wafer, the samples were hand cut into individual samples to be assembled using Southwest microwave connectors to perform RF/microwave measurement. Figure 3.24 and Figure 3.25 show a released stripline resonator and the same sample assembled with Southwest connectors, respectively. Figure 3.26 shows an assembled embedded microstrip resonator.

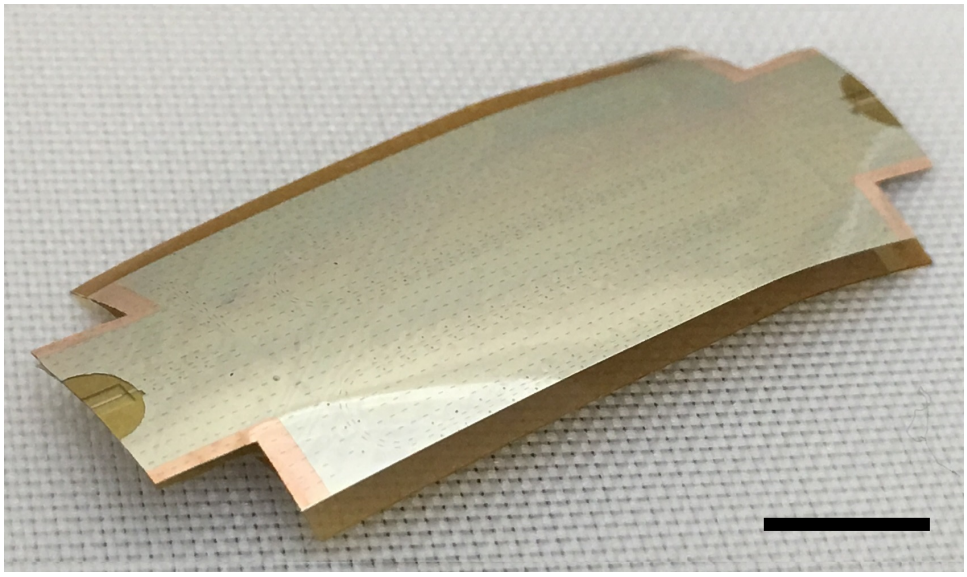

Figure 3.24: A fabricated 13 cm long stripline resonator. Scale bar: 5mm.

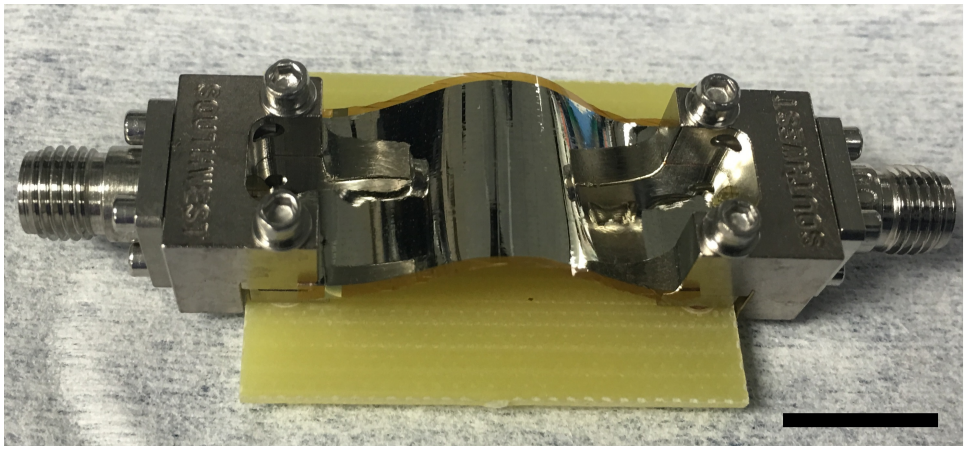

Figure 3.25: An 13 cm long stripline resonator assembled with Southwest microwave end-launch connectors. Scale bar: 1 cm.

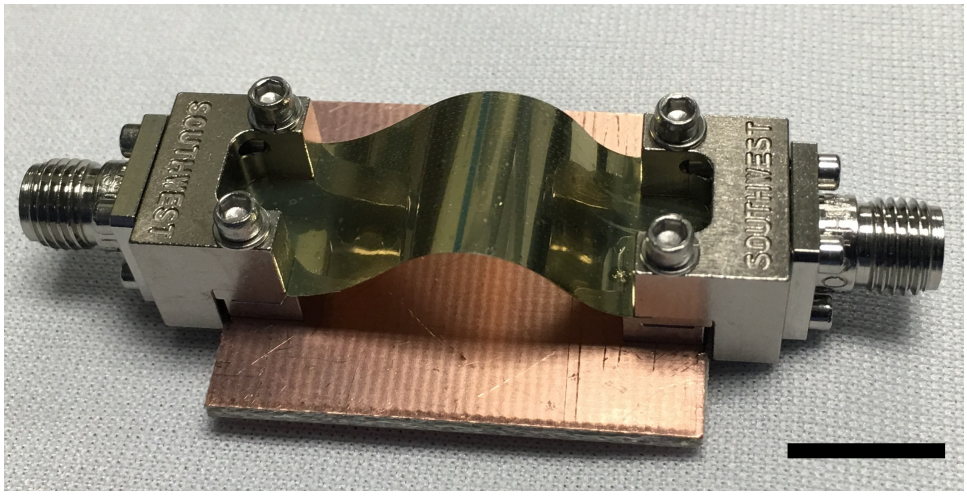

Figure 3.26: A 13 cm long embedded microstrip resonator assembled with Southwest microwave end-launch connectors.Scale bar: 1 cm.

3.3.3 Results and Discussion

Recall that we are attempting to extract tanδ and understand the loss properties of SC flexible resonators to help us understand the loss of similarly fabricated transmission lines.

Q_l of three stripline resonators and one embedded microstrip resonator were measured at various temperatures. Average Q_l of different resonators at resonant frequencies and at different temperatures were summarized in Table 3.4. The upper bound on tanδ for these resonators at multiple resonant frequencies and various temperatures was also calculated,

Frequency (GHz)	Q_l (From stripline resonators)				Q_l (From microstrip resonator)			
	1.2 K	2.0 K	3.0 K	4.2 K	1.2 K	2.0 K	3.0 K	4.2 K
0.632	10326	7421	5606	4803	11985	9086	6402	5623
1.264	10338	7472	5220	4326	12299	8440	5975	4945
1.896	10006	7345	4902	3887	11209	7809	5374	4425
2.527	10058	7277	4620	3675	10624	7586	5067	4058
3.154	9411	6955	4444	3422	9852	6888	4541	3637
3.763	9679	7200	4377	3347	9566	6681	4390	3460
4.415	8732	6610	4150	3115	8266	5888	3817	3093
5.041	8449	6426	3915	2884	7933	5533	3762	3099
5.669	8184	6226	3868	2817	7672	5422	3597	2872
6.297	7834	5882	3709	2685	7056	5330	3375	2652
6.928	7259	5774	3339	2491	6507	4621	3176	2440
7.568	6706	5322	3206	2372	6120	4355	2987	2335
8.187	6616	5286	3210	2283	5899	4010	2865	2233
8.822	6219	5082	2998	2222	5466	3933	2695	2085
9.453	5804	4694	2820	2049	5362	3855	2639	2044
10.090	5666	4492	2769	1998	4850	3677	2530	1968
10.710	5427	4316	2670	1881	4596	3500	2345	1853
11.330	5130	4136	2478	1854	4483	3372	2248	1783
11.980	4920	3931	2354	1725	4322	3222	2102	1710
12.610	4804	3854	2347	1664	4256	3156	2097	1678
13.230	4636	3700	2302	1637	4115	3099	2051	1636

Table 3.4: Average value of measured Q_l at different resonant frequencies for stripline resonators and embedded microstrip resonators. Measurements were taken at different temperatures (1.2 K, 2.0 K, 3.0 K and 4.2 K) in PT.

which are shown in Table 3.5 and Table 3.6 for stripline resonators and embedded microstrip resonators, respectively. Similar tanδ value can be observed between them.

Figure 3.27 shows the $1/Q_l$ for multiple resonant frequencies of different resonators at various temperatures. ADS simulation results for the loss-less case of two types of resonators was also included. It can be observed that embedded microstrip resonators and stripline resonators show fairly comparable results at different temperatures. Even at the lowest temperature 1.2 K, the slope of the fitting lines was not parallel with the simulation result, indicating that these resonators have relatively high BCS conductor loss. This is possibly due to using a "patterned ground method", where the Nb ground plane was deposited

Frequency (GHz)	$\tan\delta$ calculated from 3 stripline resonators			
	(1.2 K)	(2.0 K)	(3.0 K)	(4.2 K)
0.632	9.68E-05	1.35E-04	1.78E-04	2.08E-04
1.264	9.67E-05	1.34E-04	1.92E-04	2.31E-04
1.896	9.99E-05	1.36E-04	2.04E-04	2.57E-04
2.527	9.94E-05	1.37E-04	2.17E-04	2.72E-04
3.154	1.06E-04	1.44E-04	2.25E-04	2.92E-04
3.763	1.03E-04	1.39E-04	2.28E-04	2.99E-04
4.415	1.15E-04	1.51E-04	2.41E-04	3.21E-04
5.041	1.18E-04	1.56E-04	2.55E-04	3.47E-04
5.669	1.22E-04	1.61E-04	2.59E-04	3.55E-04
6.297	1.28E-04	1.70E-04	2.70E-04	3.72E-04
6.928	1.38E-04	1.73E-04	3.00E-04	4.01E-04
7.568	1.49E-04	1.88E-04	3.12E-04	4.22E-04
8.187	1.51E-04	1.89E-04	3.12E-04	4.38E-04
8.822	1.61E-04	1.97E-04	3.34E-04	4.50E-04
9.453	1.72E-04	2.13E-04	3.55E-04	4.88E-04
10.090	1.77E-04	2.23E-04	3.61E-04	5.01E-04
10.710	1.84E-04	2.32E-04	3.75E-04	5.32E-04
11.330	1.95E-04	2.42E-04	4.04E-04	5.40E-04
11.980	2.03E-04	2.54E-04	4.25E-04	5.80E-04
12.610	2.08E-04	2.59E-04	4.26E-04	6.01E-04
13.230	2.16E-04	2.70E-04	4.34E-04	6.11E-04

Table 3.5: Extracted upper bound on $\tan\delta$ at various resonant frequencies and different temperatures for stripline resonators.

Frequency (GHz)	$\tan\delta$ calculated from 1 embedded microstrip resonator			
	(1.2 K)	(2.0 K)	(3.0 K)	(4.2 K)
0.632	8.34E-05	1.10E-04	1.56E-04	1.78E-04
1.264	8.13E-05	1.18E-04	1.67E-04	2.02E-04
1.896	8.92E-05	1.28E-04	1.86E-04	2.26E-04
2.527	9.41E-05	1.32E-04	1.97E-04	2.46E-04
3.154	1.02E-04	1.45E-04	2.20E-04	2.75E-04
3.763	1.05E-04	1.50E-04	2.28E-04	2.89E-04
4.415	1.21E-04	1.70E-04	2.62E-04	3.23E-04
5.041	1.26E-04	1.81E-04	2.66E-04	3.23E-04
5.669	1.30E-04	1.84E-04	2.78E-04	3.48E-04
6.297	1.42E-04	1.88E-04	2.96E-04	3.77E-04
6.928	1.54E-04	2.16E-04	3.15E-04	4.10E-04
7.568	1.63E-04	2.30E-04	3.35E-04	4.28E-04
8.187	1.70E-04	2.49E-04	3.49E-04	4.48E-04
8.822	1.83E-04	2.54E-04	3.71E-04	4.80E-04
9.453	1.86E-04	2.59E-04	3.79E-04	4.89E-04
10.090	2.06E-04	2.72E-04	3.95E-04	5.08E-04
10.710	2.18E-04	2.86E-04	4.26E-04	5.40E-04
11.330	2.23E-04	2.97E-04	4.45E-04	5.61E-04
11.980	2.31E-04	3.10E-04	4.76E-04	5.85E-04
12.610	2.35E-04	3.17E-04	4.77E-04	5.96E-04
13.230	2.43E-04	3.23E-04	4.88E-04	6.11E-04

Table 3.6: Extracted upper bound on $\tan\delta$ at various resonant frequencies and different temperatures for embedded microstrip transmission line resonators.

first. Ground plane Nb quality was degraded during additional polyimide curing processes compared to using previous method (one additional polyimide cure for embedded microstrip resonators and two additional polyimide cure for stripline resonators). Moreover, to create the Cu vias, these resonators were immersed in Cu plating solution for hours. This process may also cause Nb quality degradation and lead to higher BCS loss, since polyimide may uptake moisture or other contaminants from the plating solution that can damage the Nb.

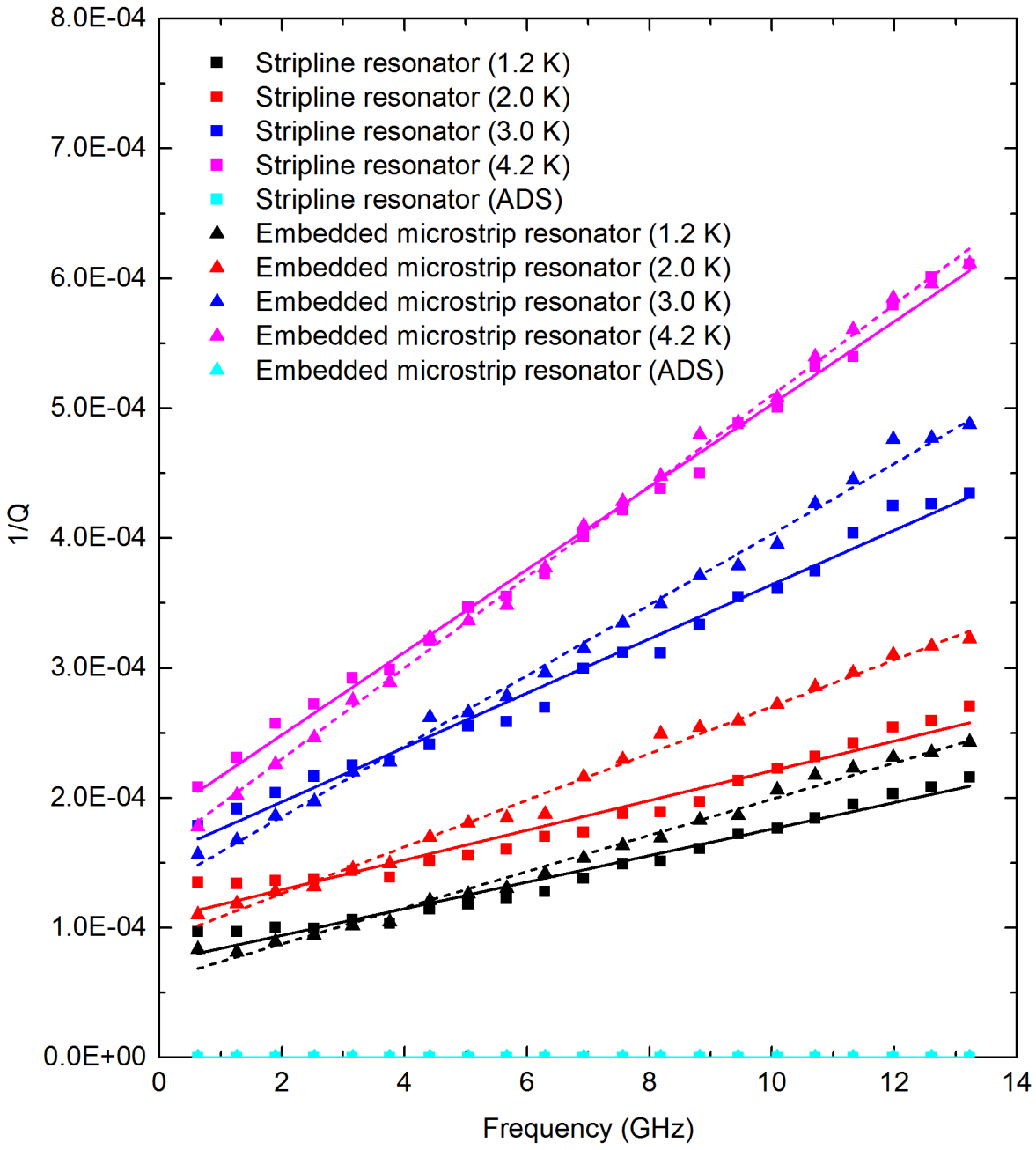

Figure 3.27: $1/Q_l$ for multiple resonant frequencies of different resonators at various temperatures. Corresponding linear fits are shown as solid and dashed lines.

3.4 Summary

In this chapter, design, fabrication procedures and characterization results of embedded and non-embedded HD-4110 resonators and PI-2611 resonators were presented. Upper bounds on the microwave loss tangent of polyimide HD-4110 were reported at cryogenic temperatures below 4 K for a wide frequency range from 1 GHz to 21 GHz, showing values as low as 5×10^{-5}. By using a reduced cure temperature for a HD-4110 polyimide embedding layer, embedded flexible superconducting microstrip exhibited very comparable microwave performance to that of non-embedded microstrip. PI-2611 resonators were mainly used to investigate the impact of different thickness of encapsulation layer on RF/microwave performance of those resonators. Also, fabrication procedures and microwave performance of stripline transmission line resonators were presented. BCS loss and dielectric loss of stripline resonators were compared with other resonator structures. To our knowledge, this work is the first time to report RF measurements results of flexible superconducting stripline resonators and they show very promising RF performance. The data presented not only provide design guidance for constructing ultra low-loss flexible thin-film superconducting interconnects using embedded structure, such as embedded microstrip and stripline, but also show the feasibility of building cables with more complex structures with excellent RF performance.

Bibliography

[1] W. Smith, A. Kou, U. Vool, I. Pop, R. Schoelkopf, and M. Devoret, "Simulation and measurement of a fluxonium qubit inductively coupled to a readout resonator," *APS Meeting Abstracts*, vol. 1, p. 39005, 2015.

[2] N. Didier, J. Bourassa, and A. Blais, "Fast quantum nondemolition readout by parametric modulation of longitudinal qubit-oscillator interaction," *Physical Review Letters*, vol. 115, no. 20, p. 203601, 2015.

[3] C. Eichler, J. Mlynek, J. Butscher, P. Kurpiers, K. Hammerer, T. Osborne, and A. Wallraff, "Exploring interacting quantum many-body systems by experimentally creating continuous matrix product states in superconducting circuits," *Physical Review X*, vol. 5, no. 4, p. 041044, 2015.

[4] J. Teufel, T. Donner, M. Castellanos-Beltran, J. Harlow, and K. Lehnert, "Nanomechanical motion measured with an imprecision below that at the standard quantum limit," *Naturenano technology*, vol. 4, no. 12, pp. 820823, 2009.

[5] J. Baselmans, S. Yates, P. De Korte, H. Hoevers, R. Barends, J. Hovenier, J. Gao,and T. Klapwijk, "Development of high-Q superconducting resonators for use as kinetic inductance detectors," *Advances in Space Research*, vol. 40, no. 5, pp. 708713, 2007.

[6] B. Collaudin and N. Rando, "Cryogenics in space: a review of the missions and of the technologies," *Cryogenics*, vol. 40, no. 12, pp. 797819, 2000.

[7] D. Moore, S. Golwala, B. Bumble, B. Cornell, P. Day, H. LeDuc, and J. Zmuidzinas, "Position and energy-resolved particle detection using phonon-mediated microwave kinetic inductance detectors," *Applied Physics Letters*, vol. 100, no. 23, p. 232601, 2012.

[8] G. Hammer, S. Wuensch, M. Roesch, K. Ilin, E. Crocoll, and M. Siege, "Superconducting coplanar waveguide resonators for detector applications," *Superconductor Science and Technology* vol. 20, no. 11, p. S408, 2007.

[9] M. Roesch, A. Benoit, A. Bideaud, N. Boudou, M. Calvo, A. Cruciani, S. Doyle, H. Leduc, A. Monfardini, L. Swenson, et al., "Development of lumped element kinetic inductance detectors for NIKA," arXivpreprintarXiv:1212.4585, 2012.

[10] O. M. Ivanyuta, O. V. Prokopenko, V. M. Raksha, and A. M. Klushin, "Microwave detection using Josephson junction arrays integrated in a resonator," *Physica Status Solidi(c)* vol. 2, no. 5, pp. 16881691, 2005.

[11] J. Mazierska, D. Ledenyov, M. V. Jacob, and J. Krupka, "Precise microwave characterization of MgO substrates for HTS circuits with superconducting post dielectric resonator," *Superconductor Science and Technology*, vol. 18, no. 1, p. 18, 2004.

[12] J. Mazierska, J. Krupka, M. V. Jacob, and D. Ledenyo, "Complex permittivity measurements at variable temperatures of low loss dielectric substrates employing split post and single post dielectric resonators," *Microwave Symposium Digest,2004 IEEE MTT-S International*, vol. 3, pp. 18251828, IEEE, 2004.

[13] M. V. Jacob, J. Mazierska, D. Ledenyov, and J. Krupka, "Microwave characterisation of CaF 2 at cryogenic temperatures using a dielectric resonator technique," *Journal of the European Ceramic Society*, vol. 23, no. 14, pp. 26172622, 2003.

[14] H. Zeng, J. Juang, J. Lin, K. Wu, T. Uen, and Y. Gou, "Temperature dependence of the penetration depth and effective dielectric constant measured by YBa2Cu3O7 microstrip ring resonators," *Physica C: Superconductivity*, vol. 351, no. 2, pp. 97102, 2001.

[15] Galt, David and Price, John C and Beall, James A and Harvey, Todd E, "Ferroelectric thin film characterization using superconducting microstrip resonators," *IEEE Transactions on Applied Superconductivity*, vol. 5, no. 2, pp. 2575-2578, 1995.

[16] D. M. Pozar, "*Microwave engineering*", 4th ed. John Wiley & Sons, 2012.

[17] R. E. Collin, "*Foundations for Microwave Engineering*", John Wiley & Sons, 2007..

[18] E. Belohoubek and E. Denlinger, "Loss considerations for microstrip resonators (short papers)," *IEEE Transactions on Microwave Theory and Techniques*, vol. 23, no. 6,pp. 522526, 1975.

[19] P. R. Bevington, D. K. Robinson, J. M. Blair, A. J. Mallinckrodt, S. McKay, et al.," Data reduction and error analysis for the physical sciences," *Computers in Physics*, vol. 7, no. 4, pp. 415416, 1993.

[20] M. Kirschning and R. H. Jansen, "Accurate model for effective dielectric constant of microstrip with validity up to millimetre-wave frequencies," *Electronics Letters*, vol. 18,no. 6, pp. 272273, 1982.

[21] HD MicroSystems 2009 PI-2600 Series-Low Stress Applications product bulletin. Available at (`http://www.dupont.com/content/dam/dupont/products-and-services/electronic-and-electrical-materials/semiconductor-fabrication-and-packaging-materials/documents/PI-2600_ProcessGuide.pdf`)

[22] HD MicroSystems 2014 HD-4100 Series product bulletin. Available at (`http://www.hdmicrosystems.com/HDMicroSystems/en_US/products/photodefineable/HD-4100_negative_solvent.html`)

[23] D. B. Tuckerman, M. C. Hamilton D. J. Reilly, R. Bai, G. A. Hernandez, J. M. Hornibrook, J. A. Sellers, C. D. Ellis, "Flexible superconducting Nb transmission lines on thin film polyimide for quantum computing applications," *Superconductor Science and Technology*, vol. 29, no. 8, pp. 084007, 2016.

[24] S. Metz, A. Bertsch, and P. Renaud, "Partial release and detachment of microfabricated metal and polymer structures by anodic metal dissolution," *Journal of Microelectromechanical Systems*, vol. 14, no. 2, pp. 383391, 2005.

[25] S. Priyabadini, T. Sterken, M. Cauwe, L. Van Hoorebeke and J. Vanfleteren, "High-yield fabrication process for 3D-stacked ultrathin chip packages using photo-definable polyimide and symmetry in packages," *IEEE Transactions on Components, Packaging and Manufacturing Technology*, vol. 4, no. 1, pp. 158167, 2014.

[26] L. Wang, T. Sterken, M. Cauwe, D. Cuypers, and J. Vanfleteren, "Fabrication and characterization of flexible ultrathin chip package using photosensitive polyimide," *IEEE Transactions on Components, Packaging and Manufacturing Technology*, vol. 2, no. 7,pp. 10991106, 2012.

[27] H. Cao, A.-L. Li, C. M. Nguyen, Y.-B. Peng, and J.-C. Chiao, "An integrated flexible implantable micro-probe for sensing neurotransmitters," *IEEE Sensors Journal*, vol. 12,no. 5, pp. 16181624, 2012.

[28] V. Misra, A. Bozkurt, B. Calhoun, T. Jackson, J. S. Jur, J. Lach, B. Lee, et al, "Flexible technologies for self-powered wearable health and environmental sensing," *Proceedings of the IEEE*, vol. 103, no. 4, pp. 665681, 2015.

[29] A. Megrant, C. Neill, R. Barends, B. Chiaro, Y. Chen, L. Feigl, J. Kelly, E. Lucero,M. Mariantoni, P. J. OMalley, et al, "Planar superconducting resonators with internal quality factors above one million," *Applied Physics Letters*, vol. 100, no. 11, p. 113510, 2012.

[30] J. Turneaure, "Measurements on superconducting Nb prototype structures at 1300 MHz," *IEEE Transactions on Nuclear Science*, vol. 18, no. 3, pp. 166167, 1971.

[31] R. Bai, "Superconducting Resonators on Thin Film Flexible Substrates," *PhD thesis, Auburn University*, 2016.

[32] S. Zou, Y. Cao, V. Gupta, B. Yelamanchili, J. A. Sellers, C. D. Ellis, D. B. Tuckerman and M. C. Hamilton, "High-Quality Factor Superconducting Flexible Resonators Embedded in Thin-Film Polyimide HD-4110," *IEEE Transactions on Nuclear Science*, vol. 27, no. 1, pp. 1-5, 2017.

[33] S. Zou, Y. Cao, G. A. Hernandez, R. Bai, V. Gupta, J. A. Sellers, C. D. Ellis, D. B. Tuckerman and M. C. Hamilton, "Embedded Niobium Using PI-2611 for Superconducting Flexible Cables," *MRS Advances*, pp. 1-6, 2017.

Chapter 4

Flexible Low-Loss Superconducting RF Cables Using HD-4110

4.1 Introduction

As has been presented in this last Chapter 3, HD-4110 showed extremely low dielectric loss at cryogenic temperatures. Also, as a photoimageable polyimide, it is useful for building more complex structures. In this chapter, design, fabrication processes and characterization results of flexible superconducting RF cables fabricated on HD-4110 polyimide are presented. Microstrip transmission lines with different length were fabricated and tested. Distributed element models were successfully implemented using Keysight ADS to simulate the RF performance of these superconducting microstrip flex cables at 4.2 K.

4.2 Details of Experiments

4.2.1 Design of Superconducting RF Cables

The mask design used in this work for microstrip transmission lines on HD-4110 dielectric is shown in Figure 4.1. The design includes three 10 cm, three 20 cm, and two 6.5 cm parallel microstrip lines as well as a 10 cm microstrip resonator. Details of each structure is shown in Figure 4.2. The transmission lines were used to measure RF properties of the microstrip lines and also used for a microwave connector study, which will be discussed in Chapter 5. The microstrip had a signal trace width of 50 µm with solder pads at each end that were 1200 µm long by 120 µm wide. The dimension of these solder pads were designed for the Southwest Microwave edge launch connectors. Nb-based and Cu-based microstrip transmission line using this mask design were fabricated. Here, the fabrication procedure for

Nb-based microstrip lines is mainly described. Fabrication processes of Cu-based microstrip lines can be found in fabrication travelers provided in Appendix A.

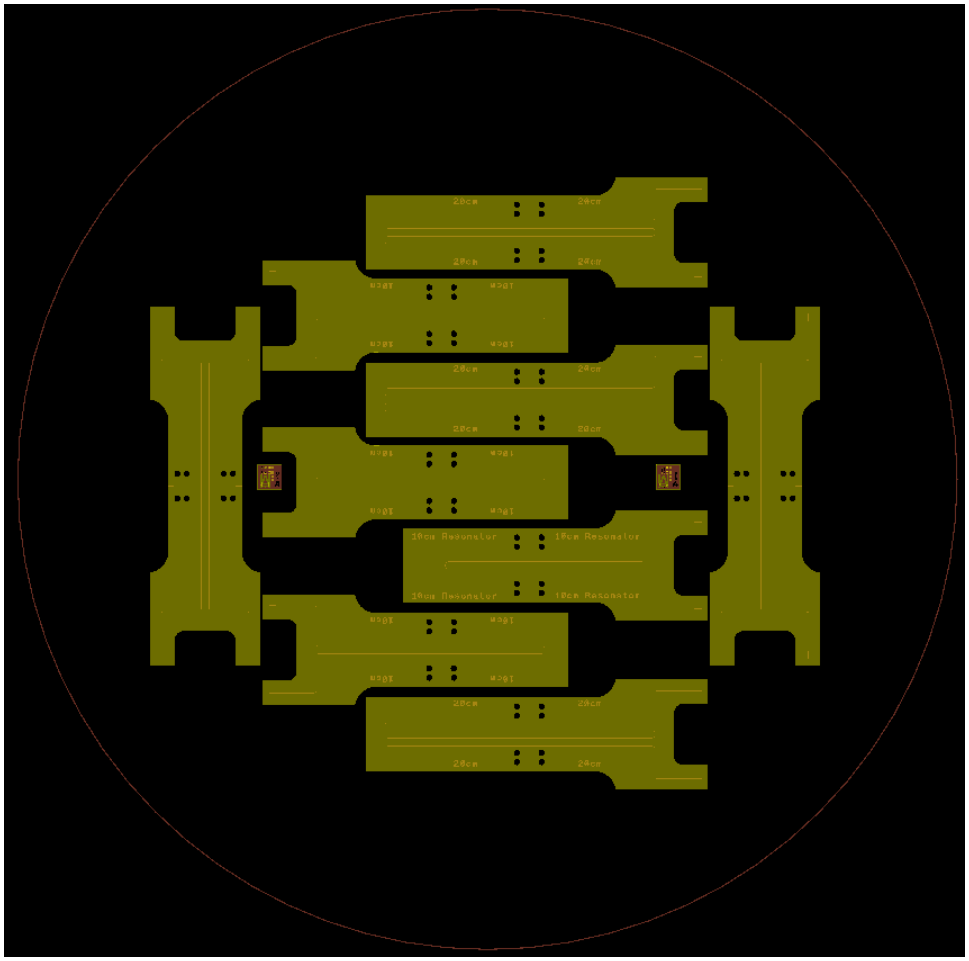

Figure 4.1: ADS layout of microstrip transmission lines on HD-4110 polyimide. The diameter of the red circle is 150 mm.

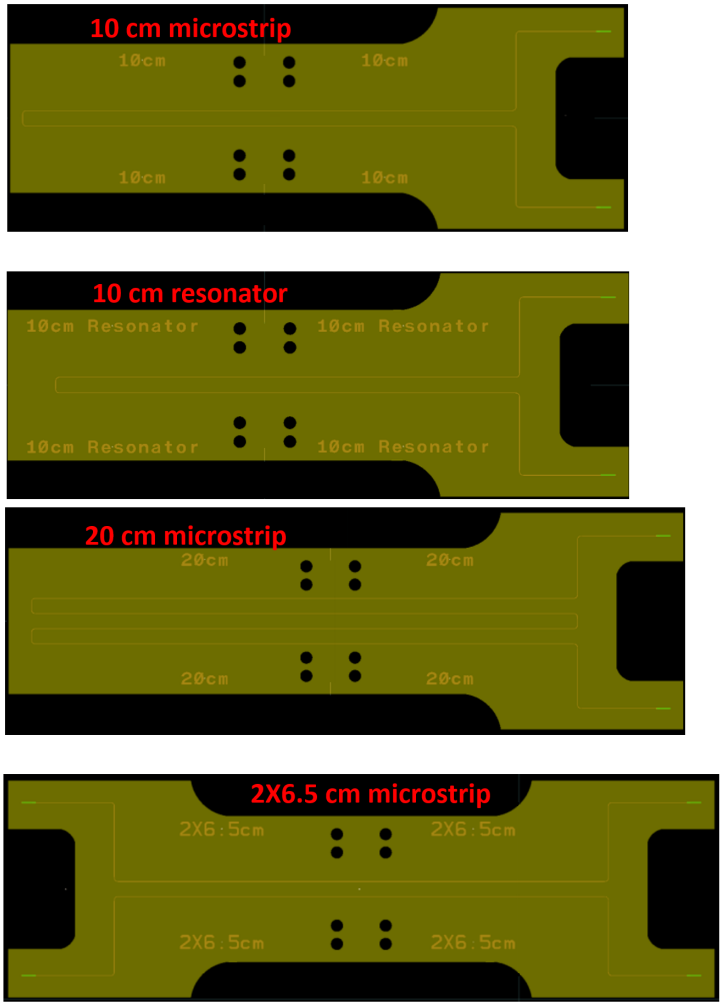

Figure 4.2: A blown-up view of each type of structures in Figure 4.1

4.2.2 Fabrication of Superconducting RF Cables

Cu-based DC cables and connectors were fabricated using similar thin-film fabrication processes, as discussed in Section 3.2.2. Here, I outline the fabrication steps and details of the fabrication processes can be found in Appendix A.

Figure 4.3 schematically illustrates the fabrication procedures for the Nb microstrip transmission lines using HD-4110 polyimide (Figure 4.3(1)-(6)). (1) A Cr (25 nm)/Al (200 nm) sacrificial release layer [1] was first deposited onto RCA cleaned and oxidized Si handle wafers. (2) Polyimide HD-4110 was deposited onto wafers using spin-coating, followed by

photolithographic definition and curing at 375°C in a N_2 atmosphere, to achieve a ∼20 µm-thick film as the flexible substrate of the microstrip. (3) Nb (250 nm)/Au (20 nm) signal traces were formed using conventional photolithography and film lift-off techniques. Using a CHA Mark 50 deposition system, a 250 nm thick Nb film was DC sputter deposited with a power of ∼8 W/cm^2 and Ar pressure of 4 mTorr [2]. Without breaking vacuum, a two minute in-situ ion beam milling surface clean of the Nb surface was performed. This was immediately followed by deposition of the 20 nm thick Au layer using electron beam physical vapor deposited at a rate of 2 Å/s after. Note that the 20 nm thick Au layer is used to reduce the contact resistance. Also, based on [3], 20 nm normal conductor can be proximitized and will not impact the RF performance of the SC cable. (4) Next, samples were coated with a layer of photoresist for protection of the structures during a film release process (5), which involved soaking in a NaCl salt bath with 0.5 V applied to the release layer. (6) After releasing of the film and stripping of the photoresist, samples were then inverted and mounted onto Si carrier wafers for Nb (250 nm)/Au (20 nm) ground plane deposition. Test structures were assembled with Southwest Microwave end-launch SMA connectors for measurement of intact microstrip lines, as shown in Figure 4.5. The SMA connectors were not soldered to the cable metallization and relied on the clamping force to achieve suitable electrical connection. Measurements were performed in a liquid He (LHe) dewar, as shown in Figure 4.6.

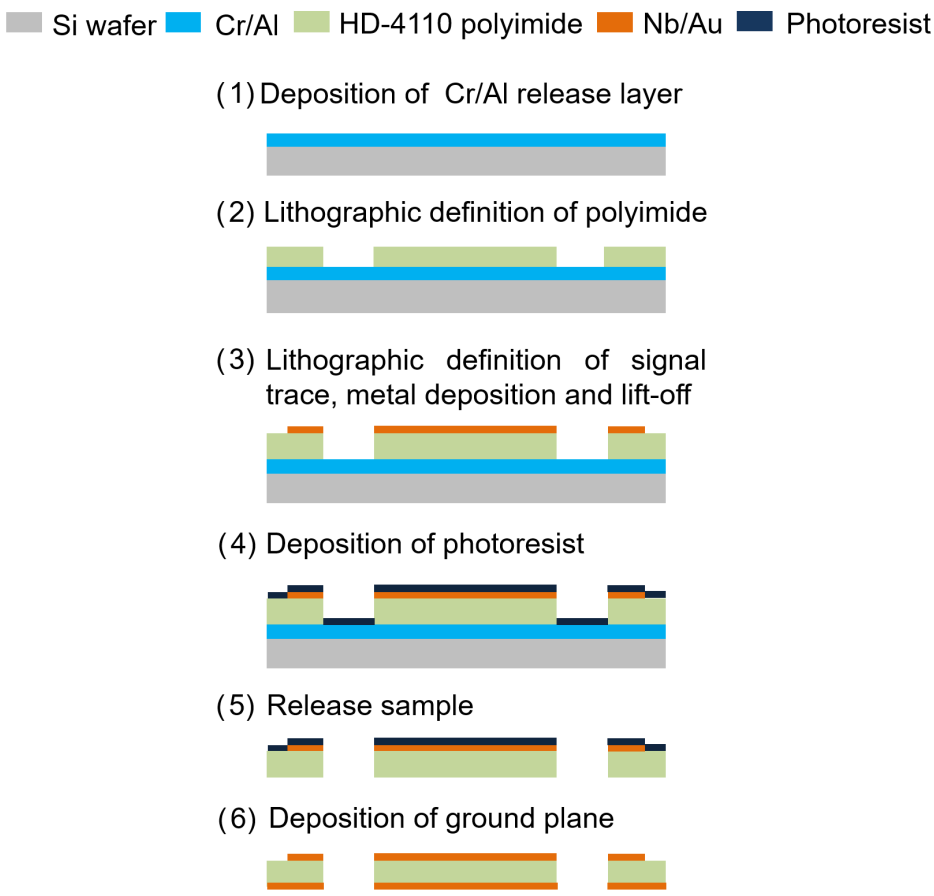

Figure 4.3: Schematic fabrication flow for superconducting flexible Nb microstrip transmission lines (step 1 to step 6). The gaps shown in (5) and (6) represent alignment holes into which polyimide pillars on a glass connector are to be inserted. The glass connector will be described in more details in Chapter 5.

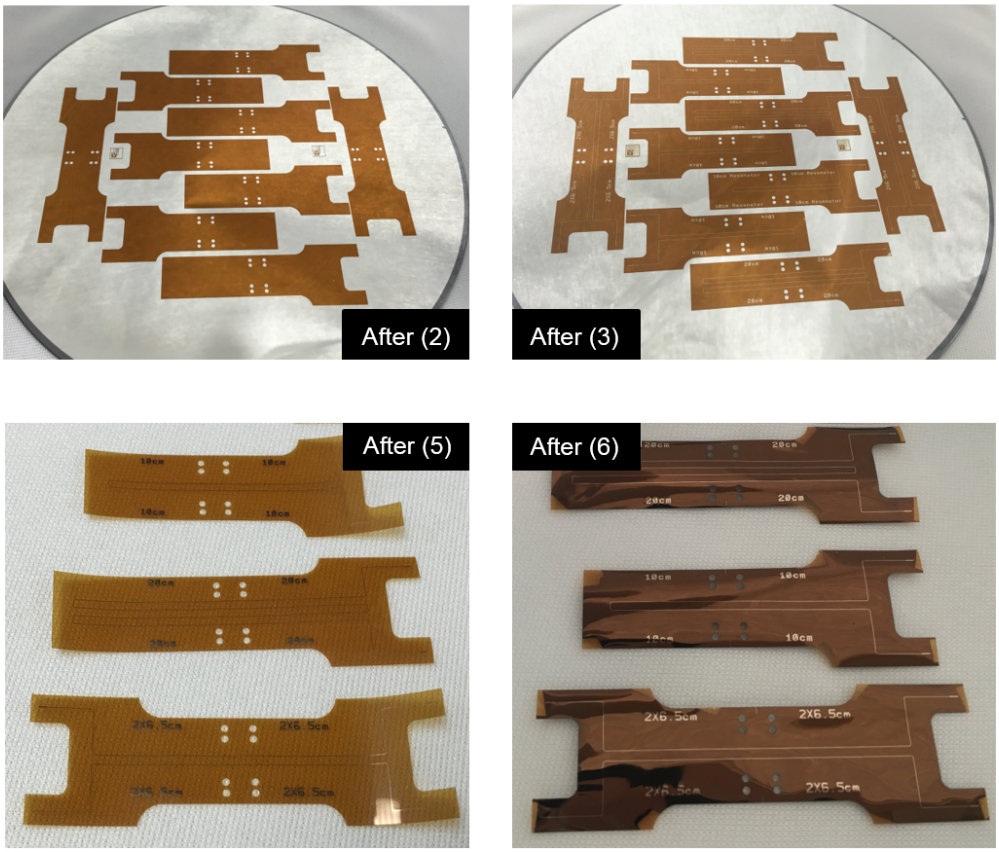

Figure 4.4: Images of Nb microstrip lines during different fabrication steps corresponding to Figure 4.3. Note that 150 mm diameter Si wafers were used in this work.

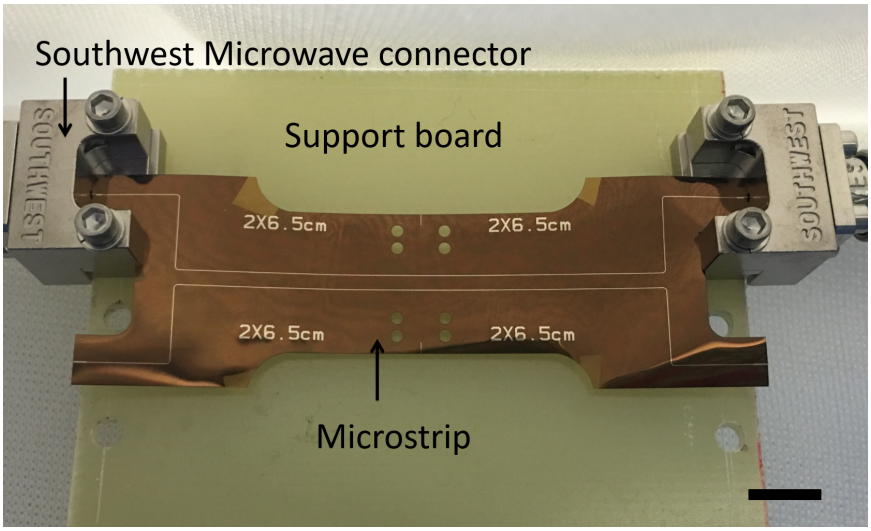

Figure 4.5: An intact 6.5 cm-long microstrip sample assembled with Southwest Microwave end launch SMA connectors mounted on a support board. One line with two end launch connectors has been assembled, while the other (lower) line is open at both ends. The alignment holes mentioned in caption of Figure 4.3 can also be seen in the middle of the cable sample. Scale bar: 5 mm.

Figure 4.6: A 100 L liquid He dewar used to perform RF measurements.

4.3 Results and Discussion

4.3.1 Characterization

DC measurement of microstrip signal and ground plane were performed using a 4-wire resistance measurement. Resistance value was subtracted with a barrel thru with the same set-up. Both signal and ground exhibited complete transition to SC state, with resistance of ∼30 mΩ and ∼3 mΩ, respectively. The critical transition temperature (T_c) of signal and ground were found to be 8.0 K and 8.3 K, respectively.

Frequency-domain measurements were performed using an Keysight PNA network analyzer (N5227A) with an incident microwave power of -20 dBm. The system was calibrated using Short-Open-Load-Reciprocal thru (SOLR) custom calibration standard based on Southwest Microwave edge launch connectors, to move the reference plane to the position of the Southwest Microwave connector pin. More calibration details can be found in Ref [4].

4.3.2 6.5 cm Long Microstrip Line

S-parameter measurement results of 6.5 cm Nb microstrip are shown in Figure 4.7(a) and (b) and includes simulation results. S_{11} and S_{21} ripples result from impedance mismatch due to the launch pad needed for the Southwest Microwave connector pin. Keysight ADS was used to simulate the response of the intact Nb microstrip and a model schematic is shown in Figure 4.8(a). In this distributed element model, all the dimensions were obtained from measurements and HD-4110 dielectric properties are based on Ref [5]. The 6.5 cm long transmission line was divided into 104 equal microstrip units. Each unit consisted of a microstrip element in series with an inductor L_K, corresponding to kinetic inductance of the thin-film, superconducting Nb. The length of the microstrip element is shorter than 1/20 th of the wavelength at the highest simulated frequency of 14 GHz [6]. To simulate the capacitive response of the launch pad, a microstrip element with the dimension of the fabricated launch pad was added in series with a shunt capacitor C_{pad} and an inductor L_{pad} at each end of the line. Extracted C_{pad} of 0.09 pF, L_{pad} of 0.3 nH and L_K of 3.5 pH (364 pH in total for entire microstrip) displays an excellent match of the S-parameter simulation to the measured results. These simulation results are noted as "NIL" (non-ideal launch) in Figure 4.7. To minimize the impact of the Southwest Microwave connector launch transition, the length of the launch pad L_{spad}, L_{pad} and C_{pad} were all set to 0 to simulate the intrinsic response of the microstrip transmission line. These simulation results are noted as "IL" (ideal launch) in Figure 4.7. The Nb transmission line exhibited an insertion loss of less than 0.056

dB up to 14 GHz (0.85 dB/m). For clarity, all the key dimensions and parameters used in the ADS model are listed in Table 4.1.

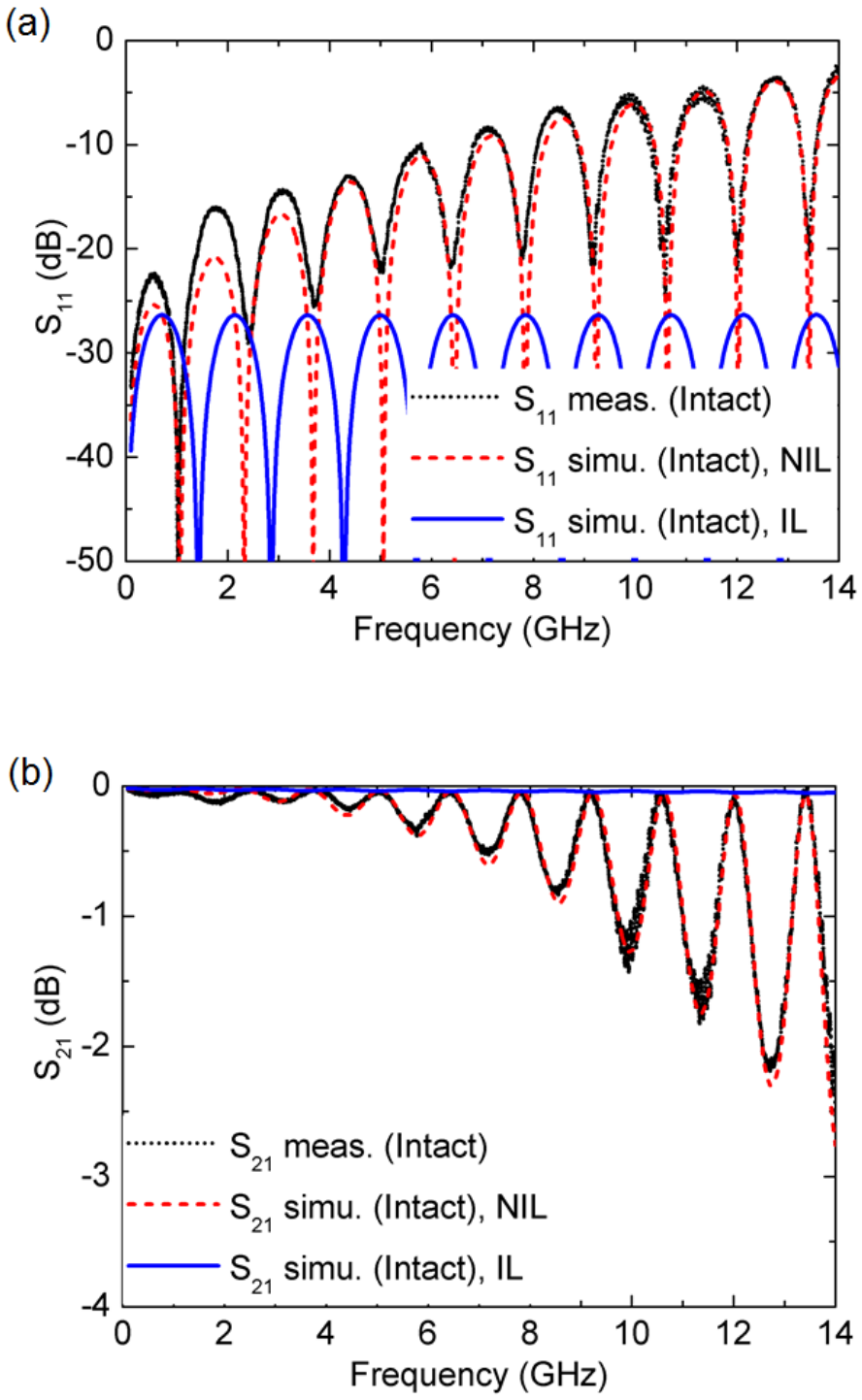

Figure 4.7: Measured and simulated S-parameters of 6.5 cm long microstrip transmission line fabricated on HD-4110 polyimide. ADS simulation results using a non-ideal launch "NIL" and with ideal launch "IL" are shown, found using the model presented in Figure 4.8.

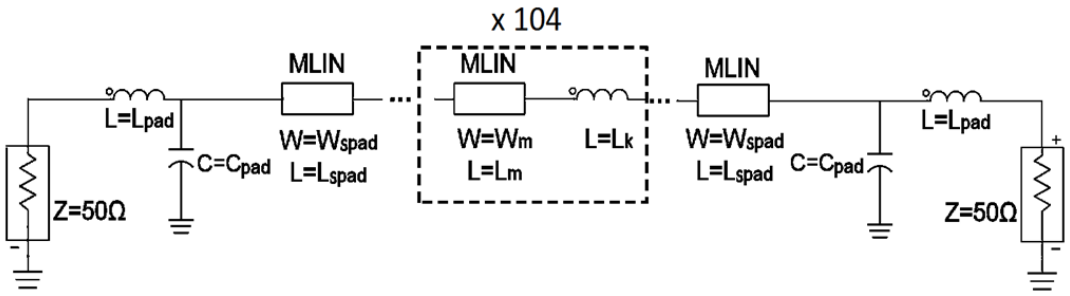

Figure 4.8: Equivalent distributed transmission-line circuit model of 6.5 cm long Nb microstrip. Note that MLIN is a microstrip element unit in ADS, repeated 104 times, with line length and width values of L_L = 0.625 mm and W_L = 52.3 µm, respectively. Launch pads have dimensions of L_{pad} = 1.1 mm and W_{pad} = 122 µm. The kinetic inductance element (L_K) of Nb was determined through simulation to be 3.0 pF.

Symbol	Value	Description
W_m	52.3 µm4	Width of microstrip unit
L_m	0.625 mm	Length of microstrip unit
W_{spad}	122 µm	Width of solder pad
L_{spad}	1.1 mm	Length of solder pad
L_{pad}	0.3 nH	Inductance introduced from the non-ideal launch
C_{pad}	0.09 pF	Capacitance introduced from the non-ideal launch
L_K	3.5 pF	Kinetic inductance of the Nb of each microstrip unit

Table 4.1: Key dimension and parameters in ADS simulation.

4.3.3 20 cm Long Microstrip Line

Figure 4.9(a) and (b) show the S-parameter measurement results and ADS simulation results of a 20 cm long microstrip. Similarly, S_{11} and the ripples of S_{21} are caused by impedance mismatch from Southwest Microwave pin to signal trace. The same distributed element model was used in ADS to model the 20 cm version microstrip, but using 320

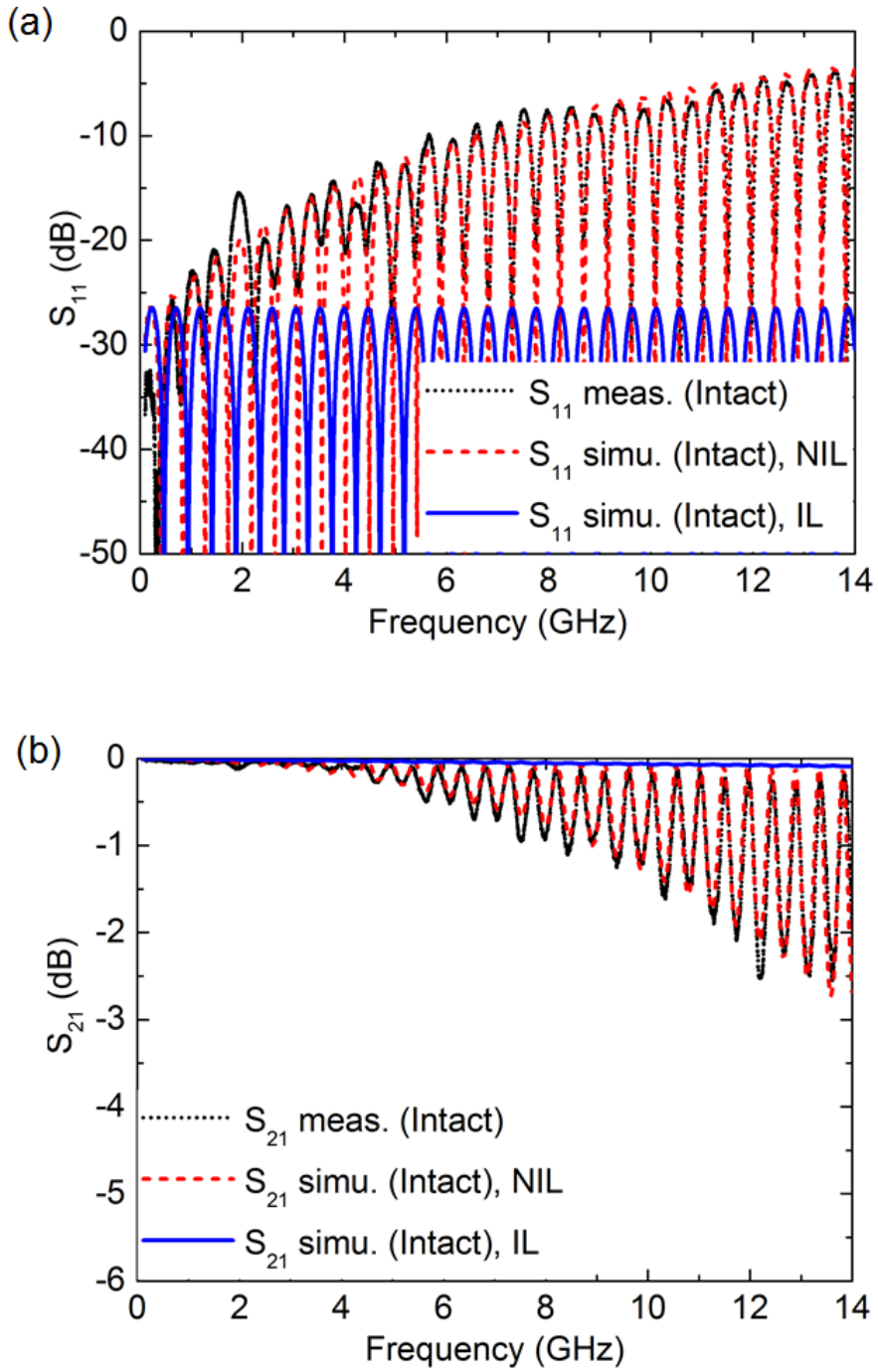

Figure 4.9: Measured and simulated S-parameters of 20 cm long microstrip fabricated on HD-4110 polyimide. ADS simulation results using a non-ideal launch "NIL" and with ideal launch "IL" are shown.

microstrip units for the longer line. All the parameter values were the same as in Table 4.1. NIL and IL cases of this microstrip were simulated. An excellent match was observed between the NIL simulation and the measurements for S_{11} and S_{21}. This indicates that our ADS model of Southwest Microwave connector launch pad is very accurate and can be applied to different microstrip transmission line cables. To simulate the intrinsic insertion loss of the 20 cm microstrip, Southwest Microwave connector was removed from the model, i.e. we removed the L_{pad}, C_{pad} and set L_{spad}=0 mm. Corresponding result is shown as simulation results IL. The intrinsic insertion loss of 20 cm long microstrip is less than 0.095 dB (0.475 dB/m) up to 14 GHz and return loss is greater than 26 dB [7]. The intrinsic insertion loss of Nb-based microstrip transmission line is far less than loss exhibited by similarly fabricated and equivalently sized Cu-based transmission lines. More details of Cu-based cables are described in Chapter 5.

4.4 Summary

In this chapter, fabrication, assembly and characterization of Nb-based SC flexible transmission lines fabricated on photoimageable polyimide HD-4110 were described and demonstrated. The microwave performance of Nb microstrip on HD-4100 exhibited very low transmission line loss of less than 0.85 dB/m from DC to 14 GHz at 4.2 K. A distributed element simulation model was successfully implemented in Keysight ADS to simulate the RF performance of microstrip flex cables. These results provide design guidance for building flexible low-loss thin-film superconducting microwave interconnects. Furthermore, the developed model may be useful for predicting the performance of similar, as well as more complex transmission lines.

Bibliography

[1] S. Metz, A. Bertsch, and P. Renaud, "Partial release and detachment of microfabricated metal and polymer structures by anodic metal dissolution," *Journal of Microelectromechanical Systems*, vol. 14, no. 2, pp. 383391, 2005.

[2] V. Gupta, J. A. Sellers, C. D. Ellis, B. Yelamanchili, S. Zou, G. A. Hernandez, R. Bai, Y. Cao, D. B. Tuckerman and M. C. Hamilton, "Minimizing Film Stress and Degradation in Thin-film Nb Superconducting Cables," *gyIMAPS 13th International Conference and Exhibition on Device Packaging*.

[3] R. Bai, "Superconducting Resonators on Thin Film Flexible Substrates," *PhD thesis, Auburn University*, 2016.

[4] G. A. Hernandez, R. Bai, Y. Cao, J. A. Sellers, C. D. Ellis, D. B. Tuckerman and M. C. Hamilton, "Microwave performance of niobium/kapton superconducting flexible cables," *IEEE Transactions on Applied Superconductivity*, vol. 27, no. 4, pp. 1-4, 2017.

[5] S. Zou, Y. Cao, V. Gupta, B. Yelamanchili, J. A. Sellers, C. D. Ellis, D. B. Tuckerman and M. C. Hamilton, "High-Quality Factor Superconducting Flexible Resonators Embedded in Thin-Film Polyimide HD-4110," *IEEE Transactions on Nuclear Science*, vol. 27, no. 1, pp. 1-5, 2017.

[6] D. M. Pozar, "*Microwave engineering*", 4$^{\text{th}}$ ed. John Wiley & Sons, 2012.

[7] S. Zou, B. Yelamanchili, V. Gupta, T. Isaacs-smith, J. A. Sellers, C. D. Ellis, D. B. Tuckerman and M. C. Hamilton, "Low-Loss Flexible Superconducting Cable and Cable-to-Cable Connection Approach," *Superconductor Science and Technology* (Will submit).

Chapter 5

Microwave Connectors for Thin-Film Transmission Line Applications

5.1 Introduction and Background

Coaxial microwave connectors are a fundamental tool of RF/microwave technology and are widely used in cryogenic research. However, coaxial connectors are not the optimal choice for connection/disconnection of thin film transmission lines at microwave frequencies. There is a need for microwave connectors that are compatible with thin-film cables, extending the scope of miniaturization with a potentially lower thermal load, lighter weight, lower loss and lower cost.

Bhuiyan et al.[1-2] reported a fork-type micro-connector with high package density and high aspect ratio, using UV thick photoresist and Ni electroforming to obtain a contact resistance of approximately 50 mΩ. A schematic view of assembled micro-connectors shown in Figure 5.1(a). The terminal size of fabricated micro-connector thickness is 50 µm with minimum width of 15 µm. SEM images of fabricated plug terminal and socket terminals are shown in Figure 5.1(b) and (c), respectively.

Jang et al.[3] developed a zero-insertion-force (ZIF) micro-connector, using a three-mask process on SOI wafer to fabricate terminals and latches simultaneously. This type of connectors was demonstrated with five 1800 µm-long, 100 µm-wide and 2 µm-high terminals on a 150 µm pitch. The terminals and latches are actuated by electrostatic force to avoid damade from kinking and wearing during the mating and de-mating process. Schematic diagram of ZIF micro-connector is shown in Figure 5.2. These ZIF micro-connectors had a contact resistance of approximately 320 mΩ and simulated and measured insertion loss and return loss are shown in Figure 5.3.

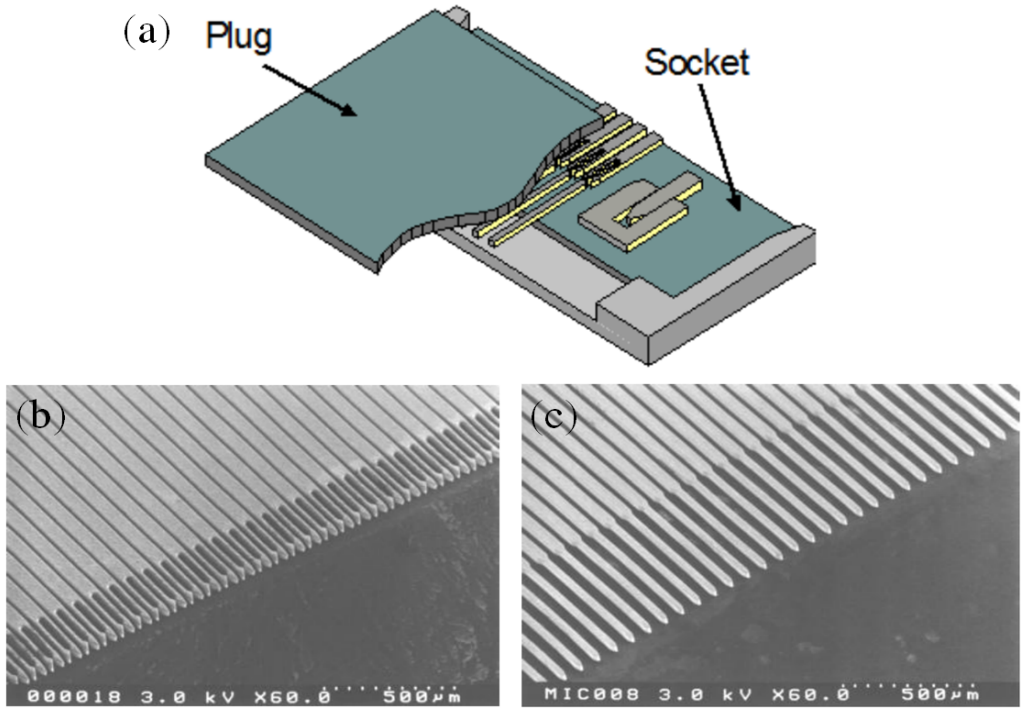

Figure 5.1: (a) 3-D schematic view of assembled fork-type micro-connector. (b) fabricated plug terminals by Ni electroforming and (c) fabricated socket terminals by Ni electroforming. Adapted from [2].

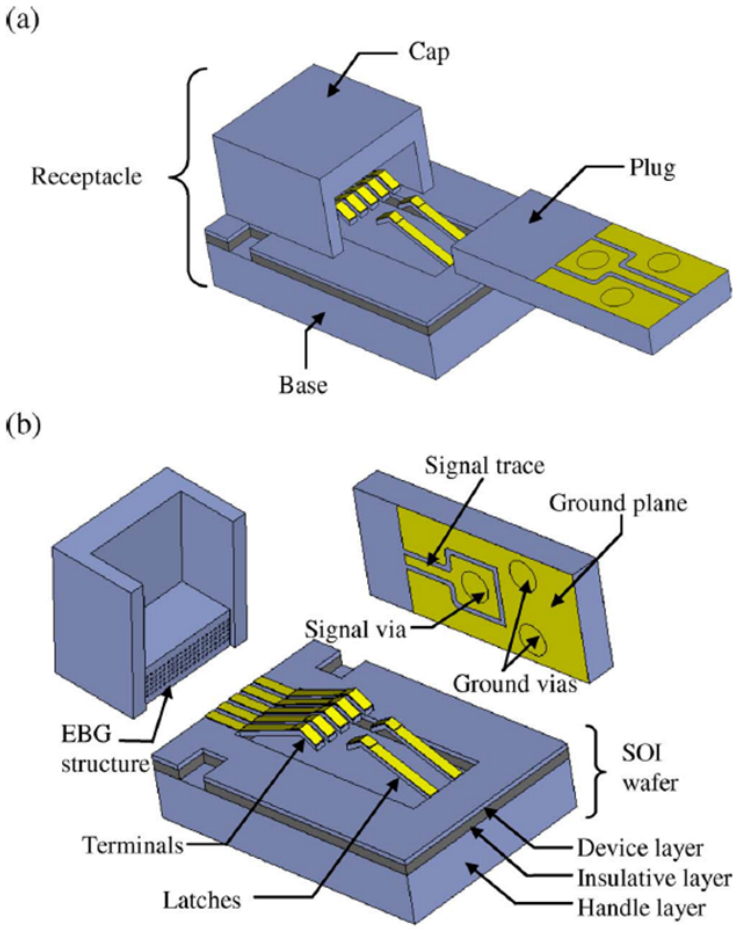

Figure 5.2: Schematic diagram of (a) the assembled ZIF micro-connector and its perspective drawing and (b) components consisting of the ZIF micro-connector. Adapted from [3].

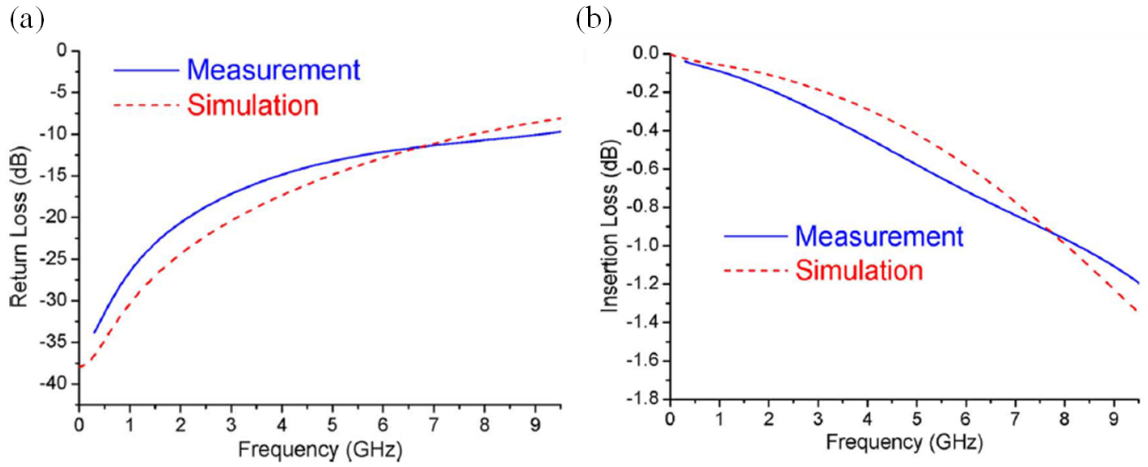

Figure 5.3: (a) Return loss and (b) insertion loss of measured and simulated mated ZIF micro-connector. Adapted from [3].

Fiedler et al.[4] presented a robust, reliable connection of commercial Nano Omnetics connectors to 10 µm flexible thin electrode devices, as shown in Figure 5.4. By using a laser-structured Al_2O_3 substrate, different connectors and thin-film devices can be applied. The ceramic adapter made it possible to minimize the width of the flexible cable by stacking different polyimide-based electrodes with a thickness of only 10 µm.

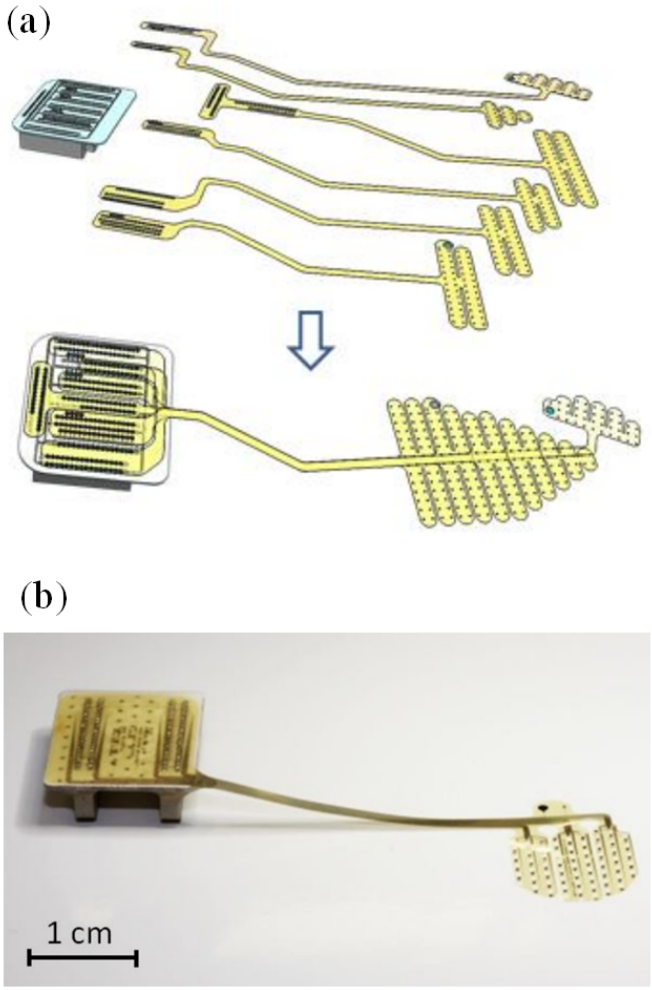

Figure 5.4: (a) Schematic diagram of a modular assembly of an electrocardiography electrode and (b) assembled polyimide-based electrode with ceramic adapter. Adapted from [4].

Williams et al.[5] reported a flex to flex mechanical device, which is used for electrically connecting a flexible assembly to another flexible assembly. Figure 5.5 and Figure 5.6 show the perspective view and exploded view of the connection device. Despite different improvements brought by all the aforementioned methods and devices, many issues still need to be

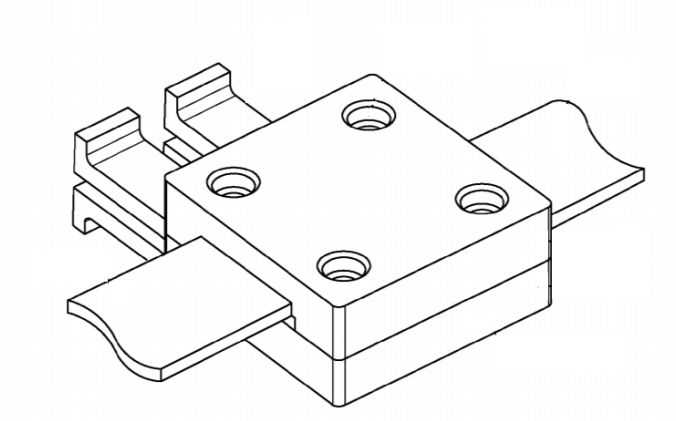

Figure 5.5: A perspective view of the flex to flex connection device. Adapted from [5].

addressed. For instance, a wearing effect is unavoidably produced at the contact interface of the terminals during the connecting and dis-connecting process, leading to signal transmission degradation problems and reduced lifetime of the connectors [6-7]. High transmission loss is yet another issue to be solved [3]. Moreover, the performance of these connectors is influenced by electromagnetic interference (EMI) shielding and impedance mismatch.

In this chapter, the design, fabrication processes, assembly method and characterization of cable-to-cable connectors are presented. Cu-based connectors and Nb-based connectors were produced for connecting Cu cables and Nb cables, respectively. For Cu-based cables, DC connection performance was first studied. DC and RF performance of intact cables were compared with reconnected cables (using the exact same cables in the intact and reconnected configurations to allow direct comparison). Return loss and insertion loss of intact and reconnected microstrips tested at different temperatures (RT, 77 K and 4.2 K) were compared. Microstrip lines with different length and numbers of reconnection regions were characterized. For Nb-based cables, a distributed element model was used in ADS to model the microstrip-to-microstrip interconnection of the reconnected structure. These superconducting thin-film, cable-to-cable connectors exhibited an insertion loss less than 0.18 dB and a return loss better than 15 dB. Thermal-cycle and re-assembly reliability of the connectors was tested, and exhibited consistent performance.

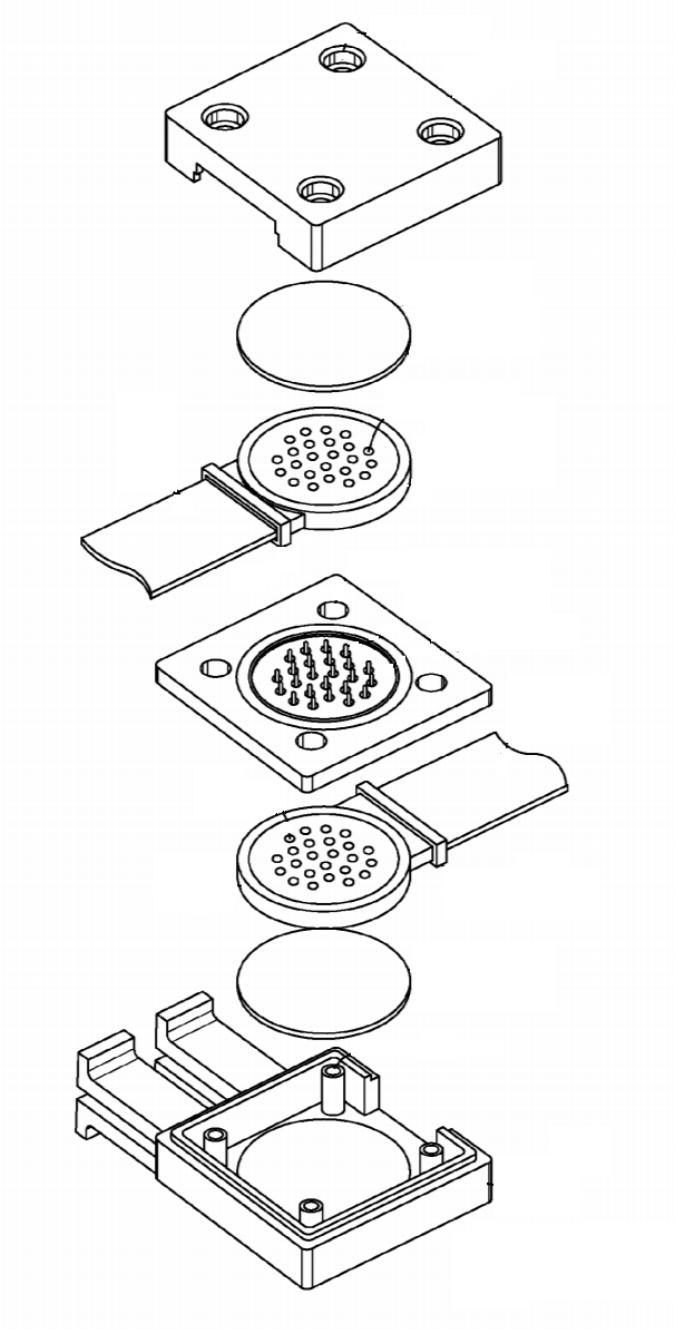

Figure 5.6: An exploded view of the flex to flex connection device. Adapted from [5].

5.2 Cu-based DC Testing Cables and Connectors

5.2.1 Design

Cu-based DC cable and connectors were designed to test the DC connection performance. Figure 5.7(a) shows the mask layout of Cu-based DC testing cables. This mask includes four cable designs with different trace gaps (G) and line widths (L). They are G100L100, G100L50, G200L100 and G200L50 cables. There are 10 parallel traces on each cable. As an example, a zoom-in image of G100l100 cable is shown in Figure 5.7 (b). G100L100 means that gap (G) between adjacent traces is 100 µm and line width (L) is 100 µm. Connectors with different connecting line gap (G) and width (W) and length (L) were designed for corresponding testing cables. The layout is shown in Figure 5.8(a) and an enlarged view of W100G100L1 connector is shown in Figure 5.8(b). Note that "L" here means the length of connecting line is 1 mm.

5.2.2 Fabrication

Cu-based DC cables and connectors were fabricated using similar thin-film fabrication processes, as discussed in Section 3.2.2. Here, I outline the fabrication steps and details of the fabrication processes can be found in Appendix A.

Figure 5.9 schematically illustrates the fabrication procedures for Cu-based DC cables fabricated using HD-4110 polyimide (Figure 5.9(a1)-(a6)) and connectors (Figure 5.9(b1)-(b4)). For the DC testing cables, (a1) a Cr (25 nm)/Al (200 nm) sacrificial release layer was first deposited on RCA cleaned and oxidized Si handle wafers. (a2) Polyimide HD-4110 was deposited onto wafers using spin-coating, followed by photolithographic definition and curing at 375°C in a N_2 atmosphere, to achieve a ∼20 µm-thick film as the flexible substrate of the microstrip. (a3) Ti (50 nm)/Cu (1000 nm)/Au (20 nm) traces were formed using conventional photolithography and film lift-off techniques. Using a CHA Mark 50 deposition system, metal layers were electron beam physical vapor deposited at a rate of 2 Å/s after a

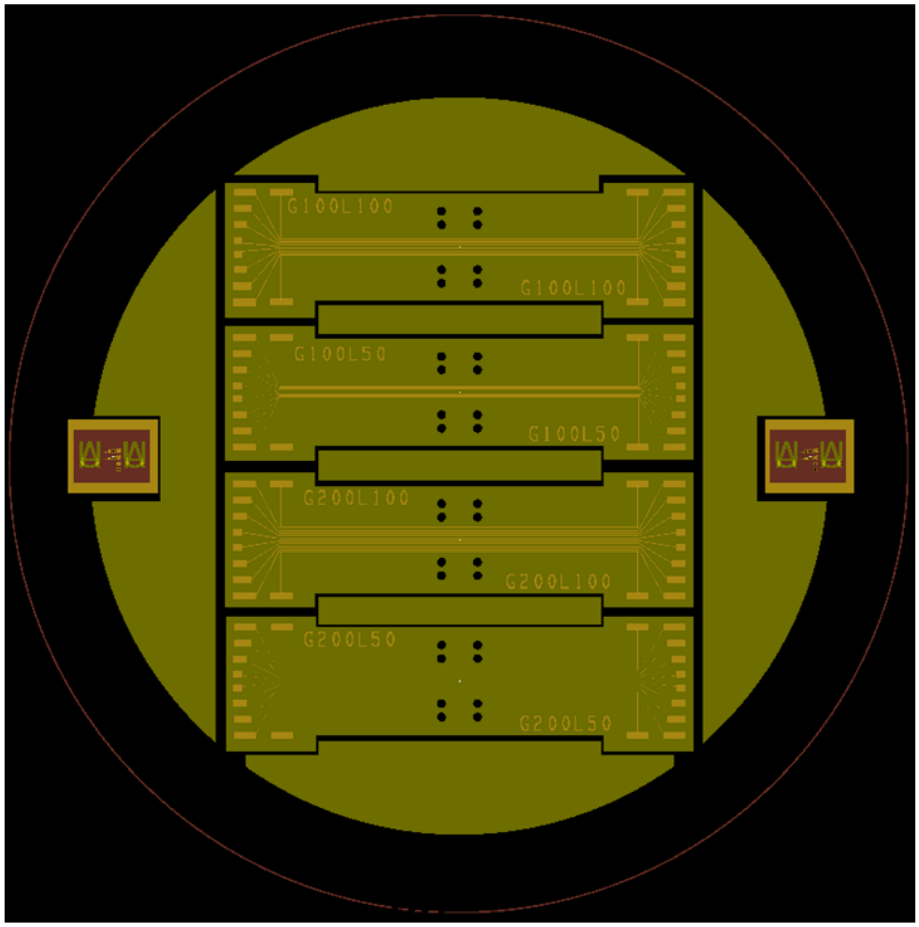

(a)

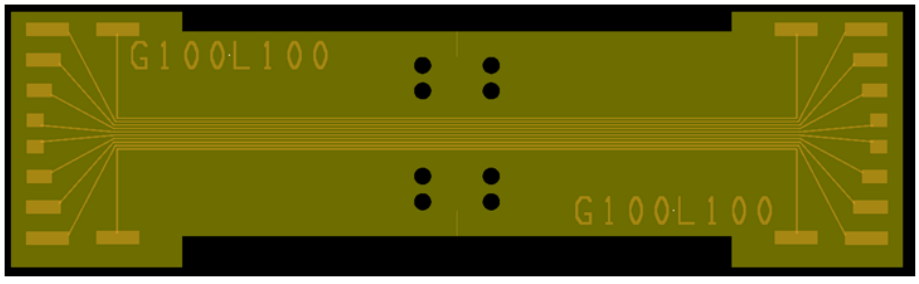

(b)

Figure 5.7: (a) Mask layout of Cu-based DC testing lines. Note that the diameter of the red circle is 150 mm. (b) An enlarged image of G100L100 testing cable.

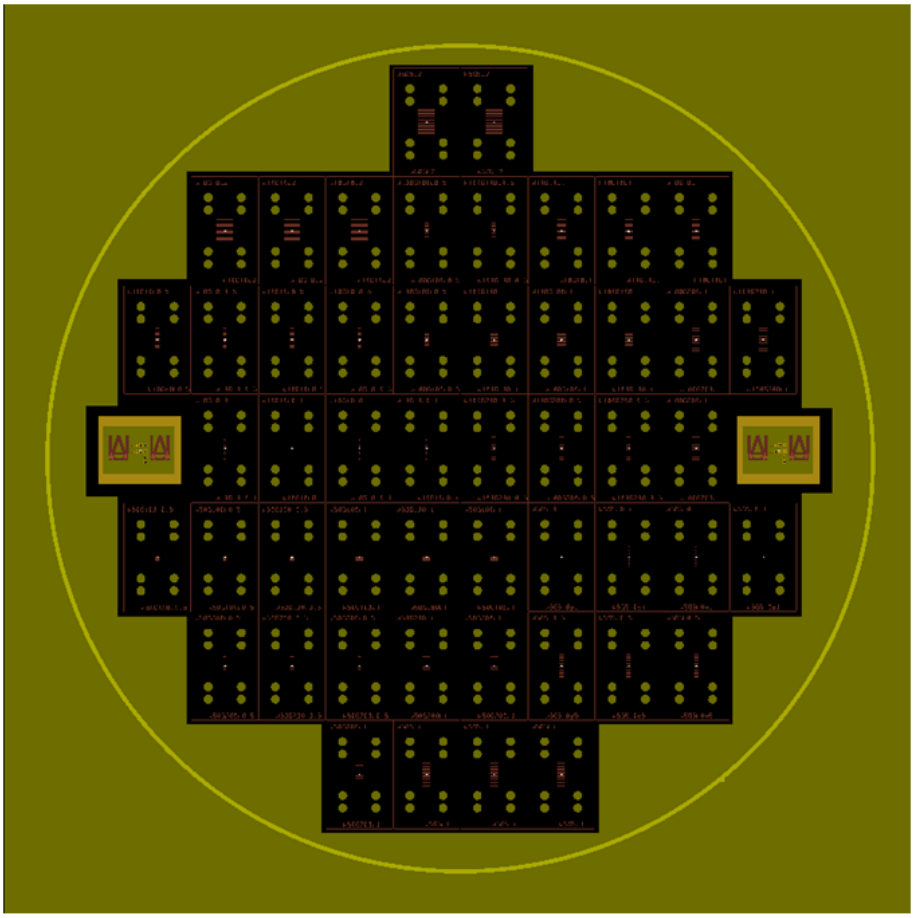

(a)

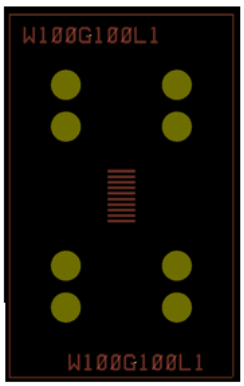

(b)

Figure 5.8: (a) Mask layout of Cu-based connectors. Note that the diameter of the yellow outer ring is 150 mm. (b) An enlarged image of W100G100L1 connector.

two minute in-situ ion beam milling surface clean. (a4) Next, samples were coated with a layer of photoresist for protection of the structures during (a5) a film release process, which involved soaking in a NaCl salt bath with 0.5 V applied to the release layer. (a6) After releasing, photoresist was stripped from the sample.

Fabrication of Cu-based connectors started with RCA cleaned Si wafers, (b1) a photoresist layer was applied to define the connecting lines. Metallization was done with Ti/Cu/Au, (b2) followed by standard lift-off process. (b3) Next, a layer of HD-4110 polyimide was deposited followed by (b4) photolithography definition and curing at 225°C to yield ∼30 µm-thick pillar alignment structures. Finally, connectors were cut into the individual connectors with dimension of 8 mm in length and 13 mm in width using an automatic dicing saw (Disco DAD 3220). Fabricated DC cables and connectors prior to dicing are shown in Figure 5.10 and Figure 5.11.

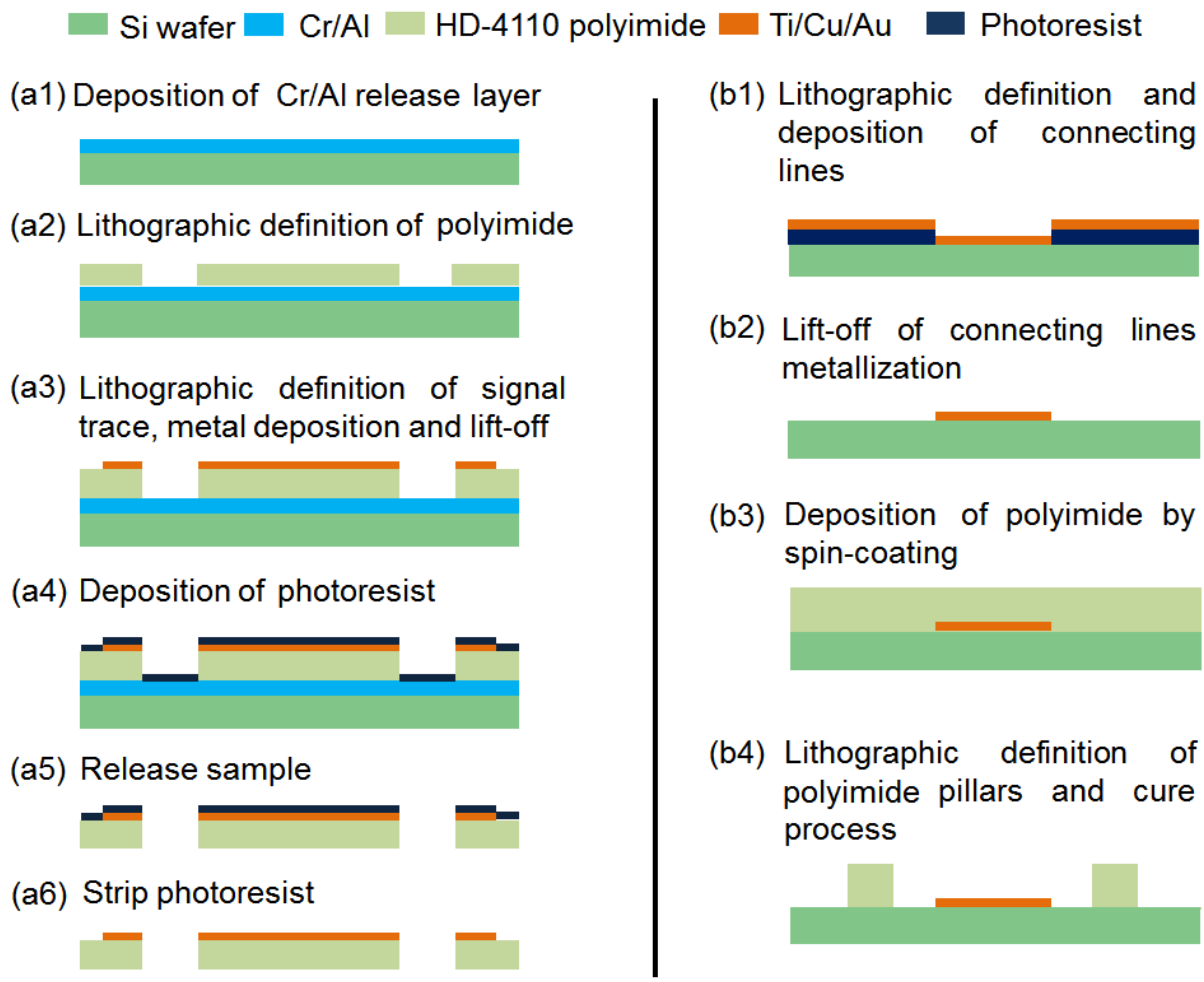

Figure 5.9: Schematic fabrication flow for Cu-based DC testing cables (a1-a6) and cable-to-cable connectors (b1-b4).

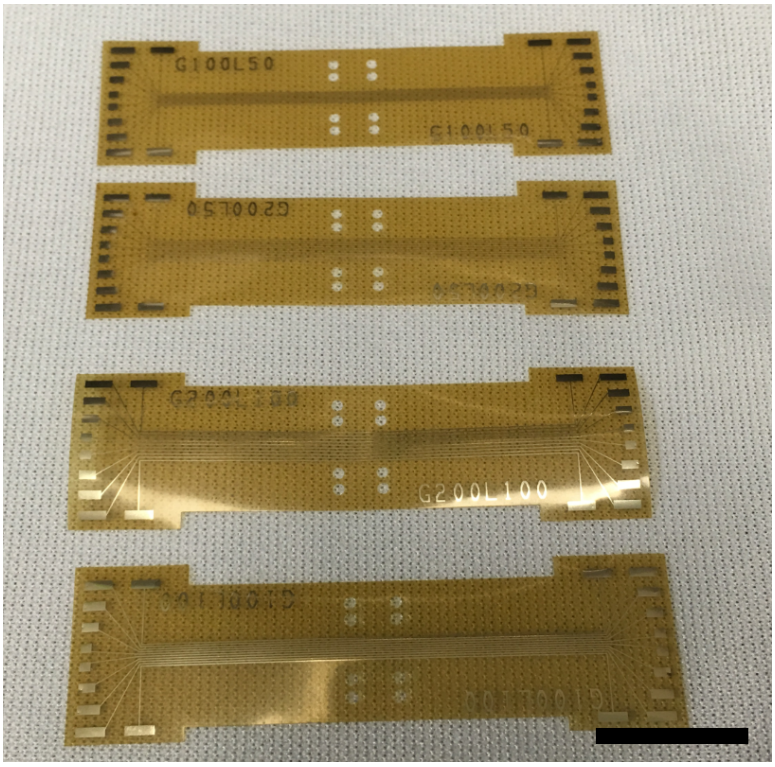

Figure 5.10: Fabricated and released Cu-based cables for DC testing. Scale bar: 1cm.

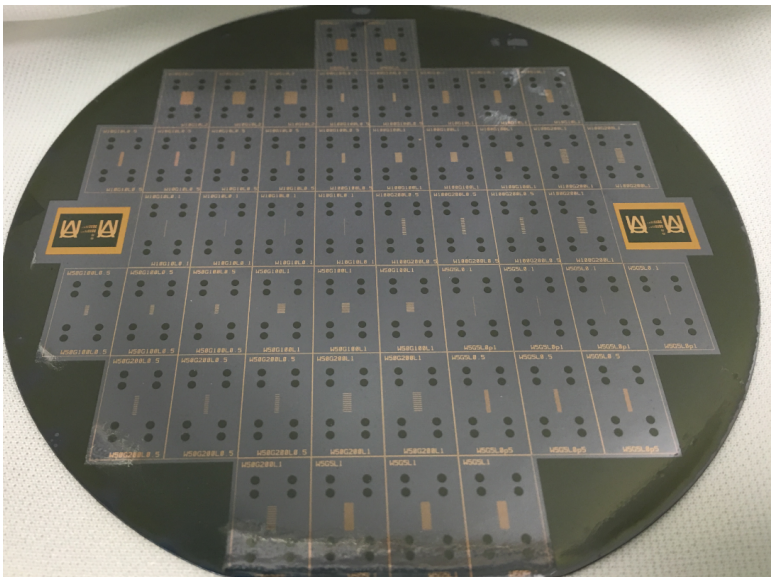

Figure 5.11: Fabricated Cu-based connectors before cutting into individual sample. Note that 100 mm Si wafer was used in this work.

To test the DC connection of reconnected cables using connectors, 4-wire resistance of intact cables was measured first as a reference. Then, the same samples were diced through

their center transversely using an automatic dicing saw (Disco DAD 3220) with a cut width of approximately 70 µm. The samples were then reconnected with connectors for reconnection testing. Figure 5.12 depicts a 3-D view of the cable-to-cable horizontal connection method. All the parts for reconnecting the cable are shown in Figure 5.13(a).

To reconnect the split DC cable, a connector was placed onto a clamp fixture with pillars and connecting lines facing up. By aligning the alignment holes of the cables with the pillars on the connector, the two halves of the DC cables were aligned with signal trace side facing down (toward the connector), to interface with the connecting lines on the connector. A 2 mm-long 1 cm-wide Si/SiO_2 piece was used between the flex and the spring. The connector-flex-shim sandwich structure was compressively held in place with the clamp fixture. By tightening the screw on the clamp fixture, the magnitude of compression can provide high-quality electrical interconnection between microstrip parts. Figure 5.13(b) shows reconnected G100L100 cable with the back side of the cable facing up.

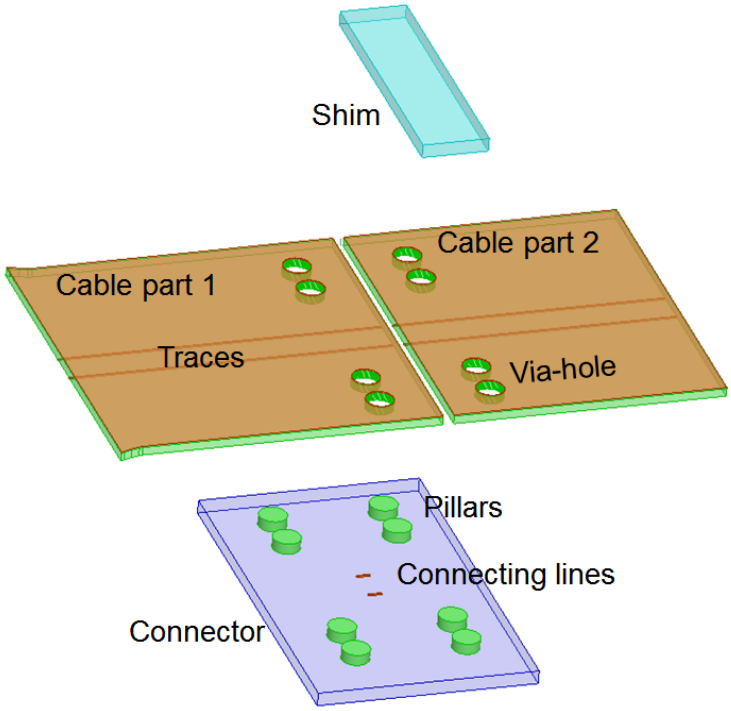

Figure 5.12: 3-D view of connector components for flexible DC cables.

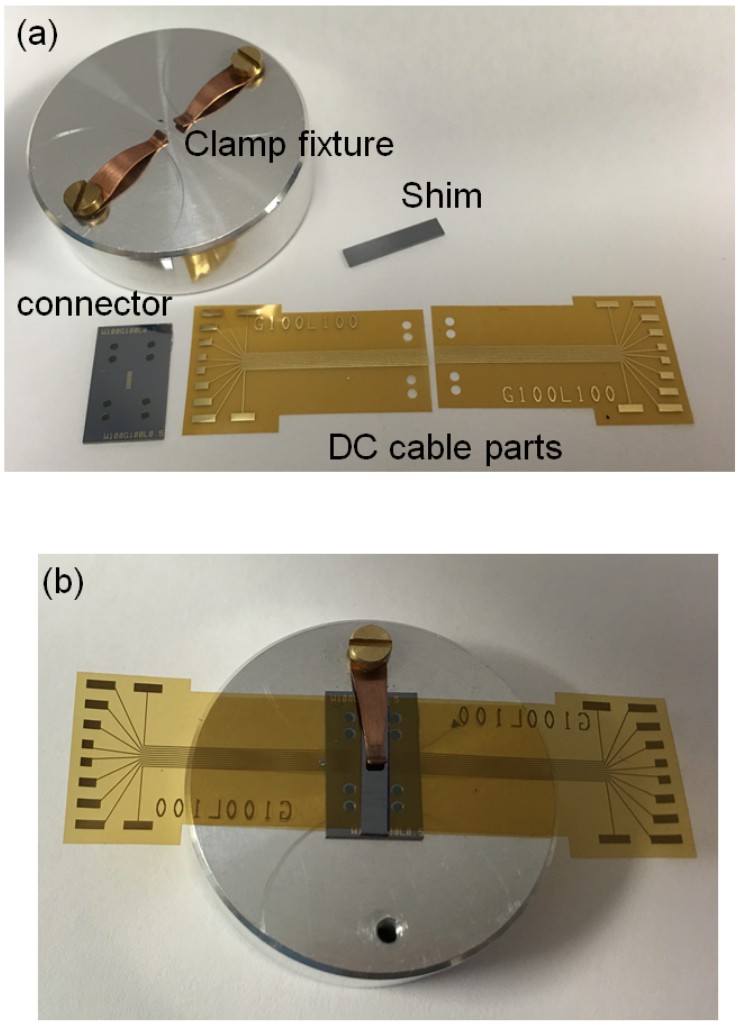

Figure 5.13: (a) All the parts for DC cable reconnection. (b) Reconnected DC cable with cable facing down.

Table 5.1 shows the 4-wire resistance measurement results of intact and reconnected G100L100 testing cables. A G100W100L0.5 connector was used in the reconnection test. The split cable was re-assembled and dis-assembled twice to check the connector re-assembly reliability. Resistance difference between reconnected cable and intact cable is shown in Figure 5.14. All ten traces on the sample were connected with the connector and during the two assemblies, consistent resistance values were achieved among 10 traces. By using the G100W100L0.5 connector, the reconnected resistance is approximately 1 Ω less than the intact cable.

	Resistance of G100L100 cable (Ω)		
	Intact	Reconnected with G100W100L0.5 connector	
		1^{st} assembly	2^{nd} assembly
Line No.1	13.142	11.994	11.874
Line No.2	13.839	13.748	13.721
Line No.3	13.305	12.380	12.298
Line No.4	12.952	11.975	11.899
Line No.5	12.967	11.948	11.826
Line No.6	12.973	12.744	12.721
Line No.7	13.022	12.162	12.100
Line No.8	13.400	12.489	12.361
Line No.9	13.928	13.030	12.871
Line No.10	13.481	12.477	12.399

Table 5.1: Resistance of intact and reconnected G100L100 cable using a G100W100L0.5 connector.

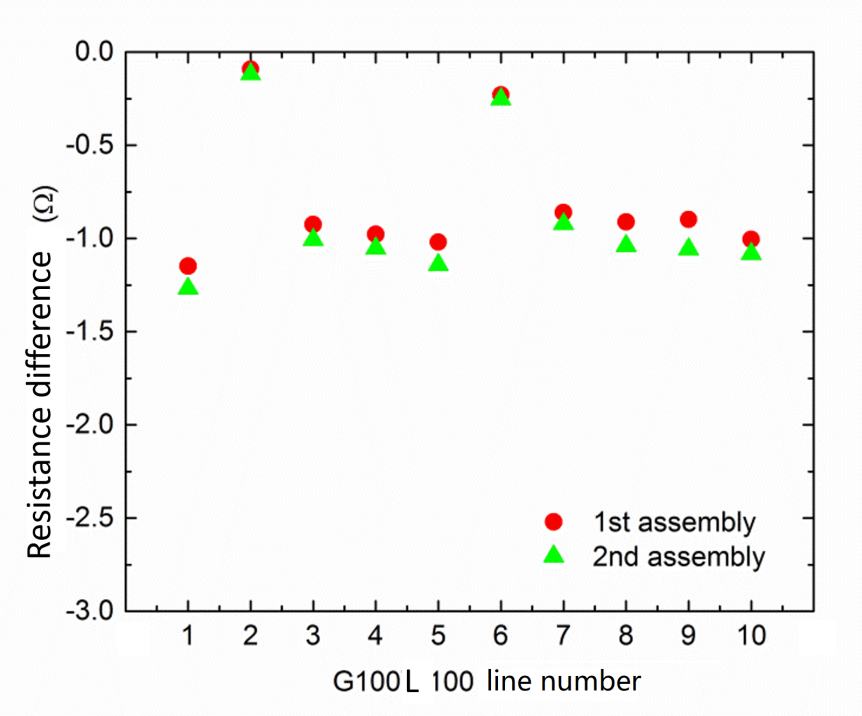

Figure 5.14: Resistance difference between intact and reconnected G100L100 cable lines using G100 W100L0.5 connector.

Similar tests were conducted on intact and reconnected G100L50 cables with a G100W50 L0.5 connector. Results are shown in Table 5.2 and Figure 5.15. Note that G100L50 cable has the smallest feature size among the entire design, the width of the trace is 50 µm, which is the same as the signal trace of corresponding RF cables. All 10 lines were successfully connected with the connector and resistance of reconnected lines were approximately 2 to 3 Ω less than the original intact sample. As can be seen from these results, consistency between two assemblies was quite good.

	Resistance of G100L50 cable (Ω)		
	Intact	Reconnected with G100W50L0.5 connector	
		1^{st} assembly	2^{nd} assembly
Line No.1	32.212	29.029	30.102
Line No.2	34.481	31.072	31.298
Line No.3	32.734	29.633	30.431
Line No.4	31.982	28.791	28.633
Line No.5	31.559	28.546	29.354
Line No.6	31.386	29.521	29.044
Line No.7	32.521	29.419	30.741
Line No.8	33.036	32.928	31.071
Line No.9	34.885	33.904	32.410
Line No.10	33.553	31.509	30.871

Table 5.2: Resistance of intact and reconnected G100L50 cable lines using a G100W50L0.5 connector.

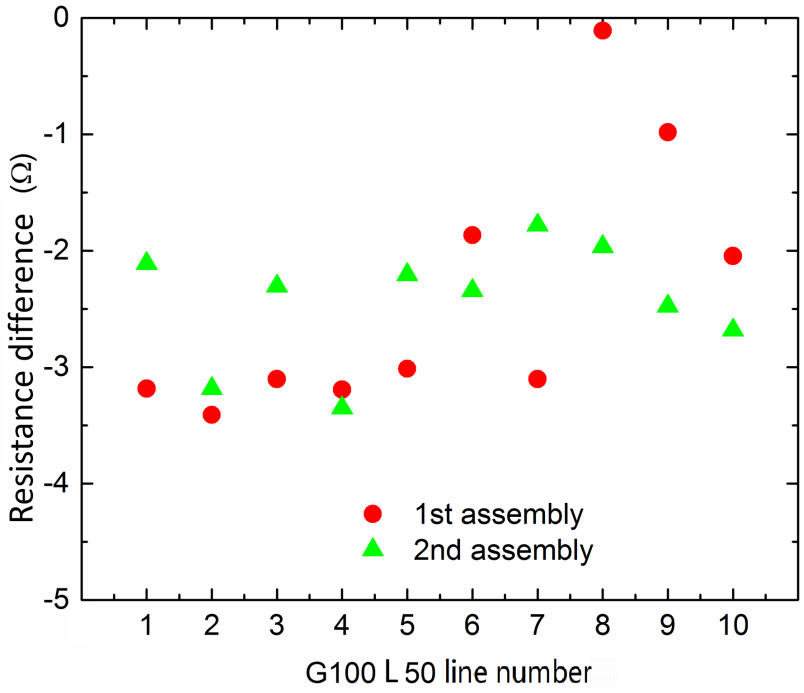

Figure 5.15: Resistance difference between intact and reconnected G100L50 cable lines using G100 W50L0.5 connector.

5.3 Cu-based RF/Microwave Cables and Connectors

After achieving promising results from using Cu-based connectors, Cu-based microwave cables and microwave connectors were built to test the microwave performance of reconnected cable at RT and at cryogenic temperatures (77 K and 4.2 K).

Cu-based microstrip transmission lines were fabricated based on the layout shown in Figure 4.1 in Chapter 3. Different lengths of microstrip were fabricated, including 6.5 cm, 10 cm and 20 cm microstrip transmission lines.

To explore performance and reliability of the microwave connectors, RF performance of intact cables were compared with reconnected cables (using the exact same cables in the intact and reconnected configurations to allow direct comparison). Figure 5.16(a) and (b) depict a 3-D view of the microstrip-to-microstrip horizontal connection design and a top view of the connection region. Metallization of the entire structure was made with Ti

(50nm)/Cu (1 µm)/Au (20 nm). Microstrip lines were ~6.5 cm long and 50 µm wide and were designed to produce a 50 Ω characteristic impedance. The widths (W_{con}) and lengths (L_{con}) of connecting lines on the connector assembly were 55 µm and 500 µm, respectively. After measuring the performance of the intact Cu microstrip lines, samples were diced down their center and reconnected using a connector, for reconnection testing.

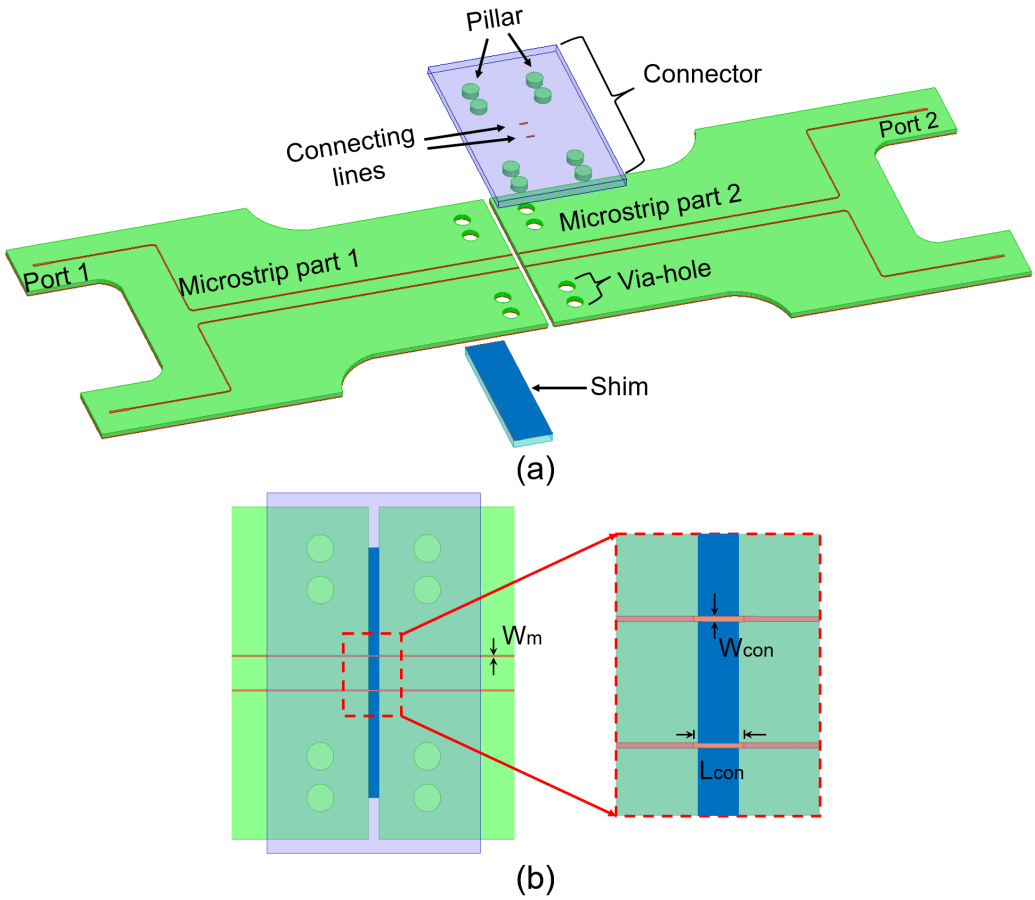

Figure 5.16: Design details and connection approach for Cu-based thin-film microstrip cables. (a) 3-D view showing cable and connector assembly in a disassembled configuration. (b) Top view of microstrip connection region. Dimensions: width of microstrip (W_m) is 50 µm, connecting line length (L_{con}) and width (W_{con}) are 500 µm and 55 µm, respectively.

Figure 5.17 schematically illustrates the fabrication procedures for Cu-based microwave connectors. Starting from RCA cleaned fused silica wafers, a photoresist layer was applied to define the connecting lines. (a) Ti (50nm)/Cu (1 µm)/Au (20 nm) metallization was deposited, (b) followed by standard lift-off process. (c) Sequentially, a layer of HD-4110

polyimide was deposited. (d) After another photolithography step, to define pillar alignment structures, samples were then cured at 225°C in N_2 ambient to yield ∼30 µm-thick pillars. Finally, connectors were diced into individual connectors with dimension of 8 mm in length and 13 mm in width. Figure 5.18 shows some images of the Cu-based microwave connector after noted fabrication steps.

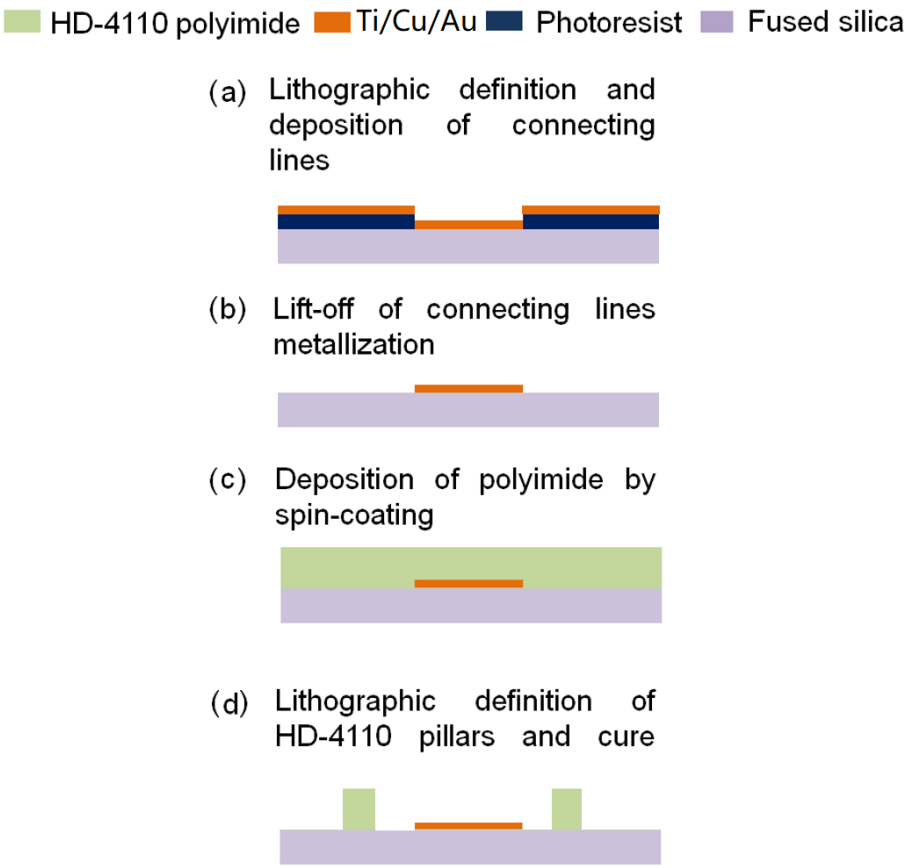

Figure 5.17: Schematic fabrication flow for Cu-based connectors.

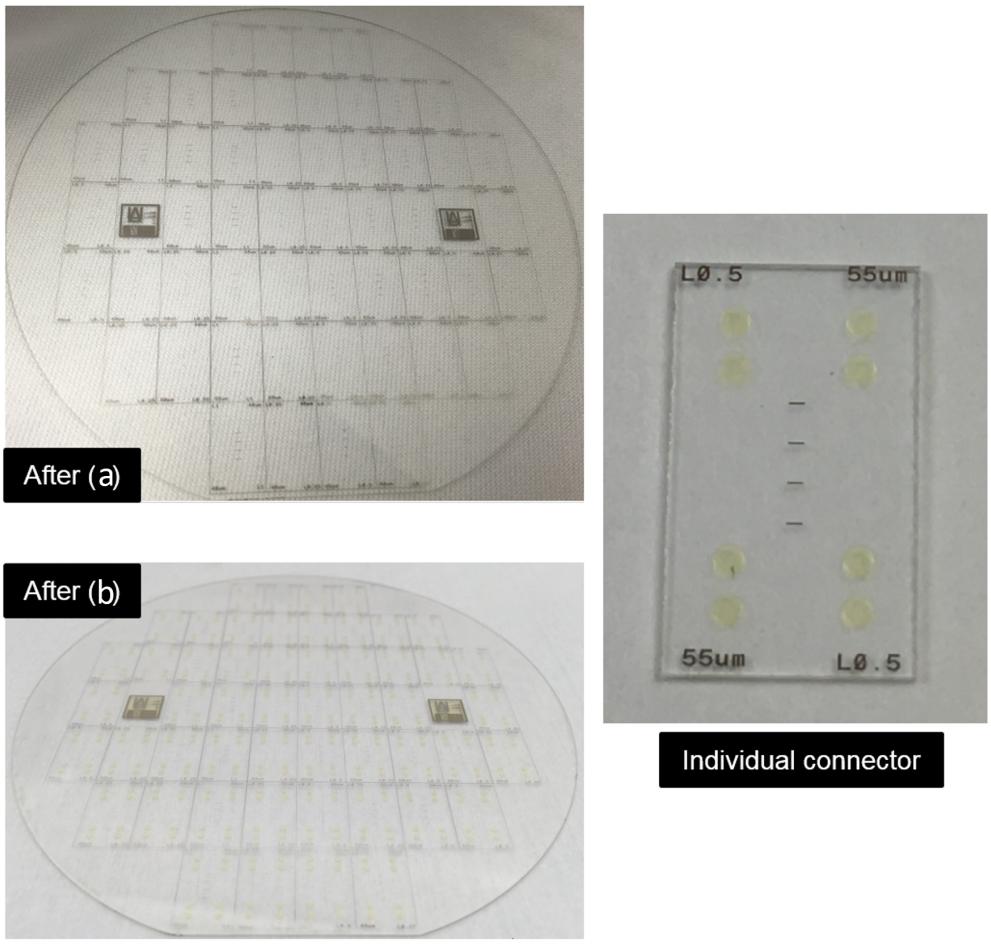

Figure 5.18: Images of Cu-based connectors on fused silica substrate during various points along their fabrication.

To reconnect the cut microstrip cable structures, a connector was placed onto a clamp fixture with pillars and connecting lines facing up. By aligning the alignment holes of the cables with the pillars on the connector, the two halves of the microstrip cables were aligned with signal trace side facing down (toward the connector), to interface with the connecting lines on the connector. A shim with a Ti (50nm)/Cu (1 µm)/Au (20 nm) stack-up was used on the back-side of the cables to bridge between the two flex strips and connect the microstrip ground planes. The connector-flex-shim sandwich structure was compressively held in place with the clamp fixture. By tightening the screw on the clamp fixture, sufficient compression can provide high-quality electrical interconnection between the microstrip cables. Figure

5.19(a) shows a photograph of the back side of the reconnected microstrip cable using the Cu-based connector. An enlarged cable-to-cable connection region is shown in Figure 5.19(b). Note that the current clamping configuration, with bulky clamp components, is not ideal and will be the subject of future work.

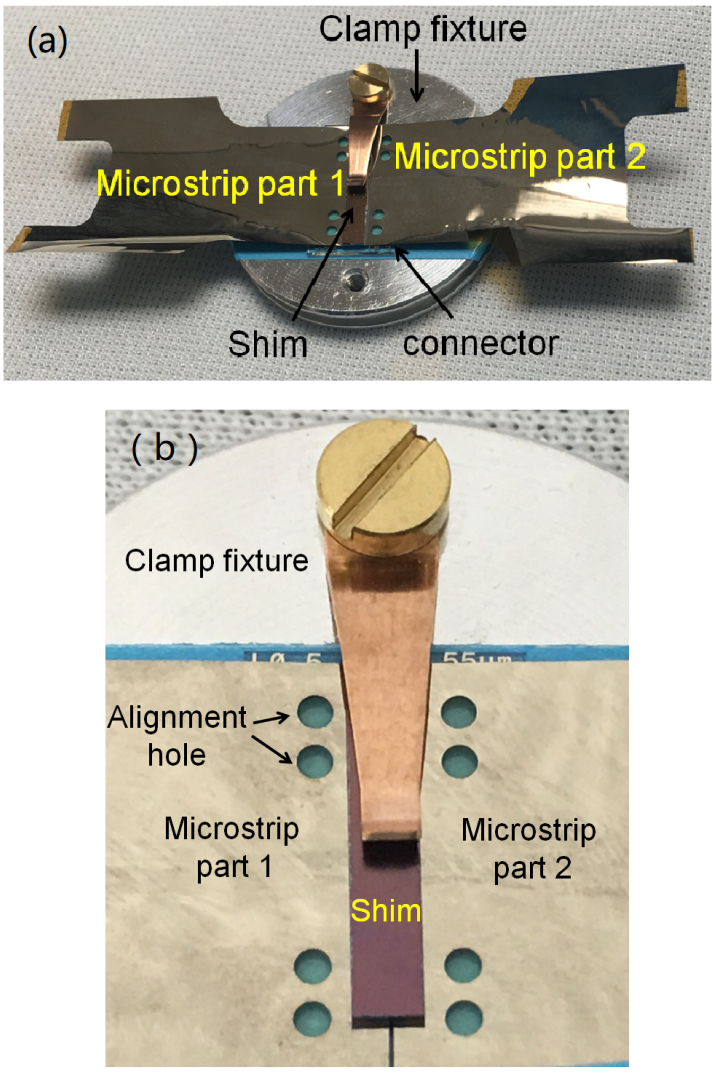

Figure 5.19: (a) A bottom-side view of a reconnected sample, with ground planes of the microstrip pieces facing up, in the clamped configuration using a connector and shim. (b) A zoom-in view of cable connection region to show additional detail.

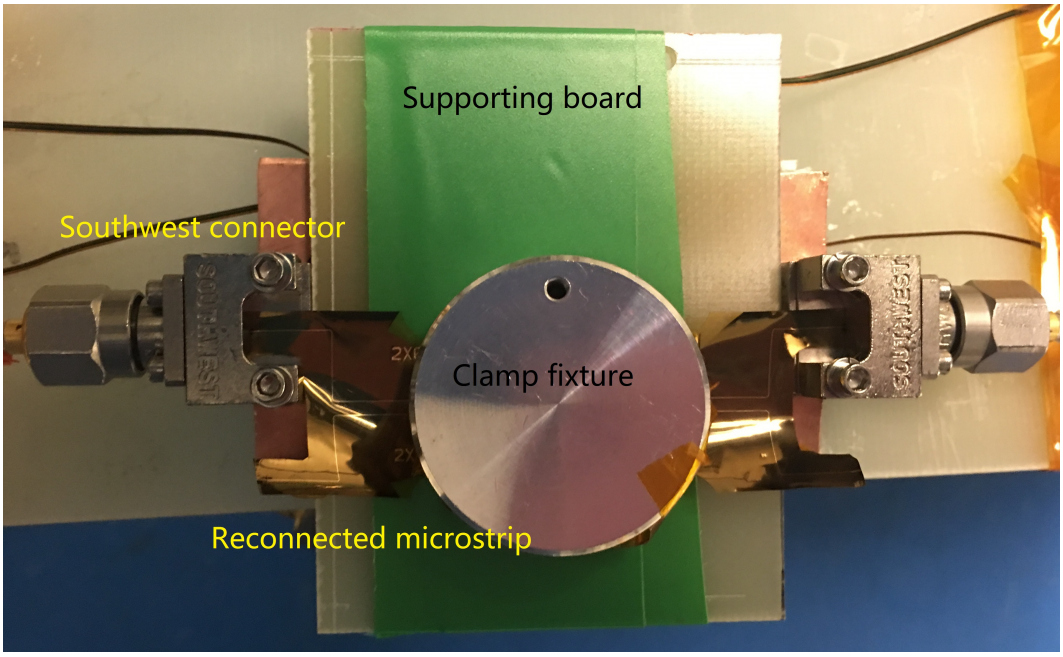

Figure 5.20: Microscopy image of a reconnected 6.5 cm Cu-based microstrip during RF measurement.

S-parameter of an intact 6.5 cm long Cu microstrip were measured at RT and 77 K. The same sample was then diced down its center and reconnected with the microwave connector. RF measurements were performed to compare the effect of reconnection at different temperatures. Note that the reconnected 6.5 cm microstrip had one reconnected line section in the cable. Figure 5.20 shows a microscopy image of the reconnected cable during RF measurement. S-parameter measurement results of intact and reconnected 6.5 cm Cu microstrip at RT are shown in Figure 5.21. The reconnected samples showed comparable return loss, as shown in Figure 5.21(a), which indicates the reconnected region does not significant impact the impedance match for this structure. From Figure 5.21(b), insertion loss of intact and reconnected microstrip showed consistent and similar performance up to 14 GHz. Figure 5.22 shows RF performance of the intact and reconnected 6.5-cm microstrip tested in LN_2 (77 K). Similarly, reconnected microstrip showed very comparable return loss and insertion loss with the intact cable.

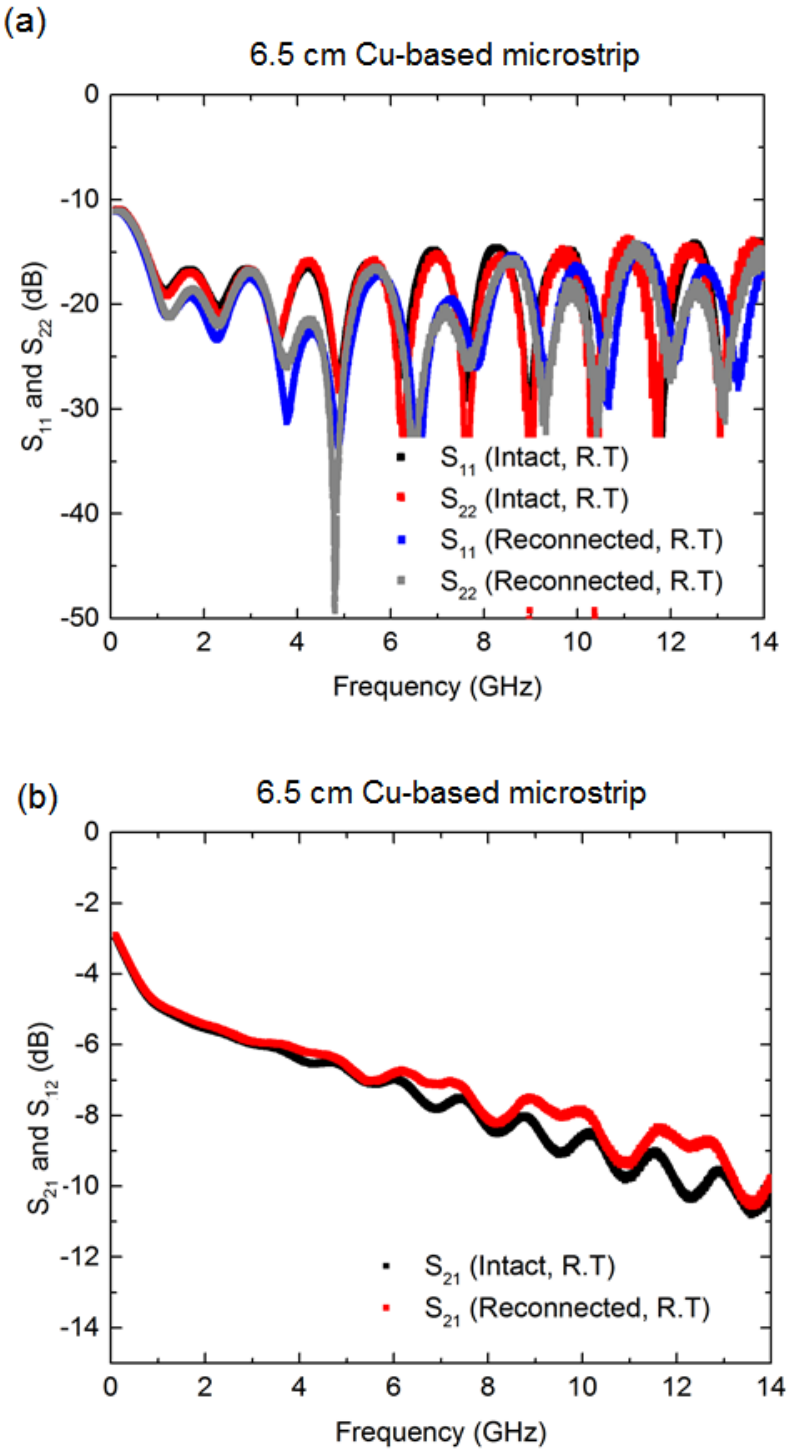

Figure 5.21: (a) S_{11} and S_{22} and (b) S_{21} and S_{12} of intact and reconnected 6.5 cm Cu-based microstrip transmission line measured at RT.

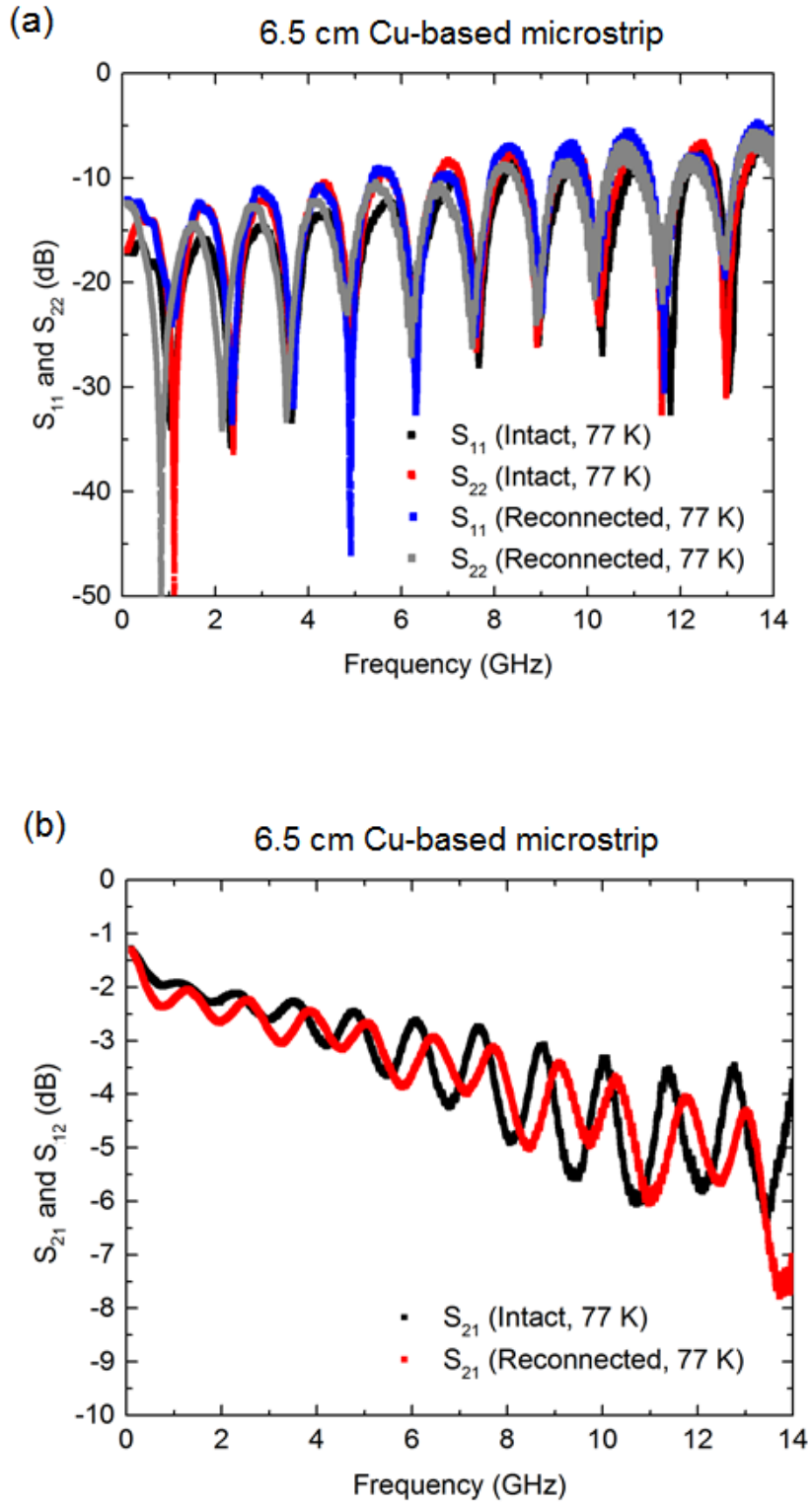

Figure 5.22: (a) S_{11} and S_{22} and (b) S_{21} and S_{12} of intact and reconnected 6.5 cm Cu-based microstrip transmission line measured at 77 K.

RF performance of a 10 cm long Cu microstrip was also tested for intact and reconnected configurations at RT, 77 K and 4.2 K. The reconnected 10 cm microstrip is shown in Figure 5.23. The measurement results are shown in Figure 5.24, Figure 5.25 and Figure 5.26, respectively. Note that the reconnected 10 cm microstrip has two reconnected line sections in the sample. Figure 5.27 shows S_{11} and S_{21} of intact and reconnected 10 cm Cu-based microstrip transmission line measured at different temperatures. It can be seen that with the decreasing temperature, the insertion loss of the cable reduced. This is because the lower the temperature, the higher the Cu conductivity and the less the conductor loss in the cable. The dielectric loss also decreases with the temperature decrease, but, in this case, compared to the conductor loss, impact of dielectric loss can be ignored. From the S-parameter performance of cables with different configurations, the return loss was relatively comparable except at RT, which indicates the reconnected region had good impedance match with the cable. Moreover, very consistent insertion loss can be observed from near DC to 14 GHz except at certain frequencies ($\sim$ 6 GHz, 8 GHz, 11 GHz and 14 GHz) due to the reconnected segment. These results indicate that, even with two reconnected segments in the cable, the total contact resistance from the reconnected segment results in a negligible impact on microwave performance.

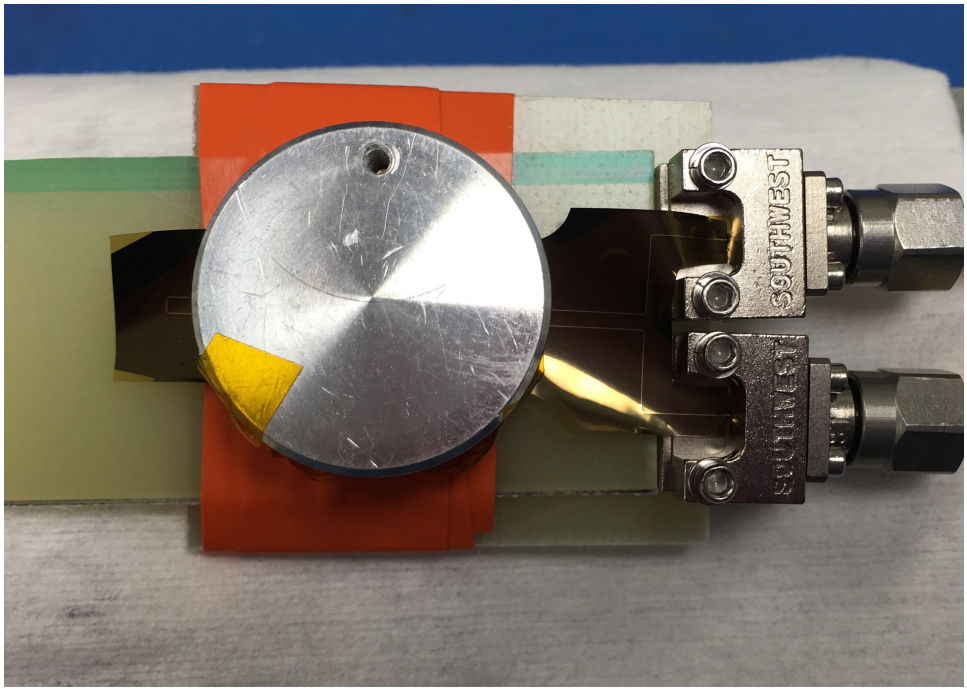

Figure 5.23: Image of the reconnected 10 cm Cu-based microstrip during RF/microwave measurement.

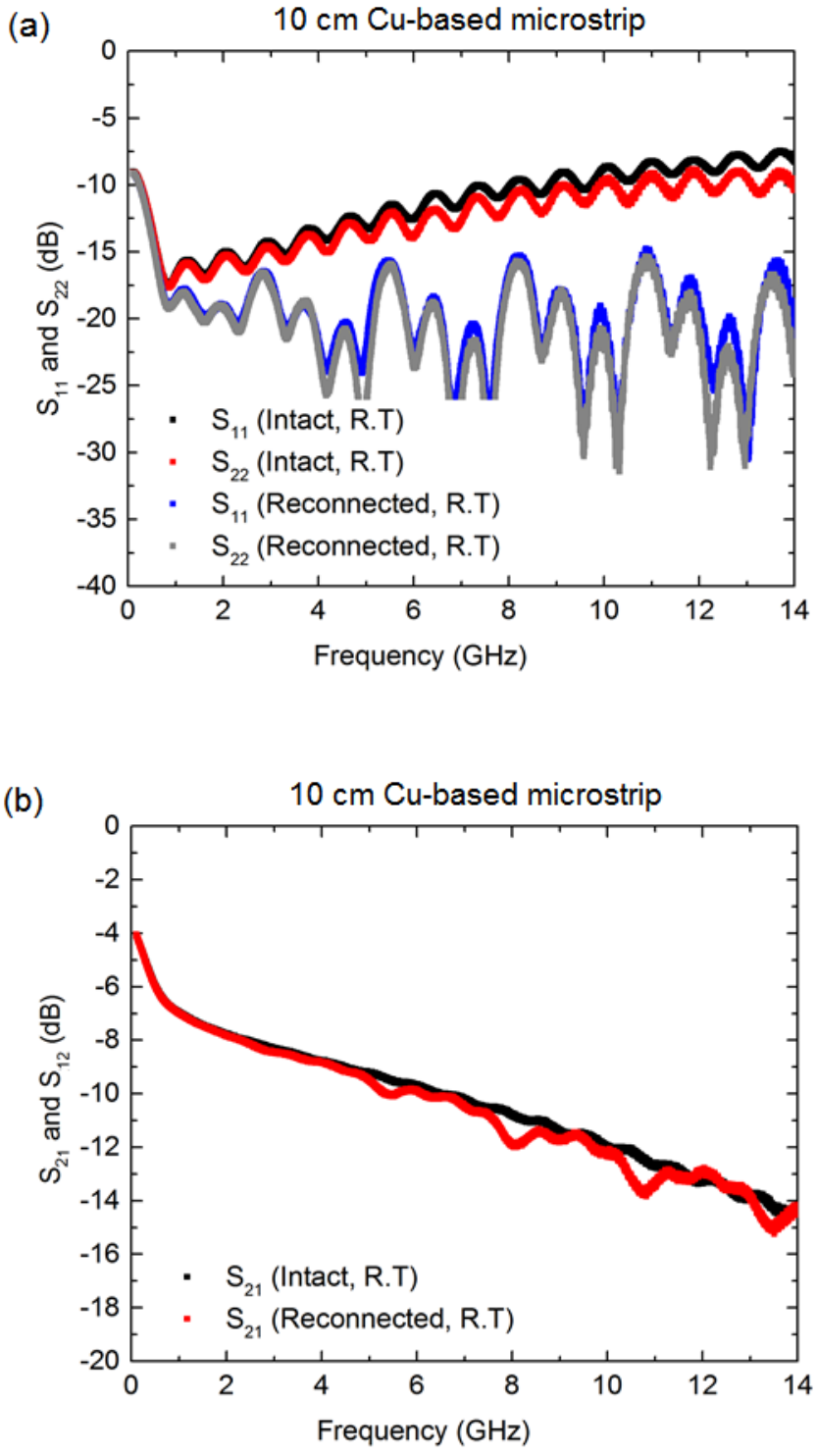

Figure 5.24: (a) S_{11} and S_{22} and (b) S_{21} and S_{12} of intact and reconnected 10 cm Cu-based microstrip transmission line measured at RT.

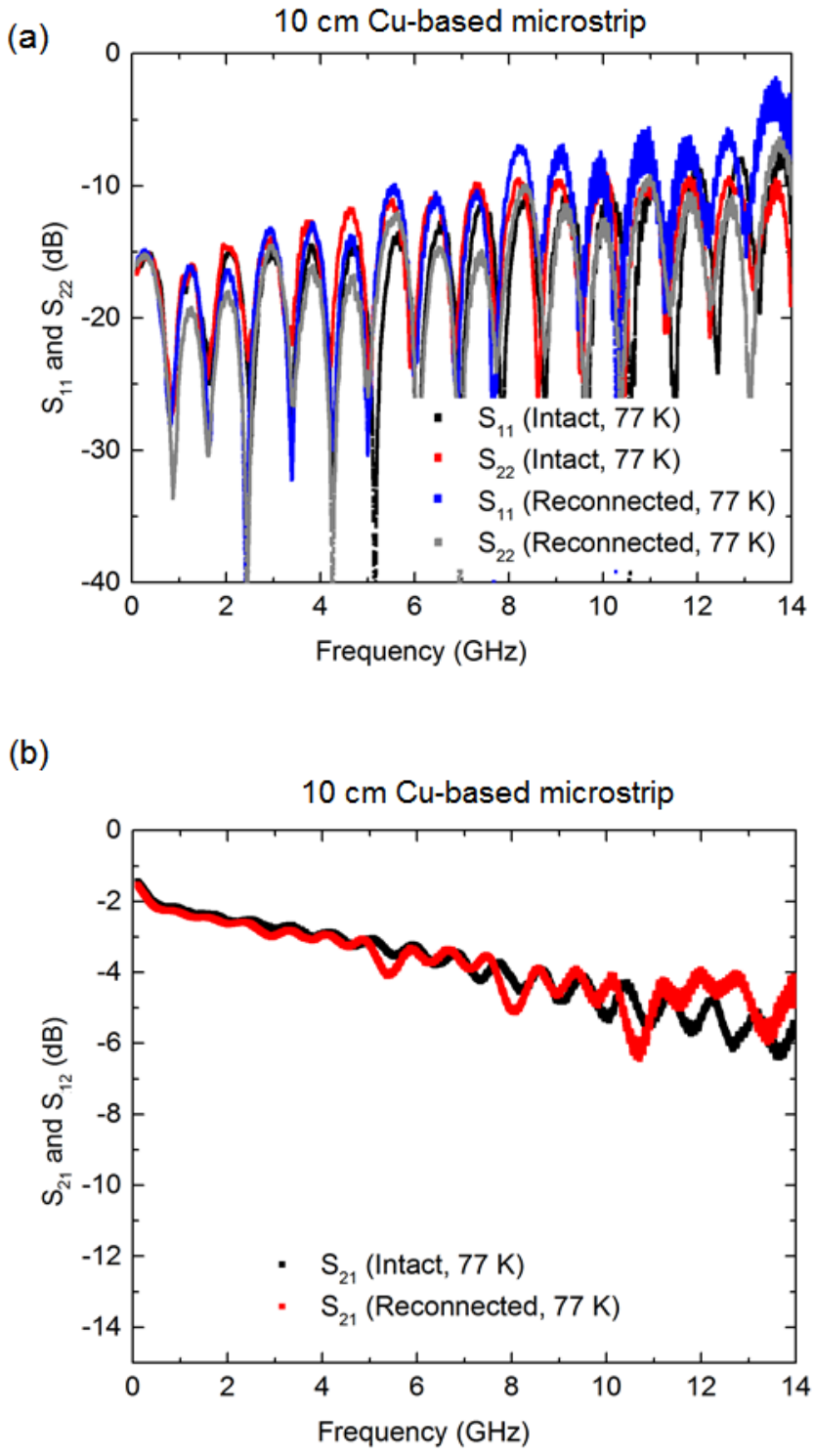

Figure 5.25: (a) S_{11} and S_{22} and (b) S_{21} and S_{12} of intact and reconnected 10 cm Cu-based microstrip transmission line measured at 77 K.

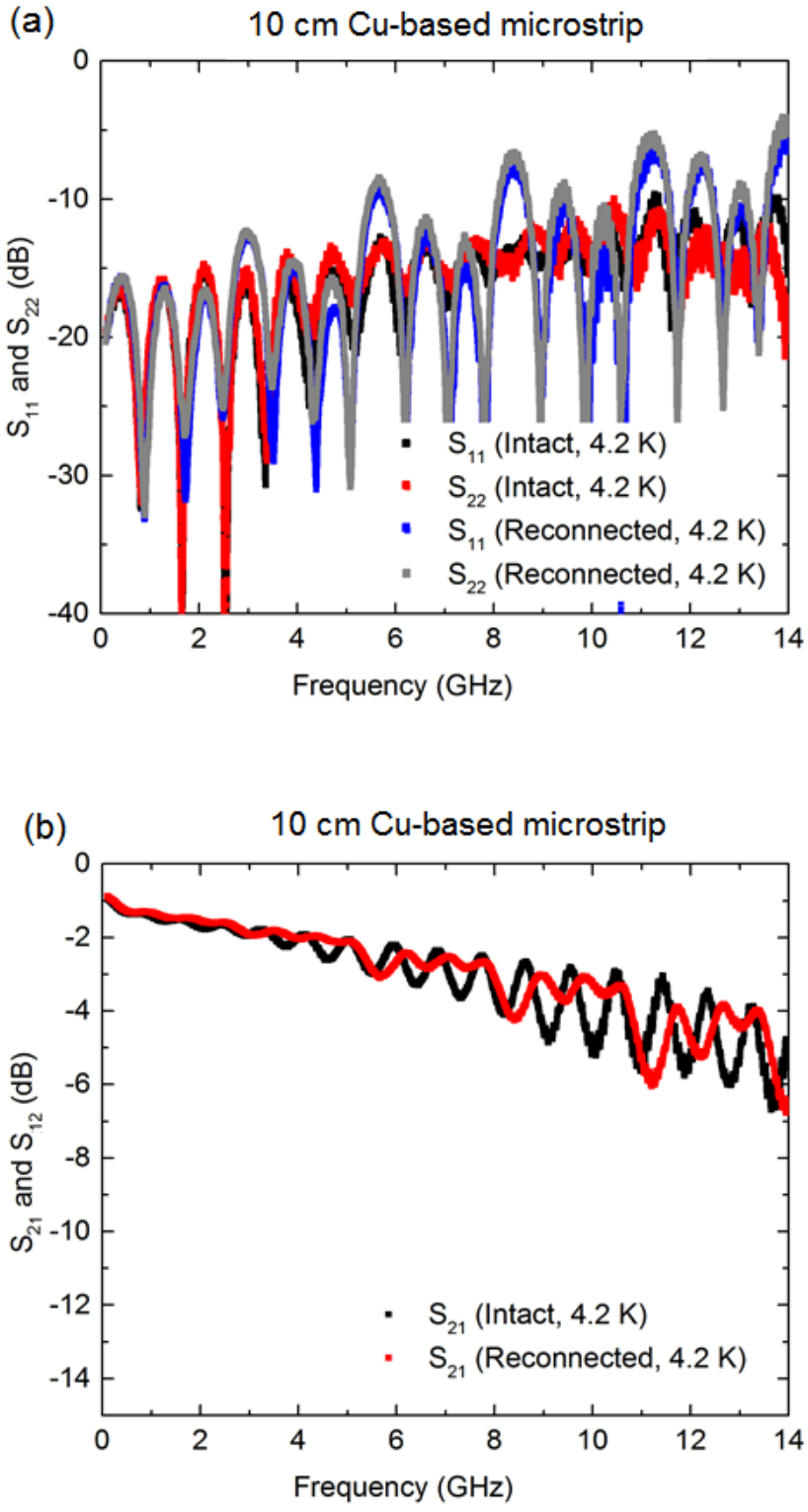

Figure 5.26: (a) S_{11} and S_{22} and (b) S_{21} and S_{12} of intact and reconnected 10 cm Cu-based microstrip transmission line measured at 4.2 K.

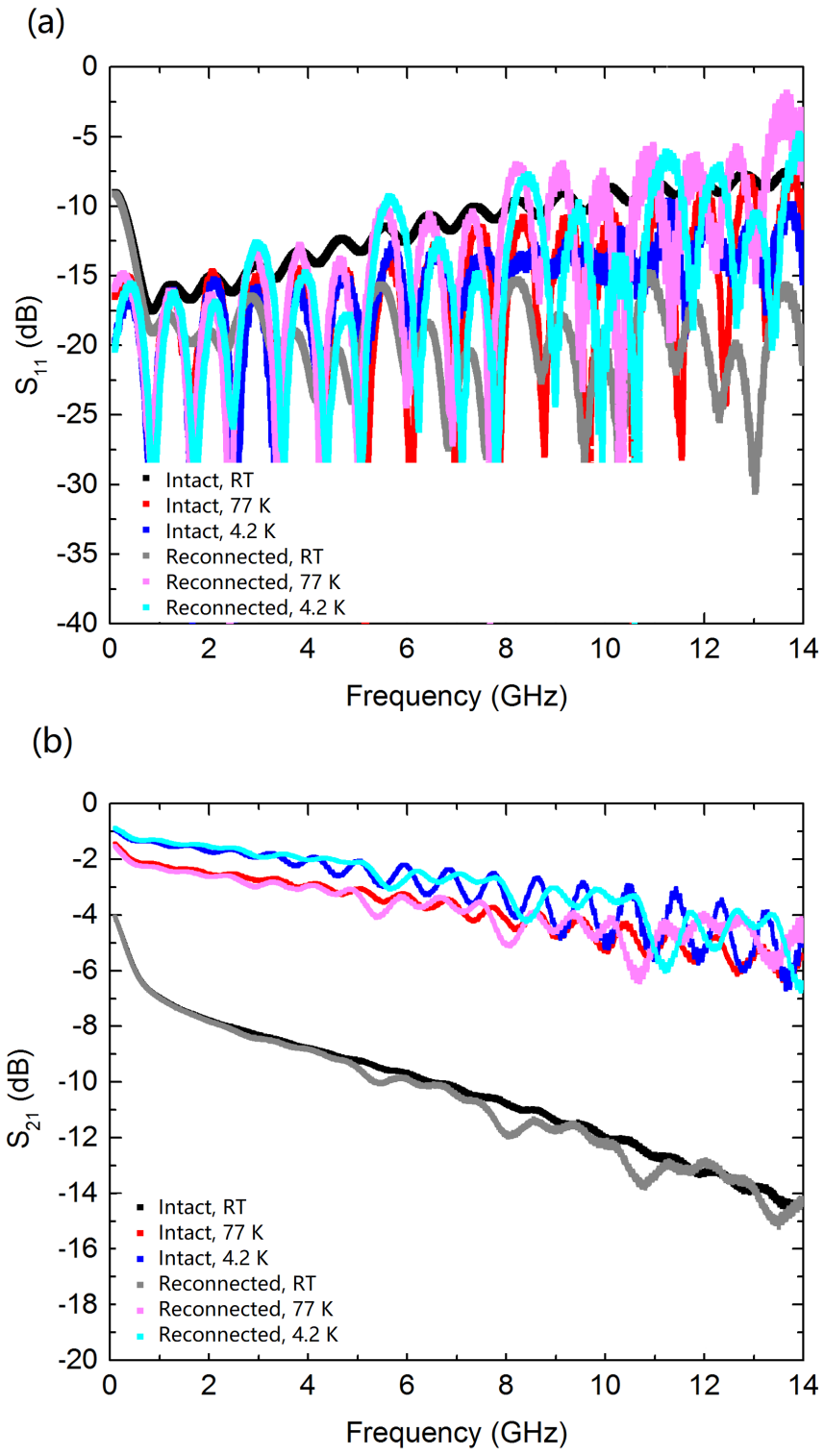

Figure 5.27: (a) S_{11} and (b) S_{21} of intact and reconnected 10 cm Cu-based microstrip transmission line measured at different temperatures.

5.4 Nb-based Superconducting Microwave Cables and Connectors

Previous results of using Cu-based microwave connectors showed quite good impedance match and negligible contact resistance. This provide design information for building superconductor version microwave connectors. Therefore, I extended this design for constructing Nb-based cable and connectors. Fabrication procedures and RF performance of intact Nb-based microstrip transmission lines were introduced in Chapter 3. For the Nb-based microwave connector, the same design as the Cu-based connectors was used. The connector material stack up was the same as the Nb microstrip transmission line, which was Nb (250 nm)/Au (20 nm).

5.4.1 6.5 cm Nb-based Microstrip and Connector

Characterization and measurement of DC resistance, time-domain reflectometry (TDR) response and microwave S-parameter was performed for the intact sample. The sample was diced down its center and reconnected with a new microwave connector and the same measurements were performed to compare the effect of reconnection. All the measurements were conducted in LHe dewar at 4.2 K.

DC measurement of microstrip signal and ground plane were performed using a 4-wire resistance measurement. Resistance value of signal trace and ground plane were subtracted with a barrel thru with the same set-up. Both signal and ground exhibited complete transition to SC state, with resistance of $\sim$30 mΩ and $\sim$3 mΩ for intact configuration and $\sim$60 mΩ and $\sim$3 mΩ for reconnected state, respectively. The critical transition temperature (T_c) of signal and ground were found to be 8.0 K and 8.3 K, respectively.

Time-domain reflectometry (TDR) is widely used to locate discontinuities in electrical paths, such as a connector or printed circuit board (PCB) [8]. TDR system transmits an incident signal pulse or stop onto a conductor and detects reflections due to impedance mismatch. If the conductor has uniform impedance, no reflections will be observed. If

impedance variations exist, then the reflected part of the signal will be observed. Impedance differences between intact and reconnected microstrip cables were compared, using an Agilent (Keysight) 86100D sampling oscilloscope equipped with a TDR module 54754A with a rise time fixed to 34 ps to make the measurements. A representative plot is shown in Figure 5.28. The two major dips in the plot at ∼13.8 ns and ∼14.5 ns, corresponding to the ends of the sample, exhibit capacitive response, which is due to the wider launch pad at Southwest Microwave connector-launch-transition region (width of launch pad = 122 µm > width of fabricated signal trace= 52.3 µm). Intact microstrip shows ∼50 Ω impedance over the entire line. The reconnected microstrip exhibits a similar response, the main difference is a slightly capacitive response of reducing impedance to 45 Ω at ∼14.15 ns, indicating an impedance mismatch generated by the connector.

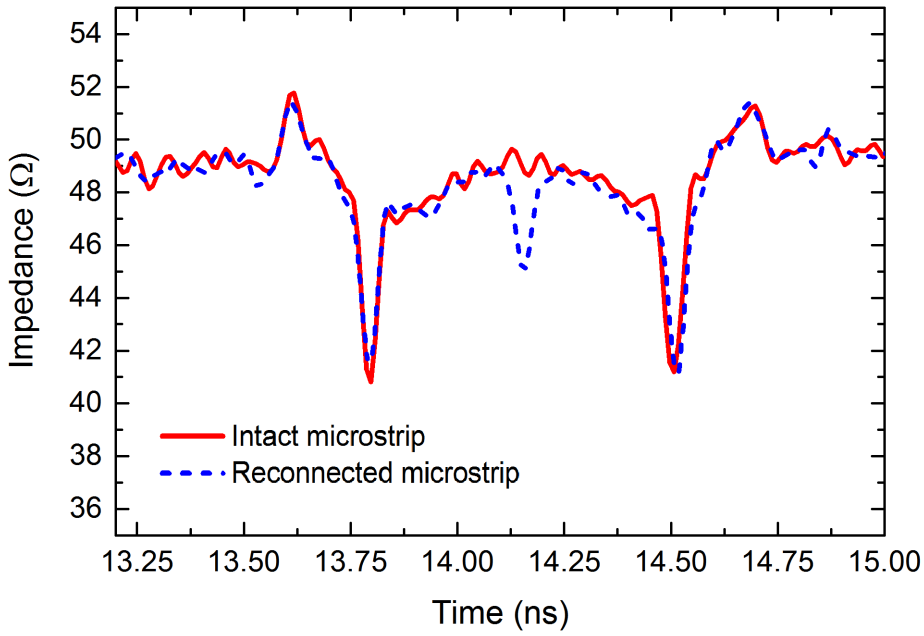

Figure 5.28: Time-domain reflectometry response of intact and reconnected 6.5 cm-long microstrip cables. The reconnected structure uses a cable-to-cable connector, directly in the middle of the cable, to bridge between the two halves. Note that this cable has a single break in the signal trace, half-way along the trace.

S-parameter measurement and simulation results of reconnected Nb microstrip are shown in Figure 5.29. An ADS simulation model is shown in Figure 5.30. Note that all the parameters had the same values for simulation of both intact and reconnected microstrip in the ADS model. The microstrip-to-microstrip interconnection was simulated using a distributed element model, as shown in the red frame. Considering the width of the shim is 2 mm-long and microstrip segment length is 0.625 mm, approximately three microstrip elements were assumed to be in intimate contact with the glass connector and have a distributed shunt capacitance C_{con}. Two series R_{con} located on either side of the middle C_{con} were used to represent the contact resistance for two connections at the break line, located between microstrip trace and connecting line on glass connector. R_{con} is 15 mΩ in the model based on 4-wire resistance measurement results. The total length of the glass connector is 8 mm, therefore, five microstrip segments, corresponding to 3.125 mm at both ends of glass connector, with smaller capacitance C_{ext}, were added to model the entire glass connector structure. C_{con} of 0.03 pF and C_{ext} of 0.002 pF were extracted to achieve excellent matching of with experimental results for the NIL reconnected case. Therefore, the total capacitance introduced from the glass connector was 0.11 pF. With these few parameters, I achieved incredibly close match between measured results of a fairly complex structure and simulation results of a relatively simple model, for both S_{11} and S_{21}.

After removing the reflections induced by the end launch, by removing the launch pad from the simulation model, reconnected structure was simulated again. The results are presented as IL simulation. The microwave connector exhibits an insertion loss less than $\sim$ 0.18 dB and a return loss better than 15 dB up to at least 14 GHz. For clarity, all the key dimensions and parameters used in the ADS model are listed in Table 5.3.

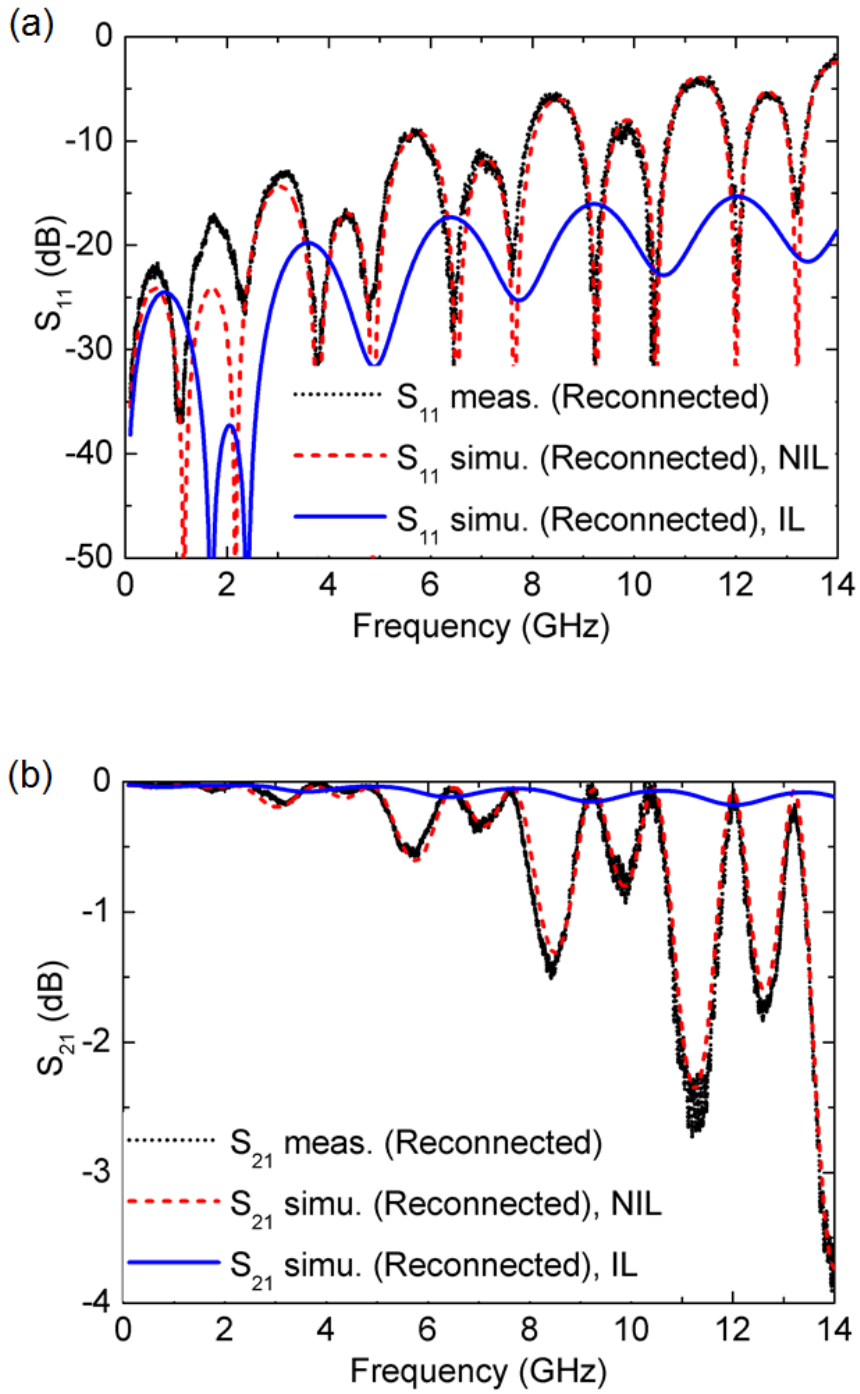

Figure 5.29: Measured and simulated S-parameters of reconnected microstrip fabricated on HD-4110 polyimide. ADS simulation results using a non-ideal launch "NIL" and with ideal launch "IL" are shown.

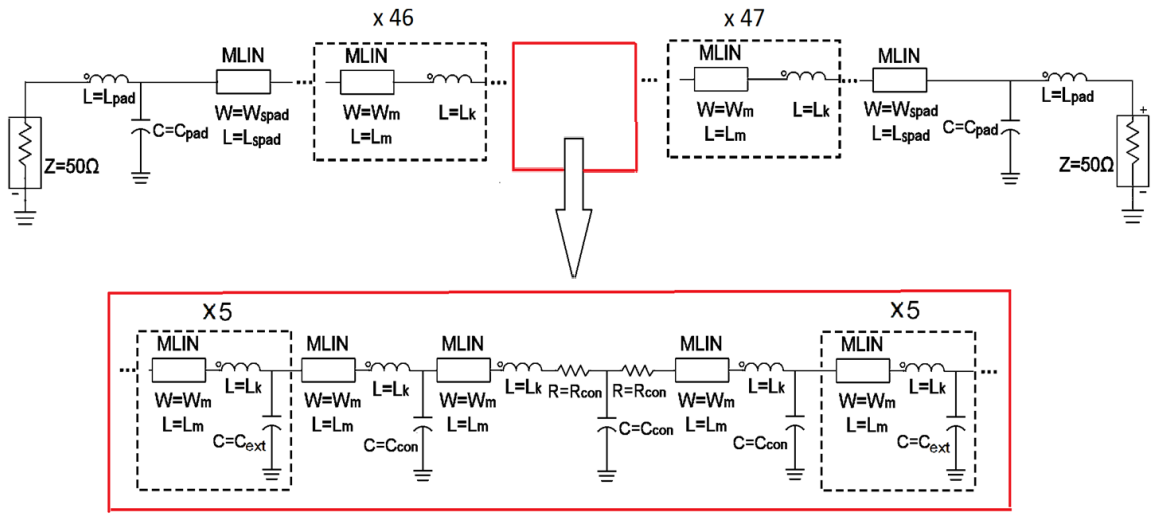

Figure 5.30: Equivalent distributed transmission-line circuit model of reconnected microstrip. Note that MLIN is a microstrip element unit in ADS, repeated 104 times, with line length and width values of $L_L = 0.625$ mm and $W_L = 52.3\,\mu$m, respectively. Launch pad is with dimension of $L_{pad} = 1.1$ mm and $W_{pad} = 122\,\mu$m. The kinetic inductance element (L_k) of Nb was determined in simulation to be 3.0 pH. In reconnected region, contact resistance (R_{con}) is 15 mΩ, major glass connector capacitance (C_{con}) is 0.03 pF and external glass connector capacitance (C_{ext}) is 0.002 pF.

Symbol	Value	Description
W_m	52.3 µm	Width of microstrip unit
L_m	0.625 mm	Length of microstrip unit
W_{spad}	122 µm	Width of solder pad
L_{spad}	1.1 mm	Length of solder pad
L_{pad}	0.3 nH	Inductance introduced by the non-ideal launch
C_{pad}	0.09 pF	Capacitance introduced by the non-ideal launch
L_k	3.5 pF	Kinetic inductance of the Nb of each microstrip unit
R_{con}	15 mΩ	Contact resistance between microstrip trace and connecting line on glass connector
C_{con}	0.03 pF	Capacitance from center of the glass connector where shim is applied
C_{ext}	0.002 pF	Capacitance from center of the glass connector where shim is not applied

Table 5.3: Key dimensions and parameters used in ADS for simulating reconnected microstrip.

5.4.2 20 cm Nb-based Microstrip and Connector

For practical uses, many thin-film transmission lines in parallel within just one single ribbon cable need be to constructed. To examine the performance of the glass connector for multiple parallel transmission lines, a 20 cm-long testing cable was designed with a meandering signal trace. The spacing between trace was 1.2 mm to avoid cross talk. A top view of an intact 20 cm version microstrip is schematically shown in Figure 5.31(a). RF performance of intact transmission line was measured first and then this cable was diced down its center as shown by the dashed line in Figure 5.31(a) and reconnected using a glass connector. The top view of the glass connector is shown in Figure 5.31(b). Four

connecting lines were designed with the same space as the signal trace and pillars were used for alignment.

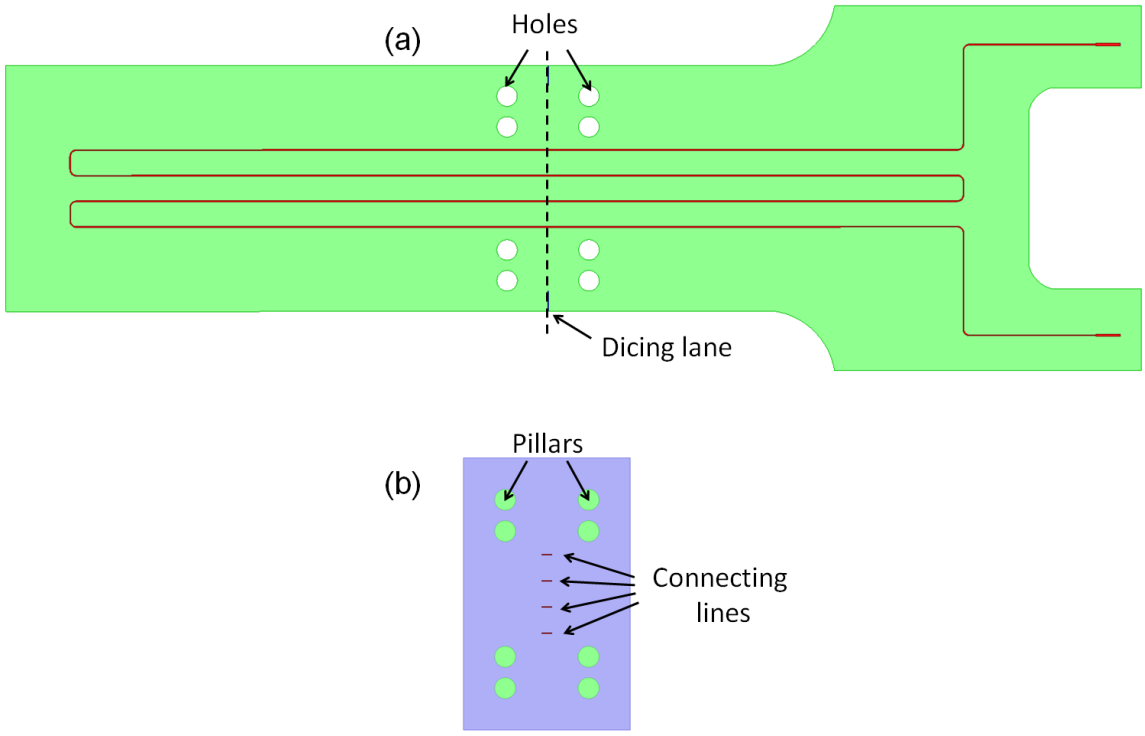

Figure 5.31: Layout of (a) 20 cm-long microstrip testing cable and (b) glass connector.

Similar to microstrip with one single break, DC resistance measurement, TDR analysis and S-parameter measurement for the intact 20 cm version microstrip cables and reconnected cables at 4.2 K were performed. Reconnected cable yielded 122 mΩ extra resistance, which was due to the contact resistance of the four breaks. The identical TDR experimental set up was used for the measurements. The comparison of intact and reconnected 20 cm-long microstrip is shown in Figure 5.32. The four reconnections lead to the four dips in the data between the two Southwest Microwave connectors, located at approximately 13.75 ns and 16.00 ns, respectively. For the entire reconnected microstrip TDR measurement, the impedance of the cable is relatively stable at ∼50 Ω and the four reconnected regions show

consistent capacitive responses, indicating a comparable RF performance at four reconnections. The impedance recorded is lower, approximately $\sim 47\ \Omega$, and is consistent with 6.5 cm-long microstrip with one reconnection.

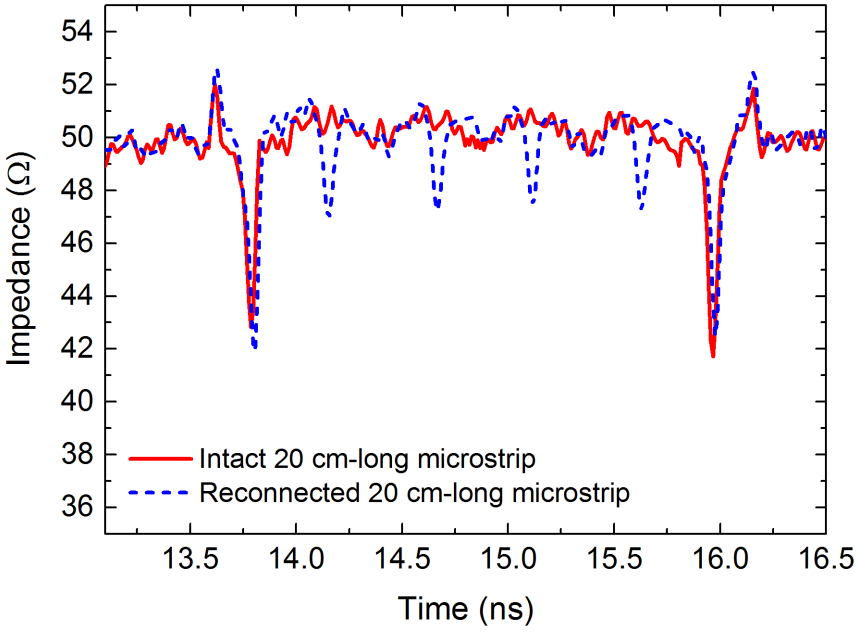

Figure 5.32: Time-domain reflectometry results of intact and reconnected 20 cm-long microstrip cable with multiple breaks. The reconnected structure uses a cable-to-cable connector, directly in the middle of the cable, to bridge between the two halves. Note that this cable has four breaks in the signal trace.

Figure 5.33(a) and (b) show the experimental and ADS simulated S-parameter results of the reconnected 20 cm version microstrip. The microstrip-to-microstrip interconnection ADS model was applied at reconnected regions, as presented in Figure 5.30. Parameter values used for microstrip-to-microstrip interconnection region were also kept the same as those used previously and as shown in Table 5.3. NIL S_{11} and S_{21} simulation results are matched very well with measurement results. After removing Southwest Microwave connector impact, microstrip cable and glass connector loss can be observed in the solid curves in the plots. The whole structure combined has an insertion loss of less than 1 dB and return loss is

better than 8 dB. Note that these results are for a microstrip transmission line with four reconnections and show the promise of this simple connection approach.

Furthermore, the match between experimental data and non-ideal launch simulation is impeccable.

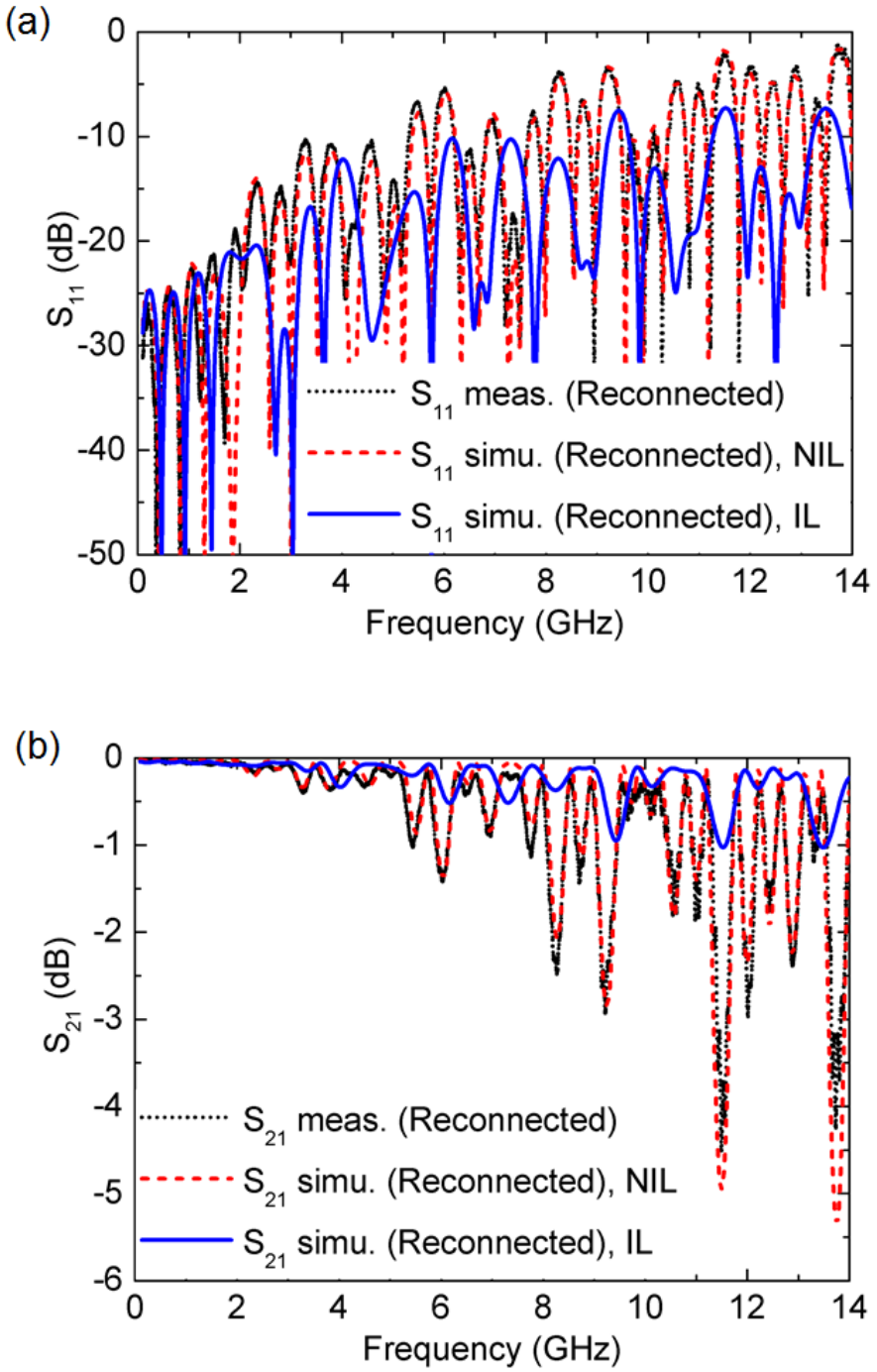

Figure 5.33: Measured and simulated S-parameters of reconnected microstrip fabricated on HD-4110 polyimide. Simulations with non-ideal launch "NIL" and with ideal launch "IL" are shown.

5.4.3 Glass Connector Loss Extraction

In order to compare the microstrip-to-microstrip interconnection loss between 6.5 cm version microstrip and 20 cm version microstrip, 20 cm-long microstrip only with one break in the middle of the cable was simulated. In Figure 5.34(a) and (b), simulation results of S_{21} of 6.5 cm intact microstrip and reconnected microstrip in IL case as well as 20 cm intact microstrip and reconnected microstrip with one single reconnection in the middle in IL case were compared. It can be seen from Figure 5.34(a) that the maximum difference between the two curves is 0.123 dB up to 14 GHz for the 6.5 cm microstrip. In Figure 5.34(b), the maximum insertion loss difference for the 20 cm microstrip is 0.118 dB up to 14 GHz. I have demonstrated that the loss at microstrip-to-microstrip interconnection is consistent between sample-to-sample, and is as low as $\sim$ 0.12 dB up to 14 GHz at 4.2 K.

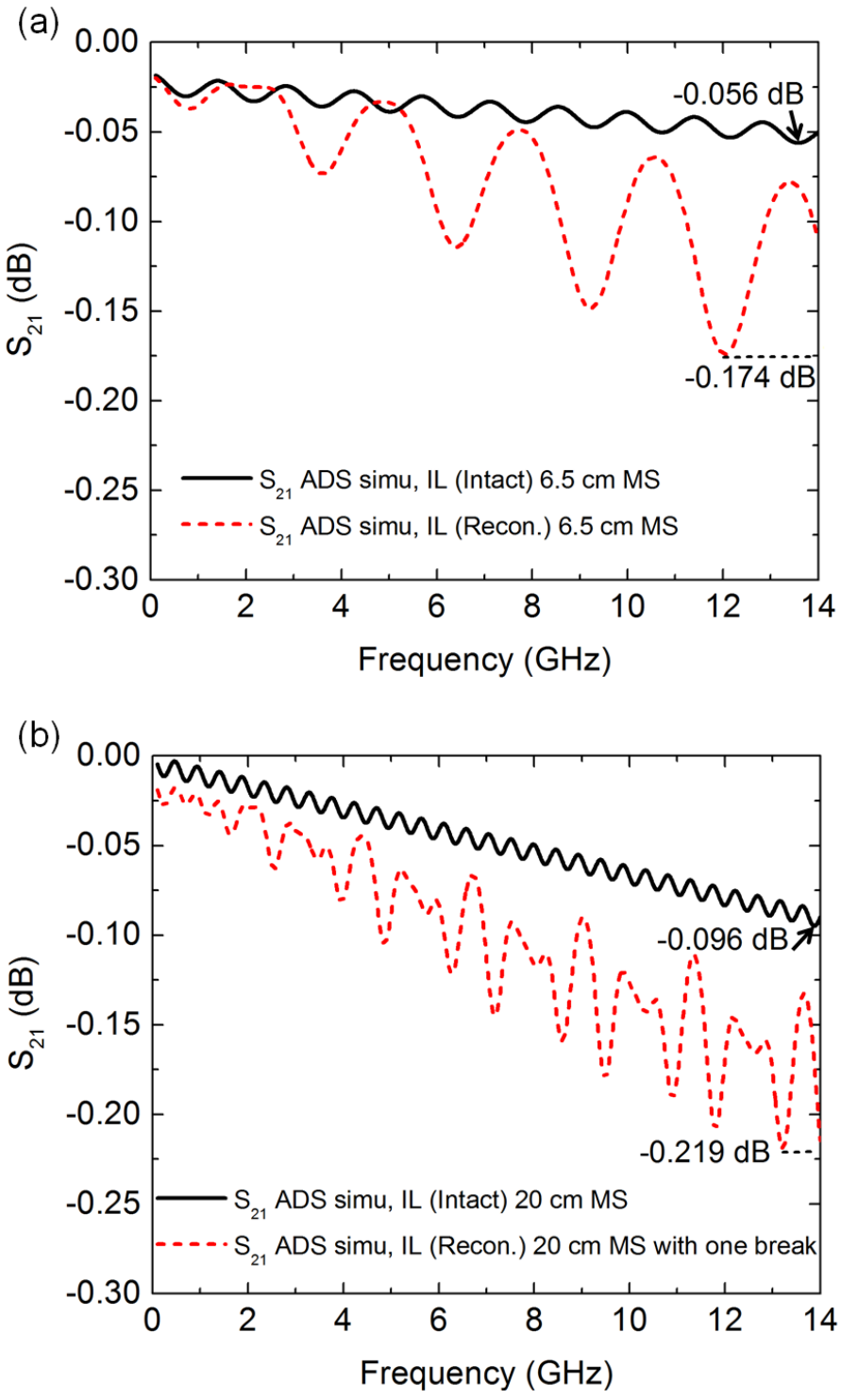

Figure 5.34: Simulation results for insertion loss comparison of (a) intact and reconnected 6.5 cm microstrip and (b) intact and reconnected 20 cm microstrip. Each reconnected structure was simulated with one break. Note that "MS" is short for microstrip in the plots.

5.4.4 Glass Connector Reliability Testing

In a real working environment, for example in a dilution refrigerator, reliability of the microwave connector is a big concern. Cables with microwave connectors usually experience many thermal cycles and assemblies. To evaluate the reliability of glass connectors, thermal reliability and re-assembly reliability tests were performed.

To examine the thermal cycling performance of the thin-film microstrip transmission line and microwave connector, a 20 cm-long microstrip with microwave connector was reconnected and tested during a series of five thermal cycles. After calibrating the system, S-parameter performance was measured in LHe dewar as cycle 1. The sample was then slowly removed from the dewar, heated to room temperature (290 K) and returned to LHe to perform the RF measurements after cycle 2. There was no dis-assembly and re-assembly of the microwave connector and cable parts during thermal reliability test. The thermal cycling test was repeated 5 times and measurement results are shown in Figure 5.35(a) and (b). It can be observed that with the glass connector, the reconnected cable shows consistent RF performance.

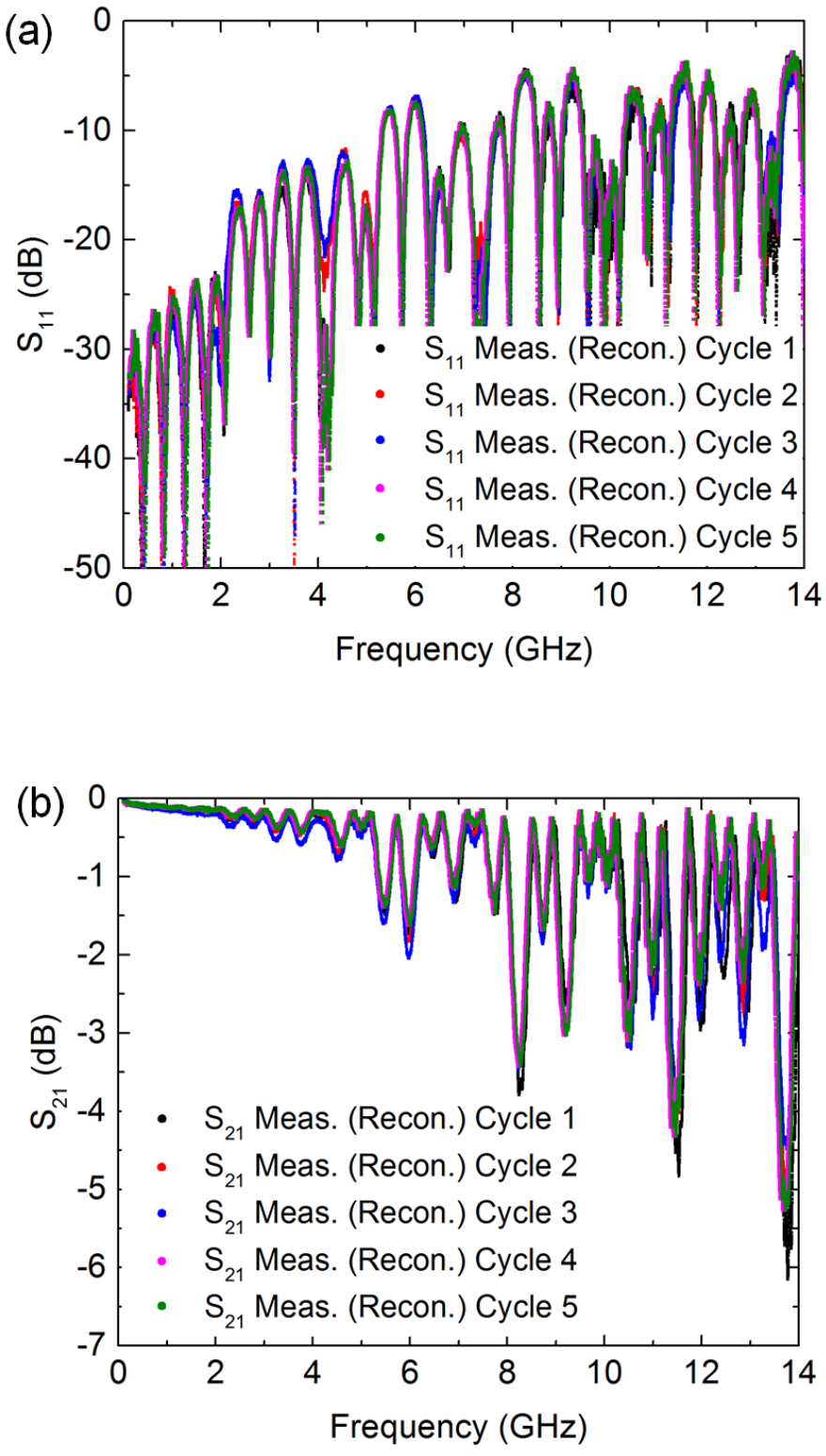

Figure 5.35: Measured (a) S_{11} and (b) S_{21} of reconnected 20 cm-version microstrip in thermal-cycle reliability tests. Results were taken for multiple, back-to-back measurements without disassembly of the structure, for temperature cycling from 4.2 K to 290 K and back to 4.2 K. Measurements were performed at 4.2 K.

To study the re-assembly reliability performance of the glass connector, following test procedure was employed. After system was calibrated, 20 cm-long microstrip parts were assembled with glass connector and its RF performance was measured in LHe dewar, assembly 1. Sample was then removed from the LHe dewar and heated to room temperature. Sequentially, entire structure was dis-assembled and re-assembled and measured in cold, assembly 2. The entire process was repeated 5 times. The measurement results are shown in Figure 5.36(a) and (b). Comparable RF performance was obtained for each re-assembly test, which indicates this proposed connection method shows reliable re-assembly performance and is promising for reuse.

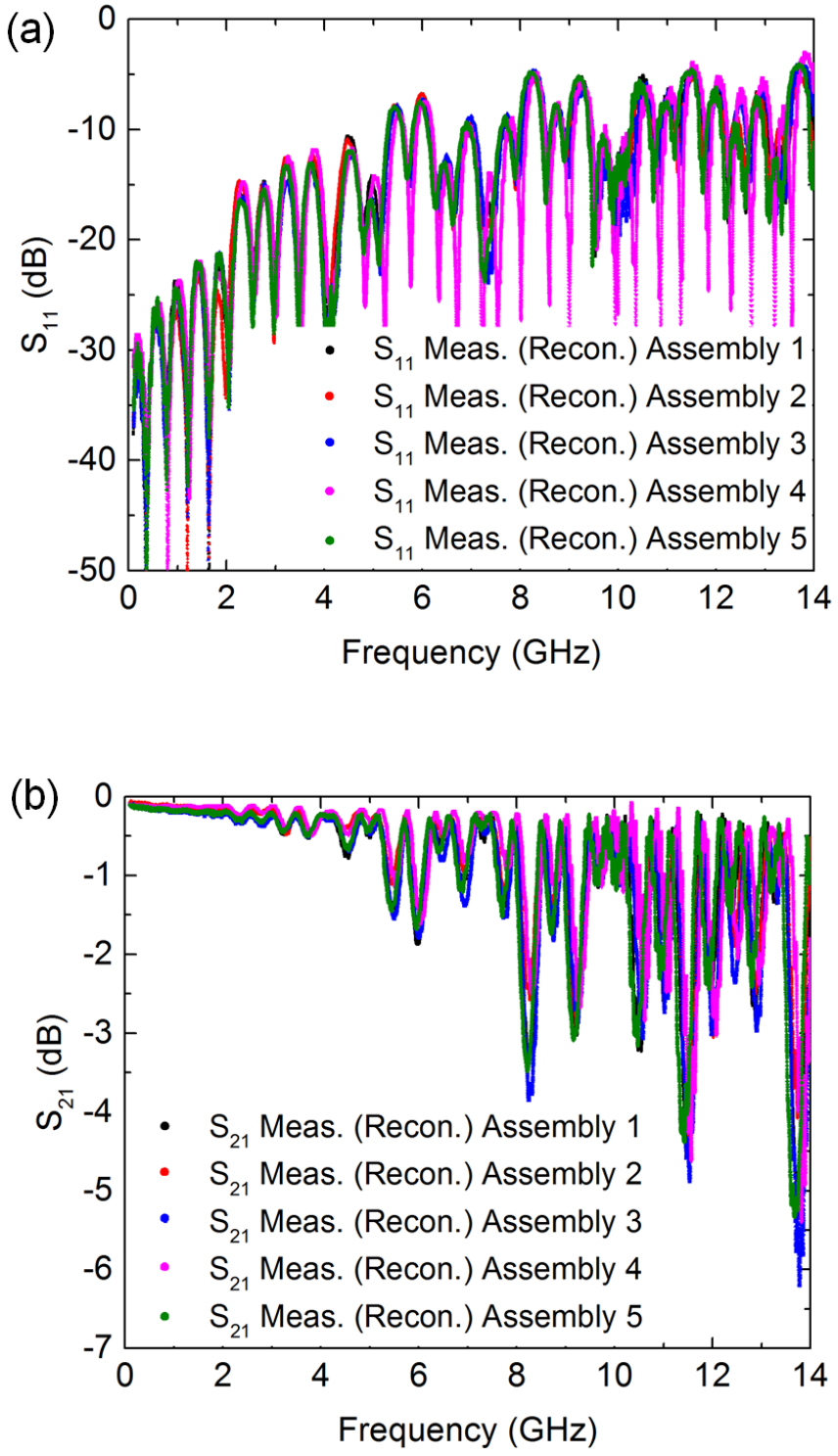

Figure 5.36: Measured (a) S_{11} and (b) S_{21} of reconnected 20 cm-version microstrip in connector re-assembly reliability test. Results are presented for multiple measurements with connector disassembled and reassembled between measurements.

5.5 Summary

In this chapter, Nb-based superconducting thin-film microstrip transmission lines and microwave connectors were designed, fabricated and characterized. To investigate the feasibility of a superconducting microwave connector, Cu-based DC cables and RF cables were used and tested at different temperatures (room temperature, 77 K and 4.2 K) with this type of connector. The RF performance of intact and reconnected Cu-based microstrip transmission lines at different temperatures were tested and compared. RF cables with different length and different numbers of reconnections were also measured. The split microstrip reconnected using the new connector exhibited very comparable RF performance as the intact cable, which indicated the glass connector introduced very limited contact resistance and good impedance matching with cable. Furthermore, fabrication procedures, assembly and characterization results of Nb microstrip samples with Nb-based microwave connectors were demonstrated. Electrical contact resistance using this type of connector is as low as 15 mΩ. A distributed element model was used to model the microstrip-to-microstrip interconnection of a reconnected structure. The proposed microwave connection methods exhibited a return loss better than 15 dB and an insertion loss less than 0.12 dB up to 14 GHz. Moreover, the microwave connector showed both encouraging thermal and re-assembly reliability and performance.

Bibliography

[1] M. Bhuiyan, A. Unno, Y. Yokoyama, T. Toriyama and S. Sugiyama, "Micro connector fabricated by micro process technology," *in Micromechatronics and Human Science, 2000. MHS 2000. Proceedings of 2000 International Symposiumon*, pp. 8388, 2000.

[2] M. Bhuiyan, T. Alamgir, M. Bhuiyan and M. Kajihara, "MEMS and EFF technology based micro connector for future miniature devices," *in IOP Conference Series: Materials Science and Engineering*, vol. 53, p. 012063, 2013.

[3] B.-H. Jang, H.-Y. Huang and W. Fang, "A Novel Zero-Insertion-Force (ZIF) Micro-Connector: Design, Fabrication and Measurements" *IEEE Transactions on Industrial Electronics*, vol. 56, no. 4, pp. 10401047, 2009.

[4] E. Fiedler, J. Ordonez and T. Stieglitz, "Laser-structured ceramic adapters for reliable assembly of flexible thin-film electrodes," *Biomedical Engineering/ Biomedizinische Technik*, 2013.

[5] W. Williams and D. Esquivel, "Flex to flex connection device," US Patent, 8529277, 2013.

[6] R. S. Mroczkowski, "Electronic connector handbook: theory and applications," McGraw-Hill New York, NY, 1998.

[7] R. S. Timsit, "High speed electronic connectors: A review of electrical contact properties," *IEICE transactions on electronics*, vol. 88, no. 8, pp. 15321545, 2005.

[8] E. Decrossas, M. D. Glover, K. Porter, T. Cannon, T. Stegeman, N. Allen-McCormack, M. C. Hamilton and H. A. Mantooth, "High-performance and high-data-rate quasi-coaxial LTCC vertical interconnect transitions for multichip modules and system-on-package applications," *IEEE Transactions on Components, Packaging and Manufacturing Technology*, vol. 5, no. 3, pp. 307313, 2015.

Chapter 6

Reliability of Flexible Superconducting Cables

6.1 Introduction

Electrical interconnect technology is one of the major limitations to progress in constructing densely-integrated cryogenic electronic systems, such as those involving cryogenic computing and future superconducting quantum computing technologies. Thin superconducting cables with small cross-sections are desirable for their high signal density and low thermal conductivity.

The superconducting characteristics of thin-film Nb make it a viable material for realizing low-temperature ($\sim$ 4.2 K) superconducting cables, such as high density DC cables [1] and RF/microwave cables including microstrip [2] and stripline. Thin flexible superconducting ribbon cables [3-5], incorporating polymer dielectrics are expected to be particularly useful for making multiple interconnections between different substrates at the same or across different temperature zones. For such applications, it is important that the cables be tolerant of routine handling and bending that may occur during room-temperature assembly, and retain their superconducting properties after multiple thermal cycles.

Mechanical properties of bulk Nb [6] and freestanding Cu/Nb multilayers [7-8] have been studied by other groups. Microvoids and microcracks have been reported to cause fracture surface on Nb. The mechanical performance and reliability of thin ($\sim$ 250 nm) and narrow Nb superconducting wires fabricated on thin flexible substrates has not been fully studied, especially when subjected to a variety of mechanical fatigue and strain conditions. The effects of fatigue and strain on the superconducting properties, for instance, critical temperature and critical current are important for practical aspects [9-11]. Concerns for reliability of Nb flexible superconducting cables are that the Nb thin films are susceptible to

cracking and delamination from the underlying substrate, which may cause fluctuations in or deterioration of the critical current I_c or transition temperature T_c of the Nb wire.

Ti is often used as an adhesion, barrier or transition layer for subsequently deposited metal layers. Cu, as an excellent electrical and thermal conductor with superior ductility and strength [12-13], can be deposited on top of the Nb thin film to improve the fracture toughness of Nb, prevent the evolution of cracking or potentially mend cracking damage, and provide enhanced thermalization to achieve more reliable cable performance at cryogenic temperatures. Furthermore, building superconducting flexible cables using an embedded structure is attractive since it has been observed to increase reliability and is necessary for cables in configurations that can provide reduced cross-talk, such as stripline. This technology is expected to be beneficial to multiple cryogenic electronics applications, including cryogenic quantum computers [14] and low-noise superconducting parametric amplifiers [15].

In this chapter, considering the mechanical reliability of Nb cables, Nb cables with different material stack-ups was investigated. Basically, there are two prototypes, as shown in Figure 6.1. The first one is normal metal/superconductor/normal metal (N/S/N) structure fabricated on Kapton substrate and the other one is embedded structure fabricated on PI-2611 polyimide. Fabrication procedures, experimental setup, superconducting properties including T_c, I_c and surface morphology of testing cables with different material stack-ups was described. In addition, the I_c degradation of different material stack-ups under mechanical testing (fatigue test and bending test) were examined.

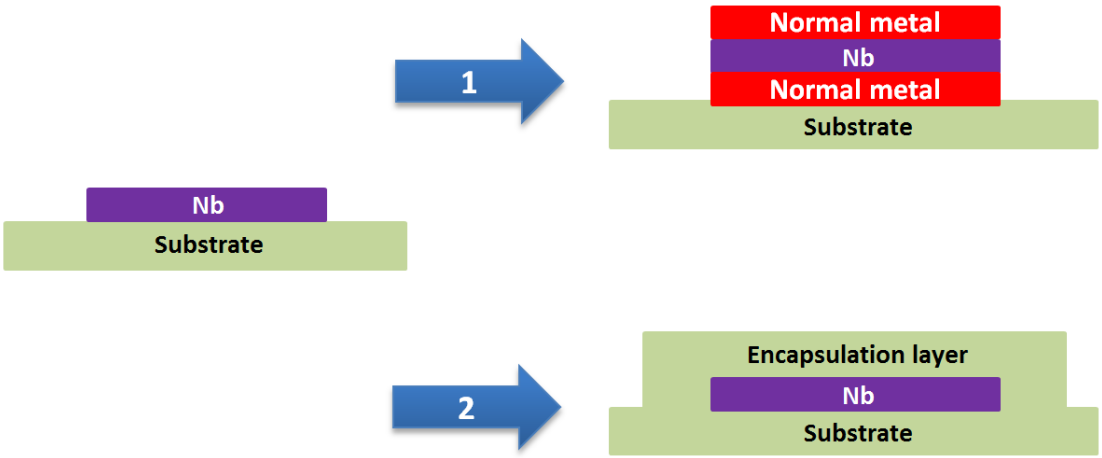

Figure 6.1: Two prototypes of the DC testing cables investigated in this chapter. The first one uses normal metal/superconductor/normal metal (N/S/N) structure and the other one uses an embedded superconducting-only structure.

6.2 Literature Review of Superconducting Flexible Cables

High temperature superconductor (HTS) material such as YBCO have been reported to construct current leads as DC bias lines to cryocoolers [16]. Reported T_c of YBCO is up to 90 K. Figure 6.2 (a) shows the 12 mm-wide YBCO tape etched to have 15 lines with 300 µm wide and with 625 µm pitch. Figure 6.2(b) demonstrates how these YBCO current leads assembly with clamped lap-joints between 50 K and 4 K stages of a cryocooler. These YBCO DC bias lines have typical I_c of $\sim$ 3 A in LN_2.

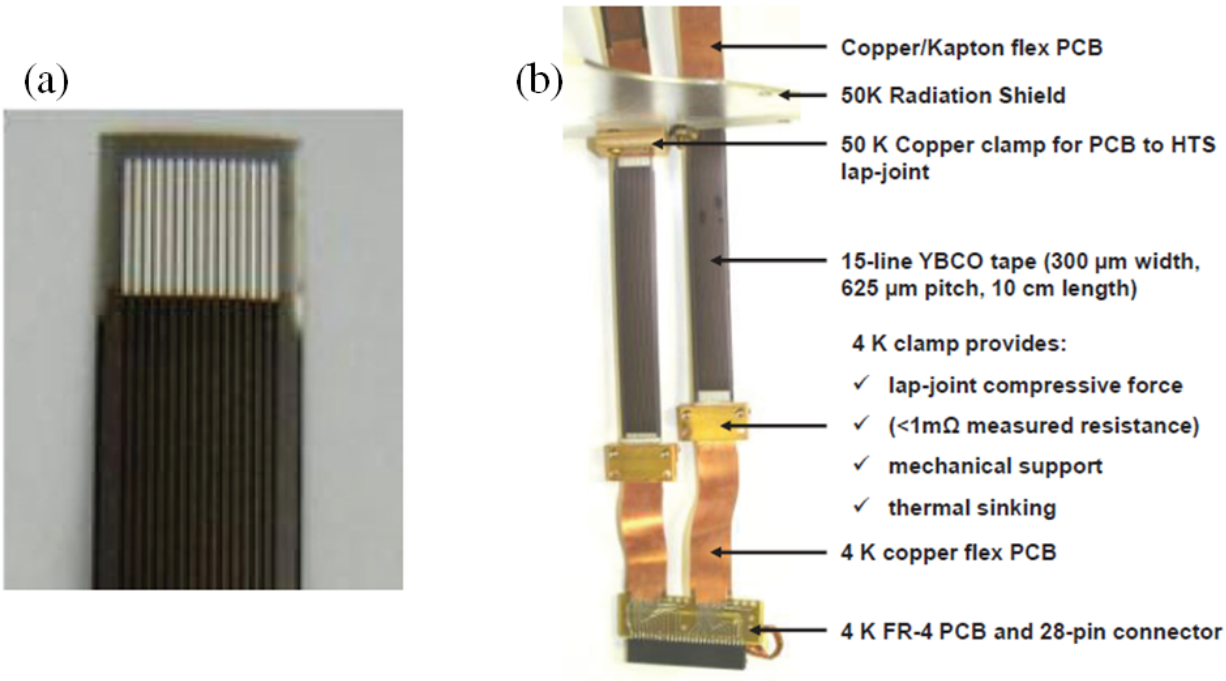

Figure 6.2: (a) YBCO current lead with 15 lines on it and (b) lap-joint connection of the patterned YBCO tape and copper-on-Kapton flexible PCB. Adapted from [16].

In the work by Yung et al., MgB_2 superconducting ribbon cables were fabricated on yttria-stabilized zirconia (YSZ) flexible substrate with a thickness of 50 µm [5]. Their flexible flat cables (FFC) with 33 traces of 300 nm-thick, 200 µm-wide of MgB_2, which is shown in Figure 6.3. The FFC before and after mating to a Hirose FFC/FPC (flexible printed circuit) connector are shown in Figure 6.3 (a) and (b). In order to perform cryogenic measurement, they used commercially FFC/FPC connector from Hirose and Japan Solderless Terminal (JST) connectors. The circuit board setup is shown in Figure 6.3(c). 100 nm-thick MgB_2 deposited on *r*-plane Al_2O_3 and flexible YSZ substrate showed comparable T_c of 37.9 K and 37.4 K, respectively, which is can be found in Figure 6.4(a). The critical current density (J_c) of 100 nm $\times$2 µm MgB_2 sample on *r*-plane Al_2O_3 and flexible YSZ are identical. J_c at 30 K is approximately 5 mA/cm^2 and by doing scaling law fit of measurement results, the calculated J_0 is 30 mA/cm^2.

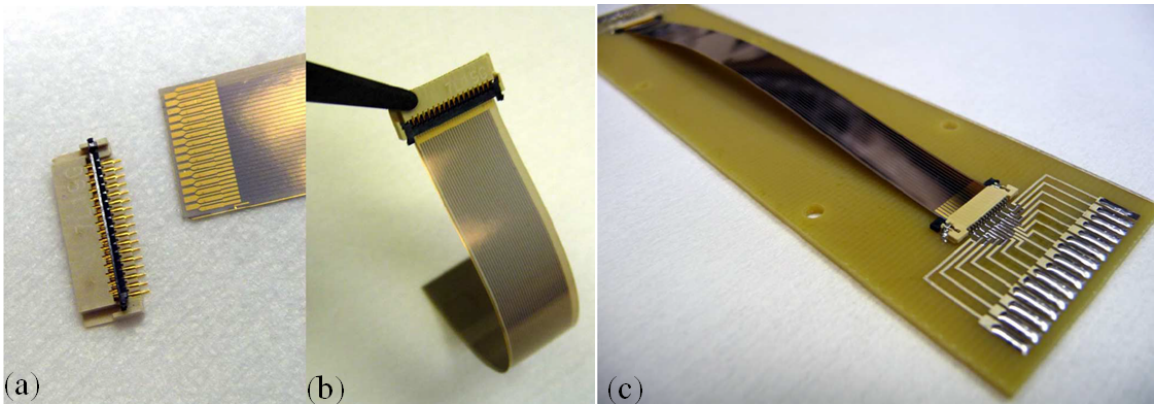

Figure 6.3: A MgB_2 FFC before (a) and after (b) assembling to FFC/FPC connector.(c) PCB setup of MgB_2/YSZ FFC for cryogenic measurement. The JST connector on PCB supports 15 0.35 mm-wide of MgB_2 traces with pitch of 0.5 mm. Adapted from [5].

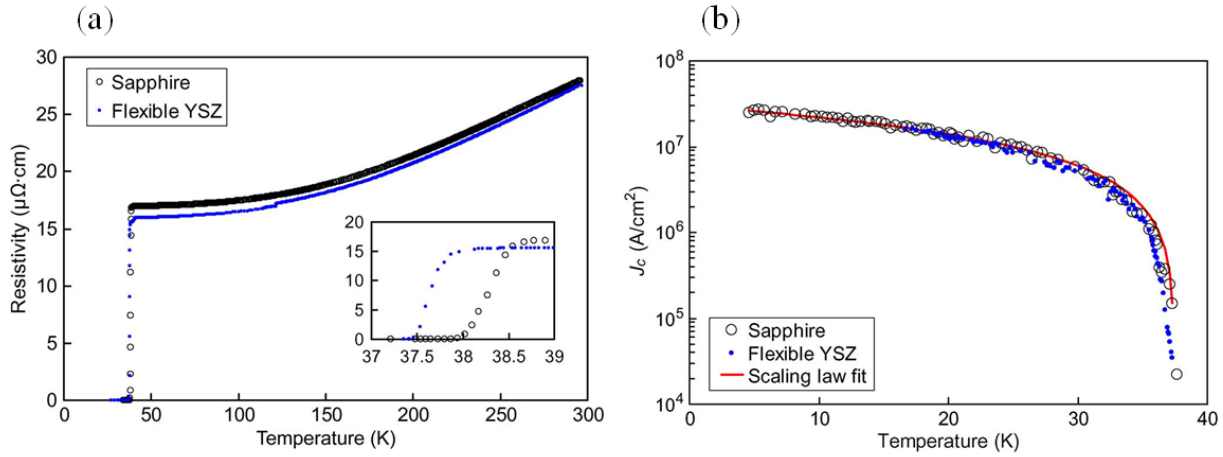

Figure 6.4: (a) Resistivity versus temprature plot of MgB_2 deposited on Al_2O_3 substrate and on flexible YSZ substrate. (b) Critical current density measurement as a function of temperature of MgB_2 deposited on Al_2O_3 substrate and on flexible YSZ substrate. Adapted from [5].

In the work by Pappas, Al high density superconducting cable interface with ACTPol detector arrays was built on thin-film polyimide PI-2611 [17]. They fabricated 50 µm-wide 400 nm-thick Al traces with pitch of 100 µm on 50 µm-thick PI-2611 substrate. These Al traces are superconducting with a T_c of 1.2 K ± 0.1 K and have I_c of above 5.7 mA at 1.0 K and below.

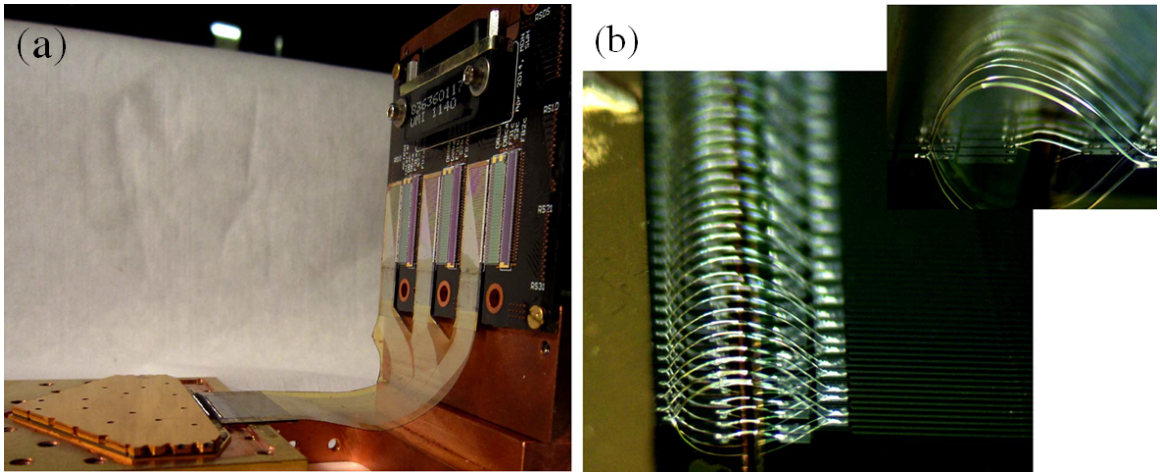

Figure 6.5: (a) High density Al superconducting cable is connected between readout printed circuit board and an ACTPol detector wafer. (b) A photograph of the wire bonds between high density Al superconducting cable and an ACTPol detector wafer. Adapted from [17].

van Weers et al., fabricated Nb flexible DC cable on polyimide PI-2611, which can be integrated with PCB directly [1]. Their experimental setup for measuring thermal conductivity of flexible cable is shown in Figure 6.6. The flex was integrated with PCB at both ends using a reflow soldering process. Different layer build-up was tested for cable metallization, such Ti/Nb and Ti/Nb/Ti. The 50 nm-thick bottom Ti layer was used as adhesion layer and the top Ti layer was used as a protection layer. The DC lines has 250 nm-thick Nb layer and thickness of polyimide substrate was 12 µm, which was released from glass substrate. RRR, T_c and I_c have been measured for DC lines. A resistance versus temperature plot of a Ti/Nb/Ti 25 µm-wide flex cable is shown in Figure 6.7. The first transition at $\sim$ 7.8 K is closed to bulk T_c of Nb and the second transition is related to SnPb solder connected between PCB and the flex. The I_c of the DC line at 4 K varies from 7 mA to greater than 60 mA and RRR is in the range from 2.9 to 4.6 according to their results.

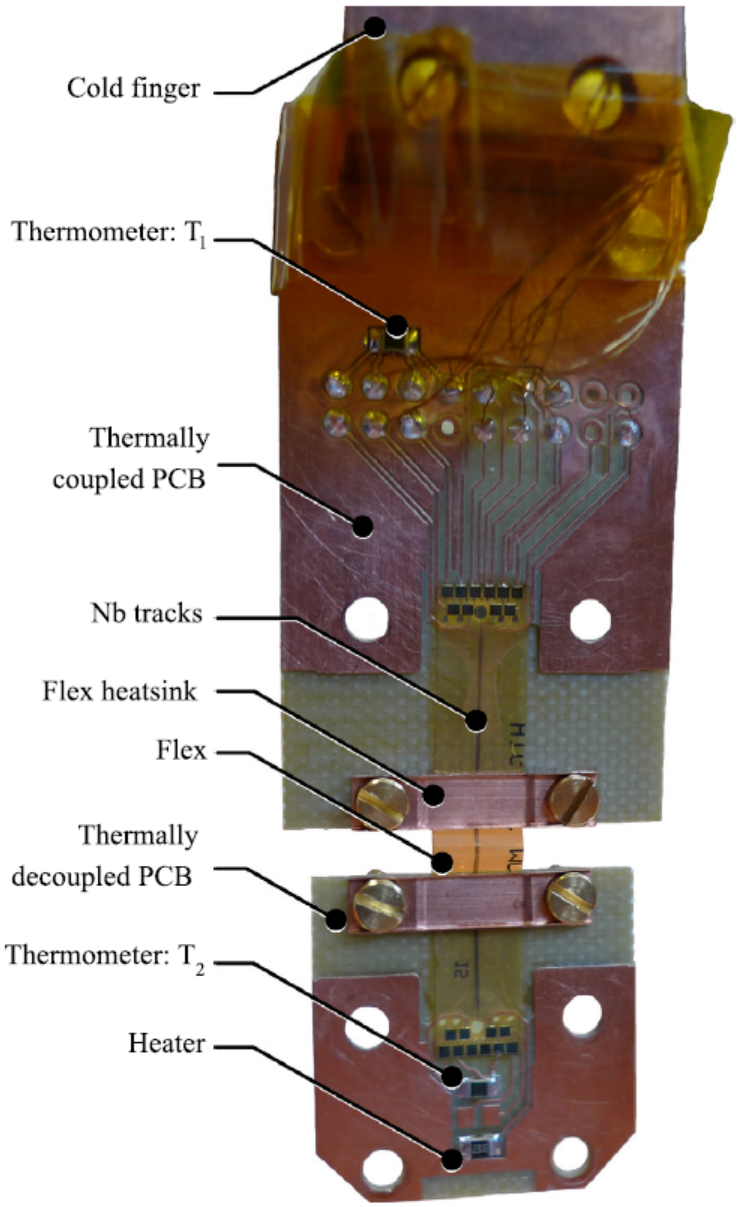

Figure 6.6: Experimental setup described by van Weers for thermal conductivity measurement of the flexible cable. Adapted from [1].

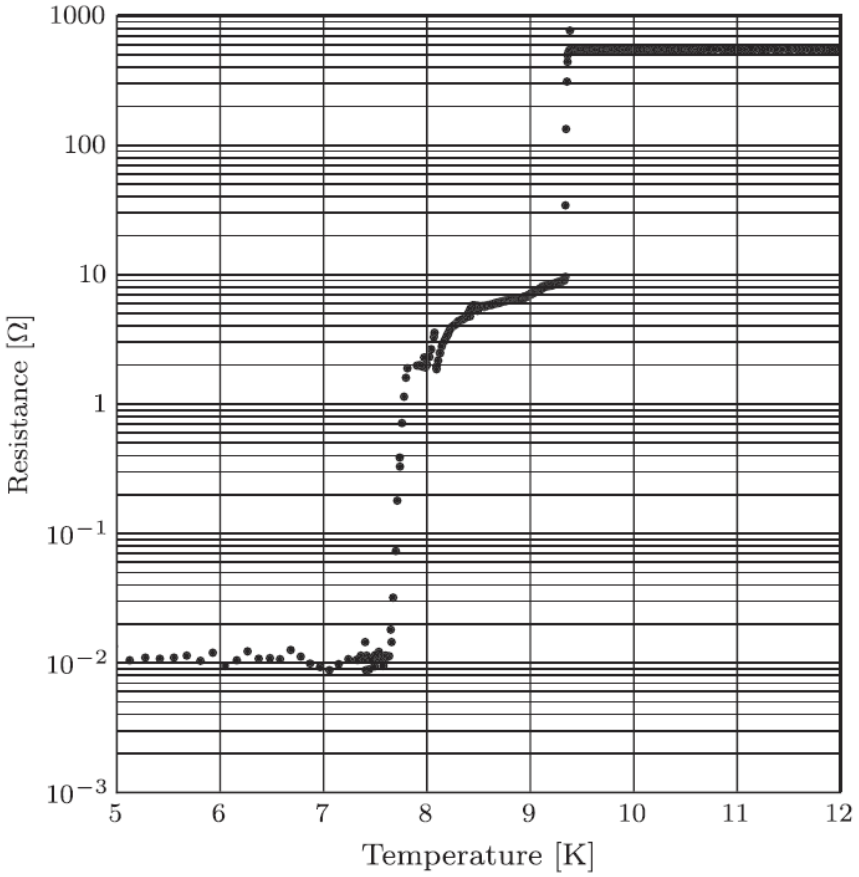

Figure 6.7: Resistance as a function of temperature plot of a Ti/Nb/Ti flex cable. Adapted from [1].

Similar normal metal/superconductor/normal metal (N/S/N) metallization layer have also been reported in their other work [18]. The Nb DC interconnect was embedded in Si substrate and connected to LC resonator chip and detector chip, which is shown in Figure 6.8. Corresponding schematic cross section of such structure is shown in Figure 6.9. It can be seen that they used Ta/Nb/Ta material stack-up. The purpose of using 10 nm-thick Ta layer on top and bottom Nb layer was to enhance the adhesion of Nb on polyimide and reduce the deterioration of Nb properties during top polyimide cure process.

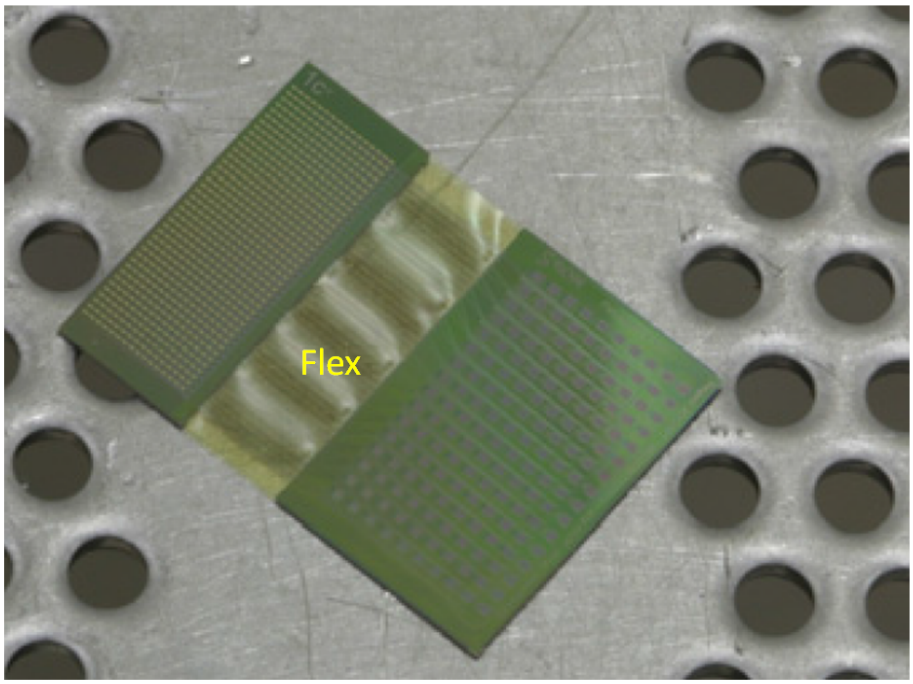

Figure 6.8: The Nb flexible cable in the detector assembly, connecting to two chips. Adapted from [18].

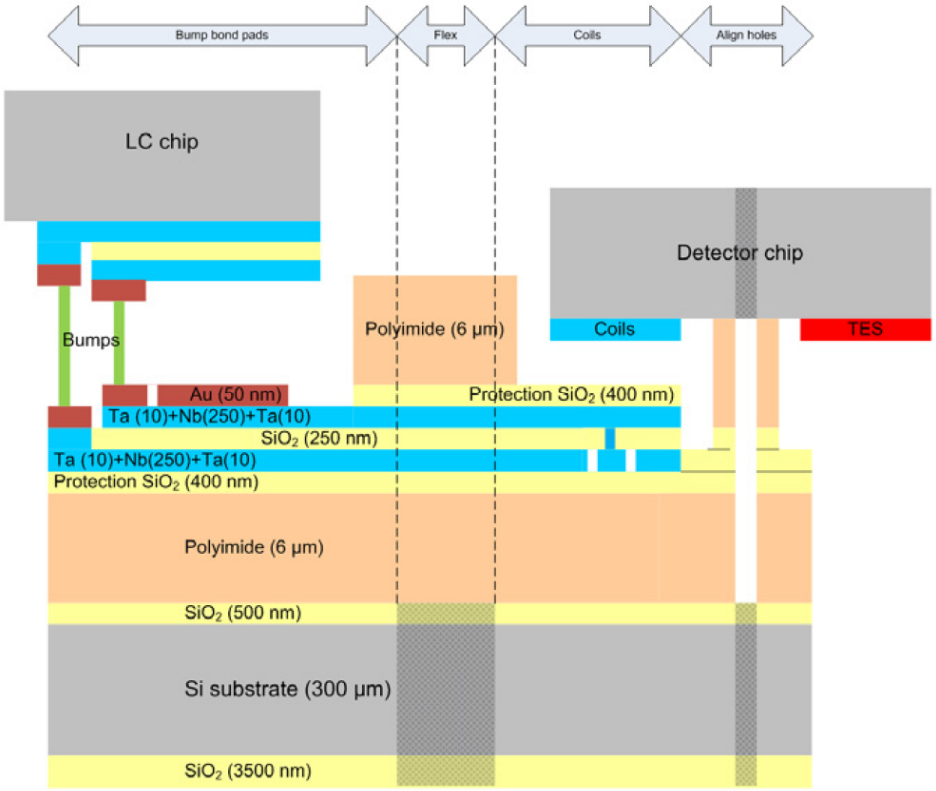

Figure 6.9: Schematic diagram of the cross section of Nb flexible DC cable connected with LC resonator chip and detector chip. Adapted from [18].

6.3 Performance and Reliability of Superconducting Cables Fabricated on Free-standing Kapton

Kapton polyimide film [1]have been applied to the industry for its high performance, durability, reliability and unique electrical, thermal and mechanical properties at extremely temperature environment [19-25]. Different series of Kapton have different effects on the properties of Nb film due to surface roughness and defects, which has been discuss in [26] already. By performing a series of experiments including atomic force microscopy (AFM) scan and transition temperature measurement, EN series Kapton was found to have the smoothest and most defect-free surface, which allowed the most repeatable and dependable results.

[1]http://www.dupont.com/products-and-services/membranes-films/polyimide-films/brands/kapton-polyimide-film.html/

Figure 6.10 shows the layout of a Nb DC cable for fabrication on a Kapton substrate. The DC line is 5 cm long and 120 µm wide. The 120 µm width was used since it achieves a 50 Ω characteristic impedance for microstrip designs. Each end of the line has two larger pads that are used for four-point resistance measurements. Instead of using right angle, where the pads connected into the line, the smooth transition design was to avoid the deterioration during handling and flexing the cable.

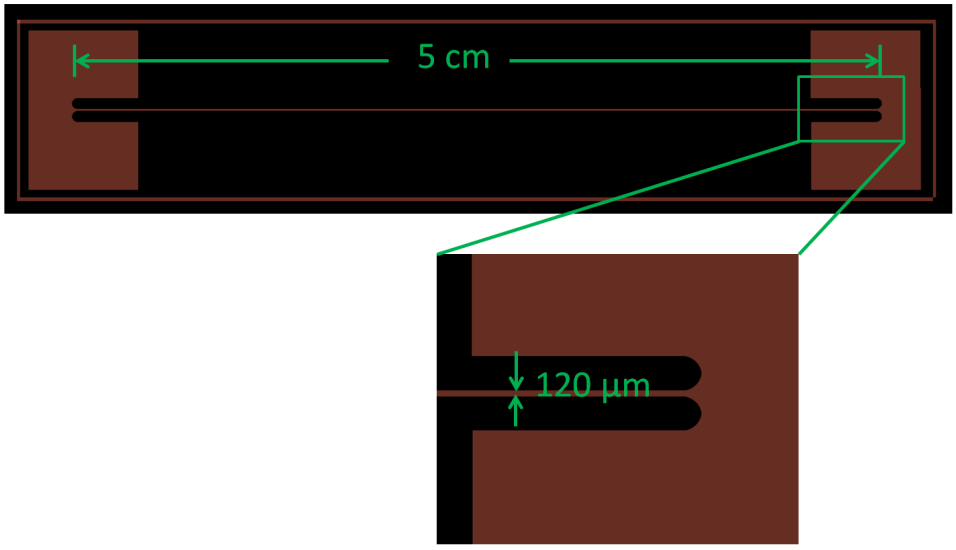

Figure 6.10: Layout of a DC testing cable on Kapton substrate. The zoom-in image shows the smooth transition from cable to pads, which help avoid the deterioration of cable during handling and flexing

Nb films for testing were fabricated on 50.4 µm-thick Kapton EN film. Kapton was cleaned by acetone, methanol and deionized water, followed by mounting onto a Si wafer and a dehydration bake. DC lines were patterned using standard photolithography techniques. Before Nb deposition, the chamber was evacuated to a base pressure below 3×10^{-7} torr. After 2 minutes in-situ surface clean by ion milling, Nb films were sputtered with a power of 1 kW. The thickness of the Nb film was nominally 250 nm. After the fabrication, the Kapton flex test cables were cut to the appropriate outline for testing. For the samples with Ti adhesion layer and/or Cu capping layers, Ti and Cu were deposited with a deposition rate of 2 Å/s by electron beam physical deposition before and after Nb-deposition, respectively.

To study the influence of Ti and Cu thin films on the DC electrical properties and mechanical performance of superconducting wires, a range of thickness of Ti and Cu were explored from 10 nm to 50 nm and 20 nm to 200 nm, respectively. Figure 6.11 shows a fabricated Nb-only cable and a Ti/Nb/Cu cable. The schematic cross-section of Nb cables and Ti/Nb/Cu cables is shown in Figure 6.12.

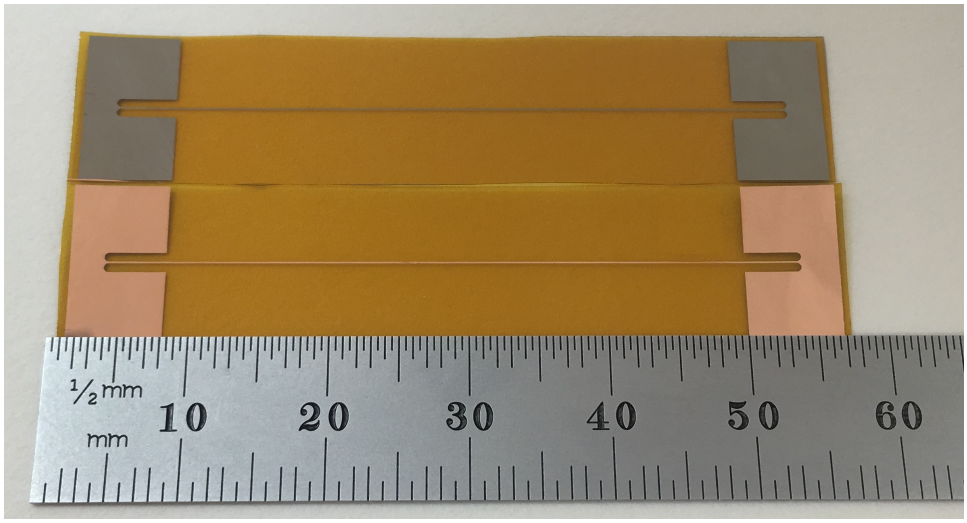

Figure 6.11: A Nb-only Kapton sample (top) and a Ti/Nb/Cu Kapton sample (bottom).

Figure 6.12: Schematic cross-section of (a) Nb-only Kapton DC sample and (b) Ti/Nb/Cu Kapton DC testing cable.

In order to accurately measure the critical temperature (T_c) and critical current (I_c) of superconducting test cables, four-point resistance measurement was performed. Figure 6.13 and Figure 6.14 show the layout of printed circuit board (PCB) and the finished PCB for four-point resistance measurements, respectively. Note that this 10-pin PCB can be used

to measure 4 samples simultaneously, which can increase the measurement throughput. T_c measurements were performed in the PT, as previously shown in Figure 3.10. A LakeShore 335 temperature controller was used to monitor the temperature in the PT and a Agilent 34420A was use to monitor the resistance of the superconducting cable during the temperature change. The set-up image is shown in Figure 6.15. A LabVIEW program was used to record temperature and resistance data from LakeShore 335 temperature controller and Agilent 34420A, respectively, which is shown in Figure 6.16. I_c measurements were conducted in a LHe dewar. A Keithley 2400 source meter was used to force the current and sense the voltage change during the I_c measurements and also shown in Figure 6.15.

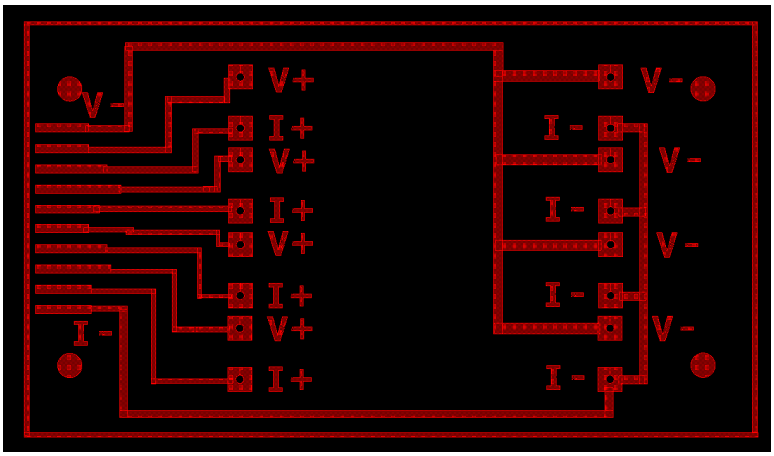

Figure 6.13: Layout of the PCB for four-wire resistance measurements.

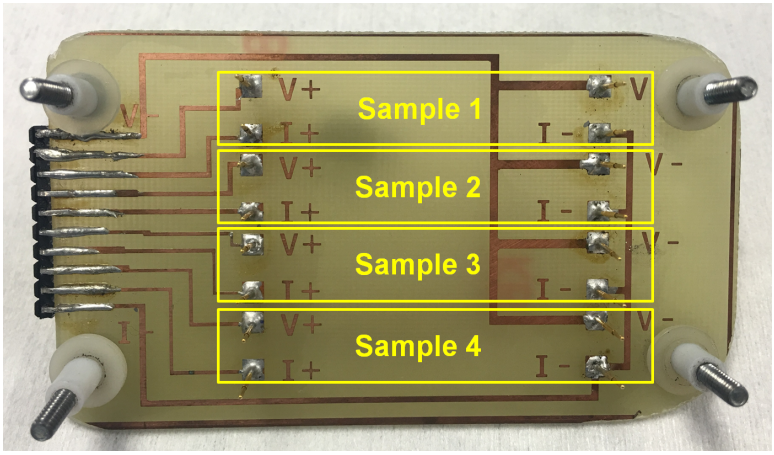

Figure 6.14: PCB for four-wire resistance measurements.

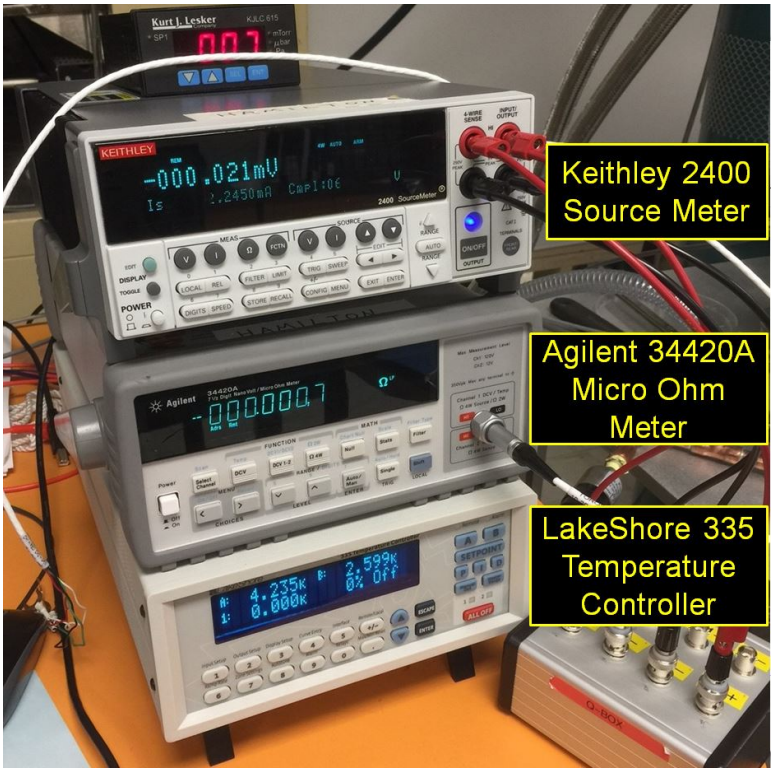

Figure 6.15: Instruments used to perform superconducting cable DC testing.

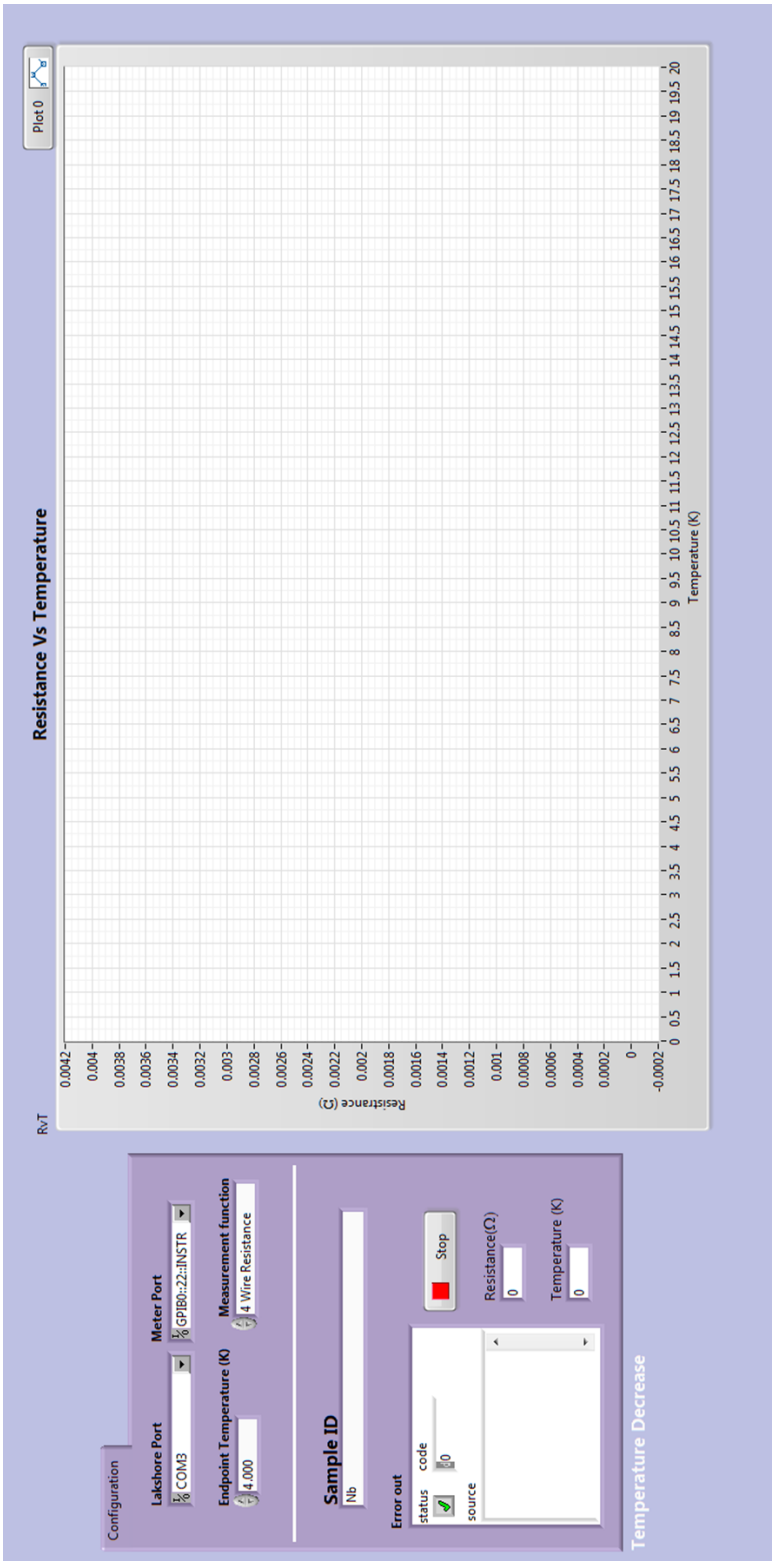

Figure 6.16: LabVIEW front panel for T_c measurement.

A smooth surface with few defects is desired to achieve excellent superconductivity for thin and narrow Nb and Ti/Nb/Cu lines [27]. As representative material stack-ups in this study, the surface morphology of Nb-only and Ti(50 nm)/Nb/Cu(200 nm) thin films on Kapton have been investigated. Three-dimensional AFM images of Nb film and Ti(50 nm)/Nb/Cu(200 nm) film on Kapton substrate are shown in Fig. 6.17. The scan area for AFM is 5 µm × 5 µm. The thickness of the Nb film is approximately 250 nm. In Fig. 6.17(a), the average surface roughness of the Nb film is ∼3.4 nm with an RMS value of 4.2 nm, which is quite comparable with results shown in [28]. In Fig. 6.17(b), the average roughness of the Ti(50 nm)/Nb/Cu(200 nm) film is ∼3.9 nm with an RMS value of 4.7 nm. These results show continuous smooth and defect-free Nb-only and Ti/Nb/Cu films on Kapton.

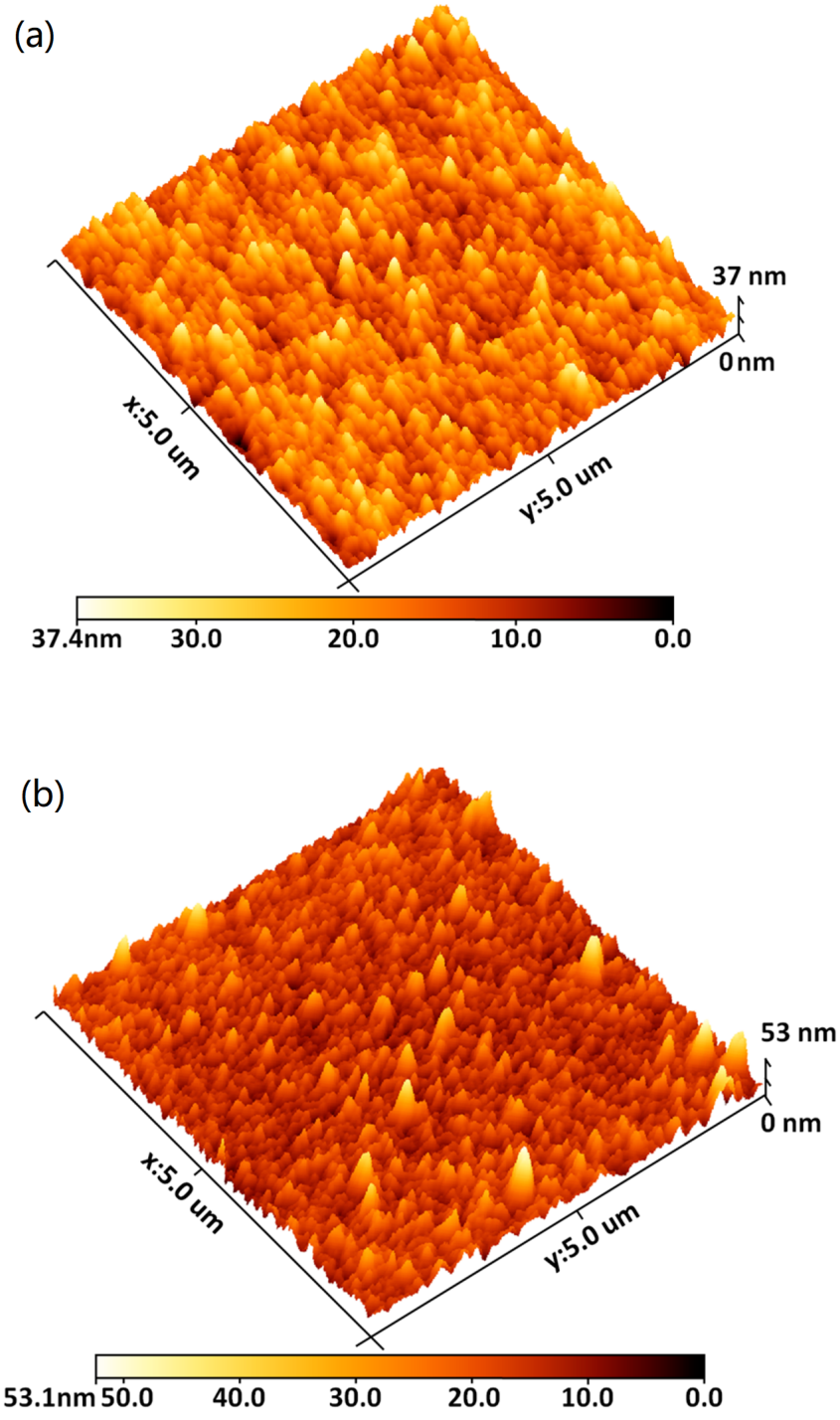

Figure 6.17: 3-D AFM micrograph showing the surface morphology of (a) 250 nm-thick Nb film and (b) Ti(50nm)/Nb/Cu(200nm) film deposited on Kapton substrate.

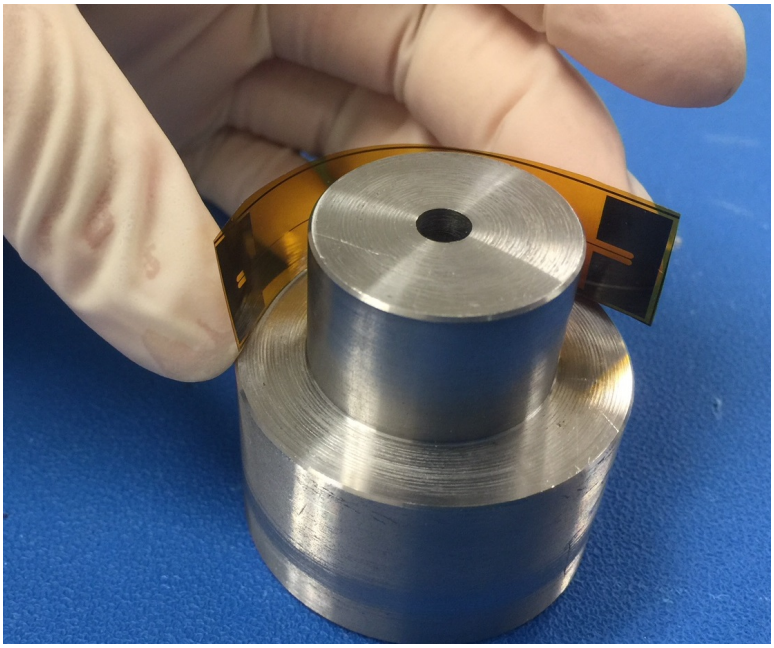

Figure 6.18: Fatigue test fixture with R = 12.5 mm.

To investigate the mechanical reliability performance of testing cables with different material stack-ups, fatigue tests and bending tests were performed on these cables. To perform the fatigue test, the samples were repetitively bent (at RT $\sim$ 297 K) around a cylinder with a specific diameter of 12.5 mm, followed by flattening and then measurement of I_c at 4.2 K in a LHe dewar. The fatigue test fixture is shown in Figure 6.18. Depending on the orientation of the superconductor (facing towards or away from the cylinder), the conductor is subjected to either compressive or tensile stress. Fatigue evaluation was done by measuring I_c after a specified number of bending-flattening cycles (50, 150 and 250 cycles) around a fixed radius of curvature for multiple samples for each material stack-up. To perform the bending tests, half-cylinder shaped sample holders with four different bending radii were built. Figure 6.19 shows all the sample holders with different bending radii that used for bent sample testing. The samples were carefully mounted onto the sample holder at RT followed by testing at 4.2 K. I verified that, before and after mounting, the I_c change due to mounting and de-mounting is negligible. Each flex cable for testing was bent with a specific bending radius R and held in that particular configuration during low-temperature

testing. The testing followed an order of largest to smallest bending radius, which was 17.5 mm, 12.5 mm, 7.5 mm and 5.0 mm. Each sample was subjected to all of these tests from largest to smallest R, returning to room temperature between tests. Using a different set of samples, both tensile and compressive bending testing were performed, depending on the orientation of the sample with respect to the sample holder.

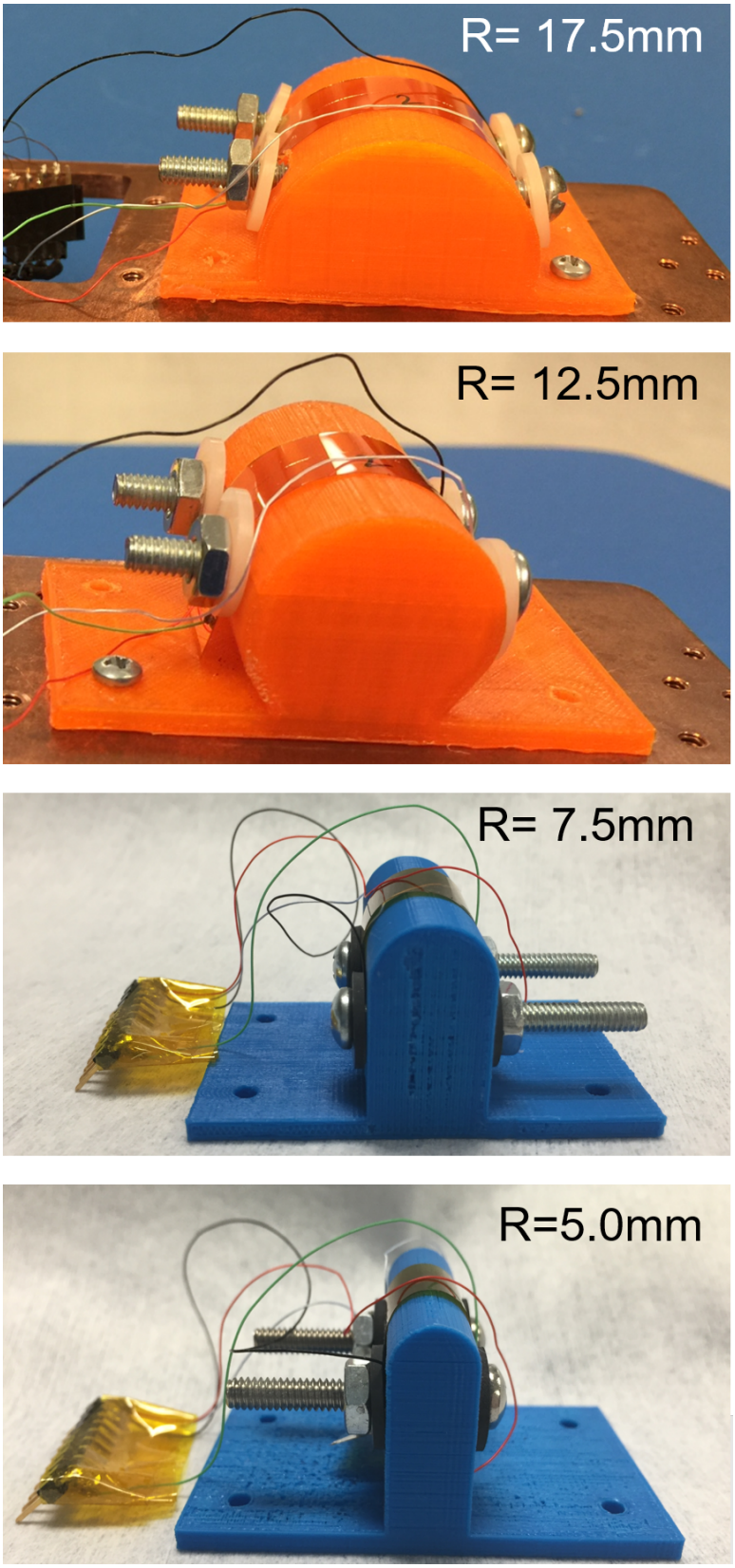

Figure 6.19: Sample holders with different bending radii used for bent sample testing.

For superconducting cables fabricated on free-standing Kapton with different material stack-ups, the critical temperature T_c and current carrying capability I_c at 4.2 K were measured [29]. For each measurement, pristine samples were used. For each of the layer stacks, multiple samples have been measured to alleviate effects of individual incidents and elucidate trends. For instance, Figure 6.20 shows a typical T_c plot of a Nb-only Kapton cable. It can be seen that with the decrease of temperature from RT to low temperature, where resistance of the cable decreases gradually until the temperature is close to T_c, resistance of the cable suddenly drops to 0 Ω. The inset of the figure shows the transition region resistance of the cable. The line fully transitioned a 8.8 K, which means the T_c of this sample is 8.8 K. Figure 6.21 shows the I_c measurement result of this Nb-only cable at 4.2 K. It can be seen from the plot the resistance of the cable remains 0 Ω until the current is greater than 0.207 A, which is the I_c of this cable. Critical current density (J_c) of this cable is $6.9\times10^5 A/cm^2$.

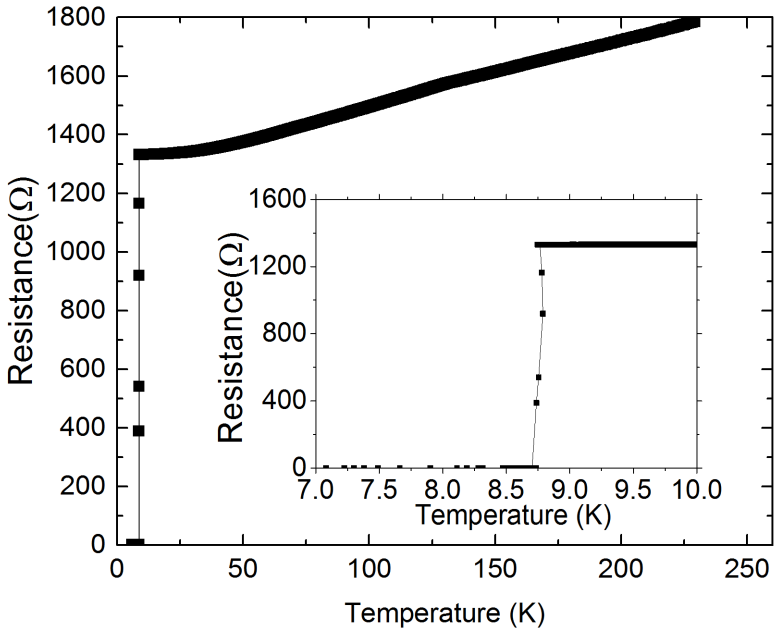

Figure 6.20: Temperature vs. resistance plot of a Nb-only Kapton sample. The inset plot shows the transition region resistance.

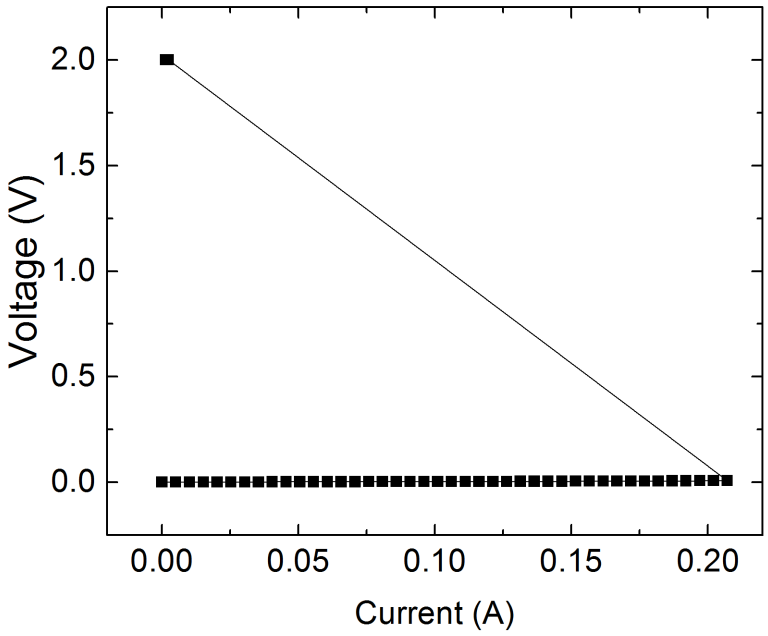

Figure 6.21: Current vs. voltage plot of a Nb-only Kapton cable. Compliance voltage was set to 2 V.

The T_c and I_c results for different layer build-ups are plotted in box chart form, which are shown in Figure 6.22 and Figure 6.23. The median value of T_c of all the material stack-ups was found to be $\sim$ 8.8 K, with a minimum of 8.4 K and a maximum of 9.1 K. I_c of the various layer build-ups exhibited a much larger variation. The highest I_c value was 553 mA for a Ti(10 nm)/Nb/Cu(50 nm) sample, while the lowest was 11 mA for a Ti(10 nm)/Nb sample. The observed T_c and I_c variations are mostly likely due to fabrication tolerances and substrate roughness variation [1], and especially due to isolated defects. Note that RRR (300 K/10 K) of all our material stack-ups on Kapton varied from 2.2 to 2.9.

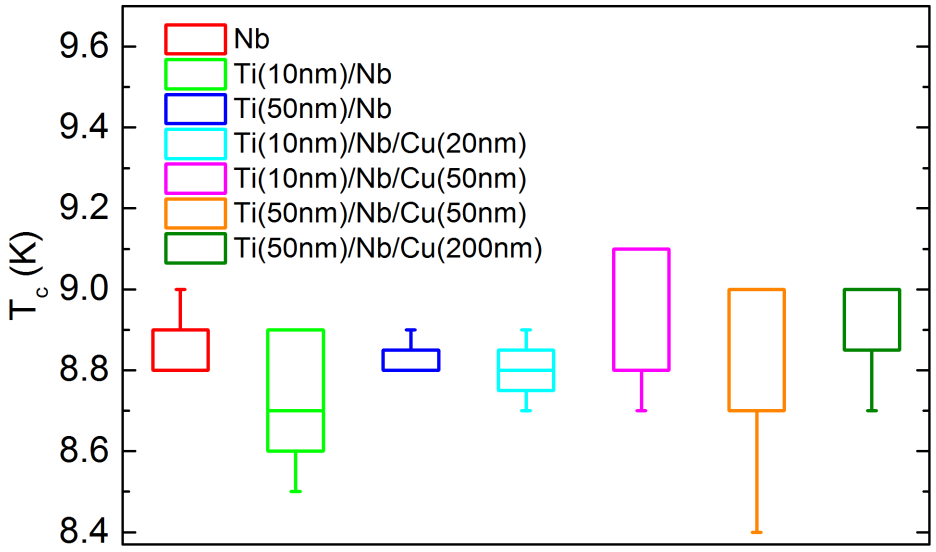

Figure 6.22: Initial T_c measurements of Nb-only cables and Ti/Nb/Cu multilayer cables.

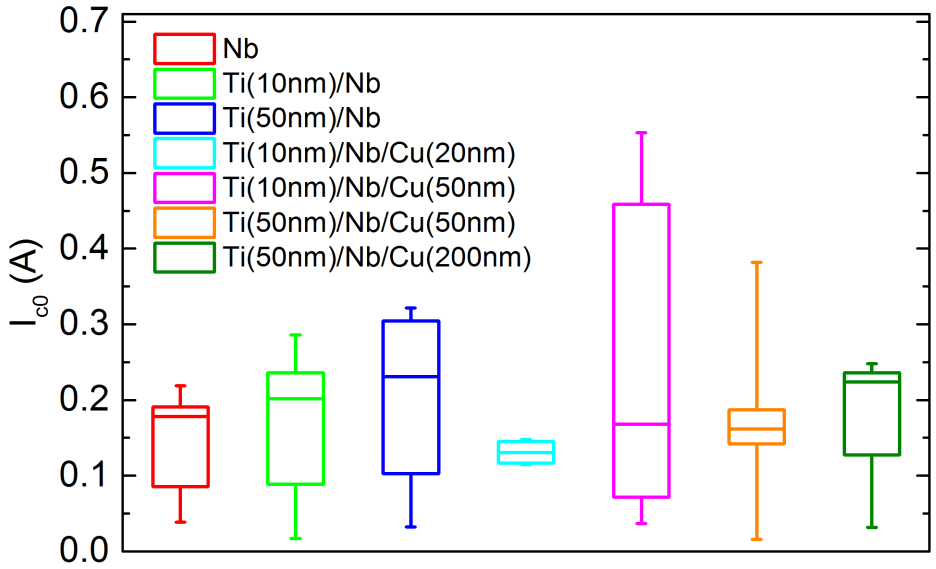

Figure 6.23: Initial I_c measurements of Nb-only cables and Ti/Nb/Cu multilayer cables.

To judge the degradation of I_c, the initial critical currents I_{c0} of pristine samples with different material stack-ups were measured, the results are shown in Figure 6.23. The fatigue tests were divided into tensile and compressive sections according to the direction of the bending of the sample with respect to its stack-up orientation.

For tensile bending-flattening fatigue testing (conductor facing away from cylinder), for each layer construction, multiple samples were tested. The behavior of I_c for different material stack-ups as a function of the number of cycles is summarized using box plots in Figure 6.24. Trends are observable for the normalized I_c, which decreases with an increase in the number of bending-flattening cycles for each material stack-up. From this figure, I can also observe the differences in the normalized I_c among different layer stack-ups. After 50 cycles, the median value of normalized I_c of pure Nb, Ti(10 nm)/Nb and Ti(50 nm)/Nb were 85.4 %, 86.1 % and 91.5 %, respectively. For the samples with a Cu capping layer, the I_c values were relatively stable, especially for the cases of thicker Ti and Cu layers. The median I_c/I_{c0} of Ti(50 nm)/Nb/Cu(200 nm) samples was 8.0 % higher than that of Ti(10 nm)/Nb/Cu(20 nm) samples. When the cycles increased to 150 and 250 cycles, the normalized I_c of pure Nb dropped from 85.4 % to 82.4 % and 67.2 % while that of Ti(50 nm)/Nb/Cu(200 nm) samples only decreased to 99.8 % to 98.8 %. I also observed that, after 50 cycles, Ti(50 nm)/Nb/Cu(50 nm) samples and Ti(50 nm)/Nb/Cu(200 nm) samples had very similar median I_c/I_{c0}. When the number of tensile bending-flattening cycle increased to 150 and 250, the advantage of thicker Cu appears to be more significant. We also note that, generally, the structures with Ti and Cu exhibit less sample-to-sample variation initially and after fatigue stressing.

For compressive fatigue testing (conductor facing cylinder), the behavior of I_c for different layer stack-ups is shown in Figure 6.25. I see from this figure that, after 50 cycles, all layer stack-ups show comparable I_c degradation, which is approximately 10 %. The Ti(50 nm)/Nb/Cu(200 nm) cables are notable exceptions, showing stable I_c. With an increase in cycle number, I_c degradation variations can be found among different cables, but the degradation is less for samples having thicker Ti or Cu layers. After 250 compressive bending-straightening cycles, I_c/I_{c0} of Nb-only cables drops to 72.8 % while that of Ti(50 nm)/Nb/Cu(200 nm) remains stable at 100 %. I also note that significantly more variation in the critical currents is observed for compressive stressing versus tensile stressing.

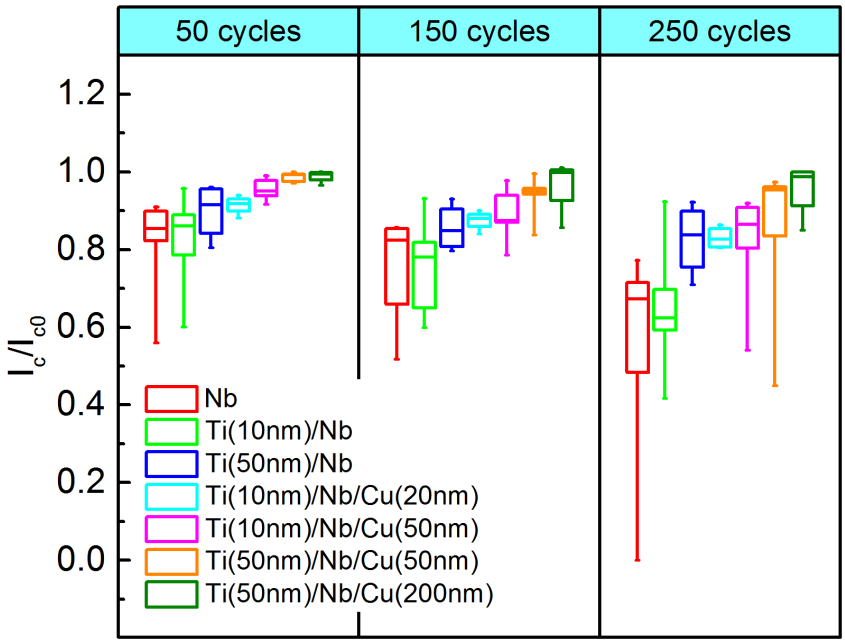

Figure 6.24: Evolution of I_c (normalized by the initial critical current I_{c0}) as a function of the number of tensile bending-flattening fatigue cycles.

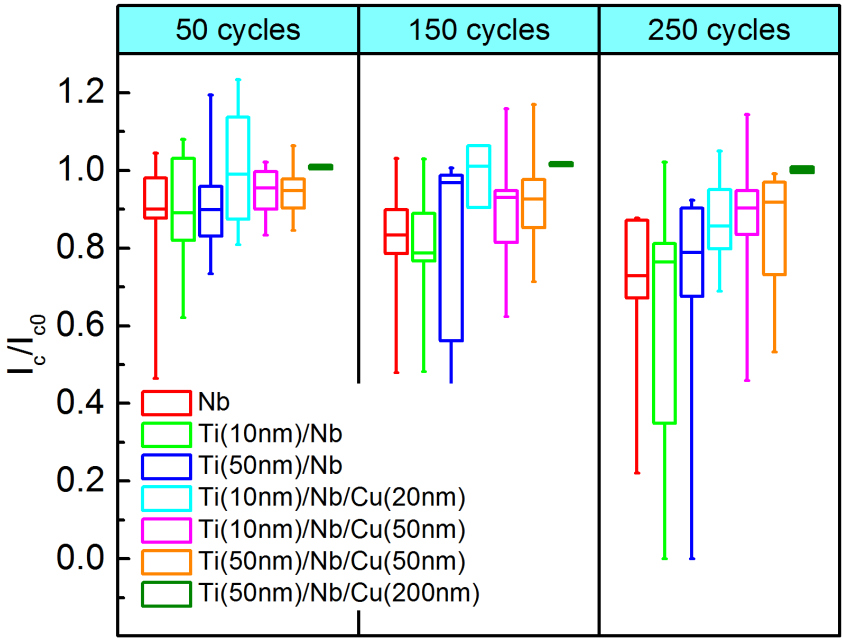

Figure 6.25: The dependence of I_c /I_{c0} on the number of compressive bending-flattening fatigue cycles.

Figure 6.26(a) and Figure 6.26(b) are SEM images of the top (exposed) surface of a Nb-only cable after 250 tensile bending-flattening and 250 compressive bending-flattening fatigue cycles, respectively. No obvious type difference was observed between the crack generated due to tensile fatigue and compressive fatigue. The direction of fatigue cracks are perpendicular to the bending direction and perpendicular to the current transport direction, which affects the current transport and most likely causes the I_c degradation. The progressive I_c reduction can be explained by the accumulation of crack damage on the surface as a result of cyclic bending, leading to crack nucleation and growth. In contrast, the Ti(50 nm)/Nb/Cu(200 nm) cables showed consistent I_c and smooth and continuous surfaces, as shown in Figure 6.27. Ti and Cu, as more ductile materials, seem to help Nb thin films withstand deformation and suppress crack propagation.

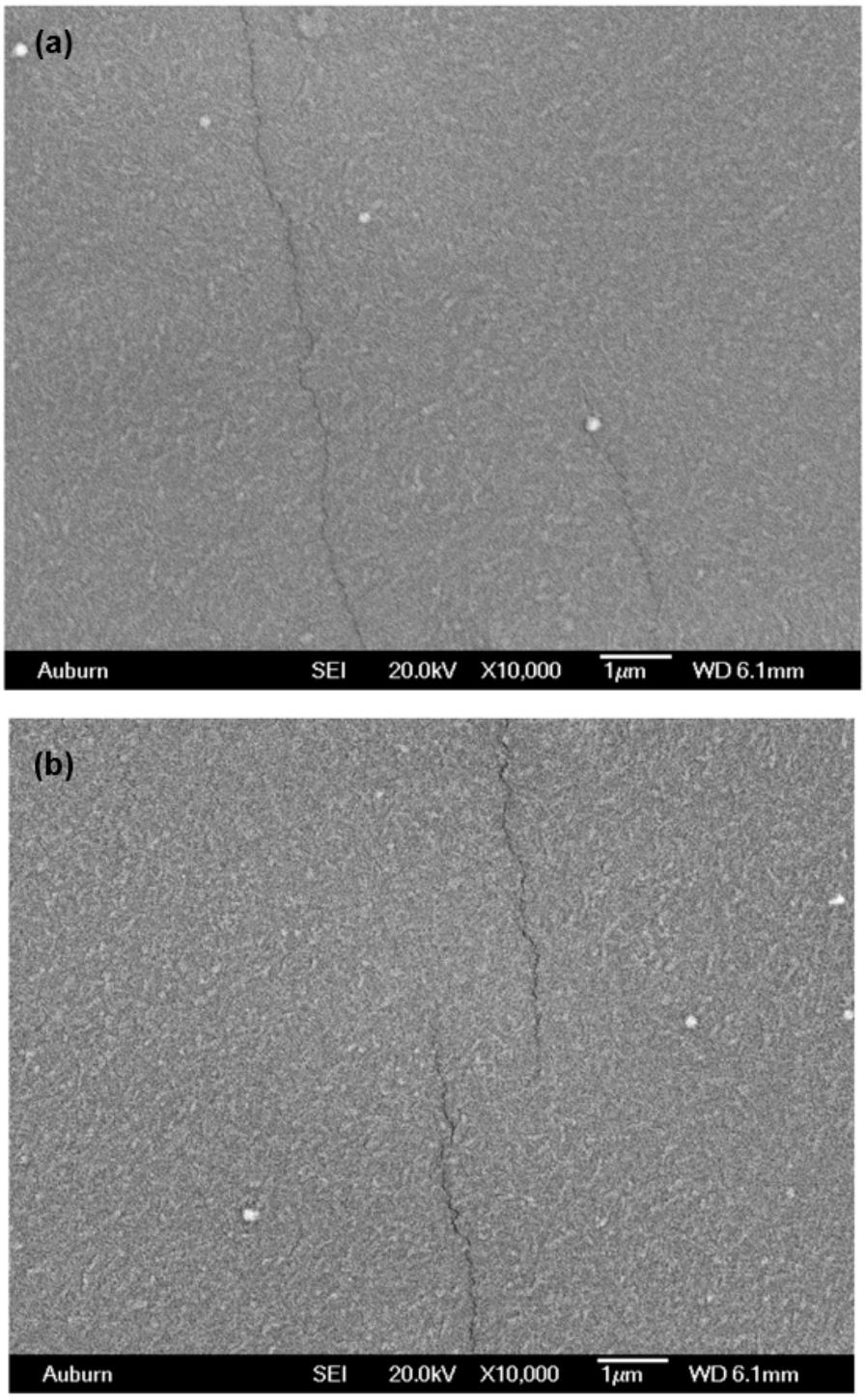

Figure 6.26: SEM images showing cracks on the top (exposed) surface of Nb-only lines on Kapton after (a) 250 tensile bending-flattening fatigue cycles and (b) 250 compressive bending-flattening fatigue cycles.

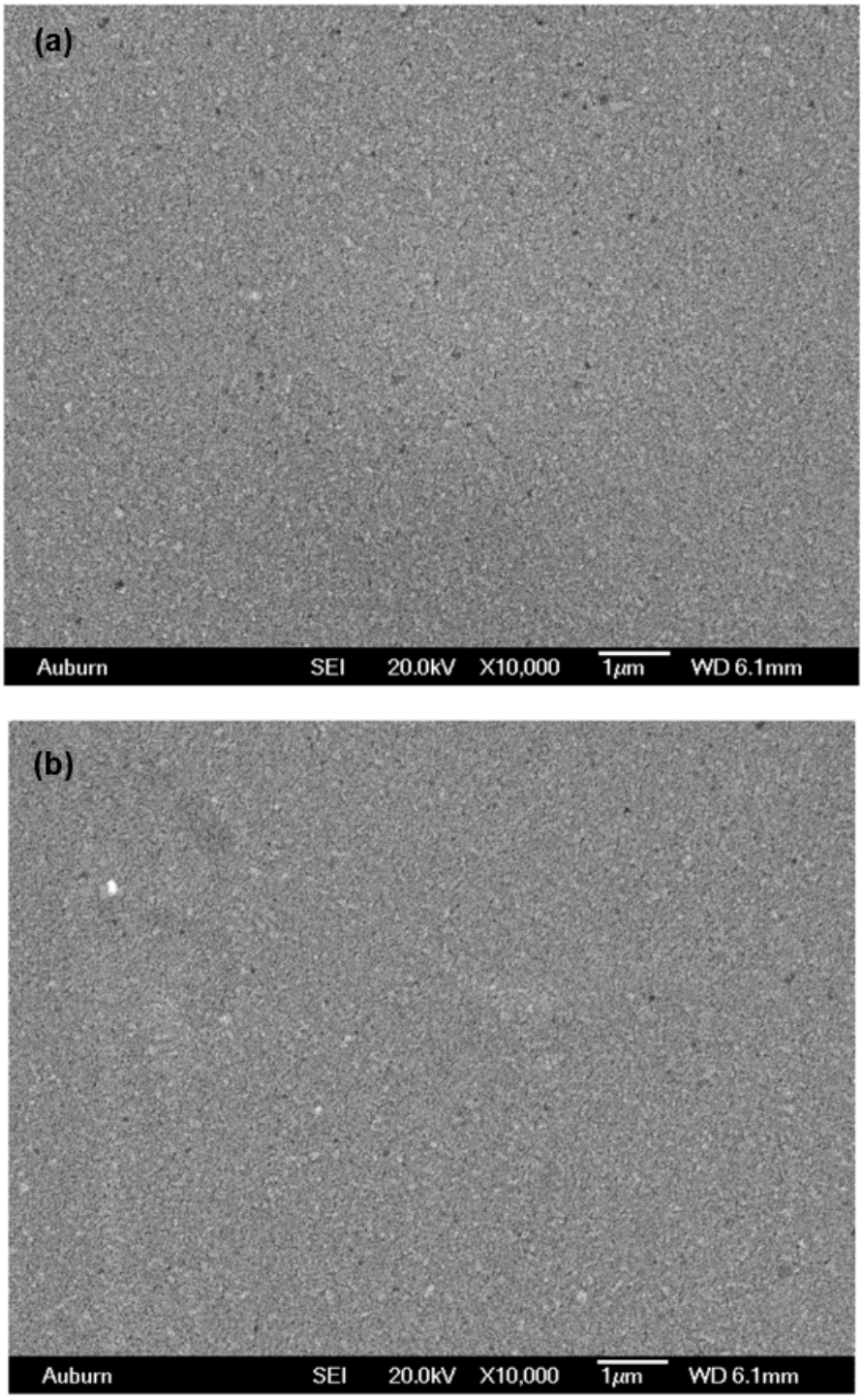

Figure 6.27: SEM images of the top (exposed) surface of Ti(50 nm)/Nb/Cu(200 nm) lines on Kapton after (a) 250 tensile bending-flattening fatigue cycles and (b) 250 compressive bending-flattening fatigue cycles.

In the bending tests, two stack-ups were tested: Nb-only cables and Ti(50 nm)/Nb/Cu (200 nm) cables. The measurement results of the I_c behavior due to tensile and compressive bending of the sample are shown in Figure 6.28 and Figure 6.29, respectively. As shown in both figures, I_c of both material stack-ups decreases when the superconducting film was subjected to stronger stress (i.e., smaller bending radius). However, compared to Nb-only wires, the Ti(50 nm)/Nb/Cu(200 nm) cables exhibited significantly smaller I_c reduction in all the bent sample tests. For example, at the largest curvature, I_c of Ti(50 nm)/Nb/Cu(200 nm) wires remained at 81.7 % in tensile case and 91.1 % in compressive case while those of Nb-only cables are only 27.0 % and 72.1 %, respectively. In addition, for Nb-only samples, sharp I_c degradations were found when the bending radius is smaller than 7.5 mm. I_c/I_{c0} declined significantly from 84.7 % to 55.6 % and 100.2 % to 89.5 % in each bending case. In contrast, for Ti(50 nm)/Nb/Cu(200 nm) cables, with increase in the bending curvature, a lower and more gradual I_c reduction was observed.

The progressive degradation of I_c in Nb-only testing cables with decrease of bending radius was explored further by examining the exposed surfaces. An SEM image of a Nb-only cable after tensile bending testing is shown in Figure 6.30(a). The orientation of the microcracks are parallel to the tape axis, which reflected a compromise between the maximum tensile stresses on the thin film and the fracture resistance of the Nb. No cracks were evident on the top surface of Nb-only cables after compressive bending testing, which is shown in Figure 6.30(b). The I_c degradation may also be due to Nb adhesion issues after compressive bending or crack distribution in longitudinal sections along the cable, which may not be visible on the top surface.

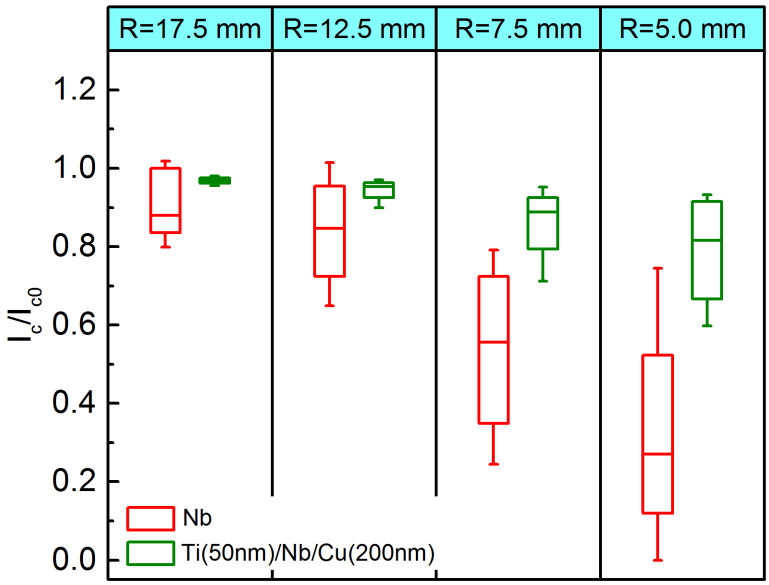

Figure 6.28: I_c/I_{c0} versus bending radius R for Nb and Ti(50 nm)/Nb/Cu(200 nm) samples at 4.2 K in tensile bent sample testing.

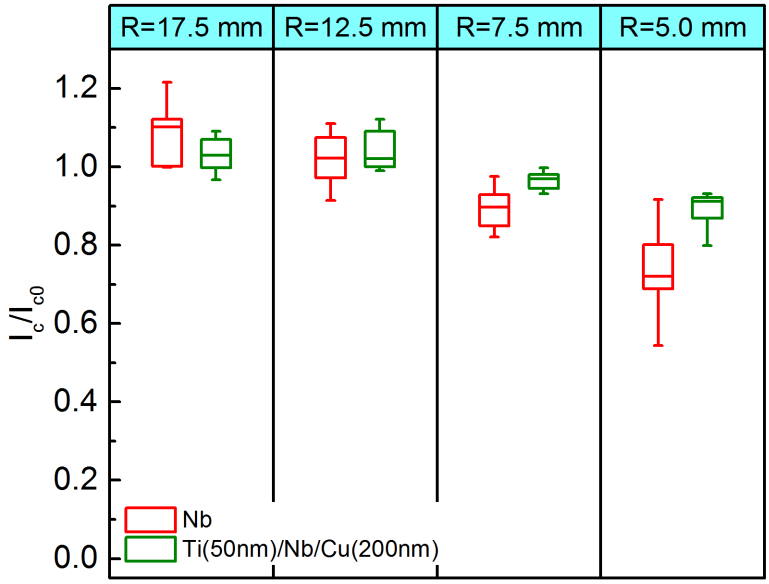

Figure 6.29: I_c/I_{c0} versus R relationship for Nb and Ti(50 nm)/Nb/Cu(200 nm) sample at 4.2 K in compressive bent sample testing.

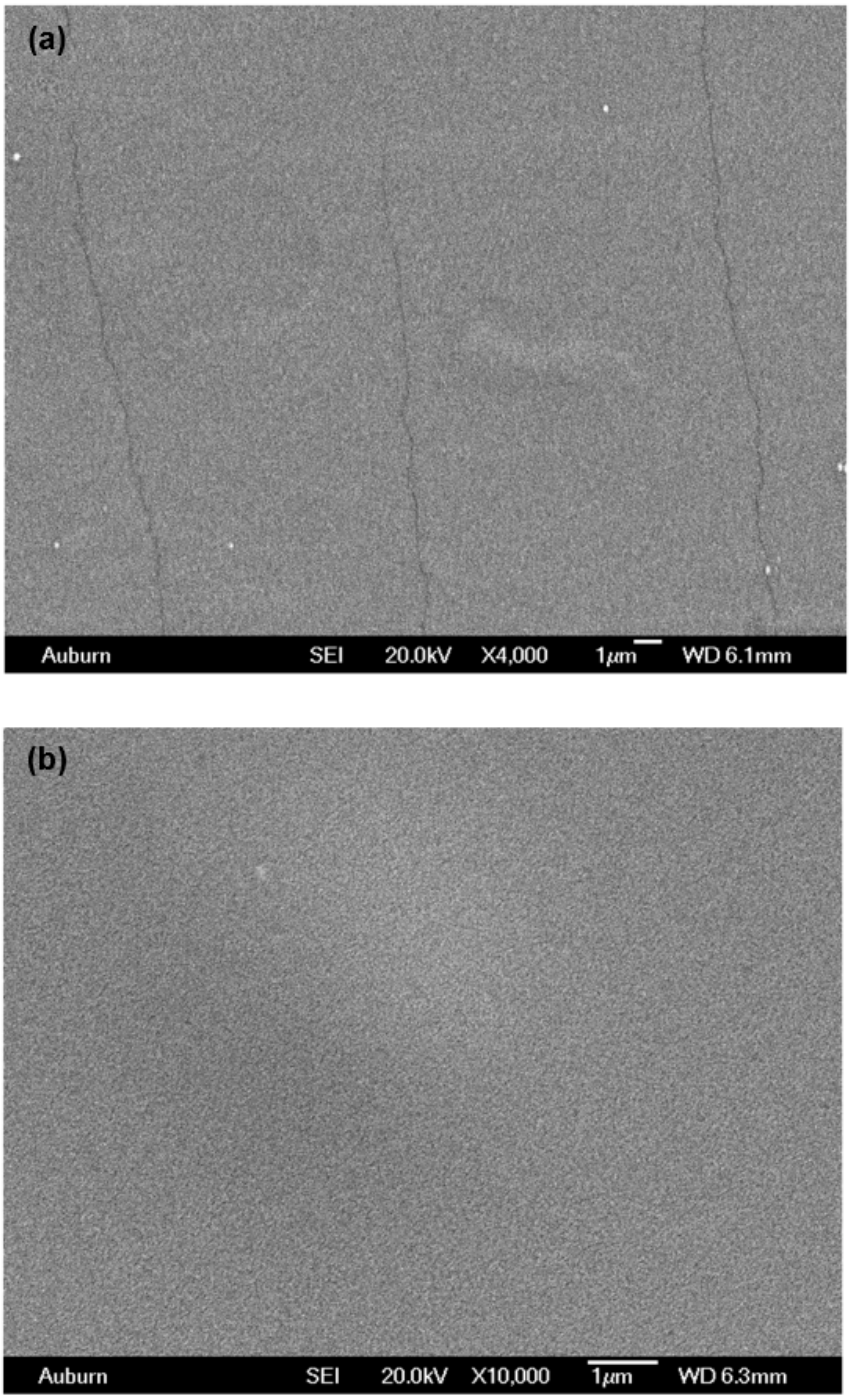

Figure 6.30: SEM images of the surface morphology of Nb-only testing cable after (a) tensile bending test (R = 5 mm) and (b) compressive bending test (R = 5 mm).

6.4 Performance and Reliability of Superconducting Cables Fabricated on Thin-film Polyimide PI-2611

Kapton is a good material to build simple structure, however, it has its limitation to build cable with complex configuration, such as embedded cables. Therefore, I investigated thin-film polyimide to build superconducting flexible cables and fabrication procedures are shown as follows.

250 Å-thick Cr and 2000 Å-thick Al was deposited on a clean Si wafer, as sacrificial layers. PI-2611 polyimide was spun onto the wafer with spin speed of 1700 rpm to yield a 10 µm-thick film, followed by curing at 350 °C in a N_2 environment. A second layer of PI-2611 was then deposited following the same procedure, to achieve a total dielectric thickness of 20 µm for the substrate. For the embedded DC lines, line traces were patterned using conventional photolithography and film lift-off techniques. Before Nb sputter deposition, the chamber was evacuated to a base pressure below 3×10^{-7} torr to ensure Nb quality. After a 2 min in-situ ion milling surface clean, a 250 nm-thick Nb film was sputtered with a power of 1 kW. After the lift-off process, small Kapton tape dots were taped on the pad area, followed by spinning-on different thicknesses of PI-2611 encapsulation layers. The Kapton dots were removed before curing the top PI-2611, in order to create openings for electrical contact. A lower curing temperature of 225 °C was used in order to protect the superconductivity of Nb. Next, samples were released in a neutral sodium chloride solution by applying 0.5 V potential to the Al with a thin layer of photoresist protecting the top surface. Finally, after stripping the protective photoresist layer, samples were ready for testing. The layout detail is shown in Figure 6.31. A fabricated non-embedded Nb/PI (0 µm) DC line and an embedded Nb/PI (4 µm) DC line are shown in Figure 6.32. The opening created by Kapton tape "dots" are highlighted in the red arrows in the figure, these opening region were used to make electric connection from the Nb pads to the pins of the testing board. The line width of the DC cables is 50 µm and line length is 5 cm. Cross sectional SEM images of

non-embedded Nb film and embedded Nb films with 4 µm and 8 µm encapsulation layers are shown in Figure 6.33(a), Figure 6.33(b) and Figure 6.33(c), respectively.

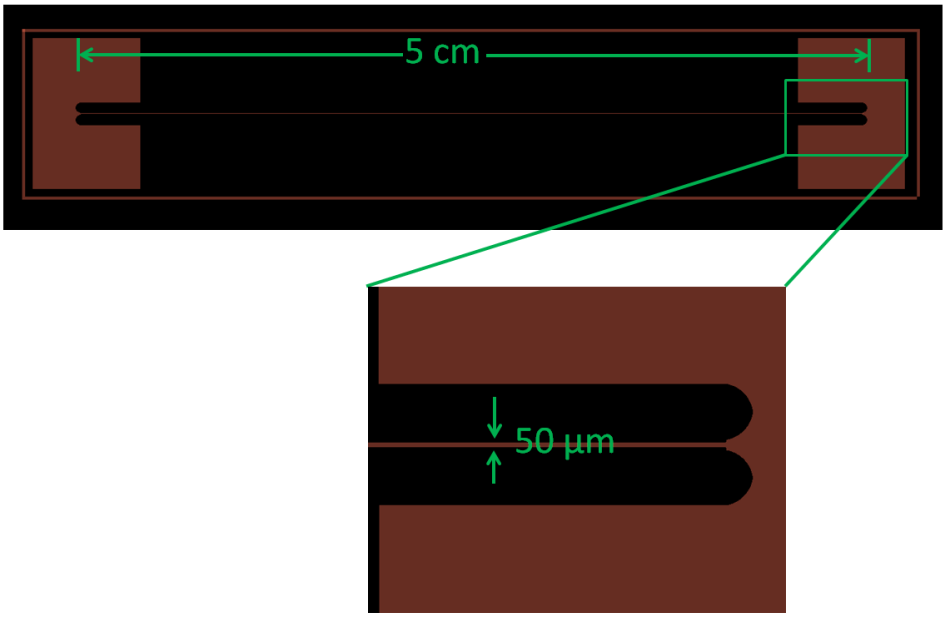

Figure 6.31: Layout of a Nb DC testing cable on PI-2611 polyimide substrate. The zoom-in image shows the line width of the cable is 50 µm.

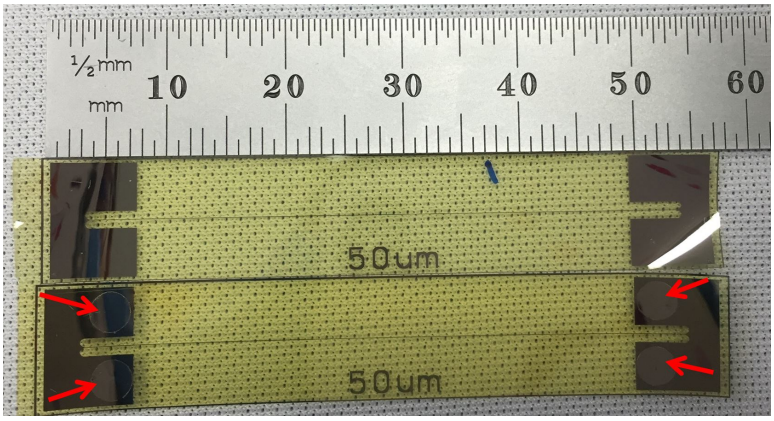

Figure 6.32: Photograph of (top) a Nb/PI (0 µm) DC line test structure and (bottom) a Nb/PI (4 µm) DC line test structure.

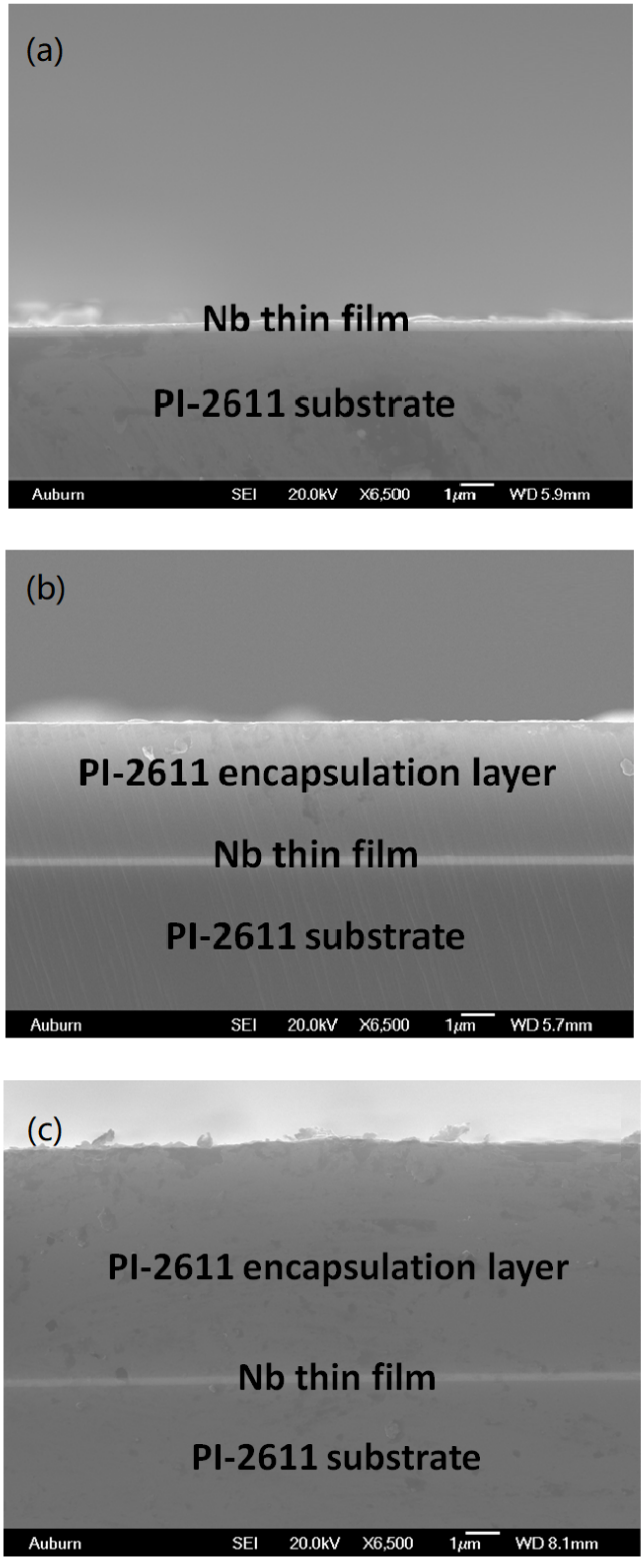

Figure 6.33: Cross-sectional SEM images of (a) Nb/PI (0 µm), Nb/PI (4 µm) and Nb/PI (8 µm) samples.

PI-2611 DC non-embedded and embedded cables with Al/Nb/Al metallization layer were also fabricated. Al layer is 20 nm-thick as a barrier layer between polyimide and Nb layer to protect the Nb superconductivity during encapsulation layer cure process. Al was deposited with a deposition rate of 2 Å/s by electron beam physical deposition before and after Nb-deposition, respectively. Figure 6.34 shows the material stack-up diagram of a Al/Nb/Al embedded DC cable.

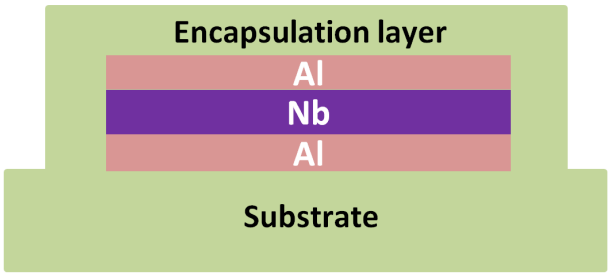

Figure 6.34: Schematic diagram of the cross section view of a Al/Nb/Al embedded DC cable. Note that substrate and encapsulation layer are all made of polyimide PI-2611.

The T_c measurement results of non-embedded and embedded Nb and Al/Nb/Al DC cables are shown in Figure 6.35. It can be seen that non-embedded Nb cables show higher T_c with a median value of $\sim$ 8.8 K. For Nb/PI (4 µm) and Nb/PI (8 µm) Nb embedded cables, slightly lower T_c of $\sim$8.15 K and $\sim$8.1 K, respectively, was observed, which is assumed to be due to degradation of the Nb that results from the PI-2611 encapsulation layer cure process. It can be seen a big improvement of T_c of embedded Al/Nb/Al lines. Non-embedded Al/Nb/Al cables show comparable T_c to non-embedded Nb cable, which is $\sim$8.75 K. By adding Al barrier layer on top and bottom of Nb layer, T_c of embedded Al/Nb/Al cable still stabilized to $\sim$8.7 K, which is $\sim$0.6 K higher than the embedded Nb cables. Also, it can be seen that, for both embedded Nb and embedded Al/Nb/Al cables, the encapsulation layer thickness does not quite affect the T_c values. Figure 6.36 illustrates the I_c measurement

results of non-embedded and embedded Nb and Al/Nb/Al DC cables with various encapsulation layer thickness. Comparable I_c values were found among embedded and non-embedded Nb DC cables, with median values of ~0.2 A. Al/Nb/Al cables show relatively higher I_c, which is ~0.24 A. The reason of higher I_c in embedded cable is possibly due to the cable have better protection in encapsulation layer during the handling and fabrication.

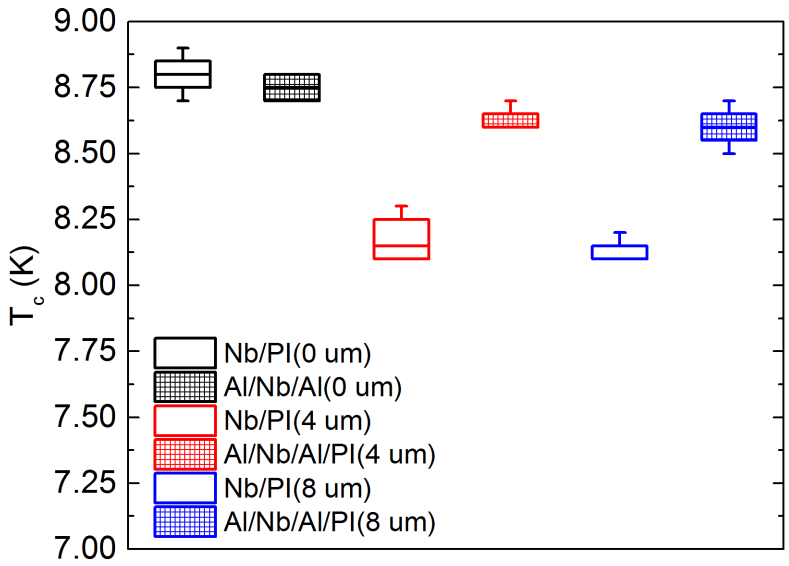

Figure 6.35: T_c measurement results of non-embedded and embedded Nb and Al/Nb/Al DC cables.

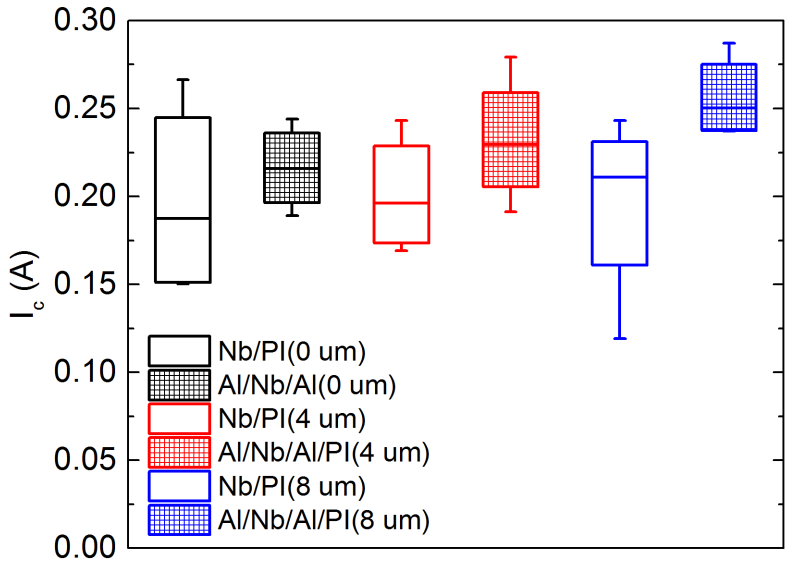

Figure 6.36: I_c measurement results of non-embedded and embedded Nb and Al/Nb/Al DC cables.

For PI-2611 polyimide DC cables, to perform the fatigue test, a custom bending fatigue test fixture was used, which is shown in Figure 6.37. These DC cables were repetitively bent (at RT) around one of the D-shaped blocks with a specific diameter of 12.5 mm, followed by bending to the opposite orientation using the other D-shaped block. Following a specified number of bending cycles, the I_c of the sample was then measured at 4.2 K in a LHe dewar. Depending on the orientation of the superconductor (facing towards or away from the block), the conductor was subjected to either tensile or compressive stress. Fatigue evaluation was done by measuring I_c after a specified number of tensile-compressive bending cycles (100, 300 and 500 cycles) around a fixed radius of curvature for multiple samples of each material stack-up [30].

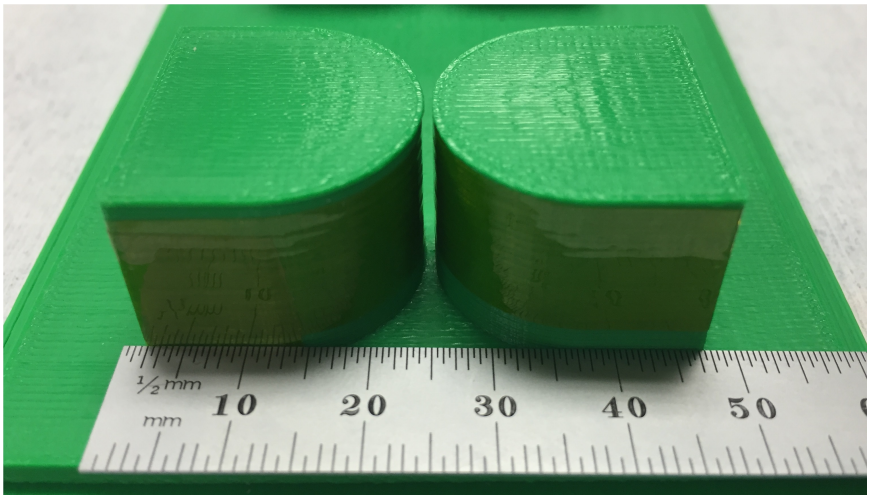

Figure 6.37: Bending fatigue test fixture with D blocks having radii of 12.5 mm.

In order to judge I_c degradation, the behavior of the I_c of pristine DC cables with different material stack-ups was measured and the results have already been presented in Figure 6.36, which served as the reference I_{c0}. The I_c degradation behavior of different material stack-ups as a function of the number of cycles is summarized using box plots in Figure 6.38. The normalized I_c changed as the number of fatigue cycles increased for each material stack-up and there are clear differences in the normalized I_c values at the same number of cycles among the different layer stack-ups. After 100 cycles, the median value of normalized I_c of Nb/PI (0 µm), Nb/PI (4 µm) and Nb/PI (8 µm) were comparable with values of 96.8 %, 96.2 % and 99.1 %, respectively. When the fatigue cycle number increased to 300, the median I_c/I_{c0} of non-embedded Nb cables dropped to 89.8 % and some of the cables had significant I_c reduction, more than 50 % in some cases, as can be seen from the box plot. On the other hand, Nb/PI (4 µm) and Nb/PI (8 µm) cables exhibited I_c/I_{c0} values of 95.2 % and 94.9 %, respectively, with relatively small sample-to-sample variation for the same number of stress cycles. After 500 fatigue cycles, the median of normalized I_c of non-embedded Nb samples further decreased to 73.5 %. On the contrary, values for the cables with 4 µm and 8 µm encapsulation layers stabilized at 93.7 % and 92.5 %, respectively. From this experiment, the advantage of using a PI-2611 encapsulation layer to help protect against

bending fatigue is clear, while the difference between thinner or thicker encapsulation layers is not clear from the current experiments.

As to the the impact of Al interficial layer, comparing non-embedded Al/Nb/Al cables with non-embedded Nb cables, the former showed more reliable performance and less sample-to-sample variation after different number of fatigue cycles. For embedded Al/Nb/Al cables, relatively comparable results can be found with embedded Nb cables with the same thickness of encapsulation layer and I_c/I_{c0} of these cables are approximately 100 %.

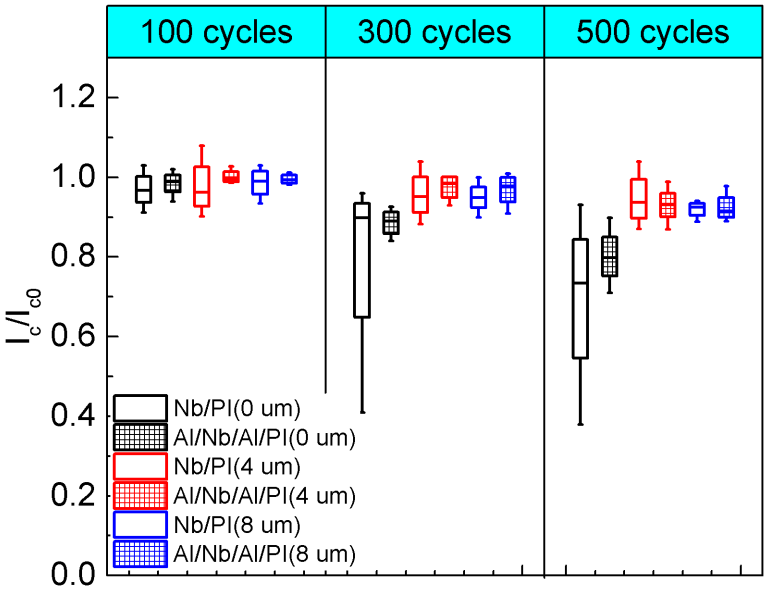

Figure 6.38: Evolution of the I_c (normalized by the initial I_{c0}) as a function of the number of fatigue cycles.

6.5 Summary

In this chapter, the superconducting and mechanical reliability performance were investigated for Nb-only cables and Ti/Nb/Cu multilayer cables on flexible Kapton substrates for samples subjected to fatigue cycles and bent sample testing at cryogenic temperatures. T_c of Nb and different stack-ups of Ti/Nb/Cu multilayer cables were comparable (approximately

8.8 K). RRR of all tested layer stacks varied from ∼ 2.2 to 2.9. In the fatigue tests, with an increase of the thickness of Ti adhesion layer and Cu capping layer, I_c degradation was significantly reduced. With 50 nm Ti and 200 nm Cu, I_c remains stable after 250 tensile and compressive bending-flattening cycles, while I_c degradation of Nb-only is 32.8 % and 27.2 % for tensile and compressive cases, respectively. In the bent sample tests, where the sample is maintained in a bent configuration during the test, the I_c degradation due to tensile stress is worse compared to compressive stress. Ti(50 nm)/Nb/Cu(200 nm) cables can sustain tight curvatures with less I_c degradation than the Nb-only cables. Generation of microcracks on the top surface appears to be the primary reason for the I_c degradation, and the use of Ti and Cu can effectively enhance the mechanical performance of Nb superconducting cable by improving the film's ability to withstand bending stresses or counteract resultant damage to Nb.

Superconducting properties (T_c and I_c) and mechanical reliability performance (fatigue behavior) were investigated for non-embedded and embedded Nb and Al/Nb/Al DC cables on flexible PI-2611 thin film substrate. A slightly lower Tc value of ∼8.2 K was found for Nb embedded cables compared to non-embedded Nb DC testing lines with a Tc of ∼8.8 K. I_c of embedded DC cables was comparable with that for non-embedded ones, with values of ∼0.2 A. Embedded Nb DC cables showed degradation of I_c less than 5 %, while that of non-embedded DC cables was more than 26.5 % after 500 fatigue cycles. By adding a 20 nm Al cladding layer on the top and the bottom of Nb layer, T_c of embedded Al/Nb/Al cables increased to ∼8.7. A improved I_c was found on Al/Nb/Al cables. Also, non-embedded Al/Nb/Al cables showed slight better mechanical reliability than non-embedded Nb cables.

While clearly beneficial for mechanical reliability, it should be noted that normal metal cladding layers may compromise the performance of superconducting cables in other areas. Specifically, RF losses may be increased, and the cable's axial thermal conductivity may be

increased (important when spanning different temperatures, such as in a dilution refrigerator). These trade-offs need to be carefully considered when designing future superconducting electronic systems.

Bibliography

[1] van Weers, G. Kunkel, M. Lindeman and M. Leeman, "Niobium flex cable for low temperature high density interconnects," *Cryogenics*, vol. 55, pp. 14, 2013.

[2] D. B. Tuckerman, M. C. Hamilton, D. J. Reilly, R. Bai, G. A. Hernandez, J. M. Hornibrook, J. A. Sellers and C. D. Ellis, "Flexible superconducting Nb transmission lines on thin film polyimide for quantum computing applications," *Superconductor Science and Technology*, vol. 29, no. 8, p. 084007, 2016.

[3] P. McGarey, H. Mani, C. Wheeler and C. Groppi, "A 16 Channel Flex Circuit for Cryogenic Microwave Signal Transmission," *in SPIEA stronomical Telescopes+ Instrumentation*, pp. 91532F91532F, 2014.

[4] T. Tighe, G. Akerling and A. Smith, "Cryogenic packaging for multi-GHz electronics," *IEEE Transactions on Applied Superconductivity*, vol. 9, no. 2, pp. 31733176, 1999.

[5] C. S. Yung and B. H. Moeckly, "Magnesium diboride flexible flat cables for cryogenic electronics," *IEEE Transactions on Applied Superconductivity*, vol. 21, no. 3, pp. 107110, 2011.

[6] K. Ishio, K. Kikuchi, J. Kusano, M. Mizumoto, K. Mukugi, A. Naito, N. Ouchi, Y. Tsuchiya and K. Saito, "Fracture toughness and mechanical properties of pure niobium and welded joints for superconducting cavities at 4K," in *Proc.9th Workshop RF Supercond.*, pp. 319323, 1999.

[7] N. Mara, D. Bhattacharyya, R. Hoagland and A. Misra, "Tensile behavior of 40nm Cu/Nb nanoscale multilayers," *Scripta Materialia*, vol. 58, no. 10, pp. 874877, 2008.

[8] L. Thilly, F. Lecouturier and J. Von Stebut, "Size-induced enhanced mechanical properties of nanocomposite copper/niobium wires: nanoindentation study," *Acta Materialia*, vol. 50, no. 20, pp. 50495065, 2002.

[9] H. Shin, M. Dedicatoria, A. Gorospe, T. Suwa, H. Oguro and S. Awaji, "Reversible strain response of critical current in differently processed GdBCO coated conductor tapes under magnetic fields," *IEEE Transactions on Applied Superconductivity*, vol. 23, no. 3, pp. 84004048400404, 2013.

[10] O. M. Ivanyuta, O. V. Prokopenko, V. M. Raksha, and A. M. Klushin, "Microwave detection using Josephson junction arrays integrated in a resonator," *Physica Status Solidi(c)* vol. 2, no. 5, pp. 16881691, 2005.

[11] K. Konstantopoulou, M. Sarazin, X. Granados, J. Pastor and X. Obradors, "Effect of the axial stress and the magnetic field on the critical current and the electric resistance of the joints between HTS coated conductors" *Superconductor Science and Technology*, vol. 28, no. 6, p. 064001, 2015.

[12] M. Sugano, S. Machiya, M. Sato, T. Koganezawa, K. Shikimachi, N. Hirano and S. Nagaya, "Bending strain analysis considering a shift of the neutral axis for YBCO coated conductors with and without a Cu stabilizing layer," *Superconductor Science and Technology*, vol. 24, no. 7, p. 075019, 2011.

[13] M. Polikarpova, P. Lukyanov, I. Abdyukhanov, V. Pantsyrny, A. Vorobyeva, N. Khlebova, S. Sudyev, A. Shikov and V. Guryev, "Bending strain effects on the critical current in Cu and CuNbstabilized YBCO-coated conductor tape," *IEEE Transactions on Applied Superconductivity*, vol. 24, no. 3, pp. 14, 2014.

[14] J. Hornibrook, J. Colless, A. Mahoney, X. Croot, S. Blanvillain, H. Lu, A. Gossard and D. Reilly, "Frequency multiplexing for readout of spin qubits," *Applied Physics Letters*, vol. 104, no. 10, p. 103108, 2014.

[15] C. Macklin, K. OBrien, D. Hover, M. Schwartz, V. Bolkhovsky, X. Zhang, W. Oliver and I. Siddiqi, "A nearquantum-limited Josephson traveling-wave parametric amplifier," *Science*, vol. 350, no. 6258, pp. 307310, 2015.

[16] R. J. Webber, J. Delmas and B. H. Moeckly, "Ultra-low heat leak YBCO superconducting leads for cryoelectronic applications," *IEEE Transactions on Applied Superconductivity*, vol. 19, no. 3, pp. 9991002, 2009.

[17] C. G. Pappas, "Towards a 100 000 TES Focal Plane Array: A Robust, High-Density, Superconducting Cable Interface," *IEEE Transactions on Applied Superconductivity*, vol. 25, no. 3, pp. 15, 2015.

[18] M. Bruijn, A. van der Linden, M. Ridder and H. van Weers, "FDM readout assembly with flexible, superconducting connection to cryogenic kilo-pixel TES detectors," *Journal of Low Temperature Physics*, vol. 184, no. 1-2, pp. 369373, 2016.

[19] F. Watson and G. Castro, "A review of high-temperature electronics technology and applications," *Journal of Materials Science: Materials in Electronics*, vol. 26, no. 12, pp. 9226-9235, 2015.

[20] S. Zou and M. C. Hamilton, "Flexible non-volatile Cu/Cu_x O/Ag ReRAM memory devices fabricated using ink-jet printing technology," *Electronic Components and Technology Conference (ECTC), IEEE 64th*, pp. 441-446, 2014.

[21] M. Grag and J. K. Quamara, "Electrical conduction behaviour of high energy ion irradiated Kapton-H polyimide film," *Nuclear Instruments and Methods in Physics Research Section B: Beam Interactions with Materials and Atoms*, vol. 179, no. 3, pp. 389-396, 2001.

[22] S. Zou and M. C. Hamilton, "Ink-jet printed Cu/Cu_x O/Ag ReRAM memory devices fabricated on flexible substrate," *MRS Online Proceedings Library Archive*, vol. 1692, 2014.

[23] E. R. Muller and F. Mast, "A new metal resistor bolometer for measuring vacuum ultraviolet and soft x radiation," *Journal of applied physics*, vol. 55, no. 7, pp. 2635-2641, 1984.

[24] S. Zou, P. Xu and M. C. Hamilton, "Resistive switching characteristics in printed Cu/CuO/(AgO)/Ag memristors," *Electronics Letters*, vol. 49, no. 13, pp. 829-830, 2013.

[25] S. Zou, "Flexible Nonvolatile Cu/CuxO/Ag ReRAM Fabricated Using Ink-Jet Printing Technology," *Auburn University PhD dissertation*, 2014.

[26] R. Bai, "Superconducting Resonators on Thin Film Flexible Substrates," *PhD thesis, Auburn University*, 2016.

[27] R. Bai, G. A. Hernandez, Y. Cao, J. A. Sellers, C. D. Ellis, D. B. Tuckerman and M. C.Hamilton, "Cryogenic microwave characterization of Kapton polyimide using superconducting resonators," in *Microwave Symposium (IMS), 2016 IEEE MTT-S International*, pp. 14, IEEE, 2016.

[28] J. Liu, J. Li, T. Li, T. Li, W. Wu and W. Chen, "Study of stress and morphology of superconducting niobium thin films," *IEEE Transactions on Applied Superconductivity*, vol. 19, no. 3, pp. 245248, 2009.

[29] S. Zou, R. Bai, G. A. Hernandez, V. Gupta, Y. Cao, J. A. Sellers, C. D. Ellis, D. B. Tuckerman, and M. C. Hamilton, "Influence of fatigue and bending strain on critical currents of niobium superconducting flexible cables containing Ti and Cu interfacial layers," *IEEE Transactions on Applied Superconductivity*, vol. 27, no. 4, pp. 1-5, 2017.

[30] S. Zou, Y. Cao, R. Bai, G. A. Hernandez, V. Gupta, J. A. Sellers, C. D. Ellis, D. B. Tuckerman, and M. C. Hamilton, "Embedded Niobium Using PI-2611 for Superconducting Flexible Cables," *MRS Advances*, pp. 1-6, 2017.

Chapter 7

Summary and Conclusions

The design, fabrication procedures and measurement results of Nb-based flexible superconducting microstrip transmission line resonators fabricated using thin-film polyimide HD-4110 were presented, including both non-embedded and embedded versions. These resonators were used to characterize the microwave dielectric loss tangent of 20-µm thick polyimide HD-4110 at deep cryogenic temperatures. High Q, up to 21040, at 1.2 K in the frequency range of 2-21 GHz for non-embedded resonators was observed, indicating that the dielectric loss tangent can be less than 5×10^{-5}. Embedded resonators with an additional 20-µm thick encapsulation layer also exhibited Q values as high as ∼19200. Dielectric and conductor (quasiparticle) loss were compared between the two types of resonators. Using a similar method, embedded and non-embedded Nb superconducting microstrip transmission line resonators based on thin-film polyimide PI-2611 was characterized. The impact of different thickness of encapsulation layer and temperature on the RF performance of resonators was investigated. With an increase in temperature, loss due to superconductor quasi-particles and loss due to the PI-2611 dielectric both increase. Furthermore, at the same temperature, with increase of the thickness of the encapsulation layer, the dielectric loss increases slightly. Also, a proportional relationship is observed between superconductor loss and embedding layer thickness, and this may be due to higher availability of degrading substances (for example acids and/or H_2O) in the thicker embedding layer that arise during the curing of the embedding layer and can lead to degradation of the superconducting properties of the Nb.

Cu-based DC cables and connectors were designed, fabricated and measured. Four-wire resistance measurement at RT was performed and the resistance of the intact cables

and reconnected cables were compared. An extra low contact resistance was achieved using new connection method. Cu-based microstrip transmission lines and microwave connectors were also fabricated. RF/microwave performance of the intact and reconnected microstrips at different temperatures (RT, 77 K and 4.2 K) were tested and compared. RF cables with different length and different numbers of reconnections were also measured. The split microstrip reconnected using the new connector exhibited very comparable RF performance as the intact cable, which indicated the glass connector introduced very limited contact resistance and good impedance matching with the cable.

Fabrication processes, assembly and characterization of Nb microstrip samples with Nb-based microwave connectors was demonstrated. A simulation model that provides the RF performance of microstrip-to-microstrip interconnection at 4.2 K was successfully implemented and matched measurement results very well. The new cable-to-cable connection approach showed an insertion loss < 0.12 dB and a return loss > 15 dB from near to DC up to 14 GHz. Electrical contact resistance using the microwave connector is as low as 15 mΩ between two cables. Encouraging thermal reliability performance and re-assembly reliability performance was observed on reconnected microstrip parts. These results provide design guidance for building flexible low-loss thin-film superconducting microwave interconnects and connectors.

In addition, superconducting and mechanical reliability performance for Nb-only cables and Ti/Nb/Cu multilayer cables on flexible Kapton substrates for samples subjected to fatigue cycles and bent sample testing at cryogenic temperatures was investigated. T_c of Nb and different stack-ups of Ti/Nb/Cu multilayer cables were comparable (approximately 8.8 K) and RRR of all tested layer stacks varied from $\sim$2.2 to 2.9. Fatigue test and in-situ bending test to these cable with different material stack-ups were performed. In the fatigue tests, with an increase of the thickness of Ti adhesion layer and Cu capping layer, I_c degradation was significantly reduced. With 50 nm Ti and 200 nm Cu, I_c remains stable after 250 tensile and compressive bending-flattening cycles, while I_c degradation of Nb-only

is 32.8 % and 27.2 % for tensile and compressive cases,respectively. In the bent sample tests, where the sample is maintained in a bent configuration during the test, the I_c degradation due to tensile stress is worse compared to compressive stress. Ti(50 nm)/Nb/Cu(200 nm) cables can sustain tight curvatures with less I_c degradation than the Nb-only cables. To explore the reason causing I_c degradation, failure analysis was conducted using SEM. The generation of microcracks on the top surface appears to be the primary reason for the I_c degradation, and the use of Ti and Cu can effectively enhance the mechanical performance of Nb superconducting cable by improving the films ability to withstand bending stresses or counteract resultant damage to Nb.

Finally, superconducting properties (T_c and I_c)and mechanical reliability performance (fatigue behavior) for embedded Nb DC cables on flexible PI-2611 thin film substrate was studied. A slightly lower T_c value of $\sim$ 8.2 K was found for Nb embedded cables compared to non-embedded Nb DC testing lines with a T_c of $\sim$8.8 K. I_c of embedded DC cables was comparable with that for non-embedded ones, with values of $\sim$0.2 A. The use of a properly-cured PI-2611 encapsulation layer can effectively enhance the mechanical reliability performance (i.e. bending fatigue behavior) of Nb superconducting cables. Embedded Nb DC cables showed degradation of I_c less than 5 %, while that of non-embedded DC cables was more than 26.5 % after 500 fatigue cycles. These results provide useful information for future generations of superconducting cables fabricated on thin film substrates in embedded or multi-layer configurations.

Chapter 8

Future Work

Based on the characterization results and analysis presented in this dissertation, the continuation of this work can branch into several directions that will further demonstrate the potential of flexible superconducting microwave interconnects and connectors.

- Embedded and non-embedded resonators fabricated on HD-4110 polyimide was investigated. But the superconducting properties and mechanical reliability of this material stack-up has not been evaluated. Therefore, creating and characterizing embedded and non-embedded DC cables based on thin-film polyimide HD-4110 would provide useful information for this type of interconnects.

- A significant effort should also be made to focus on RF/microwave measurement of stripline transmission lines. Study of cross talk and isolation performance on stripline cable with different trace pitch and pinning vias would be important for building high-density interconnects.

- For the current microwave connectors, a bulky aluminum clamp fixture was used to clamp and assembly the whole structure. A significant effort should be made to focus on the development of a small and lightweight clamp fixture with convenient assembly, which would be more practical and useful in a real working environment.

- Development of automatic fatigue test and bending test fixture is another improvement should be made in this work. Fatigue test and bending test performed by standard machine would able to minimized the errors and uncertainty bought by the experimenters, which would enhance the accuracy and credibility for this study. Also, with

automatic mechanical test fixture, testing cable to completely failure and studying the lifetime of cable with different material stack-ups would be easier and practical. This would be helpful for choosing the most reliable material stack-up.

Appendices

Appendix A

Fabrication Travelers

Step #	Process	Parameters
PI-2611 Polyimide Deposition		
1	Release layer	(1) 2 min of ion milling at 1 kW (2) 500 ÅCr/ 2000 ÅAl
2	Dehydration bake	120 °C for 30 min in oven
3	Adhesion promoter	VM652 Spin speed (1) 500 rpm for 5 s, Acc.=500 rpm/s, (2) 3000 rpm, Acc.=1000 rpm/s, time=30s
4	Soft bake	120 °C for 60 s on hot plate
5	Polyimide spin (PI-2611)	(1) 500 rpm, Acc.=500 rpm/s, time=5s, (2) 1600 rpm Acc.=1000 rpm/s, time=30s
6	Soft bake	hotplate bake at 120 °C, time=5 min.
7	Cure	(1) 90 °C, 30 min ramp at 10 C/min,(1hr) (2) 120 °C, 30 min, ramp at 10 °C/min, (1hr) (3) 350 °C, 60 min ramp at 20 °C/min, (3hr) (4) Cool back to R.T in N_2
8	Plasma	200 W for 30 s
9	Repeat step #4-9	
Signal Line Definition		
10	Dehydration bake	120 °C for 30 min in oven
11	PR definition	PR: AZ 9245 (1) 1700 rpm, for 5 s, Acc.=500 rpm/s (2) 2200 rpm, Acc.= 1000 rpm/s, Time=25 s
12	Soft bake	110 °C on hot plate for 90 s
13	Mask alignment	Exposure time: 40 s Alignment gap: 30 µm
14	Development	(1) Developer. 1: 3 developer 100 mL AZ400K: 300 mL DI H_2O (2) 2 min in developer (3) DI water rinse followed N_2 dry
15	Nb deposition	(1) 2 min of ion milling (b) Power= 1 kW/6.1 mTorr/sputtering time=30 min
16	Lift-off	(1) Rinse in acetone/methanol/IPA (2) Rinse in DI water for 2 min (3) N_2 dry.
Under Bump Metallization		
17	Dehydration bake	120 °C for 30 min in oven
18	PR definition	PR: AZ 9245 (1) 1700 rpm, for 5 s, Acc.=500 rpm/s (2) 2200 rpm, Acc.= 1000 rpm/s, Time=25 s
19	Soft bake	110 °C on hot plate for 90 s
20	Mask alignment	Exposure time: 40 s Alignment gap: 30 µm
21	Development	(1) Developer. 1: 3 developer 100 mL AZ400K: 300 mL DI H_2O (2) 2 min in developer (3) DI water rinse followed N_2 Dry

Table A.1: Traveler of Nb Microstrip Resonators Fabricated on PI-2611 Polyimide 1/2

Step #	Process	Parameters
22	UBM	(1) 2 min of ion milling at 1 kW. (2) Ti: 500 Å(2 Å/s), Cu: 5000 Å(2 Å/s), Au: 100 Å(2 Å/s)
23	Lift-off	(1) Rinse in acetone/methanol/IPA (2) Rinse in DI water for 2 min (3) N_2 dry.
Release sample		
24	Spin coat PR	PR: AZ 9245 (1) 1700 rpm, for 5 s, Acc.=500 rpm/s (2) 2200 rpm, Acc.= 1000 rpm/s, time=25 s
25	Soft bake	110 °C on hot plate for 90 s
26	Dice	Dice wafers with diamond blade into individual samples
27	NaCl Solution	(1) 2M (Moles/L) solution of NaCl based on H_2O (2) Mix 117 g NaCl in 1 L DI water with stir bar.
28	Sample Release	(1) Connect ground to platinized titanium anode mesh (2) Apply +0.6 V to the sample
29	PR Strip	(1) Rinse in acetone/methanol/IPA (2) Rinse in DI water for 2 min (3) N_2 dry
Ground Plane Deposition		
30	Sample mount	Mount sample onto a support wafer with the backside exposed
31	Nb deposition	(1) 2 s of ion milling (2) Power= 1 kW/6.1 mTorr/sputtering time=30 min

Table A.2: Traveler of Nb Microstrip Resonators Fabricated on PI-2611 Polyimide 2/2

Step #	Process	Parameters
HD-4110 Polyimide Deposition		
1	Release layer	(1) 2 min of ion milling at 1 kW (2) 500 / 2000 ÅAl
2	Dehydration bake	120 °C for 30 min in oven
3	Polyimide spin (HD-4110)	(1) 500 rpm, Acc.=500 rpm/s, time=5s, (2) 1700 rpm Acc.=1000 rpm/s, time=30s
4	Soft bake	hotplate bake at (1) 90 °C, time=3 min (2) 110 °C, time=3 min
5	Cure	(1) 90 °C, 30 min ramp at 10 °C/min,(1hr) (2) 120 °C, 30 min, ramp at 10 °C/min (1hr) (3) 375 °C, 60 min ramp at 20 °C/min (3hr) (4) Cool back to R.T in N_2
Signal Line Definition		
6	Dehydration bake	120 °C for 30 min in oven
7	PR definition	PR: AZ 9245 (1) 1700 rpm, for 5 s, Acc.=500 rpm/s (2) 2200 rpm, Acc.= 1000 rpm/s, time=25 s
8	Soft bake	110 °C on hot plate for 90 s
9	Mask alignment	Exposure time: 40 s Alignment gap: 30 µm
10	Development	(1) Developer. 1: 3 developer, 100 mL AZ400K: 300 mL DI H_2O (2) 2 min in developer (3) DI water rinse followed N_2 dry
11	Nb deposition	(1) 2 min of ion milling (2) Power= 1 kW/4 mTorr/sputtering time=30 min
12	Lift-off	(1) Rinse in acetone/methanol/IPA (2) Rinse in DI water for 2 min (3) N_2 dry.
Under Bump Metallization		
13	Dehydration bake	120 °C for 30 min in oven
14	PR definition	PR: AZ 9245 (1) 1700 rpm, for 5 s, Acc.=500 rpm/s (2) 2200 rpm, Acc.= 1000 rpm/s, time=25 s
15	Soft bake	110 °C on hot plate for 90 s
16	Mask alignment	Exposure time: 40 s Alignment gap: 30 µm
17	Development	(1) Developer. 1: 3 developer, 100 mL AZ400K: 300 mL DI H_2O (2) 2 min in developer (3) DI water rinse followed N_2 dry

Table A.3: Traveler of Nb Microstrip Resonators Fabricated on HD-4110 Polyimide 1/2

Step #	Process	Parameters
18	UBM	(1) 2 min of ion milling at 1 kW. (2) Ti: 500 Å(2 Å/s), Cu: 5000 Å(2 Å/s), Au: 100 Å(2 Å/s
19	Lift-off	(1) Rinse in acetone/methanol/IPA (2) Rinse in DI water for 2 min (3) N_2 dry.
Release sample		
20	Spin coat PR	PR: AZ 9245 (1) 1700 rpm, for 5 s, Acc.=500 rpm/s (2) 2200 rpm, Acc.= 1000 rpm/s, time=25 s
21	Soft bake	110 °C on hot plate for 90 s
22	Dice	Dice wafers with diamond blade into individual samples
23	NaCl Solution	(1) 2M (Moles/L) solution of NaCl based on H_2O (2) Mix 117 g NaCl in 1 L DI water with stir bar.
24	Sample Release	(1) Connect ground to platinized titanium anode mesh (2) Apply +0.6 V to the sample
25	PR Strip	(1) Rinse in acetone/methanol/IPA (2) Rinse in DI water for 2 min (3) N_2 dry
Ground Plane Deposition		
26	Sample mount	Mount sample onto a support wafer with the backside exposed
27	Nb deposition	(1) 2 min of ion milling (2) Power= 1 kW/4 mTorr/sputtering time=30 min

Table A.4: Traveler of Nb Microstrip Resonators Fabricated on HD-4110 Polyimide 2/2

Step #	Process	Parameters
HD-4110 Polyimide Deposition		
1	Release layer	(1) 2 min of ion milling at 1 kW (2) 500 ÅCr/ 2000 ÅAl
2	Dehydration bake	120 °C for 30 min in oven
3	Polyimide spin	(1) 500 rpm, Acc.=500 rpm/s, time=5s, (2) 1700 rpm Acc.=1000 rpm/s, time=30s
4	Soft bake	hotplate bake at (1) 90 °C, time=3 min (2) 110 °C, time=3 min
5	Cure	(1) 90 °C, 30 min ramp at 10 °C/min,(1hr) (2) 120 °C, 30 min, ramp at 10 °C/min (1hr) (3) 375 °C, 60 min ramp at 20 °C/min (3hr) (4) Cool back to R.T in N_2
Signal Line Definition		
6	Dehydration bake	120 °C for 30 min in oven
7	PR definition	PR: AZ 9245 (1) 1700 rpm, for 5 s, Acc.=500 rpm/s (2) 2200 rpm, Acc.= 1000 rpm/s, time=25 s
8	Soft bake	110 °C on hot plate for 90 s
9	Mask alignment	Exposure time: 40 s Alignment gap: 30 µm
10	Development	(1) Developer. 1: 3 developer, 100 mL AZ400K: 300 mL DI H_2O (2) 2 min in developer (3) DI water rinse followed N_2 dry
11	Nb deposition	(1) 2 min of ion milling (2) Power= 1 kW/4 mTorr/sputtering time=30 min
12	Lift-off	(1) Rinse in acetone/methanol/IPA (2) Rinse in DI water for 2 min (3) N_2 dry.
Under Bump Metallization		
13	Dehydration bake	120 °C for 30 min in oven
14	PR definition	PR: AZ 9245 (1) 1700 rpm, for 5 s, Acc.=500 rpm/s (2) 2200 rpm, Acc.= 1000 rpm/s, time=25 s
15	Soft bake	110 °C on hot plate for 90 s
16	Mask alignment	Exposure time: 40 s Alignment gap: 30 µm
17	Development	(1) Developer. 1: 3 developer, 100 mL AZ400K: 300 mL DI H_2O (2) 2 min in developer (3) DI water rinse followed N_2 dry
18	UBM	(1) 2 min of ion milling at 1 kW (2) Ti: 500 Å(2 Å/s), Cu: 5000 Å(2 Å/s), Au: 100 Å(2 Å/s)
19	Lift-off	(1) Rinse in acetone/methanol/IPA (2) Rinse in DI water for 2 min (3) N_2 dry.

Table A.5: Traveler of Embedded Nb Microstrip Resonators Fabricated on HD-4110 1/2

Step #	Process	Parameters
Encapsulation Layer		
20	Dehydration bake	120 °C for 30 min in oven
21	Kapton tape	Apply Kapton tape dots onc the UBM pad area
22	Dehydration bake	120 °C for 30 min in oven
23	Polyimide spin (HD-4110)	(1) 500 rpm, Acc.=500 rpm/s, time=5s, (2) 1700 rpm Acc.=1000 rpm/s, time=30s
24	Soft bake	hotplate bake at (1) 90 °C, time=3 min (2) 110 °C, time=3 min
25	Kapton tape removal	Remove Kapton tape dots
26	Cure	(1) 90 °C, 30 min ramp at 10 °C/min,(1hr) (2) 120 °C, 30 min, ramp at 10 °C/min (1hr) (3) 225 °C, 60 min ramp at 20 °C/min (3hr) (4) Cool back to R.T in N_2
Release sample		
27	Spin coat PR	PR: AZ 9245 (1) 1700 rpm, for 5 s, Acc.=500 rpm/s (2) 2200 rpm, Acc.= 1000 rpm/s, time=25 s
28	Soft bake	110 °C on hot plate for 90 s
29	Dice	Dice wafers with diamond blade into individual samples
30	NaCl Solution	(1) 2M (Moles/L) solution of NaCl based on H_2O (2) Mix 117 g NaCl in 1 L DI water with stir bar.
31	Sample Release	(1) Connect ground to platinized titanium anode mesh (2) Apply +0.6 V to the sample
32	PR Strip	(1) Rinse in acetone/methanol/IPA (2) Rinse in DI water for 2 min (3) N_2 dry
Ground Plane Deposition		
33	Sample mount	Mount sample onto a support wafer with the backside exposed
34	Nb deposition	(1) 2 min of ion milling (2) Power= 1 kW/4 mTorr/sputtering time=30 min

Table A.6: Traveler of Embedded Nb Microstrip Resonators Fabricated on HD-4110 2/2

Step #	Process	Parameters
PI-2611 Polyimide Deposition		
1	Release layer	(1) 2 min of ion milling at 1 kW (2) 500 ÅCr/ 2000 ÅAl
2	Dehydration bake	120 °C for 30 min in oven
3	Adhesion promoter	VM652 Spin speed (1) 500 rpm for 5 s, Acc.=500 rpm/s, (2) 3000 rpm, Acc.=1000 rpm/s, time=30s
4	Soft bake	120 °C for 60 s on hot plate
5	Polyimide spin (PI-2611)	(1) 500 rpm, Acc.=500 rpm/s, time=5s, (2) 1600 rpm Acc.=1000 rpm/s, time=30s
6	Soft bake	hotplate bake at 120 °C, time=5 min.
7	Cure	(1) 90 °C, 30 min ramp at 10 C/min,(1hr) (2) 120 °C, 30 min, ramp at 10 °C/min, (1hr) (3) 350 °C, 60 min ramp at 20 °C/min, (3hr) (4) Cool back to R.T in N_2
8	Plasma	200 W for 30 s
9	Repeat step #4-9	
Signal Line Definition		
10	Dehydration bake	120 °C for 30 min in oven
11	PR definition	PR: AZ 9245 (1) 1700 rpm, for 5 s, Acc.=500 rpm/s (2) 2200 rpm, Acc.= 1000 rpm/s, Time=25 s
12	Soft bake	110 °C on hot plate for 90 s
13	Mask alignment	Exposure time: 40 s Alignment gap: 30 µm
14	Development	(1) Developer. 1: 3 developer 100 mL AZ400K: 300 mL DI H_2O (2) 2 min in developer (3) DI water rinse followed N_2 dry
15	Nb deposition	(1) 2 min of ion milling (b) Power= 1 kW/6.1 mTorr/sputtering time=30 min
16	Lift-off	(1) Rinse in acetone/methanol/IPA (2) Rinse in DI water for 2 min (3) N_2 dry.
Under Bump Metallization		
17	Dehydration bake	120 °C for 30 min in oven
18	PR definition	PR: AZ 9245 (1) 1700 rpm, for 5 s, Acc.=500 rpm/s (2) 2200 rpm, Acc.= 1000 rpm/s, Time=25 s
19	Soft bake	110 °C on hot plate for 90 s
20	Mask alignment	Exposure time: 40 s Alignment gap: 30 µm
21	Development	(1) Developer. 1: 3 developer 100 mL AZ400K: 300 mL DI H_2O (2) 2 min in developer (3) DI water rinse followed N_2 Dry

Table A.7: Traveler of Embedded Nb Microstrip Resonators Fabricated on PI-2611 Polyimide 1/2

Step #	Process	Parameters
22	UBM	(1) 2 min of ion milling at 1 kW. (2) Ti: 500 Å(2 Å/s), Cu: 5000 Å(2 Å/s), Au: 100 Å(2 Å/s
23	Lift-off	(1) Rinse in acetone/methanol/IPA (2) Rinse in DI water for 2 min (3) N_2 dry.
Encapsulation Layer		
24	Dehydration bake	120 °C for 30 min in oven
25	Kapton tape	Apply Kapton tape dots onc the UBM pad area
26	Dehydration bake	120 °C for 30 min in oven
27	Polyimide spin (PI-2611)	a. 8 µm encapsulation layer (1) 500 rpm, Acc.=500 rpm/s, time=5s (2) 2500 rpm Acc.=1000 rpm/s, time=30s b. 4 µm encapsulation layer (1) 500 rpm, Acc.=500 rpm/s, time=5s (2) 4000 rpm Acc.=1000 rpm/s, time=30s
28	Soft bake	hotplate bake at (1) 90 °C, time=3 min (2) 110 °C, time=3 min
29	Kapton tape removal	Remove Kapton tape dots
30	Cure	(1) 90 °C, 30 min ramp at 10 °C/min,(1hr) (2) 120 °C, 30 min, ramp at 10 °C/min (1hr) (3) 225 °C, 60 min ramp at 20 °C/min (2hr) (4) Cool back to R.T in N_2
Release sample		
31	Spin coat PR	PR: AZ 9245 (1) 1700 rpm, for 5 s, Acc.=500 rpm/s (2) 2200 rpm, Acc.= 1000 rpm/s, time=25 s
32	Soft bake	110 °C on hot plate for 90 s
33	Dice	Dice wafers with diamond blade into individual samples
34	NaCl Solution	(1) 2M (Moles/L) solution of NaCl based on H_2O (2) Mix 117 g NaCl in 1 L DI water with stir bar.
35	Sample Release	(1) Connect ground to platinized titanium anode mesh (2) Apply +0.6 V to the sample
36	PR Strip	(1) Rinse in acetone/methanol/IPA (2) Rinse in DI water for 2 min (3) N_2 dry
Ground Plane Deposition		
37	Sample mount	Mount sample onto a support wafer with the backside exposed
38	Nb deposition	(1) 2 min of ion milling (2) Power= 1 kW/6.1 mTorr/sputtering time=30 min

Table A.8: Traveler of Embedded Nb Microstrip Resonators Fabricated on PI-2611 Polyimide 2/2

Step #	Process	Parameters
Connecting Line Deposition		
1	Dehydration bake	120 °C for 30 min in oven
2	HMDS	110 °C on hot plate for 90 s
3	PR definition	PR: AZ 9245 (1) 1700 rpm, for 5 s, Acc.=500 rpm/s (2) 2200 rpm, Acc.= 1000 rpm/s, Time=25 s
4	Soft bake	110 °C on hot plate for 90 s
5	Mask alignment	Exposure time: 40 s Alignment gap: 30 µm
6	Development	(1) Developer. 1: 3 developer 100 mL AZ400K: 300 mL DI H_2O (2) 2 min in developer (3) DI water rinse followed N_2 dry
7	Metal deposition	(1) 2 min of ion milling at 1 kW. (2) Ti: 200 Å(2 Å/s), Cu: 10000 Å(2 Å/s), Au: 500 Å(2 Å/s
8	Lift-off	(1) Rinse in acetone/methanol/IPA (2) Rinse in DI water for 2 min (3) N_2 dry.
Pillars		
9	Dehydration bake	120 °C for 30 min in oven
10	Polyimide spin (HD-4110)	(1) 500 rpm, Acc.=500 rpm/s, time=5s, (2) 1400 rpm Acc.=1000 rpm/s, time=30s
11	Soft bake	Hotplate bake at (1) 90 °C, time=3 min (2) 110 °C, time=3 min
12	Mask alignment	Exposure time: 30 s, Alignment gap: 30 µm
13	Development	(1) Regular shake in PA-401D for 20 s (2) Ultrasonic in PA-401D for 30 s (3) PA-400R Rinse for 30 s followed N_2 dry
14	Cure	(1) 90 °C, 30 min ramp at 10 C/min,(1hr) (2) 120 °C, 30 min, ramp at 10 °C/min, (1hr) (3) 225 °C, 60 min ramp at 20 °C/min, (2hr) (4) Cool back to R.T in N_2
15	Dice	Dice wafers with diamond blade into individual samples

Table A.9: Fabrication Traveler of Cu-based Glass Connectors

Step #	Process	Parameters
HD-4110 Dielectric Definition		
1	Release layer	(1) 2 min of ion milling at 1 kW (2) 500 / 2000 ÅAl
2	Dehydration bake	120 °C for 30 min in oven
3	Polyimide spin (HD-4110)	(1) 500 rpm, Acc.=500 rpm/s, time=5s, (2) 1700 rpm Acc.=1000 rpm/s, time=30s
4	Soft bake	Hotplate bake at (1) 90 °C, time=3 min (2) 110 °C, time=3 min
5	Mask alignment	Exposure time: 30 s, Alignment gap: 30 µm
6	Development	(1) Regular shake in PA-401D for 20 s (2) Ultrasonic in PA-401D for 30 s (3) PA-400R Rinse for 30 s followed N_2 dry
7	Cure	(1) 90 °C, 30 min ramp at 10 °C/min,(1hr) (2) 120 °C, 30 min, ramp at 10 °C/min (1hr) (3) 375 °C, 60 min ramp at 20 °C/min (3hr) (4) Cool back to R.T in N_2
Signal Line Definition		
8	Dehydration bake	120 °C for 30 min in oven
9	PR definition	PR: AZ 9245 (1) 1700 rpm, for 5 s, Acc.=500 rpm/s (2) 2200 rpm, Acc.= 1000 rpm/s, time=25 s
10	Soft bake	110 °C on hot plate for 90 s
11	Mask alignment	Exposure time: 40 s Alignment gap: 30 µm
12	Development	(1) Developer. 1: 3 developer, 100 mL AZ400K: 300 mL DI H_2O (2) 2 min in developer (3) DI water rinse followed N_2 dry
13	Signal line deposition	(1) 2 min of ion milling (2) Power= 1 kW/6.1 mTorr/sputtering time=30 min (3) Au: 200 Å(2 Å/s)
14	Lift-off	(1) Rinse in acetone/methanol/IPA (2) Rinse in DI water for 2 min (3) N_2 dry.
Release sample		
15	Spin coat PR	PR: AZ 9245 (1) 1700 rpm, for 5 s, Acc.=500 rpm/s (2) 2200 rpm, Acc.= 1000 rpm/s, time=25 s
16	Soft bake	110 °C on hot plate for 90 s
17	Dice	Dice wafers with diamond blade into individual samples
18	NaCl Solution	(1) 2M (Moles/L) solution of NaCl based on H_2O (2) Mix 234 g NaCl in 2 L DI water with stir bar.
19	Sample Release	(1) Connect ground to platinized titanium anode mesh (2) Apply +0.6 V to the sample
20	PR Strip	(1) Rinse in acetone/methanol/IPA (2) Rinse in DI water for 2 min (3) N_2 dry

Table A.10: Fabrication Traveler of Nb/Au Microstrip Transmission Line on HD-4110 Polyimide 1/2.

Step #	Process	Parameters
Ground Plane Deposition		
21	Sample mount	Mount sample onto a support wafer with the backside exposed
22	Ground plane deposition	(1) 2 min of ion milling (2) Power= 1 kW/6.1 mTorr/sputtering time=30 min (3) Au: 200 Å(2 Å/s)

Table A.11: Fabrication Traveler of Nb/Au Microstrip Transmission Line on HD-4110 Polyimide 2/2.

Step	Process	Parameters and Details
Release Layer		
1	Metal deposition	Deposition of Cr/Al for release layer 500ÅCr/2000ÅAl, 2 min of ion milling
HD-4100 Protecive Base Layer		
2	Dehydration bake	110 °C for 30 min in oven
3	Polyimide spin	HD-4100: 1. Spin speed 500 rpm. Acc.=500 rpm/s time=5 s 2. 2000 rpm Acc.=1000 rpm/s Time=30 s
4	Soft bake 1	90 °C on hot plate for 100 s
5	Soft bake 2	100°C on hot plate for 100 s
6	Cure in N_2 oven	Profile 7: 1. 90 °C, 30 min ramp @ 10 °C/min 2. 120 °C, 30 min, ramp @ 10C/min 3. 375 °C, 60 min ramp @20 °C/min 4. Cool back to RT in N_2, Desired thickness: 10 µm
M0: Ground Plane		
7	Dehydration bake	110 °C for 30 min in oven
8	Spin coat	PR: AZ 9245 1. Spread: 1700 rpm for 5 s. 500 rpm/s 2. Spin speed: 2200 rpm Acc.=1000 rpm/s, Time=25 s
9	Soft bake	110 °C on hot plate for 90 s
10	Mask alignment	Exposure time: 45 s
11	Development	Developer. 1: 3 developer, 100 mL AZ400K: 300 mL DI H_2O 1 min 30 s in developer. Followed by 2 min DI water rinse. N_2 dry
12	Metal deposition	Deposition of Al/Nb/Al for bottom ground plane 200ÅAl/2500ÅNb/200ÅAl , 2 min of ion milling
13	Lift-off	Rinse in Acetone/IPA. Followed by 2 min DI water rinse/N_2 dry
M1: Electroplating Seed Layer		
14	Dehydration bake	110 °C for 30 min in oven
15	Spin coat	PR: AZ 9245 1. Spread: 1700 rpm for 5 s. 500 rpm/s 2. Spin speed: 2200 rpm Acc.: 1000 rpm/s, Time=25 s
16	Soft bake	110 °C on hot plate for 90 s
17	Mask alignment	Exposure time: 45 s
18	Development	Developer. 1: 3 developer, 100 mL AZ400K: 300 mL DI H_2O 1 min 30 s in developer Followed by 2 min DI water rinse. N_2 dry
19	Metal deposition	Deposition of Ti/Cu for via plating pads
20	Lift-off	Rinse in Acetone/IPA. Followed by 2 min. DI water rinse/N_2 dry

Table A.12: Fabrication Traveler of Stripline Transmission Lines 1/5.

M2: Electroplating vias - HD 4110 - 1		
21	Dehydration bake	110 °C for 30 min in oven
22	Polyimide spin	HD-4110: 1. Spin speed 500 rpm. Acc.=500 rpm/s time=5 s 2. 1900 rpm Acc.=1000 rpm/s Time=30 s
23	Soft bake 1	90 °C on hot plate for 180 s
24	Soft bake 2	110°C on hot plate for 180 s
25	Mask alignment	Exposure time: 18 s
26	Development	Develop: PA-401D and PA-400R. Followed by N_2 dry
27	Cure in N_2 oven	Profile 6: 1. 90 °C, 30 min ramp @ 10 °C/min 2. 120 °C, 30 min, ramp @ 10 °C/min 3. 225 °C, 60 min ramp @20 °C/min 4. Cool back to RT in N_2
28	O_2 plasma	1 min O_2 plasma
29	Seed layer clean	Clean seed layer in 50:1 (DI : HCl). 10 s
30	Electroplating	Electroplate Cu vias
M3: Signal Line		
31	Dehydration bake	110 °C for 30 min in oven
32	Spin coat	PR: AZ 9245 1. Spread: 1700 rpm for 5 s. 500 rpm/s 2. Spin speed: 2200 rpm Acc.=1000 rpm/s Time=25 s
33	Soft bake	110 °C for 30 min in oven
34	Mask alignment	Exposure time: 45 s
35	Development	Developer. 1: 3 developer, 100 mL AZ400K: 300 mL DI H_2O 1 min 30 s in developer. Followed by 2 min DI water rinse
36	Metal deposition	Deposition of Al/Nb/Al for signal line
37	Lift-off	Rinse in Acetone/IPA/Water. Use profilometer to determine Nb thickness

Table A.13: Fabrication Traveler of Stripline Transmission Lines 2/5.

Step	Process	Parameters and Details
M4: Electroplating Seed Layer - On Signal		
38	Dehydration bake	110 °C for 30 min in oven
39	HMDS	HMDS - 10 min.
40	Spin coat	PR: AZ 9245 1. Spread: 1700 rpm for 5 s. 500 rpm/s 2. Spin speed: 2200 rpm Acc.=1000 rpm/s Time=25 s
41	Soft bake	110 °C on hot plate for 90 s
42	Mask alignment	Exposure time: 45 s
43	Development	Developer. 1: 3 developer, 100 mL AZ400K: 300 mL DI H_2O. 1 min 30 s in developer Followed by 2 min DI water rinse. N_2 dry
44	Metal deposition	Deposition of Ti/Cu for via plating pads 500ÅTi/2000ÅCu, 2 min of ion milling
M5: Electroplating vias - HD 4110 - 2		
45	Dehydration bake	110 °C for 30 min in oven
46	Soft bake 1	90 °C on hot plate for 180 s
47	Soft bake 2	110 °C on hot plate for 180 s
48	Mask alignment	Exposure time: 18 s
49	Development	Develop: PA-401D and PA-400R. Followed by 2 min DI water rinse. N_2 dry
50	Cure in N_2 oven	Profile 6: 1. 90°C, 30 min ramp @ 10°C/min 2. 120°C, 30 min, ramp @ 10°C/min 3. 225°C, 60 min ramp @20°C/min 4. Cool back to RT in N_2 Desired thickness: 20 µm
51	O_2 plasma	1 min O_2 plasma
52	Seed layer clean	Clean seed layer in 50:1 (DI : HCl). 10 s
53	Electroplating	Electroplate Cu vias

Table A.14: Fabrication Traveler of Stripline Transmission Lines 3/5.

Step	Process	Parameters and Details
M6: Top Ground		
54	Dehydration bake	110 °C for 30 min in oven
55	Spin coat	PR: AZ 9245 1. Spread: 1700 rpm for 5 s. 500 rpm/s 2. Spin speed: 2200 rpm Acc.=1000 rpm/s Time=25 s
56	Soft bake	110 °C for 30 min in oven
57	Mask alignment	Exposure time: 45 s
58	Development	Developer 1: 3 developer, 100 mL AZ400K: 300 mL DI H_2O 1 min and 30 s in developer. Followed by 2 min DI water rinse
59	Metal deposition	Deposition of Al/Nb/Al for top ground 200ÅAl/2500ÅNb/200ÅAl, 2 min of ion milling
60	Lift-off	Rinse in Acetone/IPA/Water Use profilometer to determine Nb thickness
HD-4100 Protecive Top Layer		
61	Dehydration bake	110 °C for 30 min in oven
62	Polyimide spin	HD-4100: 1. Spin speed 500 rpm. Acc.=500 rpm/s time=5 s 2. 6000 rpm Acc.=1000 rpm/s Time=30 s
63	Soft bake 1	90 °C on hot plate for 100 s
64	Soft bake 2	100 °C on hot plate for 100 s
65	Mask alignment	Exposure time: 18 s
66	Development	Develop: PA-401D and PA-400R. Followed by 2 min DI water rinse. N_2 dry.
67	Cure in N_2 oven	Profile 6: 1. 90 °C, 30 min ramp @ 10 °C/min 2. 120 °C, 30 min, ramp @ 10 °C/min 3. 225 °C, 60 min ramp @20 °C/min 4. Cool back to RT in N_2 Desired thickness: 4 µm

Table A.15: Fabrication Traveler of Stripline Transmission Lines 4/5.

Step	Process	Parameters and Details
M7: UBM Contact to Signal Line		
68	Dehydration bake	110 °C for 30 min in oven
69	Spin coat	PR: AZ 9245 1. Spread: 1700 rpm for 5 s, 500 rpm/s 2. Spin speed: 2200 rpm, Acc.=1000 rpm/s Time=25 s
70	Soft bake	110 °C on hot plate for 90 s
71	Mask alignment	Exposure time: 45 s
72	Development	Developer. 1: 3 developer, 100 mL AZ400K: 300 mL DI H_2O 1 min and 30 s in developer. Followed by 2 min DI water rinse. N_2 dry
73	Metal deposition	Deposition of Ti/Au for UBM 500ÅTi/2500ÅAu, 2 min of ion milling
74	Lift-off	Rinse in Acetone/IPA/Water Use profilometer to determine UBM thickness
Release sample		
75	Dehydration bake	110 °C for 30 min in oven
76	Spin coat	PR: AZ 9245 1. Spread: 1700 rpm for 5 s . 500 rpm/s 2. Spin speed: 2200 rpm Acc.=1000 rpm/s Time=25 s
77	Soft bake	110 °C on hot plate for 90 s (1 minute and 30 s)
78	Dice	Dice wafers with silicon blade
79	Release solution	Make solution consisting of 700 mL of H_2O, 81.9 g of Nacl and mix with stir bar
80	Release sample	Bias wafer at 0.6 V

Table A.16: Fabrication Traveler of Stripline Transmission Lines 5/5.